# Design and Characterization of Multiband and Broadband Printed Patch Antennas for Wireless Applications

*A Thesis*

*Submitted in Partial Fulfillment of the Requirements for the Award of the Degree of*

**DOCTOR OF PHILOSOPHY**

By

**BUDHADEB MAITY**

SCHOOL OF ENERGY SCIENCE AND ENGINEERING

INDIAN INSTITUTE OF TECHNOLOGY GUWAHATI

GUWAHATI - 781039, ASSAM, INDIA

MAY 2023

*Dedicated*

***To***

*My supervisor* ***Prof. Sisir Kumar Nayak***

*for his guidance and support*

*&*

*My* ***Parents****,*

*my wife* ***Debasmita****, my* ***brother****, my* ***sister-in-law****,*

*my* ***sisters*** *and my three little nieces* ***Chinky****,* ***Pinky***

*and* ***Rinky***

*for their blessings, support and love*

# Certificate

This is to certify that the thesis entitled **"Design and Characterization of Multiband and Broadband Printed Patch Antennas for Wireless Applications"**, submitted by **Budhadeb Maity**, a research scholar in the *School of Energy Science and Engineering, Indian Institute of Technology Guwahati*, for the award of the degree of **Doctor of Philosophy**, is a record of an original research work carried out by him under my supervision and guidance. The thesis has fulfilled all requirements as per the regulations of the institute and has reached the standard needed for submission. The results embodied in this thesis have not been submitted to any other University or Institute for the award of any degree or diploma.

Dated:

Guwahati.

Dr. Sisir Kumar Nayak
Professor
Dept. of Electronics and Electrical Engg.
Indian Institute of Technology Guwahati
Guwahati - 781039, Assam, India.

# Acknowledgments

First and foremost, I would like to express my deep and sincere regard for my best teacher, *i.e.,* my supervisor ***Prof. Sisir Kumar Nayak*** for providing me the opportunity, support, and freedom to carry on this research work. His encouragement, dedication, and hard work helped me to keep pushing myself. His timely corrections of my research articles and reports made me complete my research on time with a lot of confidence. He made a researcher out of an engineer and also taught me to value time. I want to thank him again from the bottom of my heart. I want to thank my doctoral committee members **Prof. Rakhesh Singh Kshetrimayum, Prof. Harshal B. Nemade**, and **Dr. Mahima Arrawatia** for their advice and suggestions throughout my research work.

I would also like to thank *Prof. Amalendu Patnaik*, Indian Institute of Technology Roorkee, Roorkee, India for providing measurement facilities at his anechoic chamber. Thanks also to *Prof. Animesh Biswas*, Indian Institute of Technology Kanpur, Kanpur, India for providing measurement facilities at his anechoic chamber. I am especially indebted to *Dr. T Tiwari*, Program Director In-charge and *Dr. Narugopal Nayek*, Scientist D, Society for Applied Microwave Electronics Engineering & Research (SAMEER), Centre for High Power Microwave Tube and Component Technology, (CHMTCT), IIT Guwahati, Assam, India for carrying out measurement facilities in their laboratory towards the furtherance of this research work.

Last, but not least I would express my sincere gratitude to my family for their love, sacrifice, and moral support for without their continued support this work would never have been possible. Also, my sincere gratitude goes to *Mr. Anil Kumar Nayak*, Indian Institute of Technology Roorkee, Roorkee, India whose initial help and encouragement motivated me in this work. Finally, my gratitude goes to Shashank Satish Kulkarni who kept me company throughout the day and night in our microwave and antenna lab for the measurement of research work. It inspired me to carry my work diligently and we have yet to learn so many things from our mother nature and an array antenna is one such inspired beautiful gift. We met many great people in our research area and held an excellent discussion. I thank Niharika Baruah, Shashank Kumar, Kanumuri Deepak, Sangineni Rohith, and Ambuj Kumar who made my research life enjoyable

and taught me how to laugh on oneself.

Lastly, I would like to thank my parents, my wife, my brother, my sister-in-law, and my sisters, who believed in me and always motivated me to not worry and keep on doing the work. I am also thankful to my three beautiful nieces who brought more love to my life.

***Budhadeb Maity***

# Abstract

In the last decade, wireless communication systems have spread widely and become an essential tool in every days life. A tremendous increase in the demand for small Personal Mobile Devices (PMD) has been observed with wide model ranges and applications. A novel approach is presented to make compact multiband, broadband, ultra wideband (UWB), CP band microstrip patch antennas (MPAs), and array antenna with improved stable radiation patterns at a higher frequency for wireless communication systems. The challenges with the fabrication and utilization of traditional MPA and array antenna designs at UWB frequency are solved by the method presented here. Also, UWB is rapidly improving as a high-data-rate wireless communication technology. Like in regular wireless communication systems, an antenna is a very important part of UWB systems. But designing a UWB antenna is harder than designing a narrow-band antenna. A good UWB antenna should be able to work over the Federal Communications Commission's (FCC) ultra-wide bandwidth at the same time, it must have good radiation properties across the entire frequency range.

This thesis focuses on the design and analysis of small multiband, broadband, UWB, and CP band antennas. Broadband and UWB fundamentals and antenna theory have both been the subject of studies. In recent years, the slotted, slit, defected ground structure (DGS), and array patch antenna has been known to be a flexible, low-profile, and cost-effective antenna that can be fine-tuned for UWB operations. The main objective of this thesis is to come up with a practical way to design slotted, slit, and array antennas that works well with the use of full wave analysis methods to show how the design works physically.

A first approach addressed in this thesis work is the application of a technique which includes a double annular ring slot, two L-shaped slots, one I-shaped slot, and a DGS based on an ellipse-shaped slit structure for the purpose of reducing antenna size. Using this methodology one electrically small antenna for triple band for WLAN/WiMAX/C-band downlink satellite communications that can cover almost the entire commercial available frequency bands were developed and their performances are discussed. To reduce the size and enhance the impedance bandwidth (IBW) of the designed antenna using symmetrical staircase-shaped notches, a study is carried out in the next part.

The second part of this thesis work examines the design process for a slotted radiator that will be integrated into a small patch. The main objective of the proposed design structure is to reasonably maintain the radiation properties of the antenna by compacting, enhancing IBW, and controlling the coupling coefficient due to the fraction of the $TM_{01}$ mode current introduced by the C-shaped slot. As a result, the proposed antenna is shown to have a wider IBW (1.55-16.95 GHz (166.51%)), enhanced gain (2-8.3 dBi), and improved impedance matching. The transmission line model (TLM) of the proposed antenna, which depicts the behavior of the antenna based on the influence of each constituent, is provided. It is noted that the properties of the TLM model closely match with the outcomes of simulations performed using the CST simulator. The prototype is successfully implemented, fabricated, and the results of the experiment are compared with the simulation results. To further reduce the size and enhance the IBW of the designed star-shaped monopole antenna and maintain better gain, a study is carried out in the next work.

The third part of this thesis discusses the compact UWB CPW-fed 9-point star-shaped antenna. A novel concept for efficiently using the reduced space and enhanced IBW (measured IBW 2.2-12.21 GHz) for the proposed antenna is discussed in detail. The functioning theory, design process, simulated, and measured results of the proposed antenna are presented. To study the linear polarization to circular

polarization (CP) using traveling wave series-fed circular slits array with DGS and compact structure, a study is carried out which is discussed in the next work.

In the fourth part of this thesis discusses a compact dual-circular polarized traveling waves series-fed circular slit microstrip array (TWSCSMA) antenna. The proposed design gives the left-hand circular polarization (LHCP) wave when the input RF signal for port 1 has a 45° phase increment in clockwise direction. Similarly, the right-hand circular polarization (RHCP) wave is generated, when the input RF signal for port 2 has a 45° phase increment in anticlockwise direction. Using this concept dual-CP radiation can be realized. In this design, due to the two ports formation of the traveling wave series-fed circular slit microstrip array antenna, it gives dual-CP with minimum axial ratio quad-band and two wider IBWs. To further enhance the impedance as well as the axial ratio bandwidth of the proposed monopole CP antenna with extended ground loop plane and compact structure is presented in the final work.

Finally, an inverted L-shaped hook monopole (ILSHM) antenna is designed and fabricated to get UWB impedance and axial ratio bandwidth for CP operational bands. The design process of making CPW-fed two L-shaped conductor strips with two rectangular slits is discussed. By analyzing the simulation and experiment results, it is observed that the proposed antenna shows a compact size, UWB IBW and UWB axial ratio bandwidth, and small bandwidth ratio $BR|_{(10/3)dB} \approx 1.121$. It has demonstrated the essence of the design of a UWB CP antenna for wireless applications.

# Contents

# List of Figures

# List of Tables

# List of Common Abbreviations

| | |
|---|---|
| TV | Television |
| PIFA | Planar inverted-F-shaped antenna |
| PCB | Printed circuit board |
| RFID | Radio frequency identification |
| MIMO | Multiple-input multiple-output |
| GPS | Global positioning system |
| CP | Circular polarized |
| FCC | Federal communications commission |
| WLAN | Wireless local area network |
| IEEE | Institute of Electrical and Electronics Engineers |
| GSM | Global System for Mobile Communications |
| UMTS | Universal Mobile Telecommunications System |
| WiMAX | Worldwide Interoperability for Microwave Access |
| DVB | Digital Video Broadcasting |
| PCS | Personal Communication System |
| IMT | International Mobile Telecommunication |
| LTE | Long Term Evolution |
| LoRa | Long Range Radio |
| WBAN | Wireless Body Area Network |
| MEMs | Microelectromechanical systems |
| AWGN | Additive White Gaussian Noise |
| SNR | Signal-to-noise ratio |

| | |
|---|---|
| UWB | Ultrawide band |
| LP | Linear polarized |
| TLM | Transmission line model |
| MMIC | Monolithic microwave integrated circuit |
| CPW | Coplanar waveguide |
| SRT | Sequential rotation technique |
| BDR | Bandwidth dimension ratio |
| Wi-Fi | Wireless Fidelity |
| GHz | Gigahertz |
| THz | Terahertz |
| BW | Bandwidth |
| VSWR | Voltage standing wave ratio |
| CST | Computer simulation technology |
| AWR | Applied wave research |
| RLC | Resistor Inductor Capacitor |
| SSMA | Star shaped monopole antenna |
| PHRS | Partly hexagonal ring slit |
| QCRS | Quarter circular ring slit |
| DGS | Defected ground structure |
| TWSCSMA | Traveling wave series fed circular slit microstrip array |
| LHCP | Left hand circular polarization |
| RHCP | Right hand circular polarization |
| ILSHM | Inverted L-shaped hook monopole |
| TBSA | Triple band slot antenna |
| DARS | Double annular ring slot |
| ESS | Ellipse shaped slit |
| NI | National Instrumentation |
| EM | Electromagnetics |

| | |
|---|---|
| TM | Transverse magnetic |
| FR4 | Flame retardant 4 |
| VNA | Vector network analyzer |
| CP | Coaxial probe |
| CFR | Center frequency ratio |
| MS | Microstrip line |
| SSS | Symmetrical staircase shaped |
| CMT | Coupled mode theory |
| FBW | Fractional bandwidth |
| PG | Peak gain |
| GV | Gain variation |
| QCS | Quarter circular slit |
| SMA | Sub Miniature version A |
| ARBW | Axial ratio bandwidth |
| IBW | Impedance bandwidth |
| SRR | Split ring resonator |
| AR | Axial ratio |
| MLR | Machine learning regression |
| RF | Radio frequency |
| SCSA | Series-fed circular slit array |
| QLR | Quasi lumped resonator |
| ANN | Artificial neural network |
| DTR | Decision tree regression |
| DFR | Decision forest regression |
| MATLAB | Matrix Laboratory |
| MSE | Mean squared error |
| RMSE | Root mean squared error |
| RAE | Relative absolute error |

| | |
|---|---|
| LM | Levenberg Marquardt |
| MLPs | Multilayer perceptrons |
| MLPDN | Microstrip line power divider network |
| BR | Bandwidth ratio |
| AUT | Antenna under test |
| DRGH | Double ridge guide horn |

# List of Symbols

| | |
|---|---|
| $E$ | Time varying electric field |
| $H$ | Time varying magnetic field |
| $C$ | Channel capacity |
| $B$ | Channel bandwidth |
| $\eta$ | Free space impedance |
| $t$ | Time varying component |
| $r$ | Distance from the transmit antenna |
| $\theta$ | Vertical angle from the antenna |
| $\psi$ | Horizontal angle from the antenna |
| $f$ | Frequency |
| $\alpha_s$ | Antenna loss factor |
| $c$ | Speed of light |
| $S_{11}$ | Reflection coefficient |
| $dB$ | Decibel |
| $f_{ext}$ | External current path frequency of the antenna |
| $L_{path}$ | External path length of the antenna |
| $\epsilon_{eff}$ | Effective dielectric constant |
| $f_r$ | Resonant frequency |
| $f_{rp1}$ | First resonant peak frequency |
| $f_{rp2}$ | Second resonant peak frequency |
| $f_{rp3}$ | Third resonant peak frequency |
| $f_{rp4}$ | Fourth resonant peak frequency |

| | |
|---|---|
| $f_{rp5}$ | Fifth resonant peak frequency |
| $C_{eq}$ | Equivalent capacitance |
| $\beta$ | Propagation constant |
| $\lambda g$ | Guided wavelength |
| $\lambda o$ | Free space wavelength |
| $k$ | Coupling coefficient |
| $\omega_+$ | Coupled mode angular frequency |
| $\omega_-$ | Uncoupled mode angular frequency |
| $l_1$ | Slot length |
| $\mathbf{E}$ | Electric field vector |
| $\mathbf{H}$ | Magnetic field vector |
| $\epsilon_r$ | Relative permittivity |
| $\mu_r$ | Relative permeability |
| $S_{11}$ | Ports reflection coefficient |
| $S_{21}$ | Transmission coefficient |
| J | Electric coupling admittance inverter |
| $\omega$ | Angular frequency |
| M | Magnetic coupling admittance inverter |
| $K$ | Un-normalized coupling coefficient |
| $\lambda_{LfL}$ | Electrical length of the antenna |
| $\lambda_{WfL}$ | Electrical width of the antenna |
| nH | Nanohenry |
| pF | Picofarad |
| $J_1$ | Bessel function |
| $G(\theta, \phi)$ | Gain of the antenna |
| $D(\theta, \phi)$ | Directivity of the antenna |
| $\Gamma$ | Reflection coefficient of the antenna |
| $L$ | Inductor |

| | |
|---|---|
| $C$ | Capacitance |
| $\lambda$ | Operating frequency |
| $E_\phi$ | Far-field electric field component in H–plane |
| $E_\theta$ | Far-field electric field component in E–plane |
| $l$ | Length of the waveguide |
| $\mathbf{k}$ | Wave number |
| $G_r$ | Gain of the receiver antenna |
| $\eta_c$ | Conversion efficiency |
| $N$ | Number of circular elements |
| $\theta_p$ | Angle between adjacent elements |
| $\varphi_{en}$ | Excitation current phase of the $n^{th}$ element |
| $\boldsymbol{E}_{RHCP}$ | Electric field vector component of the RHCP |
| $\boldsymbol{E}_{LHCP}$ | Electric field vector component of the LHCP |
| $\boldsymbol{E}_{HOR}$ | Complex voltage in the horizontal plane |
| $\boldsymbol{E}_{VER}$ | Complex voltage in the vertical plane |
| $\alpha$ | Power coupling coefficient |

# 1

# Introduction

## Contents

## 1.1 Introduction

The need for high-speed data services has grown over the last few years as a result of the exponential growth of wireless communication technology and internet services. Due to this, the number of users have increased significantly, and it is clear that future communication networks will suffer from severe traffic congestion. The biggest difficulty for manufacturers and service providers is to increase the network capacity to provide efficient communication services to the users. Another major problem is the reduction of network devices. The signal quality is deteriorated in wireless communication services due to problems such as multipath fading, co-channel interference, and delay spread [1]. Researchers are investigating a variety of strategies to improve the efficiency of communication networks. The most advanced and rapidly expanding technology in the communication sector is wireless communication, which allows data to be transported from one end to the other without the need for physical connections, as depicted in Figure 1.1. It's interesting to note that every communication system relies on the transmission of signals (or information) through a transmitter and receiver, which can be placed anywhere from a few meters to thousands of kilometers away, like in satellite and television (TV) remote control systems, respectively [2]. Antennas are utilized to transmit and receive signals because no directed medium is employed. An antenna is a component that transforms electrical signals into electromagnetic waves on both the transmitter and receiver ends. There are numerous varieties of antennas on the market, including horn antennas, dipole antennas, planar inverted-F antenna (PIFA), microstrip patch antennas, etc. [3]. Low-profile antennas are desired today in communication systems to achieve great performance over a wide frequency range. Microstrip patch antennas are becoming increasingly popular in this field as a result of their numerous benefits, including their low profile, low cost, planar structure, high robustness, conformability to curved surfaces, ease of installation, ease of fabrication, and low cost due to their simple PCB fabrication. Since then, microstrip patch antennas have attracted interest due to their many benefits, including their light weight, ease of manufacture utilizing PCB technology, low cost, compact design, and simplicity of microwave circuit integration [4].


**Figure 1.1:** Wireless communication networks.

More multifunctional systems are needed today, which increases the demand for small mobile terminals like smart phones, handheld wireless devices for internet access, short- and long-range communication equipment, radio frequency identification (RFID), TV, and multiple-input multiple-output (MIMO) systems [5], as well as satellite communications, remote sensing, radar systems, surveillance, missile guidance, and other similar technologies. Similar to this, small-size antennas are needed for devices and equipment used for GPS, navigation, and data transfer. The development of low-profile, compact, multiband, broadband, ultra-wideband, and circular polarized (CP) antennas continues to be a challenge for the community due to these applications and the expansion of wireless devices. The rectangular and circular shorting posts [6], meandering slots at the non-radiating edges of the patch [7], and low and high permittivity substrates of varying thickness loading [8] are used to reduce the size and volume of antennas. Low radiation efficiency, small bandwidth, and undesirable radiation patterns are frequently the

results of the above mentioned antenna. As a result, employing periodic structures to reduce antenna profiles has recently attracted significant interest to enhance antenna performance.

## 1.2 Wireless Communication Services

There are several uses of antennas across the entire electromagnetic spectrum. The Federal Communications Commission (FCC), an independent regulatory body established under the authority of the Communications Act of 1934, assigned various frequency bands for various applications in order to avoid congestion, and minimize multipath interference or fading from multiple users during the communication process. Table 1.1 lists the various frequency bands that the governing council has designated, along with the category of antennas that correspond to each band. The wireless local area network (WLAN) applications represent a significant advancement in antenna technology and the growth of their importance in the future. Figure 1.2 shows the development of WLAN communications. The IEEE 802.11n standard required that MIMO techniques be used, which indicates that a device must have more than one antenna [9]. As part of the more recent IEEE 802.11ac standard, improvements to 802.11n are currently being worked on.

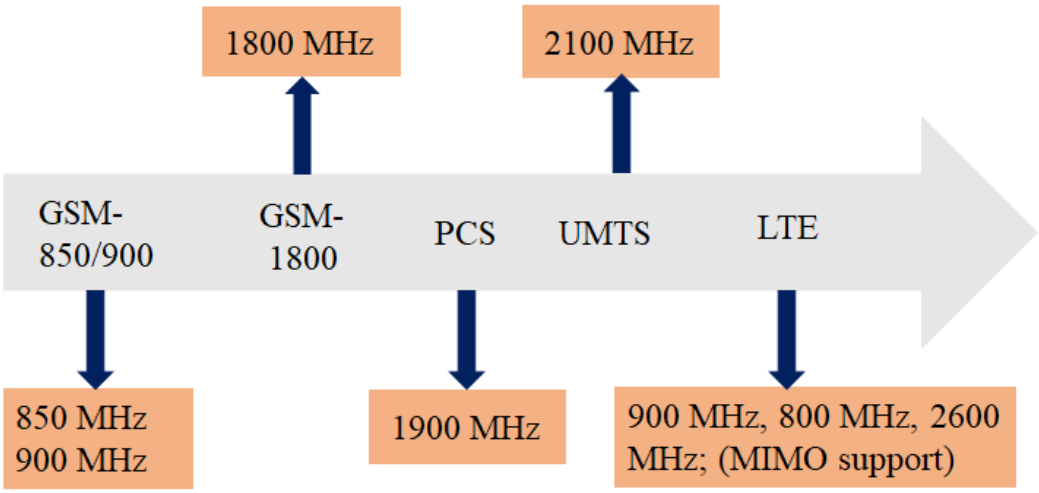


**Figure 1.2:** The evolution of the wireless communication standards [7].

**Table 1.1:** Different wireless standards used with a frequency of operation and bandwidth [5], [6]

| Wireless standards | Frequency Band (MHz) | Occupied BW (MHz) | Commonly used antennas |
|---|---|---|---|
| Digital Video Broadcasting (DVB-H) | 470–702 | 232 | Compact printed antennas |
| Radio Frequency Identification (RFID) | 868–930/<br>2446–2454 | 62/<br>8 | Loops, Folded-F, Patch and Monopole |
| Global System for Mobile (GSM-900) | 890–960 | 70 | Dipole, patch arrays and Monopoles |
| Global System for Mobile (GSM-1800) | 1710–1805 | 95 | |
| Global System for Mobile (GSM-1900) | 1850–1990 | 140 | |
| Global Positioning System (GPS1400, GPS1575) | 1227–1575/<br>1565–1585 | 348/<br>20 | Microstrip patch or bifilar helix |
| Personal Communication System (PCS 1900) | 1850–1990 | 140 | Conformal Slot and Slot-Dipole Antennas |
| International Mobile Telecommunication -2000 (3G IMT-2000) | 1885–2200 | 315 | |
| Universal Mobile Telecommunication Systems (UMTS 2000) | 1920–2170 | 250 | |
| WLAN ISM-2.4 (Bluetooth)/ ISM-5.2, ISM-5.8 Industrial/ Scientific, Medical (ISM) | 2400–2484/<br>5150–5350/<br>5725–5825 | 84/<br>200/<br>100 | Dipole, patch arrays, Microstrip patch |
| WiMAX (Worldwide Interoperability for Microwave Access) | 2500–2690/<br>3400–3690/<br>5250–5850 | 190/<br>290/<br>600 | Dipole, patch arrays, Microstrip patch |
| Bluetooth | 2400–2500 | 100 | |
| LTE (Long Term Evolution) | 1710–1755/<br>1710–1785/<br>1850–1910/<br>1920–1980 | 45/<br>75/<br>60/<br>60 | Microstrip patch |
| LoRa (Long Range Radio) in Europe, India, United States, South Korea | 863–870/<br>865–867/<br>902–928/<br>920–923 | 07/<br>02/<br>26/<br>03 | |
| WBAN | 2360–2400 | 40 | Microstrip patch, wearable antenna |

## 1. Introduction

Recent advancements in wireless technology have led to a wider range of working frequencies and narrow assigned frequency bands, which increases the need for larger antennas and larger devices overall, particularly in handheld and portable devices. As a result, physical size has become more crucial in antenna design. Designing small-size antennas or antenna arrays that can function at multiple commercial frequency bands, including the Global System for Mobile Communications (GSM), Universal Mobile Telecommunications System (UMTS), WLAN, and Worldwide Interoperability for Microwave Access (WiMAX) applications, is becoming more and more popular in the field of antenna engineering. The key design considerations for practical applications are size minimization, improved bandwidth, multimode operation, circular polarization, etc.

The need for low-profile, compact size, planar multi-band antennas are growing daily in wireless communication applications. The design problems for portable, wireless devices that are lightweight and small never end. Recently, a variety of low-profile efficient radiators that are simple to produce and affordable have been developed. Due to some drawbacks including narrow bandwidth and larger size, the standard microstrip patch is not a strong fit for wireless applications. As a result, new novel strategies are being looked into for the multiband antenna that operates at a smaller size. Other microstrip devices with various geometric radiators are suitable possibilities for microstrip Planar Inverted F-Antennas (PIFA).

The main objective is to design antennas for wireless communication applications where the space value of the antenna is quite constrained while it reserves the characteristics of multiband, wideband, lightweight, affordable, robust, diverse, packaging capabilities, and the ability to integrate microelectromechanical systems (MEMs) for smart antenna systems. These antenna types and their developments are the focus of many literary study types. The difficulty of designing a compact, multiband antenna that can simultaneously fit in multiple wireless communication systems is demonstrated in the previous research work. Acceptable antenna bandwidth was reached in all earlier configurations. However, in contrast to directional antennas, several other wireless communication applications need for broadband and even ultra-wideband antennas. Because of the growing need for communication bandwidth to support high-speed data appli-

cations like video-on-demand, broadband antennas are in great demand. The Shannon-Nyquist criterion relates the bandwidth and signal-to-noise ratio (SNR) to achieve the maximum data rate or capacity for the ideal band-limited additive white Gaussian noise (AWGN) channel, as given in (1).

$$C = B \log_2(1 + SNR) \tag{1.1}$$

where $B$ is the channel bandwidth and $C$ is the maximum transmission data rate or channel capacity. According to (1), increasing the bandwidth occupied or transmission power will increase the transmit data rate. Since many portable devices run on batteries, it is difficult to increase the transmission power, and interference should also be avoided. Thus, a large frequency bandwidth will be the solution to achieve a high data rate. Instead of modulating sinusoidal signals, ultra-wideband (UWB) technology relies on sending pulses with widths in order of nanoseconds or even picoseconds, which enlarges its spectrum and tunes its power density above the noise level (FCC, 2002). This type of transmission has several benefits, including resistance to jamming and the capacity to counteract fading brought on by multipath effects. Additionally, the UWB spectrum contains low-frequency components, which have the ability to penetrate. The UWB technology has several uses in wireless communications as a result of the above mentioned benefits. Because UWB offers security and low power consumption, the portable terminals' batteries last longer. However, there are many difficulties with UWB technology and broadband communication systems, including polarization purity, radiation pattern stability, and other issues.

The above two paragraphs illustrate the design of compact, multiband, and ultra-wideband antennas that can simultaneously operate in multiple wireless communication systems. In a wireless communication system, when the gain of the transmission antennas is increased, the range of wireless coverage is improved, mistakes are reduced, achievable bit rates are increased, and the battery consumption of wireless communication devices is decreased. Matching the polarization of the transmitting and receiving antennas is one of the key variables in boosting this gain. The transmitter and receiver must have the same axial ratio, spatial orientation, and sense of polarization in order to achieve this polarization matching. Since wireless devices

frequently alter their location and orientation, it is almost difficult to match the spatial orientation of the wireless devices in mobile and portable wireless applications. Circularly polarized (CP) antennas can be matched in a range of orientations because the orthogonal components of along emitted waves oscillate their own axis which are perpendicular to the direction of transmission. Compared to their linearly polarized (LP) counterparts, the CP band antennas are more suitable. The CP antenna is becoming more and more used in wireless communication systems because of its benefits of overcoming multipath fading, non-line-of-sight applications, and giving superior mobility than the linear polarized antennas. In recent years, numerous researchers have focused on designing CP antennas and employing various approaches to reduce their size. Dipole, horn, microstrip, and dielectric resonator antennas are only a few examples of the many different antenna configurations. However, the large antenna apertures produced by these designs prevent them from exhibiting stable radiation patterns, which is a crucial prerequisite for wireless communication technology. Additionally, by integrating an additional antenna element to create an antenna array, the range of operation of multiband, broadband, UWB, and CP band antennas is enhanced. However, the volume that is used for antenna design keeps getting smaller as people want a portable wireless device. Theoretically, it is generally known that as the size of the antenna is decreased, its performance degrades in turn the following parameters suffer:

- Decreased efficiency (or gain)
- A smaller range
- Lower effective bandwidth
- More fine tuning
- Increase sensitivity to PCB and component spread
- Increase sensitivity to external factors

The fundamental performance of electrically compact antennas is already being pushed to its absolute limit by current internal antenna designs. A zeroth-order resonating antenna

exhibits minimal dissipative losses and supports zeroth order propagating mode. In order to design compact, multiband, broadband, UWB, and CP band antennas using various structural designs, further research work needs to be carried out.

## 1.3 Free Space, Fixed Transmit and Receive Antennas

First, consider a fixed antenna radiating EM waves into free space. In the far-field, the electric field and magnetic field at any given location are perpendicular both to each other and related by free-space wave impedance, i.e.,

$$E = \frac{H}{\eta} \tag{1.2}$$

where $E$ and $H$ are the time-varying electric and magnetic fields, respectively. The free space impedance $\eta \approx 377\ \Omega$.

A transmitted sinusoid $\cos 2\pi ft$, the electric far-field at time $t$ can be expressed as:

$$E(f, t, (r, \theta, \psi)) = \frac{\alpha_s(\theta, \psi, f) \cos 2\pi f(t - r/c)}{r} \tag{1.3}$$

Here, $(r,\ \theta,\ \psi)$ represents the point $\mathbf{u}$ in space at which the electric field is being measured, where $r$ is the distance from the transmit antenna to $\mathbf{u}$ and where $(\theta,\ \psi)$ represents the elevation and azimuth angles. The constant $c$ is the speed of light, and $\alpha_s(\theta, \psi, f)$ is the scaling factor for antenna losses.

It is observed that, with increase in distance $r$ increases, the electric field decreases as $r^{-1}$, and thus the power per square meter in the free space wave decreases as $r^{-2}$. This is expected since if we look at concentric spheres of increasing radius $r$ around the antenna, the total power radiated through the sphere remains constant, but the surface area increases as $r^2$. Thus, the power per unit area must decrease as $r^{-2}$. Next, suppose there is a fixed receive antenna at the location $\mathbf{u} = (r,\ \theta,\ \psi)$. The received waveform in response to the above transmitted sinusoid is then

$$E_r(f, t, \mathbf{u}) = \frac{\alpha(\theta, \psi, f) \cos 2\pi f(t - r/c)}{r} \tag{1.4}$$

where $\alpha(\theta, \psi, f)$ is the product of the antenna patterns of transmitting and receiving antennas in the given direction. Placing a receive antenna there changes the electric field in the vicinity of **u**, but this is taken into account by the antenna pattern of the receive antenna. Therefore, using this concept, a new technique for designing small size multiband, broadband, UWB, and CP band antennas needs to be investigated, which is the key motivation of this thesis work.

## 1.4 Literature Survey

As the demand for low-profile compact planar multi-band, wideband, CP band antennas has increased in wireless communication technology and high-speed internet services, there is a need to develop a compact and wider bandwidth antenna with a high gain for an entire band of frequency operation and better cross-polarization levels regardless of the direction of propagation. In order to replace narrow bandwidth, larger size, and low gain antennas with a compact superior antenna performance for wireless communication applications, the research work has advanced to the next stage. The goal of the literature review is to lay the groundwork for an inquiry into how reported antennas are used, along with their operating bands and physical characteristics. In preview of this, a literature review on the slot, slit, monopole, defective ground structure, and array antennas as they relate to microstrip line and coplanar waveguide (CPW)-fed patch antennas utilized for multiband, broadband, UWB, and CP band applications are presented below.

### 1.4.1 Compact and Multiband Antennas

Numerous antenna researchers were attracted to the compact, multiband, low-cost, lightweight microstrip antenna due to the rapid development of wireless communications. In various wireless communications, microstrip patch antennas are found to be a suitable choice and encouraging [10]. Numerous design strategies have been reported for size minimization, including the use of metamaterial structures [11], arc-shaped tuning stubs [12], split-ring resonators [13], and ground planes by shorting pins [14]. This is because the majority of devices require compact sizes and simple structures. In contrast, a multi-band antenna is necessary to implement various

multiband function antennas, including a defective ground structure [15], a wearable open-ring antenna that is shorted to the ground plane [16], a circular ring with a Y-shaped strip [17], and a bow-tie monopole antenna [18]. The majority of previous multiband miniaturized antennas have problems because the radiation patterns are unstable [19–22]. An antenna with triple-band frequency as a result of cutting various U-slots has been described in [19]. The design and presentation of a pentaband microstrip antenna with metal sheets that resemble a combs-like metal sheet and an omnidirectional radiation pattern in the H-plane are described in [20]. Multiple resonators are added to a slot antenna in [21] to produce multiple resonances. Similar to [21], multiple resonant frequencies are generated by adding inverted multiple U-shaped slots to the radiating patch [22]. It has been stated that a different kind of compact, multiband patch antenna with directional radiation patterns exists [23]. The triple-band dual-polarized is achieved by utilizing a corner truncated sectoral radiating patch by Mathew et al. [24].

A compact, microstrip-coupled, triple-band H-shaped slot antenna has been proposed by Chang et al [25]. These four resonant frequencies have measured gains of 0.2 dBi, 3.5 dBi, 2.37 dBi, and 3.7 dBi, respectively. The triple-band metal-framed tablet to produce triple-wideband long-term evolution (LTE) is mentioned in [26] and the L-shaped radiator to produce a circularly polarized wave is presented in [27]. The equivalent transmission line model (TLM) circuit of the antenna are derived using the optimization method as presented in [28, 29]. As a result, the necessity for antenna systems with multiband and small omnidirectional antennas to handle several communication protocols is increasing. Considering the size of the antenna such as thickness and aperture size, a compact triple-band microstrip patch antenna with light weight is proposed in this thesis. Also, the proposed antenna has a high center frequency ratio and can significantly suppress the cross-polarization level by employing a symmetrical double annular ring slot patch.

### 1.4.2 Compact Broadband and UWB Antennas

Because of less weight, low profile, low cost, and ease of integration with monolithic microwave integrated circuits (MMIC), printed microstrip slot and monopole antennas are exten-

sively used in wireless communications systems. However, the microstrip slot antennas limited bandwidth is the major constraints, which is crucial to the fidelity of ultra-wideband (UWB) communications. Since CPW-fed antennas provide several advantages over microstrip antennas, including a relatively wide impedance bandwidth, high data rate, low fading sensitivity, flexibility, and ability to be integrated with surface-mount devices, it is sidely UWB communications [30, 31]. Figure 1.3 depicts the printed monopole structures, where the radiating patch may be supplied by a CPW-fed or a microstrip line.

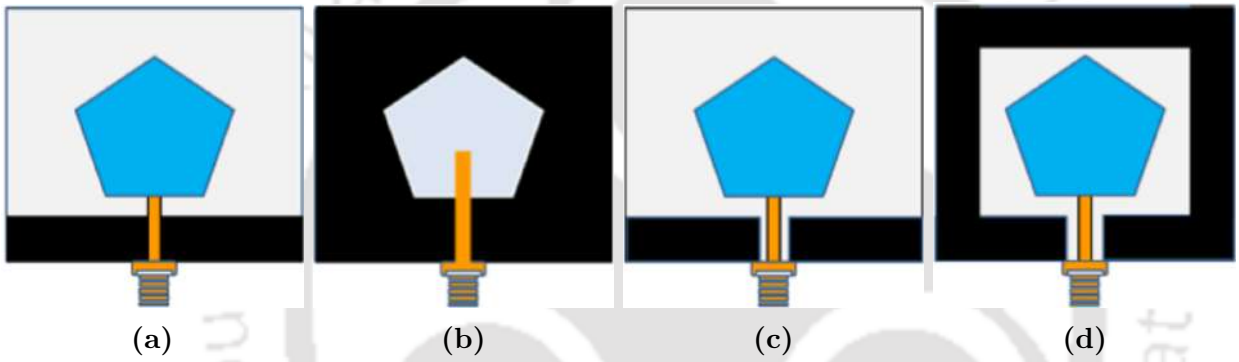


**Figure 1.3:** (a), (b) Microstrip line and (c), (d) CPW-fed monopole and slot antennas.

The need of various CPW-fed printed antennas with wider impedance bandwidth and compact sizes has been significantly grown in recent wireless communication applications. The usage of monopole and Vivaldi antennas, which have a wide bandwidth and good radiation patterns, is widespread [32]. A rather large area is needed in both antennas since Vivaldi antennas need a tapered slot and monopole antennas are mounted perpendicular to the carriers. Recently, the slot antenna design is enhanced to take the demand for a wider impedance bandwidth. Numerous concepts with small footprints and increased bandwidth have been put forward [33–38] for the Vivaldi antenna. As proposed by Chiu et al. [33], the central metallic strip length of the CPW transmission line is extended beyond the ground plane to create a monopole antenna.

Similar to above, Orazi et al. [34] developed a UWB triangular slot antenna by using the dual-reverse-arrow fractal (DRAF) geometry with a CPW-fed which is covering WLAN (2.4

and 3.65 GHz) and WiMAX (2.3, 2.5, and 3.5 GHz) frequencies. Sallam et al. [35], Safia et al. [36], and Azari et al. [37] propose a bow-tie antenna, a rose-curve monopole antenna, and a wideband fractal shape structure for UWB applications. The wideband fractal structure antenna has a large dimension but can perform well in terms of impedance bandwidth.

Since compactness is a key requirement in modern wireless devices for UWB applications, numerous amount of research work is going on across the globe to reduce the size of the CPW-fed tapered slot structure UWB antenna. Tu et al. [38] add a pair of half-wavelength stubs and slits into the tapered slot and the circular patches, respectively, in order to get the controllable notch-band feature. The proposed antenna has less cross-polarization than a single-ended CPW-fed UWB antenna as it uses a differential feeding mechanism. Tasouji et al. [39] proposed a modified rectangular radiation patch with three rectangular slots and one circular slot. The operation bandwidth of proposed antennas cannot be easily increased due to the slot width limits their bandwidth [39]. In [40-48], UWB and compact antennas are presented. A planar microstrip line-fed super wideband monopole antenna is presented by Chen et al. [40]. The asymmetrical ground plane is used to insert a semi-elliptically fractal-complementary slot, which results in a bandwidth ratio of 12:1 and a 10 -dB bandwidth of 172% (1.44–18.8 GHz) but the antenna size is large of 77×35 $mm^2$.

In addition to modified Y-shaped components, a compact multiple resonance modes structure with wideband capabilities has been examined by Fang et al. using a CPW-fed meandered-slot antenna. This antenna offers wider bandwidth and is a good option for 2.6 GHz Wi-Fi, WiMAX, and 5G applications [41]. The antenna proposed in [42–44] printed an E-shaped slot, an arc shape stub, and a fishtail shape structure apart from the conventional CPW-fed slot antennas and possess wider impedance bandwidth. A stepped connection structure is introduced with a Vivaldi antenna to improve the impedance matched antenna feed and impedance bandwidth [45]. A novel hybrid design for a microstrip line-fed, parasitic-coupled monopole antenna was put forward by Eshtiaghi et al. In this antenna two sectors are carved out from the bottom side of the parasitic patch to increase the impedance bandwidth. In [46], the main patch is coupled to a second patch with an inverted semi-ellipse which serves as a filter. This

UWB antenna operates between 3–11 GHz with a stop band frequencies from 5.1 to 5.9 GHz.

In [47], it is observed that the traditional multiple $\lambda/4$ or $\lambda/2$ resonant modes can exist due to the capacitive effect with regard to four open end L-slot patch structures and that the lower and upper resonant frequency can vary with respect to L-width slot. Additionally, a UWB slot antenna with a broad bandwidth and small dimensions that differ from conventional wideband slot antennas is presented [48]. Utilizing the $S_{11}$ simulated parameters [28, 49–54] of the proposed antenna, optimization is employed in the Applied Wave Research (AWR) simulator to determine the circuit parameters such as resistance (R), inductance (L), and capacitance (C) of the TLM equivalent circuit.

Various fractal antennas employing wideband fractal shapes, CPW-fed antennas with dual-reverse-arrow fractal structure, flexible bow-tie slot antenna, rose-curve shape monopole antenna, tapering slot antenna, and space-filling concepts are used to achieve the wideband impedance bandwidth [10, 34–37, 55–62] with bandwidth from 40% to 122%. A semi-circular patch [38], quasi-radiating patch [63], modified meandering slot [64], microstrip-fed parasitic-coupled monopole hybrid design [41], and improved surrogate-based patch [28, 29, 46, 49, 65] are presented to provide wider bandwidth and better impedance matching. However, in order to actualize the necessary operational frequency bands, the monopole antennas indicated above have a large physical dimension and complex shape. In order to span the UWB frequency band, a compact, simple slotted and monopole antenna with a wider bandwidth is required.

### 1.4.3 Compact Broadband and UWB CP Antennas

Recent years have seen a significant increase in interest in research on compact and microstrip antenna arrays, radiating elements, feeding arrangements, and polarizations for contemporary wireless communication systems. The popularity of the circularly polarized (CP) antenna is growing in wireless communication systems due to its advantages over linearly polarized antennas in terms of multipath fading resistance, non-line-of-sight applications, and better mobility. Numerous researchers have been working to reduce the size of CP antennas in various ways in recent years [66–68]. Exciting two orthogonal modes with equal amplitude and

in-phase quadrature is the basis for CP antenna operation.

By introducing different design techniques, the above mentioned CP band antenna can achieve multiband CP for various communication systems such as global positioning systems (GPS) and satellite communications [69–73]. The dual-band CP antennas have been proposed with a single feed, cavity-backed square annular slot [69], truncated corner square slots loaded with a set of split-ring resonators [70], and an S-shaped slot center of the square radiator [71]. The single-feed microstrip patch antennas with the annular-ring slot on the square radiator or $4 \times 4$ arrays with $90^o$ phase difference power dividers have also been demonstrated for dual-band applications [72], [73]. Although these antennas generate a CP wave in their two bands, the antenna size is increased and 3 dB axial ratio bandwidths (ARBW) are narrowed. Furthermore, single-feed microstrip patch antennas with loading stubs and etching slots on the square patch or multi-stacked patches with a slit have also been discussed for triple-band applications [74], [75]. However, the above mentioned single-feed CP patch antennas have less than 3.5% axial ratio bandwidth (ARBW) with large sizes. In [76], multiple L-shaped slits on the hexagonal slot as a radiator is proposed and triple CP bands i.e., 1.7%, 3.86%, and 5.23% are achieved. In [77], a square slot with metallic strips and split-ring resonator configuration shows an improvement in 3 dB ARBW. Though these antennas are small in size, the ARBW are still less than 11%. Recently, a quad-band CP antenna with Inverted-U-shaped radiators [78], the ARBWs of 5.4%, 8.3%, 3.7%, and 2.9% are achieved.

The sequential rotation technique (SRT) which is one of the many well-established methods for designing an antenna array, is found to be useful for CP array antennas for enhancement of array bandwidth, radiation patterns, and polarization purity. Numerous CP array antenna designs have been proposed, but the SRT is one of the approaches that has received the most attention in the literature [79–83]. In SRT, phase shifting of $90^o$ and $180^o$ are achieved by applying $\lambda/4$ transmission lines with an L-shaped radiator [79]. A series feed network reported in [80] consists of $\lambda/4$ transformer sections with an L-shaped ground strip in the radiator array to reduce the cross-polarization. In [81–83], the array elements are fed by different feeding networks like rat-race, Wilkinson power divider, and microstrip line. However, antenna

configurations of these designs are usually large and the use of a complex feeding network structure complicates the fabrication of the antenna. The antennas mentioned above are either thick in profile or large in aperture size, which motivates us to develop a compact multiband CP antenna to some extent as well as improve the ARBW and impedance bandwidth (IBW) with minimum axial ratio using a series-fed circular slit array patch.

Furthermore, UWB-IBW as well as ARBW can be achieved by introducing some symmetric and/or asymmetric monopole or slotted radiator with CPW-fed extended defected ground structure (DGS) antennas [84–89]. These include a printed square slot patch and a halberd-shaped metal strip on the ground plane [84], two rectangular parasitic elements and an I-shaped grounded stub [85], a rectangular monopole and a square-ring with an open gap at the bottom [86], and an L-shaped monopole patch with inverted L-shaped ground strips [87] to enhance the ARBW as well as reduce the antenna size. By using an I-shaped rectangular patch with adding a stub on the ground plane, the antenna achieves an ARBW of 44.9% and IBW of 76.9% [88]. A monopole radiator with an L-shaped slot on the ground plane achieves ARBW of 33% and IBW of 40% [89]. However, these CPW-fed CP monopole antennas have less than 64% ARBW with less gain. It is very difficult to meet the requirements of wider IBW and ARBW simultaneously of antenna for wideband communication systems. However, 44.9% and 76.9% are the maximum achievable values for ARBW and IBW, respectively, while considering both separately. The art of the microstrip patch CP antenna design is to customize the frequency of ARBW close to the IBW so that a wide overlapped bandwidth CP antenna can be achieved. In [90], a C-shaped monopole with a rectangular vertical stub connected to the ground plane as a CP radiator is proposed. In a hexagon-shaped monopole with a slotted patch, a wide ARBW has been achieved [91]. Though these antennas are small in size, the ARBW are still less than 66%.

Recently, an ultra-wideband CP antenna with semicircular patches on the top and bottom sides is reported in [92], where 89% and 103% ARBW and IBW, respectively are achieved. A UWB 2 × 2 array CP antenna is introduced in [93], which is a larger size than other UWB CP antennas. The size of this UWB array is 200×200 mm$^2$, while the ARBW of 92.5%, IBW

of 132.8%, and $BR|_{(10/3)dB} \approx 1.435$. The antennas mentioned above are either thick in profile or large in aperture size, which motivates us to develop a compact UWB CP antenna to some extent as well as improve ARBW and IBW with the minimum AR and $BR|_{(10/3)dB}$ using an asymmetrical Inverted L-Shaped-Hook Monopole antenna.

## 1.5 Motivation

After discussion of the limitations of wireless communication systems which are not addressed in the present literature in the previous section, the motivations to carry out this research work are as follows:

- The demand for compact devices is increased by the rapid development of wireless communication technologies. Antenna tuning is also required to overcome the systems' overall size. Research work in the minimization and better performance of the antenna needs to be studied.

- A multiband antenna supports various wireless frequency standards for multiband communication applications. Furthermore, improvement techniques in radiation patterns are still to be explored. Therefore, it is necessary to focus on improving antenna design for better antenna radiation patterns and reduction of the antenna size by employing various slot structures.

- Bandwidth dimension ratio (BDR) is an important parameter of a UWB antenna. To the best of author's knowledge, there are no designs for UWB that concurrently reduce the antenna size while increasing the BDR ratio. As a result, designing an antenna that is capable of both functions is a research topic for effective wireless communication technology.

- The communication systems as mentioned in Friis transmission equations is highly dependent on polarization of the signals. Polarization mismatch prevents the maximum signal from reaching the receiver. According to the power density contour at the receiver

end, a linear polarized antenna may occasionally be positioned at $90^o$ or $180^o$ orientation. Additionally, the circularly polarized (CP) antenna is growing in popularity in wireless communication systems due to its advantages over linearly polarized antennas in terms of non-line-of-sight applications, multipath fading resistance, and better mobility. The CP antenna must be developed to maintain the same state of polarization without changing the orientation in order to have lower or no polarization loss.

- This thesis presents slotted, slit, and DGS microstrip patch antennas for applications such as Bluetooth, ZigBee, WLAN, WiMAX, Wi-Fi, LoRa, GSM, LTE, etc. The frequency range for above applications from 1 to 20 GHz. To get multi-band, broadband, UWB, and CP band characteristics, five distinct prototype antennas are designed and tested based on the slot, slit, series-fed array, and defective geometry.

## 1.6 Objective of the Thesis

The objective of the thesis are as follows:

- Design a compact, triple-band antenna with a high center frequency ratio, low cross-polarization levels, stable radiation patterns, and constant gain over the working band.
- Design a compact novel CPW-fed symmetrical staircase-shaped slotted patch antenna to enhance IBW, improve peak gain, and BDR.
- Design a new, compact star-shaped monopole antenna to increase the IBW and maintain constant gain throughout an operational band.
- Design a novel compact, dual-band, dual-CP, series-fed circular slit microstrip array quad-band CP antenna with improved cross-polarization levels in all directions.
- Design a compact, inverted L-shaped-hook monopole CP antenna to improved IBW and ARBW with a minimum $BR|_{(10/3)dB}$.

## 1.7 Contribution of the Thesis

The design and fabrication of multi-band, broadband, UWB, and CP band microstrip patch antennas for wireless applications is the primary contribution of the current study. The following steps are taken to design the proposed antennas using slotted, slit, series-fed array, and defected ground structures in order to optimize the antenna parameters and performance, such as reflection coefficient, voltage standing wave ratio (VSWR), minimum axial ratio, peak gain, radiation efficiency, E-plane, and H-plane radiation patterns, etc.

The main contribution of this thesis is as follows:

- The use of several existing antennas with varied antenna characteristics, and their analysis.
- To improve the center frequency ratio and reduce the cross-polarization levels of a multi-band antenna.
- A compact structure CPW-fed symmetrical staircase-shaped antenna is designed, fabricated, and tested to improve the impedance bandwidth. It maintains constant gain between the operational frequency bands.
- Compared to conventional antennas, a lower-volume, CPW-fed star-shaped monopole antenna radiator is designed and fabricated. It has a wider IBW and a higher gain.
- A novel dual circular polarized, quad-band CP with two broadband impedance bandwidths antenna designed and experimented. The antenna exhibits improved gain that provides the same circular polarization regardless of propagation direction has been designed and fabricated.
- A compact extended CPW-fed UWB circular polarized inverted L-shaped hook monopole antenna is designed and fabricated. It has a UWB-IBW, minimum AR, $BR|_{(10/3)dB}$, and higher gain.

Due to the complexity of the slotted and slit geometry, it is important to develop an effective method to support the design of slotted or slit-based antennas in the area of antenna modeling. The slotted or slit geometry for antenna modeling is developed using a macro script, which can be run by most of the antenna simulation software. Figure 1.4 illustrates this technique in a straightforward manner.

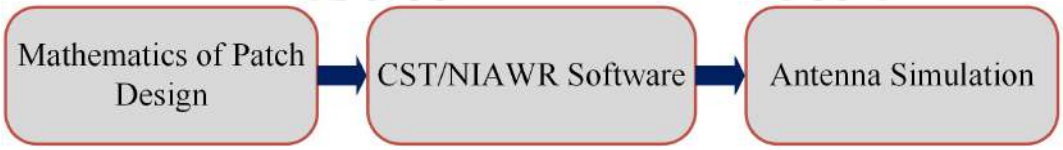


**Figure 1.4:** The general working flow of creating antenna modeling.

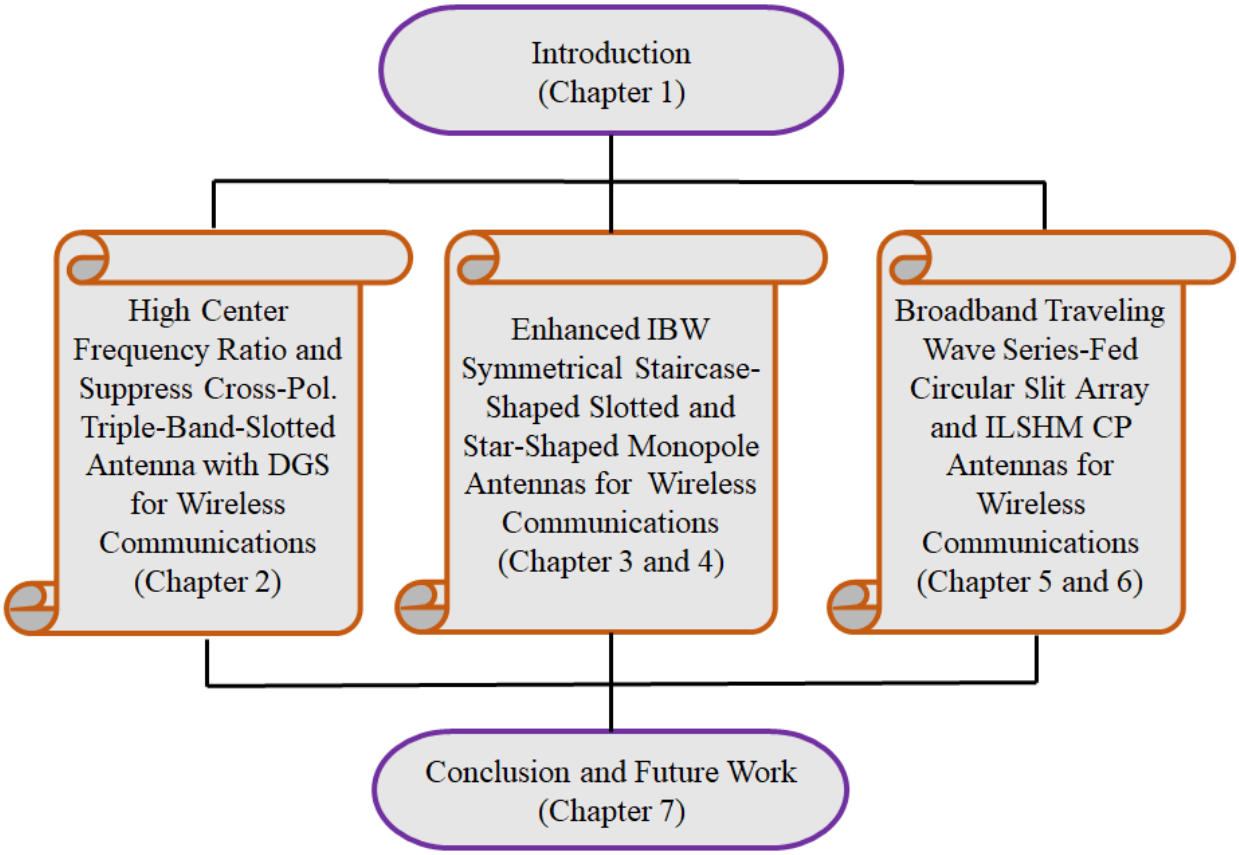


**Figure 1.5:** Chapter structure diagram.

## 1.8 Organization of the Thesis

This thesis provides a complete review of the methods for analyzing, designing, fabricating, measuring and optimizing different types of microstrip multi-band, broadband, UWB, and CP band antennas for wireless applications. The content of this thesis is divided into seven chapters as indicated in Figure 1.5.

**Chapter 2:** This chapter addresses a low profile triple-band slot antenna having a high center frequency ratio and low cross-polarization levels for WLAN/WiMAX/C-band downlink satellite communications. This antenna has a double annular ring slot, two L-shaped slots, one I-shaped slot, and a defected ground structure based on an ellipse-shaped slit. The transmission line model of the proposed antenna is also shown, and it depicts the behavior of the antenna based on the impact of each component. It is seen that the properties of the output from an equivalent transmission line model (TLM) of the configured proposed antenna closely resemble with those of the simulation results obtained from CST simulator software. Thus, the requirements and difficulties associated with designing a triple-band antenna are investigated. The simulation and the measured results of the fabricated antenna agree with and validate the design.

**Chapter 3** investigates the practical difficulties of integrating a slotted UWB antenna into a small device platform. This chapter examines the design process for a slotted radiator that will be integrated into a small patch. The main objective of the proposed design structure is to reasonably maintain the radiation properties of the antenna by compacting, enhancing impedance bandwidth, and controlling the coupling coefficient due to the fraction of the $TM_{01}$ mode current introduced by the C-shaped slot. As a result, the proposed antenna is shown to have a wider impedance bandwidth (1.55-16.95 GHz (166.51 %)), enhanced gain (2–8.3 dBi), and improved impedance matching. The transmission line model (TLM) of the proposed antenna, which depicts the behavior of the antenna based on the influence of each constituent, is provided. It is noted that the properties of the TLM model closely match the outcomes of simulations performed with the CST simulator. The prototype is successfully implemented,

fabricated, and the results of the experiment are compared with the simulation results.

**Chapter 4:** This chapter introduces an antenna solution for a compact 9-point star patch radiator. A novel concept for efficiently using the reduced space and enhanced impedance bandwidth (measured impedance bandwidth 2.2-12.21 GHz) for the proposed antenna is discussed in detail. The functioning theory, design process, and simulated and measured results of the proposed antenna are presented.

**Chapter 5** introduces a new design of compact dual-band and dual-CP traveling wave series-fed circular slit microstrip array (TWSCSMA) antenna operating in quad-band CP at 2.5/3.5/3.8 GHz WiMAX and 5.2 GHz WLAN applications. The radiating structure consists of an annular ring traveling wave series-fed circular slit array elements which rotate in sequence with seven circular quasi-lumped resonators contributing to two-impedance bandwidth (IBW) and quad CP bands. The proposed design gives the left-hand circular polarization (LHCP) wave when the input RF signal for port 1 has a 45° phase increment clockwise direction. Similarly, the right-hand circular polarization (RHCP) wave, when the input RF signal for port 2 has a 45° phase increment anticlockwise direction. Using this concept, dual-CP radiation can be realized. The four split-ring resonators with double-annular rings are introduced on the defected ground plane to improve the impedance matching, IBW, and axial ratio bandwidth (ARBW) effectively. Thus, measured IBW (two $S_{11} \leq 10$ dB IBW of 33.85% and 50.73%) and AR (four $<$ 3 dB ARBW of 16.26%, 12.52%, 8.22%, and 13.82% for port 1) characteristics validate and ensure the polarization quality of traveling-wave series-fed arrays. Furthermore, modern machine learning regression techniques are used to predict the parameter accuracy of the model performance requirements for the optimal design of the proposed antenna. The TWSCSMA antenna demonstrates a compact, low profile, wide impedance bandwidth, and minimum AR which is making it a good candidate for WiMAX and WLAN applications.

**Chapter 6:** The practical difficulties in designing and integrating a compact UWB monopole CP antenna with a small bandwidth ratio into the device platform are further explored. It is possible to produce the measured IBW (VSWRmax 2) result from 2.243 to 20.653 GHz (160.82%) and 3 dB ARBW from 3.216 to 18.985 GHz (143.45%). This chapter examines the design

process for a CPW-fed monopole for integration into a compact patch. The major objective of the proposed approach is to reduce the radiator's bandwidth ratio $BR_{(10/3)dB} \approx 1.121$ in order to reasonably preserve the radiation properties of the monopole antenna. When the proposed antenna is designed, and the simulation results are verified by measurements, which validate the design.

**Chapter 7:** The work is finally concluded in chapter 7. The main goals are examined, and noteworthy accomplishments are emphasized. The issues that are still extant and desirable for investigation as future research subjects are also presented in this chapter. Figure 1.6 provides an overview of the subjects that are addressed in this work.

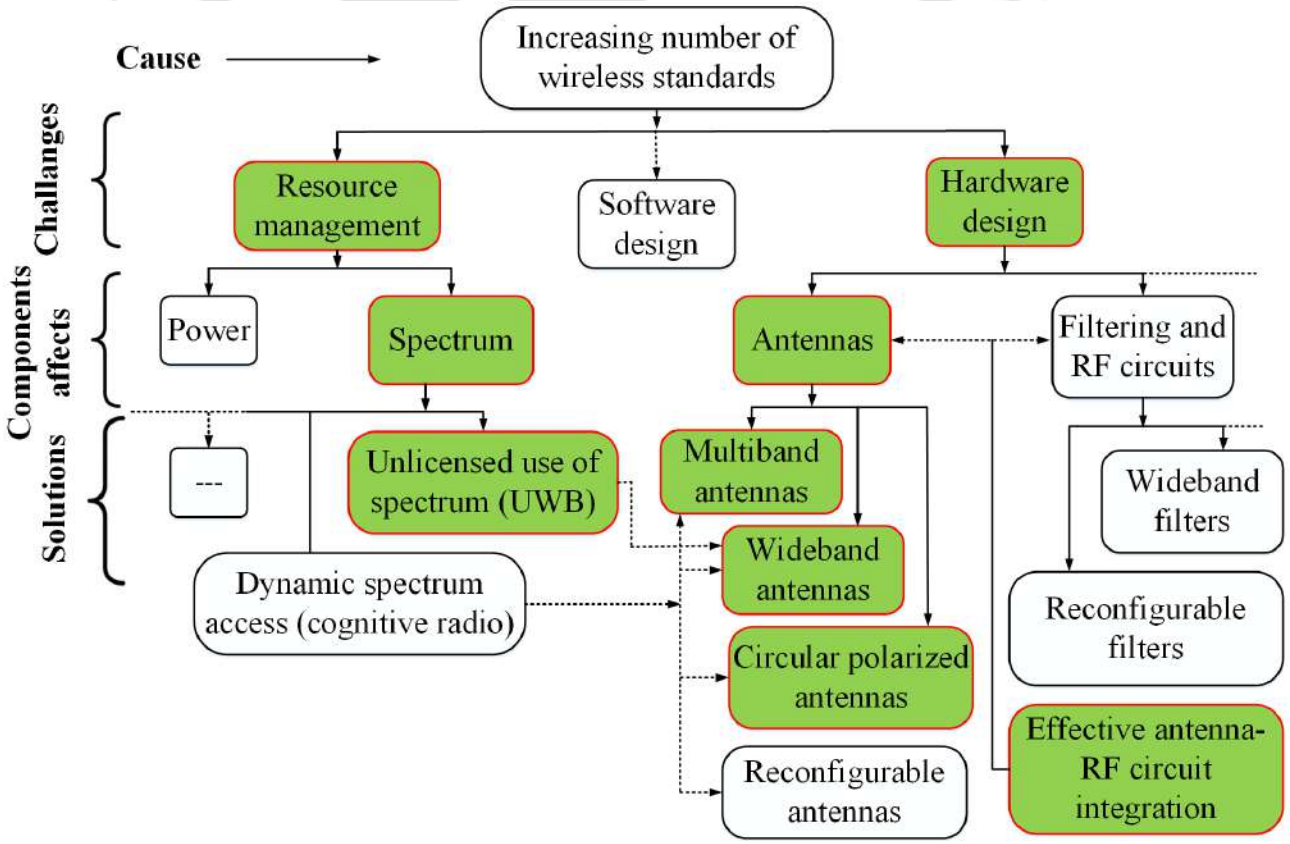


**Figure 1.6:** Challenges in wireless technology and the highlighted boxes are discussed in this dissertation.

भारतीय प्रौद्योगिकी संस्थान गुवाहाटी
Indian Institute of Technology Guwahati

# 2

# Design of Compact Microstrip-fed Triple-Band Slot Antenna with Defected Ground Structure for Wireless Communications

Contents

## 2.1 Introduction

With the rapid development of wireless communications, the design of the multiband, low-cost, compact size, lightweight patch antenna has attracted many antenna researchers. Microstrip patch antennas are found to be a suitable choice and encouraging in different wireless communications [10]. Since most of the devices require compact size and simple structures, several design techniques have been reported for size minimization, such as using metamaterial structures [11], arc-shaped tuning stub [12], split-ring resonator [13], and ground plane by shorting pins [14]. On the other hand, the multiple-band antenna is essential for adaptability to various wireless communication and to realize the different multiband function antennas, such as defected ground structure [15], wearable open-ring shorted to the ground plane antenna [16], a circular ring with a Y-shape-like strip [17], and bow-tie monopole antenna [18]. Most of the previous multiband miniaturized antennas face difficulty due to the instability of the radiation patterns [19–22]. In [19], an antenna with triple-band frequency due to the cutting of different U-slots has been reported. In [20], a penta-band microstrip antenna with comb-like metal sheets is designed and presented with an omnidirectional radiation pattern in H-plane. These slot antennas are smaller than the conventional modified monopoles, but their structures are more complex for practical applications. In [21], multiple resonances are obtained by introducing multiple resonators on a slot antenna. Similarly in [22], by introducing inverted multiple U-shaped slots on the radiating patch, multiple resonant frequencies are obtained. A different type of compact multiband patch antenna with directional radiation patterns is reported [23]. Triple and multi frequency band antenna such as dual-polarized using corner truncated sectoral radiating patch [24], higher-order modes are excited using H-shaped slot [25], metal-framed tablet to generate triple-wideband LTE [26], and L-shaped radiator to produce a circularly polarized wave [27] are reported and also the researchers have tried to reduced the size. Thus, there is a growing need for antenna systems where multiband and compact size omnidirectional antennas are needed for coverage of multi-communication standards.

In this chapter, a low profile triple-band slot antenna (TBSA) for WLAN/WiMAX/C-band

downlink satellite communication applications are presented. In this design, the L-shaped slot is used to control a first band (2.257–2.523 GHz) centered at 2.39 GHz and a double-annular-ring-slot (DARS) which controls the second resonant frequency (3.455–3.655 GHz) centered at 3.55 GHz. The third resonant frequency (4.012–4.262 GHz) centered at 4.13 GHz of the proposed antenna is achieved by introducing DGS along with DARS and L-shaped slots. The proposed antenna is compact in size ($0.36 \times 0.35 \times 0.012\lambda_0$ mm$^3$) and relatively simple in structure. The proposed antenna has the advantages of the easy tuning of individual resonant frequency which maintains a better center frequency ratio $f_2/f_1 = 1.49$ and $f_3/f_1 = 1.73$, low cross-polarization nearly -38.85 dB in E-plane, omnidirectional radiation patterns and better gain with compact size. Then, an equivalent transmission line model (TLM) of the configured proposed antenna is developed. The TLM equivalent circuit model and the optimization method have been reported in [28, 29]. Finally, the proposed model using the Applied Wave Research (AWR) software is optimized.

This chapter is divided into the following sections: section 2.2 states the design steps and discussed the parametric studies and generation of triple-band. The mathematical modeling of the proposed antenna and derived analytical expression for the transmission line model (TLM)-RLC circuit model are presented in section 2.3. The reflection coefficient $S_{11}$, peak gain, and radiation patterns parameters at different frequencies like 2.41, 3.53, and 4.14 GHz are compared. The simulation and experimental results of the $S_{11}$, peak gain, and radiation patterns in both the planes are presented in section 2.4. The experimental results match quite well with the simulation results, thus validating the practical feasibility of the design. The principal outcomes of this research work are explained in section 2.5.

## 2.2 Antenna Design and Analysis

### 2.2.1 Antenna Structure

Figure 2.1 shows the structure of a compact triple-band slot microstrip-fed antenna. The proposed antenna having an area of $44 \times 45$ mm$^2$ ($S_L \times S_W$) and a thickness of 1.6 mm is fabricated on the FR-4 substrate. The dielectric constant and loss tangent of the substrate

are 4.3 and 0.025 respectively. The CST Microwave Studio (CST vers. 17) software is used to design and optimize the proposed antenna. The dimensions of the proposed antenna are listed in Table 2.1.

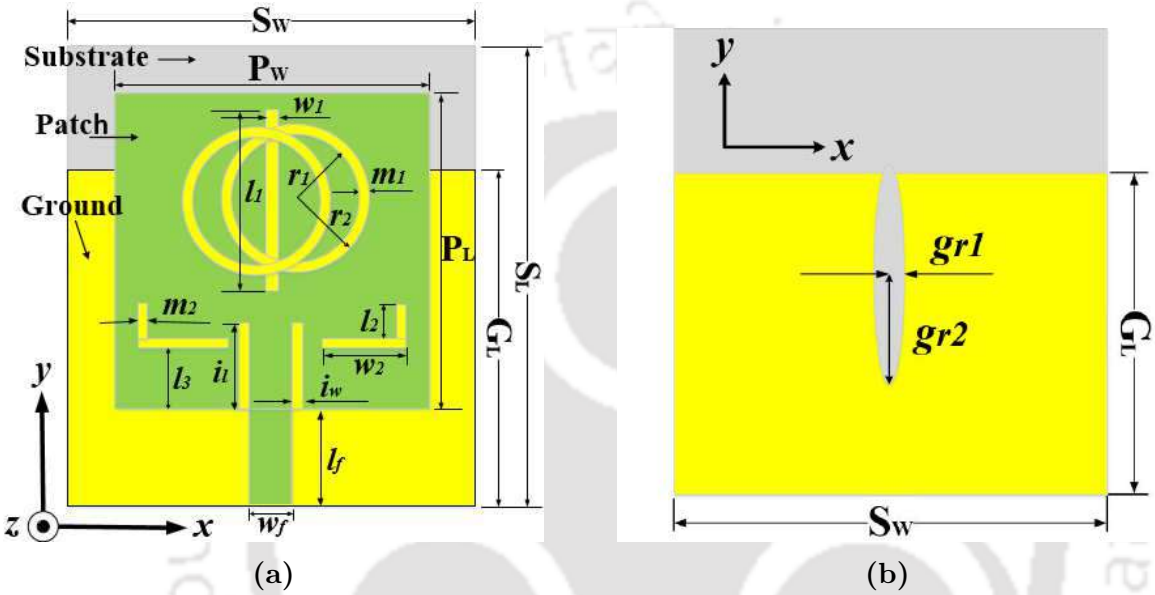


**Figure 2.1:** Antenna geometry (a) top view and (b) bottom view.

**Table 2.1:** Geometric parameters of the proposed antenna

| Parameters | Value (mm) | Parameters | Value (mm) | Parameters | Value (mm) |
|---|---|---|---|---|---|
| $S_L$ | 44 | $i_w$ | 0.8 | $m_1$ | 1.1 |
| $S_W$ | 45 | $i_l$ | 6 | $m_2$ | 0.5 |
| $P_W$ | 38.98 | $l_1$ | 25 | $r_1$ | 9.6 |
| $P_L$ | 32.6 | $l_2$ | 3 | $r_2$ | 10.7 |
| $G_L$ | 31.72 | $l_3$ | 3.5 | $g_{r1}$ | 1.1 |
| $w_f$ | 2.5 | $w_1$ | 1 | $g_{r2}$ | 7.4 |
| $l_f$ | 8.8 | $w_2$ | 10.5 | $h$ | 1.6 |

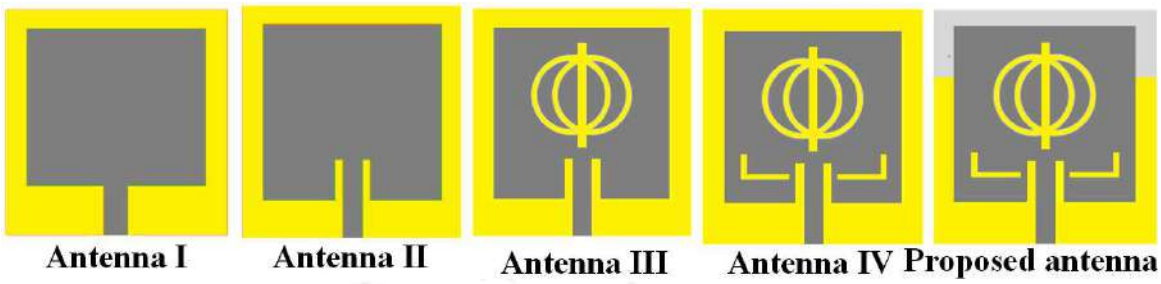


(a)

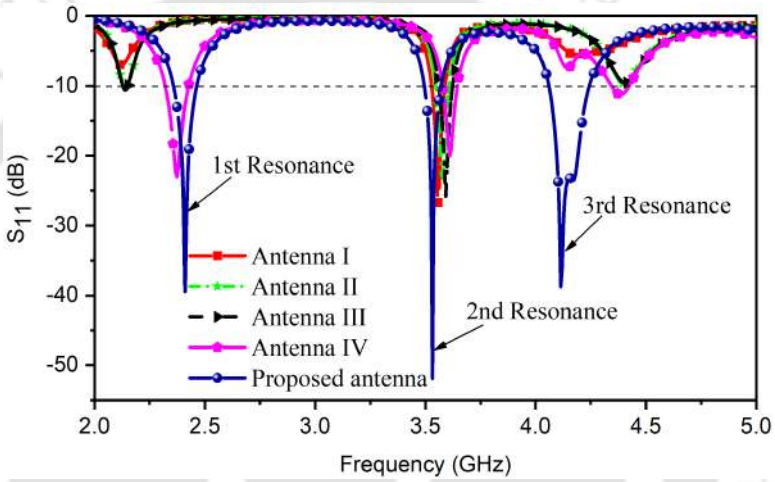


(b)

**Figure 2.2:** Antenna design evolution (a) Antenna I, Antenna II, Antenna III, Antenna IV, proposed antenna, and their corresponding (b) $S_{11}$.

### 2.2.2 Design Antenna Evolution

The antenna design process and triple-band frequency response are shown in Figures 2.2(a) and 2.2(b) respectively.

**First step:** Antenna I is a simple rectangular patch with a microstrip line fed as shown in Figure 2.2(a). It is observed that the single band from 3.523–3.587 GHz, which covers the 3.5 GHz WiMAX standard application but other resonance at a higher frequency does not provide better characteristics of $S_{11} \leq -10$ dB.

**Second step:** To excite other resonant modes, a rectangular shape slit is introduced in the rectangular radiator Antenna I, which is called Antenna II. And their corresponding $S_{11}$ perfor-

mance is provided in Figure 2.2(b), which gives nearly 3.5 GHz and another higher frequency resonance at 4.4 GHz but does not provide better return loss performance.

**Third step:** Antenna III, a conventional symmetrical double annular ring slot (DARS) is introduced in Antenna II which generates three resonant frequencies 2.14, 3.59, and 4.4 GHz. However, the first and third bands have very poor return loss.

**Fourth step:** Antenna IV, two L-shaped slots are introduced in Antenna III, at first and second resonant frequency −10 dB return loss is good.

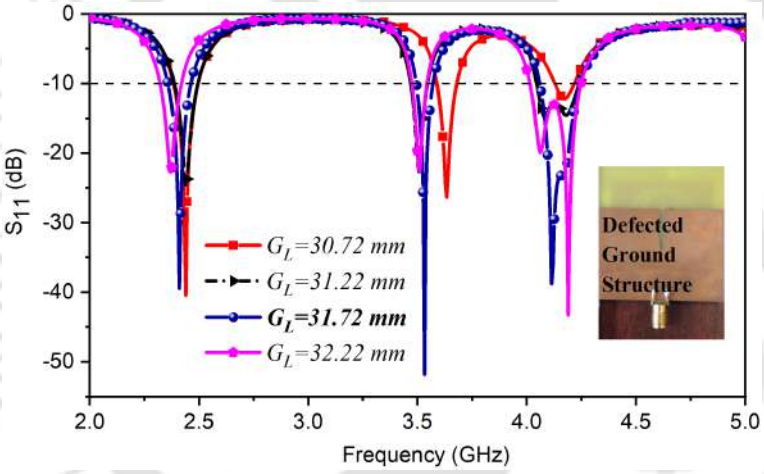


**Figure 2.3:** Simulated $S_{11}$ results variation with $G_L$.

**Fifth step:** The ground plane $G_L$ is reduced to 31.72 mm and cut into an ellipse-shaped slit (ESS) to improve the return loss and impedance matching. The designed antenna covers WLAN (2.41 GHz), WiMAX (3.53 GHz), and C-band downlink satellite communications (4.1 GHz) bands, with an overall percentage of impedance bandwidth 2.415 GHz (8.11%), 3.53 GHz (3.12%), and 4.14 GHz (5.31%), respectively. The simulated center frequency ratio are $f_2/f_1 = 1.49$ and $f_3/f_1 = 1.73$. Figure 2.3 shows that by increasing the ground length $G_L$ from 0 to 31.72 mm, all modes are excited and improved appreciably impedance bandwidth and impedance matching. Further increasing the ground length $G_L$ from 31.72 to 32.22 mm, all resonance frequency band's return loss performances are reduced. Therefore, we found a suitable length of the ground plane $G_L$ of about 31.72 mm.

### 2.2.3 Surface Current Distribution Performance

To study the operating principle and the relationship between different resonant frequencies with their essential parameters of the proposed antenna, the simulated surface current distributions at 2.41, 3.53, and 4.14 GHz are shown in Figure 2.4. In Figure 2.4(a), the strong surface current concentration on the radiating patch and both sides of the L-slot are observed. Therefore, it can be found that the 2.41/2.5 GHz WLAN resonant occurs due to both sides of the patch. In Figure 2.4(b) the concentration of the surface current on the DARS and partly main rectangular radiator indicates the resonant frequency at 3.53 GHz. As shown in Figure 2.4(c), the concentration of the current on the lower part of the double annular ring slot, L-shaped slots of the radiating patch and microstrip-fed line contribute towards the third resonance frequency.

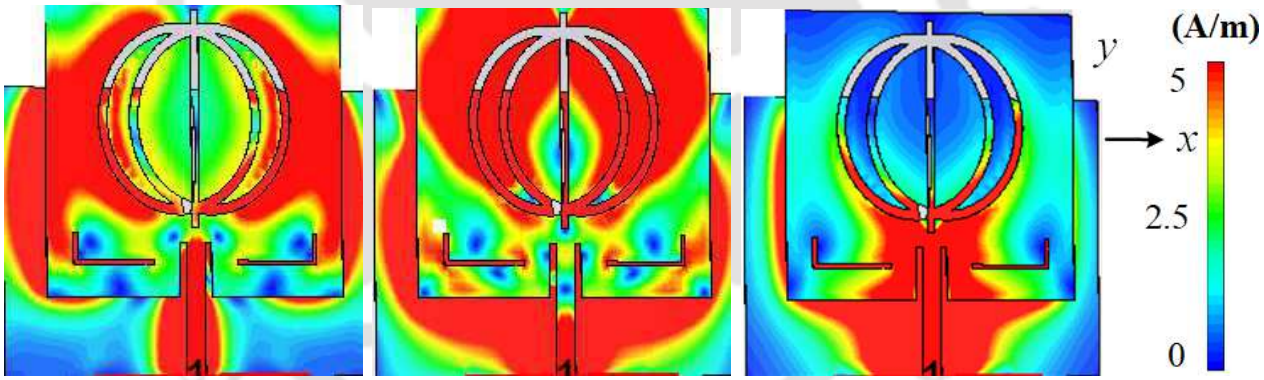


**Figure 2.4:** Simulated surface current distributions at (a) 2.41 GHz, (b) 3.53 GHz, and (c) 4.14 GHz.

### 2.2.4 Design Approach for Triple-Band Frequency

The design approach of the triple-band slot antenna and the calculation of the dimensions of different slots of the patch radiator is explained below.

**First Resonance:**

From Figure 2.4(a), it is seen that the boundary condition for the first resonance, in which the maxima of the electric field occur at both sides of the L-shaped slot patch. Therefore, the

first resonance frequency ($f_{r1}$) can be calculated as:

$$f_{r1} \approx \frac{c}{2L_{r1}\sqrt{\epsilon_{eff}}} \tag{2.1}$$

where $L_{r1}$ and $\epsilon_{eff}$ (effective dielectric constant) are expressed as:

$$L_{r1} = 2(w_2 + l_2 + m_2) \tag{2.2}$$

$$\epsilon_{eff} = \frac{\epsilon_r + 1}{2} + \frac{\epsilon_r - 1}{2}\left(1 + 12\frac{h}{P_W}\right)^{-1/2} \tag{2.3}$$

$$P_W = \frac{c}{2f_r}\sqrt{\frac{2}{\epsilon_r + 1}} \tag{2.4}$$

where $c$ is the speed of light in a vacuum, $f_r$ (=2.5 GHz) is the designed antenna resonant frequency, and $\epsilon_r$ (= 4.3) is the permittivity of the substrate.

By substituting $c$, $\epsilon_r$, $f_r$, $h$ and $P_W$ in Eq. (2.3) and (2.4), $\epsilon_{eff}$ is calculated as 4.001. Substituting $\epsilon_{eff}$, $L_{r1}$ = 28.4 mm as given Table 4.2 and $c$ in Eq. (2.1), $f_{r1}$ = 2.61 GHz is obtained.

**Table 2.2:** Comparison between design equation and full-wave simulation for first resonance

| $w_2$ (mm) | $L_{r1}$ (mm) | Resonant frequency (GHz) Design equation | Resonant frequency (GHz) Full-wave simulation | Error |
|---|---|---|---|---|
| 9.5 | 21.6 | 3.45 | 3.22 | 0.066 |
| 10.0 | 25.0 | 2.98 | 2.71 | 0.090 |
| 10.5 | 28.4 | 2.61 | 2.41 | 0.076 |
| 11.0 | 30.0 | 2.48 | 2.28 | 0.070 |

**Second Resonance:**

As seen in Figure 2.1(a), the double-annular-ring-slot has an outer radius of $r_2$ and an inner radius of $r_1$. Figure 2.5 shows the $S_{11}$ performance with a variation of $m_1$ from 0.5 to 1.4 mm. It is observed that the resonance frequencies shift to higher frequencies with a decrease

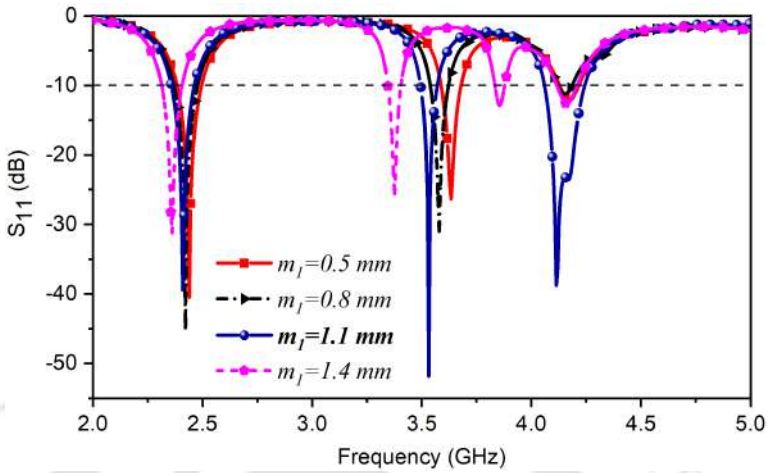


**Figure 2.5:** Simulated $S_{11}$ results of the proposed antenna with a variation of $m_1$.

of $m_1$. As $m_1$ increases, the capacitance $C_{eq}$ of the DARS decreases which in turn decreases the propagation constant $\beta$ ( i.e., $\beta \propto \sqrt{C_{eq}}$). As a result, there is a decrease in the effective dielectric constant $\sqrt{\epsilon_{eff}} = \beta \ / \ C_{eq}$. The guided wavelength $\lambda_g = \lambda_0 \ / \ \sqrt{\epsilon_{eff}}$ satisfies the resonance condition when the circumference of the radiating slot is kept constant. For slot width $m_1 = 1.1$ mm, the second resonance frequency of the antenna shows better return loss and impedance bandwidth as shown in Figure 2.5. For the conventional double-annular-ring-slot antenna, the second resonant frequency ($f_{r2}$) occurs at the frequency whose wave-length in the ring slot approximately corresponds to the mean circumferences of the ring slot. The expression of the second resonance frequency ($f_{r2}$) is given as follows:

$$f_{r2} \approx \frac{c}{\pi(r_1 + r_2)} \left( \frac{1 + \epsilon_r}{2\epsilon_r} \right)^{\frac{1}{2}} \tag{2.5}$$

where $f_{r2}$ is the second fundamental frequency and $\pi(r_1 + r_2)$ is the mean circumferences of the annular-ring-slot of the proposed antenna. The second resonance is excited due to the annular-ring-slot, which is apparent from Figure 2.2(b). Substituting $r_1$ ( = 9.6 mm), $r_2$ ( =10.7 mm), $\epsilon_r$ ( = 4.3) and $c$ (vacuum) in Eq. (2.5), $f_{r2} = 3.69$ GHz is achieved. Table 2.3 shows the second resonant frequency as a function of the inner radius ($r_1$) and outer radius ($r_2$) of the proposed antenna.

**Table 2.3:** Comparison between design equation and full-wave simulation for second resonance

| $r_1$ (mm) | $r_2$ (mm) | Resonant frequency (GHz) Design equation | Resonant frequency (GHz) Full-wave simulation | Error |
|---|---|---|---|---|
| 10.2 | 10.9 | 3.55 | 3.37 | 0.050 |
| 9.9 | 10.8 | 3.62 | 3.47 | 0.041 |
| 9.6 | 10.7 | 3.69 | 3.53 | 0.043 |
| 9.3 | 10.6 | 3.78 | 3.58 | 0.052 |
| 9.0 | 10.5 | 3.84 | 3.63 | 0.054 |

**Table 2.4:** Comparison between design equation and full-wave simulation for third resonance

| $w_2$ (mm) | $L_{r3}$ (mm) | Resonant frequency (GHz) Design equation | Resonant frequency (GHz) Full-wave simulation | Error |
|---|---|---|---|---|
| 9.5 | 34.6 | 4.33 | 4.52 | 0.043 |
| 10.0 | 35.8 | 4.28 | 4.35 | 0.016 |
| 10.5 | 37 | 4.05 | 4.15 | 0.024 |
| 11.0 | 38.2 | 3.92 | 3.72 | 0.051 |

**Third Resonance:**

The third resonance mode occurs due to the an L-shaped slot at the left and right-hand side and a slit near to the feed line of the radiating patch. This can be established by studying the surface current distribution as shown in Figure 2.4(c). From Figure 2.4(c), it is clear that the current maxima occurs partly at a L-shaped slot of the radiator and insert feed line at the end of the edge. Therefore, the third resonance $f_{r3}$ can be calculated as follows:

$$f_{r3} \approx \frac{c}{2L_{r3}\sqrt{\epsilon_{eff}}} \tag{2.6}$$

where $L_{r3}$ is expressed as:

$$L_{r3} = 2(w_2 + l_2 + i_l) \tag{2.7}$$

By substituting $\epsilon_{eff} = 4.001$ calculated using Eq. (2.3), $L_{r3} = 37$ mm as given in Table 2.4 and $c$ in Eq. (2.6), $f_{r3} = 4.05$ GHz is achieved.

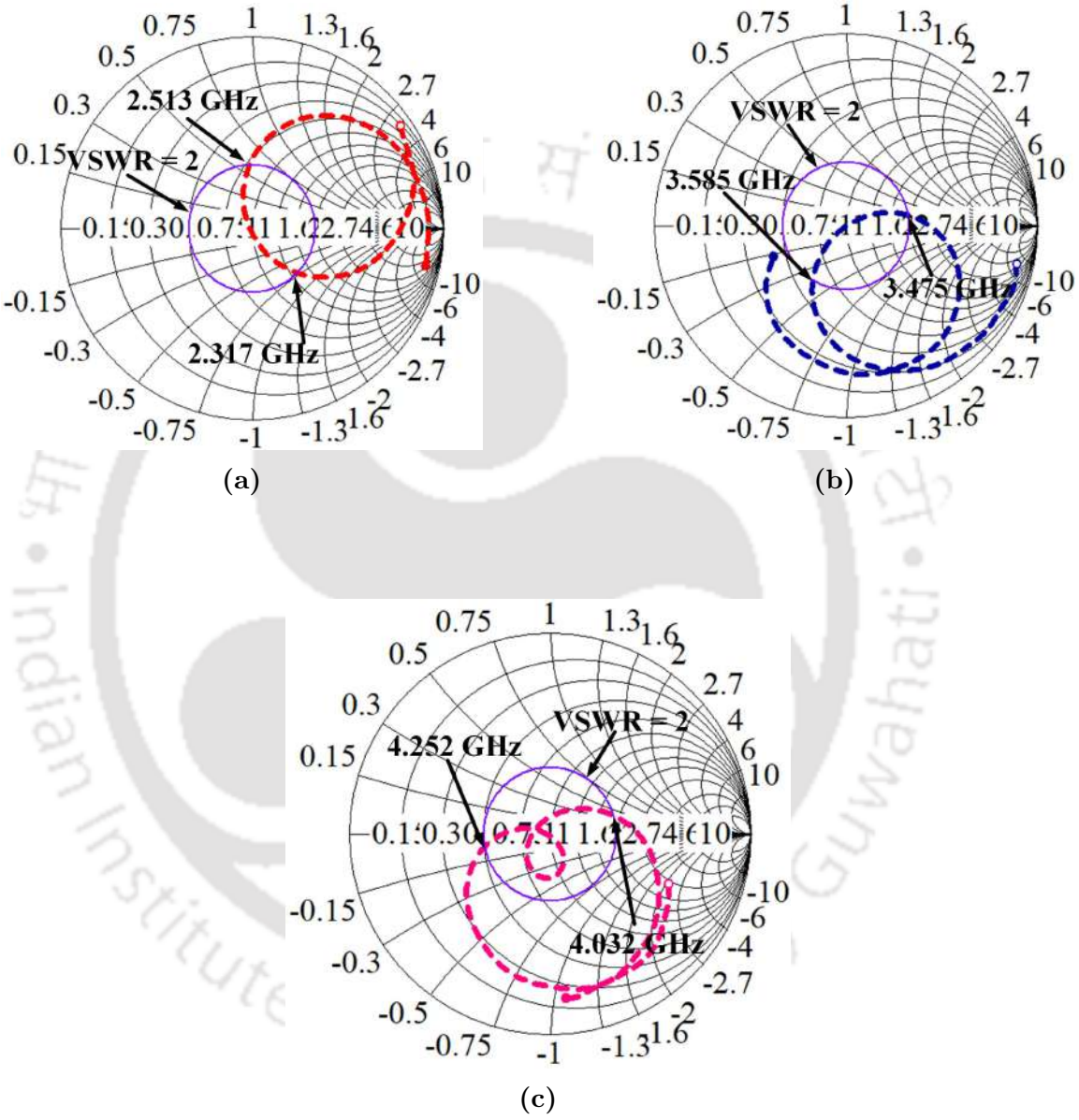


**Figure 2.6:** Simulated impedance matching on Smith chart of the proposed antenna at (a) 2.41 GHz, (b) 3.53 GHz, and (c) 4.14 GHz.

The simulated impedance bandwidth behavior of the proposed triple-band antenna is presented in Figure 2.6. It is seen from the figure that loop-like impedance curves are generated for the proposed antenna in the first, second and third band resonances at 2.41, 3.53 and 4.14 GHz, respectively which explains the first, second and third resonance excitation as seen in the

proposed antenna triple band in Figure 2.2. The −10 dB impedance bandwidth is observed to be 196, 110, and 220 MHz. The simulated triple-band frequencies and their corresponding impedances are presented in Table 2.5.

**Table 2.5:** Simulated triple-band frequencies and corresponding impedance of the proposed antenna

| Band | Simulated frequency (GHz) | Impedance (Ω) |
|---|---|---|
| First resonance | $f_1 = 2.41$ | $Z_1(f_1) = 58.25 - j7.36$ |
| Second resonance | $f_2 = 3.53$ | $Z_1(f_2) = 36.18 - j16.02$ |
| Third resonance | $f_3 = 4.14$ | $Z_1(f_3) = 50.39 - j5.41$ |

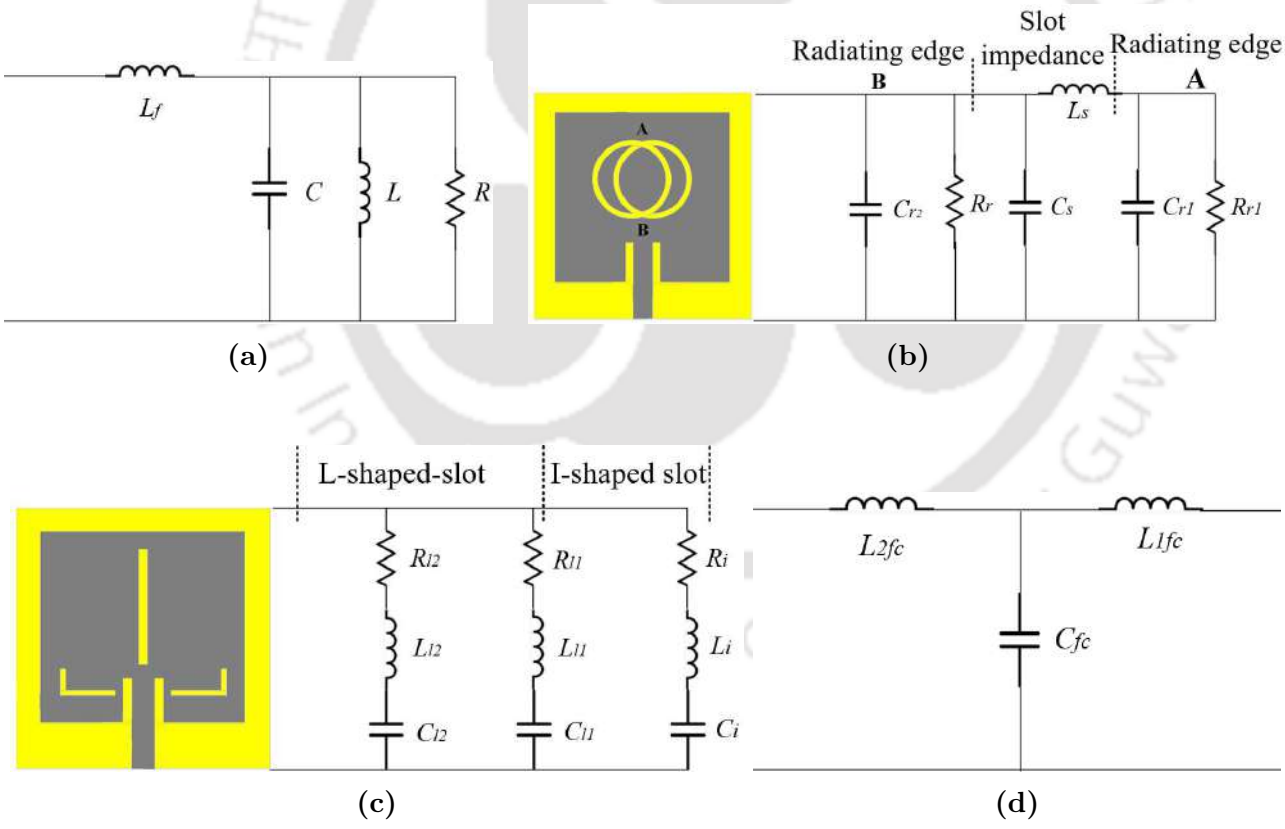


**Figure 2.7:** Equivalent circuit models of antenna elements (a) patch antenna, (b) annular ring slot, (c) L - and I -slot, and (d) fed-cut-slot.

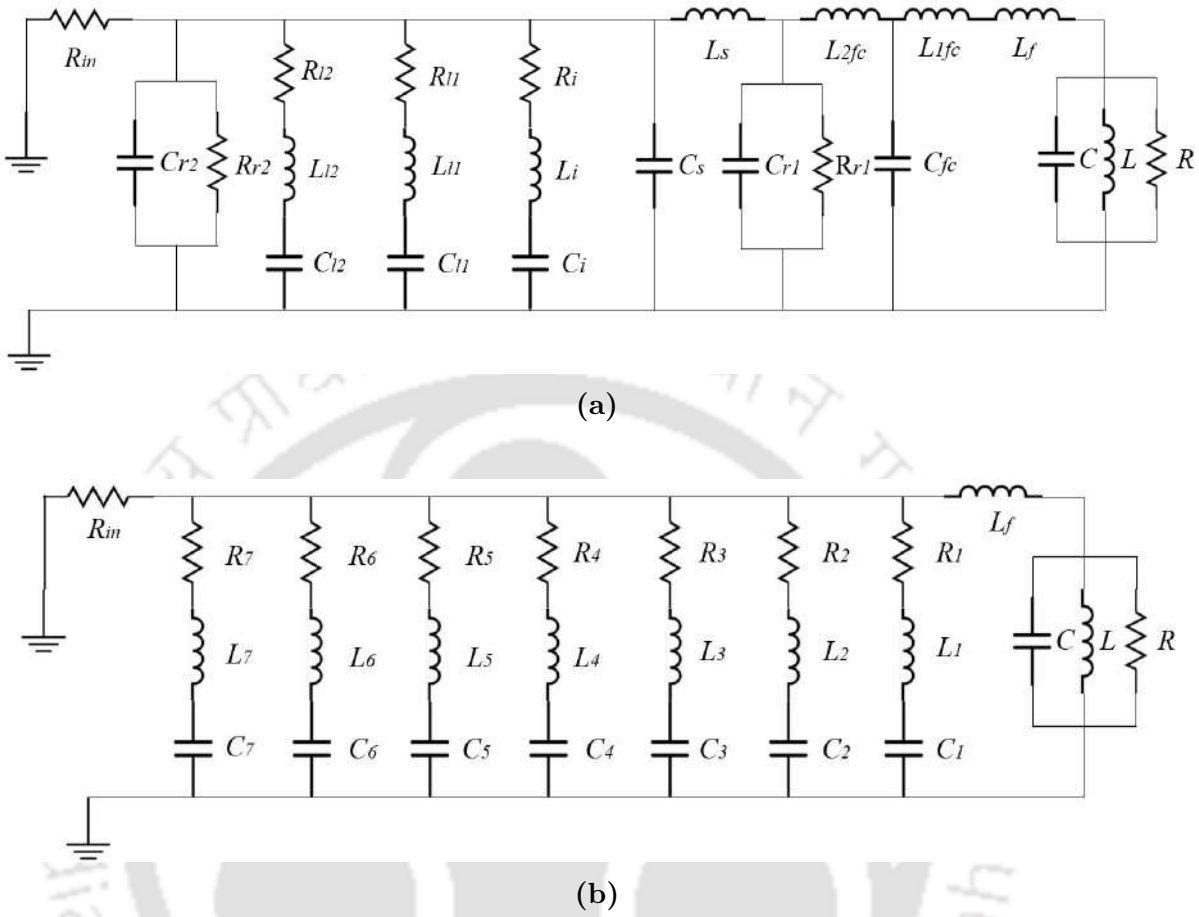


**Figure 2.8:** Equivalent TLM-circuit models of proposed antenna (a) equivalent circuit model and (b) simplified circuit model with RLC values [$R_{in}$ = 50, $R$ = 5.105, $R_1$ = 3.6, $R_2$ = 0.605, $R_3$ = 2, $R_4$ = 0.85, $R_5$ = 1.93, $R_6$ = 0.5, $R_7$ = 0.5] all dimensions are in Ω, [$L$ = 574000, $L_f$ = 5.69× $10^{-5}$, $L_1$ = 32100, $L_2$ = 0.3061, $L_3$ = 11.2, $L_4$ = 1.482, $L_5$ = 20.51, $L_6$ = 1.446, $L_7$ = 1.01] all dimensions are in nH, and [$C$ = 3.51× $10^{-12}$, $C_1$ = 0.7455, $C_2$ = 2.869, $C_3$ = 182.1, $C_4$ = 0.424, $C_5$ = 11.24, $C_6$ = 0.625, $C_7$ = 1.03] all dimensions are in pF.

## 2.3 TLM-RLC Equivalent Circuit Model

The electrical equivalent resistor-inductor-capacitor (RLC) circuit model of the proposed antenna is achieved by dividing the antenna into several segments where each segment proposes an individual equivalent circuit and the final equivalent circuit of the antenna is obtained by assembling the equivalent circuit of all segments.

The inductance $L_f$ is introduced by the microstrip feed line as shown in Figure 2.7(a). To draw the transmission line model (TLM)-RLC circuit of the DARS, the lower part A and upper

part B of the antenna as shown in Figure 2.7(b) are considered. Here the patch is considered as a parallel plate transmission line connecting two radiating slots. The gap capacitance $C_s$, and $R_{r1}$, $R_{r2}$, $C_{r1}$, $C_{r2}$ are the parallel resistor-capacitor branch of the patch. The slot inductance $L_s$ appears due to the current distribution in the patch. The L-shaped slot considering a combination of two rectangular slots (one vertical slot and another base slot) and an I-shaped slot as only one vertical slot which is represented in Figure 2.7(c). The rectangular patch of the proposed antenna which contains fed cut edges is shown in Figure 2.7(d). To simplify the TLM-RLC circuit model as shown in Figure 2.8(a), all shunt $R$-$C$, and series $L$ are converted into equivalent series $RLC$ branches as shown in Figure 2.8(b). An optimization process is performed using the NI AWR simulator and all parameter values ($R$ in ($\Omega$), $C$ in (pF), and $L$ in (nH)) are labeled in Figure 2.8(b). Finally, the result of the TLM-RLC circuit model of the proposed antenna using AWR software is the same as the simulation results obtained using CST simulator as shown in Figure 2.9.

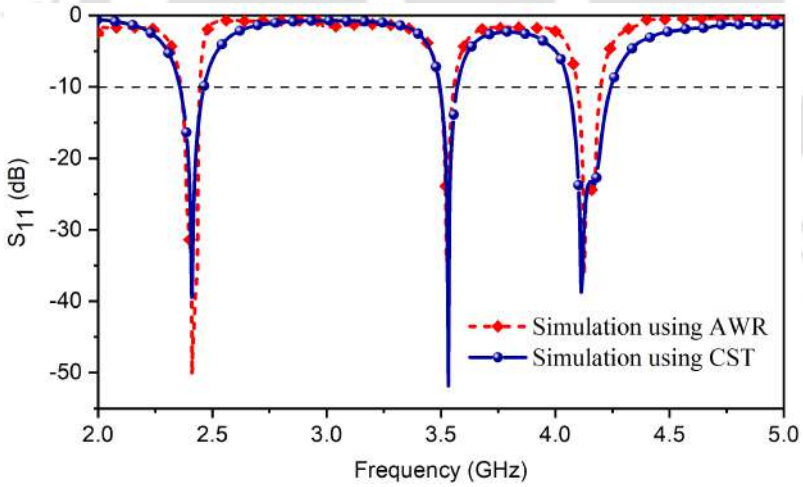


**Figure 2.9:** Simulated and equivalent TLM response of the proposed antenna.

## 2.4 Simulation and Measurement Performance

The performance of the proposed antenna is analyzed using CST software and the simulation results are verified with experimental results. The $S_{11}$ parameter, peak gain and the radiation

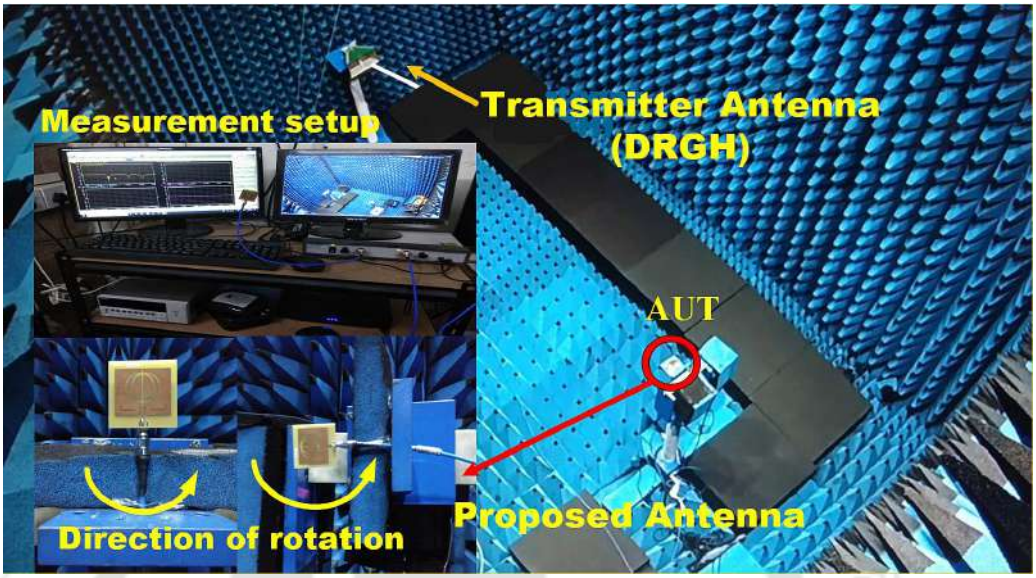


(a)


(b)

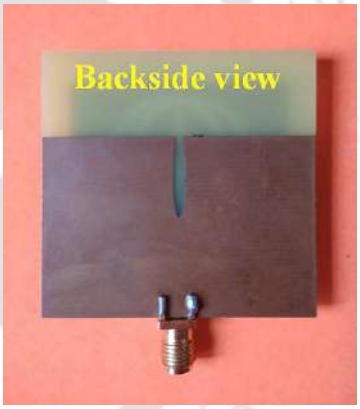


(c)

(d)

**Figure 2.10:** (a) Antenna measurement in an anechoic chamber, (b) topside view, (c) bottom view, and (d) $S_{11}$ measured with VNA.

patterns of the antenna are measured using system controlled vector network analyzer (VNA) (Anritsu-MS-46122B) in the anechoic chamber (size: 6×4×6 $m^3$) as shown in Figure 2.10(a). The prototype triple-band antenna top, bottom view, and $S_{11}$ measured using VNA are shown in Figures 2.10(b), 2.10(c), and 2.10(d), respectively.

### 2.4.1 Reflection Coefficient Performance

The reflection coefficient $S_{11}$ measured and simulated results are shown in Figure 2.11. The measured operating frequencies of the proposed antenna are 2.257–2.523 GHz (11.13%), 3.455–3.655 GHz (5.63%), and 4.012–4.262 GHz (6.05%) which can satisfy the 2.4 GHz WLAN, 3.5 GHz WiMAX, and 4.1 GHz C-band downlink satellite communications. It is observed that the measured result is in good agreement with the simulated $S_{11}$ result which validates the proposed antenna design approach.

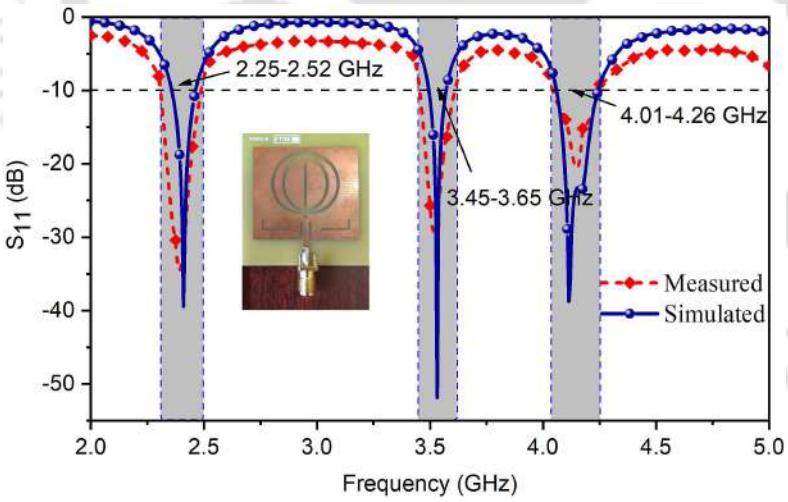


**Figure 2.11:** Measured and simulated $S_{11}$ results of the proposed antenna.

### 2.4.2 Gain Performance

Figure 2.12 shows the measured and simulated peak gains (dBi) against frequency (GHz). For the 2.25–2.52 GHz working for the first band, the peak gain is about 4.05 dBi. For the second and third bands, the antenna is with a relatively small gain of 2.52 and 2.15 dBi, respectively. Discrepancies between the measured and simulated results can be attributed to

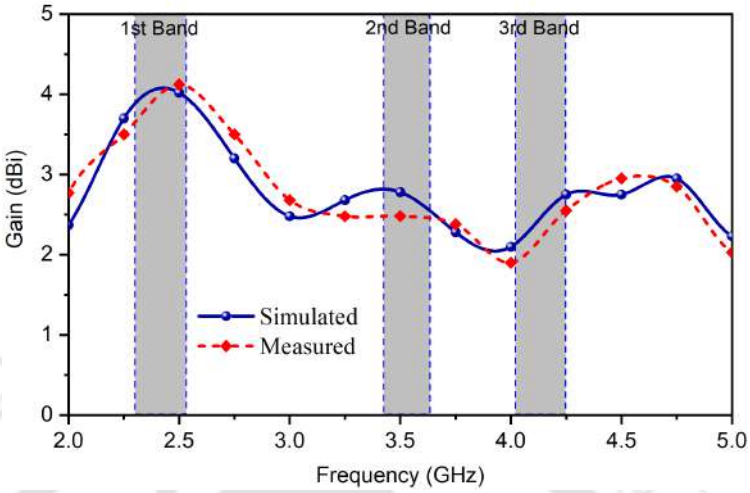


**Figure 2.12:** Measured and simulated peak gain of the proposed antenna.

**Table 2.6:** Performance parameters of the proposed antenna

| Parameter(s) | Resn. (1st) (Sim.) | Resn. (2nd) (Sim.) | Resn. (3rd) (Sim.) | Resn. (1st) (Mea.) | Resn. (2nd) (Mea.) | Resn. (3rd) (Mea.) |
|---|---|---|---|---|---|---|
| Frequency [GHz] | 2.41 | 3.53 | 4.14 | 2.39 | 3.55 | 4.13 |
| $S_{11}[dB]$ | -39.45 | -51.87 | -38.76 | -36.25 | -30.18 | -26.27 |
| Bandwidth [MHz] | 196 | 130 | 225 | 266 | 200 | 250 |
| Gain [dBi] | 4.18 | 2.75 | 2.32 | 4.05 | 2.52 | 2.15 |
| E-plane Cross-polarization [dB] | -37.26 | -36.3 | -40.1 | -35.2 | -34.1 | -38.85 |

the effects of measurement cables radiation and manufacturing imperfections. As a result, the peak gain of the proposed antenna within the operating bands satisfies the requirement of wireless communication terminals.

### 2.4.3 Radiation Patterns Performance

Figure 2.13 shows the simulated and measured E- and H-plane radiation patterns of the proposed antenna at 2.41, 3.53, and 4.14 GHz. The measured and simulated results match reasonably well. The two dimensional radiation patterns are represented close to the omnidirectional radiation within all bands. All the performance parameters of the proposed antenna

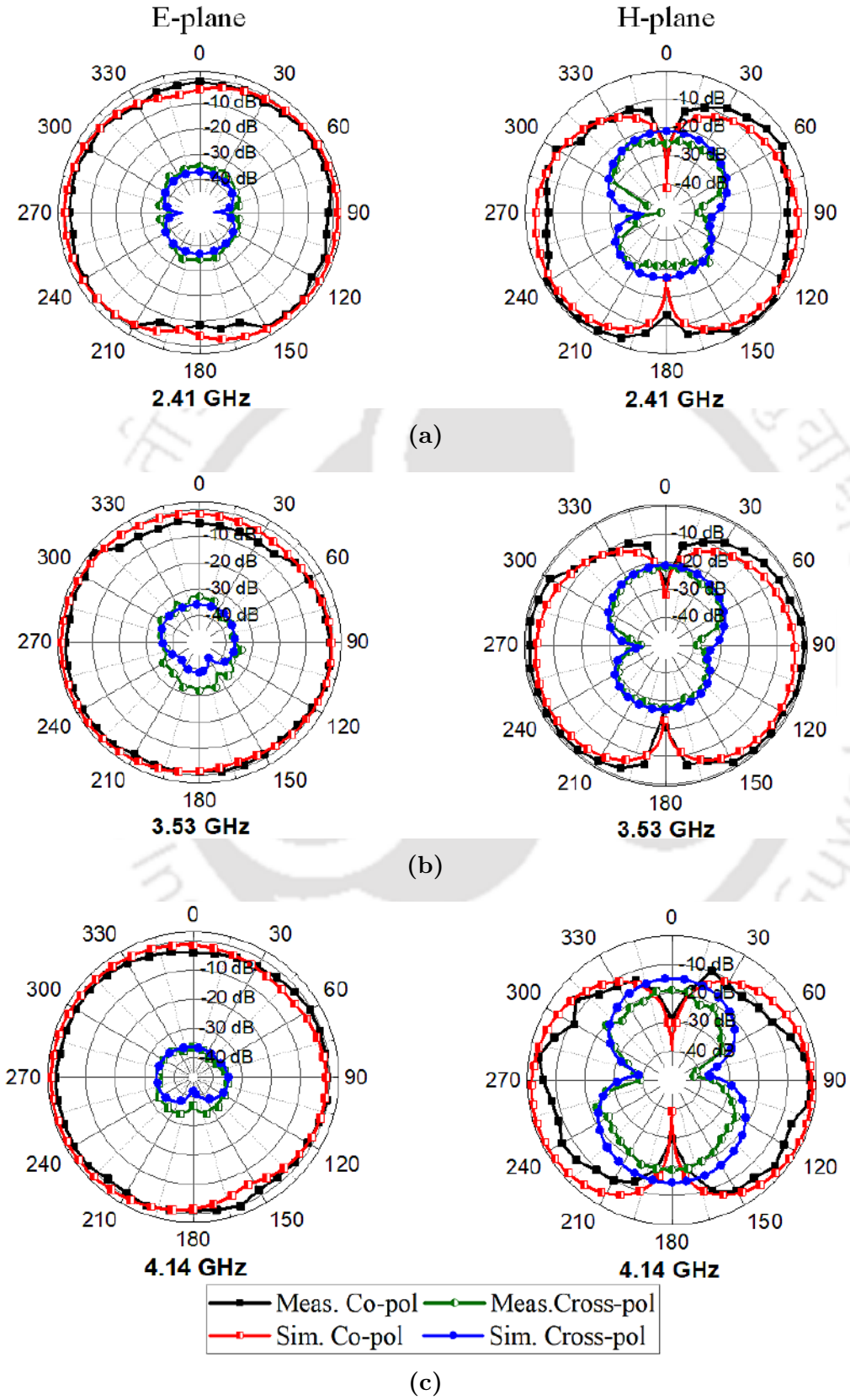


**Figure 2.13:** Measured and simulated radiation patterns of the proposed antenna (a) 2.41 GHz, (b) 3.53 GHz, and (c) 4.14 GHz.
TH-3087_176151008

**Table 2.7:** Comparison of proposed antenna with other recently reported antennas

| Ref. | Type | Feed line (type) | Dimension ($mm^3$) | Freq. (GHz) | Gain ($dBi$) | CFR | EX-pol. (dB) | Rad. pattern |
|---|---|---|---|---|---|---|---|---|
| [16] | Slot antenna | CP | 0.50×0.50× 0.06 $\lambda_0^3$ | 2.45/ 3.0/ 3.45 | 4.2/ 6.6/ 5.0 | 1.22/ 1.40 | -16.0 | Directional |
| [18] | Monopole antenna | CPW | 0.51×0.85× 0.006 $\lambda_0^3$ | 2.55/ 3.55/ 4.5 | 3.75/ 3.56/ 4.91 | 1.39/ 1.75 | -10.0 | Omni-directional |
| [19] | Slot antenna | CP | 0.85×0.62× 0.012 $\lambda_0^3$ | 3.62/ 5.02/ 5.6 | 7.2/ 2.2/ 3.9 | 1.33/ 1.63 | NR | Bidirectional |
| [23] | Slot antenna | CP | 1.0×1.0× 0.003 $\lambda_0^3$ | 2.4/ 2.8/ 3.4 | 0.27/ 3.31/ 4.45 | 1.16/ 1.41 | -17 .0 | NR |
| This work | Slot antenna | MS | 0.36×0.35× 0.012 $\lambda_0^3$ | 2.39/ 3.55/ 4.13 | 4.05/ 2.52/ 2.15 | 1.49 1.73 | -34.1 | Omni-directional |

CPW: Coplanar waveguide. MS: microstrip. CP: coaxial probe. CFR: center frequency ratio ($f_2/f_1$),($f_3/f_1$). NR: not reported. EX-pol: E-plane cross-pol. according to the criteria $|S_{11}| \leq$ -10 dB.

are listed in Table 2.6. The measured broadside cross-polarization level in E-plane is −38.85 dB while the simulated cross-polarization level is −40.1 dB. It is observed from Table 2.6 that all the measured results corresponding to their simulated counterparts of the antenna are within the acceptable limit which ensures a good design.

Table 2.7 gives the comparison of performance between the proposed antenna and other triple-band antennas in the literature. The antenna type, feed line, dimension, operating bands, peak gain, center frequency ratio, E-plane cross-polarization level, and types of radiation pattern are listed. It is noticed from Table 2.7 that the proposed structure gives a compact size among the others. Furthermore, it gives the better center frequency ratio $f_2/f_1 = 1.49$ and

$f_3/f_1 = 1.73$ and the lowest cross-polarization of $-34.1$ dB in the E-plane along the main beam direction, which is far better than the other literature operating in the same band as mentioned in Table 2.7. It is seen that this design performs better in almost all the parameters. Therefore, considering all the performance of the proposed antenna, it will be a good candidate for wireless applications.

## 2.5 Summary of the Chapter

In this chapter, a compact microstrip-fed triple-band slot antenna for WLAN/WiMAX/C-band downlink satellite communications is proposed. The newly designed proposed simple structure is having a considerably high center frequency ratio and can significantly suppress cross-polarization levels. This antenna consists of a double annular ring slot (DARS), two L- and one I-shaped slot on the radiator, and an ellipse-shaped-slit (ESS) based defective ground structure (DGS). Furthermore, to achieve a better impedance bandwidth and impedance matching, an insert-fed has been implemented in the proposed structure. The proposed antenna has the advantages of easy tuning of individual resonant frequencies and a relatively simple antenna structure. The fabricated prototype resonates at 11.13% (2.257–2.523 GHz), 5.63% (3.455–3.655 GHz) and 6.05% (4.012–4.262 GHz) having a peak gain of 4.05, 2.52, 2.15 dBi, respectively, with approximate cross-polarization of −38.85 dB. The transmission line model of the proposed antenna is presented and it shows the antenna behavior based on the effect of each element. It is observed that the characteristics of the RLC circuit model result are close to the simulated result using the CST simulator. Because of the above-said advantages, the proposed antenna can be used where the narrow band is required such as wireless, mobile, satellite applications, radio determination applications, etc. The reduced size and enhanced impedance bandwidth of design antenna using symmetrical staircase-shaped notches and slotted CPW-fed patch is discussed in the next chapter.

*Note: This work, Design of Compact Microstrip-fed Triple-Band Slot Antenna with Defected Ground Structure for Wireless Communications has been published in Journal of Electromagnetic Waves and Application.*

**2. Design of Compact Microstrip-fed Triple-Band Slot Antenna with Defected Ground Structure for Wireless Communications**

# 3

# Design of Compact CPW-Fed Symmetrical Staircase-Shaped UWB Antenna using Transmission Line Model

Contents

## 3.1 Introduction

Printed microstrip slot antennas are widely adopted in wireless communications systems due to their advantages such as lightweight, low profile, low cost, and easy to integrate with monolithic microwave integrated circuits (MMIC). However, the use of microstrip slot antennas bring a new problem, i.e., the narrow bandwidth, which is important to the fidelity of ultra-wideband (UWB) signals. Compared to microstrip antennas, coplanar waveguide (CPW)-fed antennas offer relatively broad bandwidth, high-speed data rate, low sensitivity to fading, flexible, allow the integration with surface-mount devices and can be used for ultra-wideband (UWB) antennas operation [30, 31]. But in modern wireless communications, there is a significant increase in the demand for various CPW-fed printed antennas with wider bandwidth and miniaturized size. The monopole and Vivaldi antennas having wide bandwidth and good radiation are extremely used as reported in [32]. Monopole antennas are installed perpendicularly to carriers and a Vivaldi antenna needs a tapered slot, so in both cases, a relatively large area is required.

In recent years, for the requirement of enhanced impedance bandwidth, the slot antenna has been further developed. A large number of designs have been proposed in a compact size and enhanced bandwidth [33–38]. In [33], the length of the central metallic strip line is stretched beyond the CPW plane to achieve an improved radiation performance like the monopole antenna. Similarly, the central strip plays a significant role in finding the wider bandwidth with the subsequent creation of different shapes such as CPW-fed antennas with dual-reverse-arrow fractal structure [34], flexible bow-tie slot antenna [35], rose-curve shape monopole antenna [36], wideband fractal shapes structure [37], etc. Although the wideband fractal shapes structure antenna is capable of providing wider impedance bandwidth performance but the size of this antenna is large.

The compactness is the major necessity for today's wireless applications devices e.g., UWB applications and for this encouraging the exploration in the direction of smaller size CPW-fed tapered-slot structures [38]. Since the bandwidth of traditional slot antennas is confined by slot width, the operation bandwidth is not easily enhanced [39]. A UWB and compact

antenna are presented in [40–48]. In [40], a semi-elliptically fractal slot patch antenna with an asymmetrical ground plane, having an impedance bandwidth of 172% is proposed. However, the dimension is $77 \times 35$ mm$^2$. The Y-shaped central monopole meandered-slot miniature antenna structure is used for wider bandwidth [41]. The antenna proposed in [42–44], printed E-shape slot, arc shape stub and fishtail-shape different from other coplanar waveguide-fed slot antennas are used only for exciting the slot and it has a very good impedance bandwidth. A Vivaldi antenna uses a stepped connection structure to enhance the impedance bandwidth and the matched antenna feed [45]. In [46], a microstrip line-fed hybrid monopole antenna which is electromagnetically coupled band-notched is presented. In [47], the change of lower and upper resonant frequency with respect to the width of a U-slot and the existence of only modes 1 and 3 due to the capacitive effect with respect to the U-slot patch structure are discussed. Besides, a wide bandwidth and compact size UWB slot antenna different than the traditional wideband slot antennas is proposed [48].

In this chapter, considering the enhanced impedance bandwidth (BW), gain and compact size, a CPW-fed symmetrical staircase-shaped UWB antenna is presented. Since the design and the fabricated antenna has a symmetrical pair of C-shaped slot, two pairs of quarter-circular-ring-slit (QCRS), and three pairs of rectangular notches which are sequentially embedded in the bottom corners of the rectangular patch, five resonant peaks i.e., 2.31, 4.85, 8.33, 12.11 and 16.41 GHz are achieved. As a result, the widest impedance bandwidth, better impedance matching, a high value of bandwidth dimension ratio (BDR), and the stability of the E- and H-plane are obtained. Then, an equivalent transmission line model (TLM) of the proposed antenna is developed. An optimization is used in Applied Wave Research (AWR) simulator to find the circuit parameters such as resistance (R), inductance (L) and capacitance (C) of the TLM equivalent circuit using the $S_{11}$ simulated parameters [49, 28, 29] of the proposed antenna.

This chapter is divided into the following sections: section 3.2 explains the design process and working principle such as design evolution, enhancement in impedance bandwidth, and the impedance matching of the proposed antenna. The parametric studies, analysis of coupled

mode theory (CMT), bandwidth dimension ratio (BDR) of the antenna of the proposed antenna and the derived analytical expressions for the tangential component of the electric field at the patch are presented in section 3.3. The mathematical modeling of the proposed antenna and derived analytical expression for the transmission line model (TLM)-RLC circuit model are presented in section 3.4. The reflection coefficient $S_{11}$, peak gain, efficiency and radiation pattern parameters at different frequencies like 1.55, 2.31, 4.85, 8.33, 12.11 and 16.41 GHz are compared. The simulation and experimental results of the $S_{11}$, peak gain, efficiency and radiation patterns in both the planes are presented in section 3.5. The experimental results match well with the simulation results, thus validating the practical feasibility of the design. The principal outcomes of this research work are explained in section 3.6.

**Table 3.1:** Geometric parameters of the UWB proposed antenna

| Parameters | Value (mm) | Parameters | Value (mm) | Parameters | Value (mm) |
|---|---|---|---|---|---|
| $L_s$ | 46.32 | $w_2$ | 3.99 | $w_f$ | 2 |
| $W_s$ | 43.48 | $w_3$ | 7.97 | $w_g$ | 20 |
| $l$ | 28.52 | $w_4$ | 11.95 | $l_g$ | 12.9 |
| $w$ | 33.88 | $m_1$ | 2 | $r_1$ | 2 |
| $l_1$ | 13.95 | $g_p$ | 1.9 | $r_2$ | 2.4 |
| $l_2$, $l_3$,$l_4$ | 3.99 | $g_f$ | 0.74 | $r_3$ | 5.75 |
| $w_1$ | 12 | $l_f$ | 14.8 | $r_4$ | 6.75 |

## 3.2 Design Process and Working Principle

### 3.2.1 Antenna Configuration

The structure of a proposed co-planar waveguide (CPW)-fed symmetrical staircase-shaped (SSS) antenna with enhanced bandwidth is depicted in Figure 3.1. A wider impedance bandwidth and higher gain performances are achieved by cutting SSS and symmetrical two C-slot on the rectangular radiator. The antenna is fabricated on a $46.32 \times 43.48$ mm$^2$ (Ls $\times$ Ws) with a thickness of 0.8 mm Rogers (RT/5880) substrate having a dielectric constant of $\epsilon_r = 2.2$ and

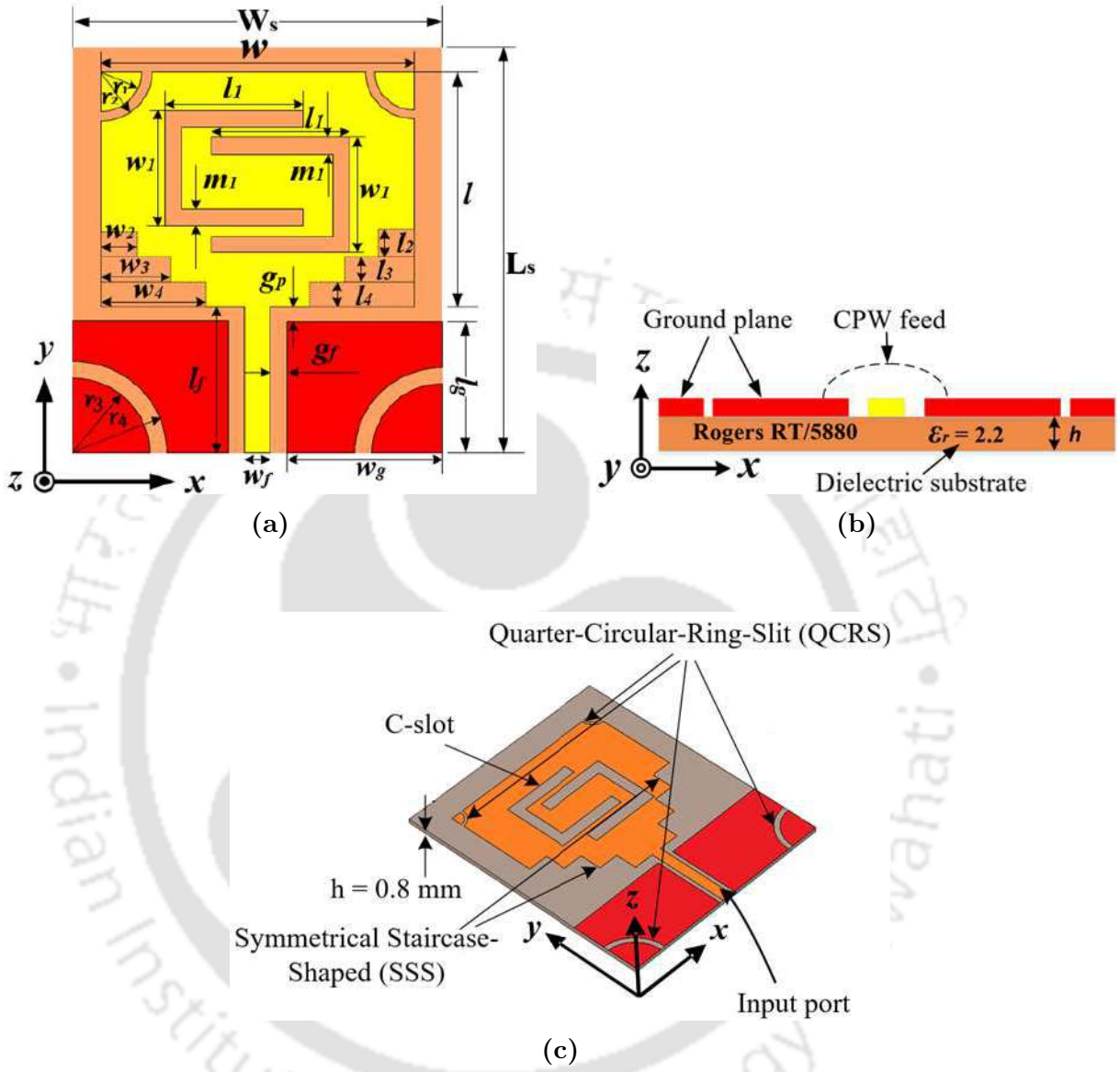


**Figure 3.1:** Geometry of the proposed CPW-fed symmetrical staircase-shaped UWB antenna (a) top view, (b) front view, and (c) configuration in three dimensions.

loss tangent of 0.0009. The electromagnetic software CST simulator (CST vers. 17) is used for simulation. The specific dimensions of the proposed UWB antenna are given in Table 3.1.

### 3.2.2 Design Evolution and Enhanced Bandwidth

The evolutions for designing the antennas are summarized in five steps as follows:

**First Step:** The evolution steps of the antenna design is shown in Figure 3.2. Antenna 1 is a

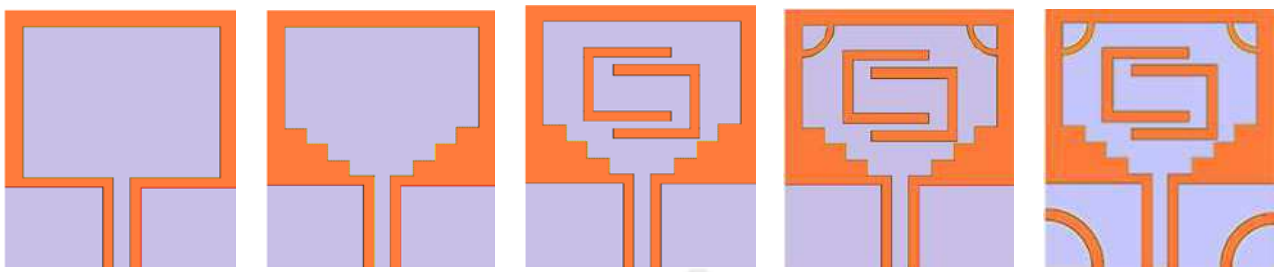


**Figure 3.2:** Evolution of the proposed symmetrical staircase-shaped UWB antenna (a) Antenna 1, (b) Antenna 2, (c) Antenna 3, (d) Antenna 4, and (e) Antenna 5 (proposed).

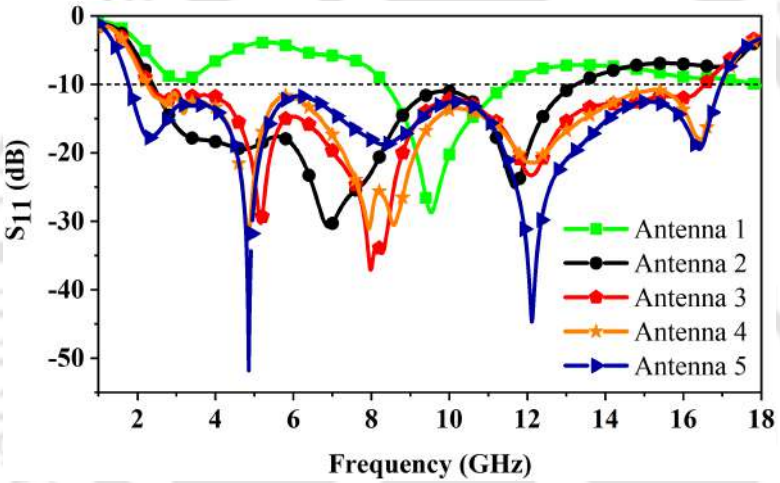


**Figure 3.3:** Reflection coefficients versus frequency characteristics for different structures of design antenna.

simple rectangular patch antenna with CPW-fed whose simulated $S_{11}$ results are presented in Figure 3.3. It is observed from Antenna 1, that the impedance bandwidth performance from 8.35–11.45 GHz (normalized bandwidth 31.31%). It shows only one resonance band (it cannot provide better characteristics performance of $S_{11} \leq -10$ dB) due to the external current path and its frequency can be expressed as [41]:

$$f_{ext} \approx \frac{c}{\sqrt{\epsilon_{eff}} L_{path}} \tag{3.1}$$

where $L_{path}$ is the external path length, $c$ speed of light in a vacuum and $\epsilon_{eff}$ is the effective dielectric constant.

**Second Step:** The three pairs of notches are sequentially introduced with dimensions of $w_2$

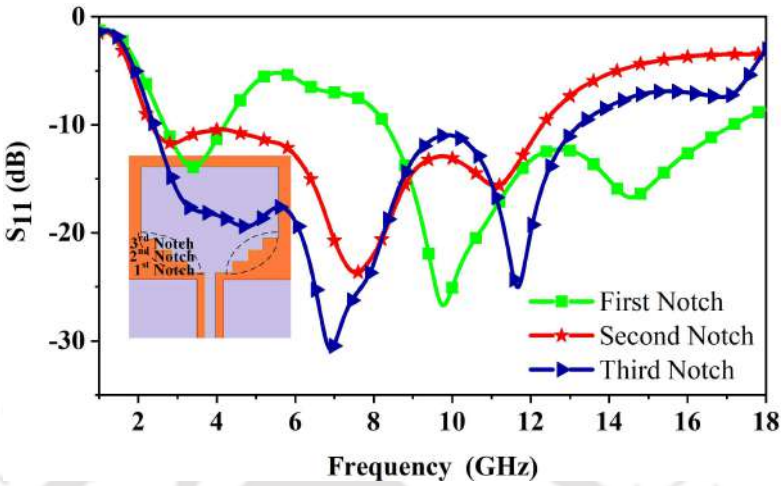


**Figure 3.4:** Simulated $S_{11}$ performance of the staircase-shaped Antenna 2.

$\times$ $l_2$, $w_3$ $\times$ $l_3$, and $w_4$ $\times$ $l_4$ to generate the frequency of the resonant peaks at 6.9 GHz and 11.68 GHz. A wide bandwidth i.e, from 2.40–13.24 GHz (normalized bandwidth 138.62%) and better return loss performances are achieved by inserting the first, second, and third pairs of notches as shown in Figure 3.4.

**Third Step:** A conventional symmetrical two C-shaped slot patch antenna with parameters $w$, $l$, $h$, $l_1$, $m_1$, and $w_1$ are designed by using the approximate formulae [54, 10]:

$$w = \frac{c}{2f_r}\sqrt{\frac{2}{\epsilon_r + 1}} \tag{3.2}$$

$$l = \frac{c}{2f_r\sqrt{\epsilon_{eff}}\sqrt{\mu_o\epsilon_o}} - 2\Delta l \tag{3.3}$$

where $l$ and $\Delta l$ are the actual length and effective length of the patch respectively and $\epsilon_{eff}$ is expressed as:

$$\epsilon_{eff} = \frac{\epsilon_r + 1}{2} + \frac{\epsilon_r - 1}{2}\left(1 + 12\frac{h}{w}\right)^{-1/2} \tag{3.4}$$

$$\Delta l = 0.412h\frac{(\epsilon_{eff} + 0.3)\left(\frac{w}{h} + 0.264\right)}{(\epsilon_{eff} - 0.258)\left(\frac{w}{h} + 0.8\right)} \tag{3.5}$$

$$w_1 = \frac{c}{f_r\sqrt{\epsilon_{eff}}} - 2(l + 2\Delta l - m_1) \tag{3.6}$$

$$m_1 = \frac{\lambda_r}{60} \tag{3.7}$$

where $\lambda_r$ is the wavelength in vacuum

$$\frac{l_1}{w} \geq 0.3, \frac{l_1}{w_1} \geq 0.75 \tag{3.8}$$

$$h \geq 0.06\frac{\lambda_r}{\sqrt{\epsilon_r}} \tag{3.9}$$

where $f_r$ ( = 2.5 GHz) is the designed antenna resonant frequency.

A pair of symmetrical C-slots is introduced at the center on the radiating patch to generate the five peak resonant frequencies at 2.76, 5.16, 7.98, 12.09, and 16.13 GHz, respectively of the Antenna 3. Due to the introduction of the C-slot, the improvement in the return loss and impedance bandwidth from 2.32 to 16.52 GHz (BW = 150.74%) (Figure 3.3) is achieved.

**Fourth Step:** In the fourth evolution of the antenna (Antenna 4), a pair of symmetrical quarter-circular-ring-slit (QCRS) to Antenna 3 is introduced to improve the $S_{11}$ (slightly improved the bandwidth 2.25 GHz–16.96 GHz and the percentage of bandwidth 153.15%) performance as shown in Figure 3.3. From the $S_{11}$ performance, it is observed that five peak resonant frequencies i.e., 4.84, 7.94, 8.58, 12.18, and 16.44 GHz are achieved. For further improvement in peak gain, return loss, and impedance bandwidth Antenna 4 is modified in the fifth step.

**Fifth Step:** In the final design of Antenna 5, a pair of the symmetrical quarter-circular-ring-slit is introduced on both sides of the ground plane of Antenna 4 to improve $S_{11}$ further. From the $S_{11}$ parameter, it is observed that the excellent impedance bandwidth from 1.77–16.96 GHz (normalized bandwidth 162.2%) is achieved. From the $S_{11}$ performance, we have observed five peak resonant frequencies i.e., 2.31, 4.85, 8.33, 12.11, and 16.41 GHz, and the approximate expression of these frequencies are given as follows:

$$f_{rp1} \cong \frac{c}{2\sqrt{\epsilon_{eff}}(2l_1 + w_1 - m_1)} \tag{3.10}$$

$$f_{rp2} \cong \frac{c}{2\sqrt{\epsilon_{eff}}(l_1 + w_1 - 2m_1)} \tag{3.11}$$

$$f_{rp3} \cong \frac{c}{\sqrt{\epsilon_{eff}}(l_1 + w_1 - m_1)} \tag{3.12}$$

$$f_{rp4} \cong \frac{c}{2\sqrt{\epsilon_{eff}}(l_4 + w/2 - w_4 - w_f/2)} \tag{3.13}$$

$$f_{rp5} \cong \frac{c}{\sqrt{\epsilon_{eff}}(l_4/2 + w/2 - w_4 - w_f/2)} \tag{3.14}$$

**Table 3.2:** Comparison between theoretical and simulation results for peak resonant frequencies

| Name | $f_{rp1}$ (GHz) | $f_{rp2}$ (GHz) | $f_{rp3}$ (GHz) | $f_{rp4}$ (GHz) | $f_{rp5}$ (GHz) |
|---|---|---|---|---|---|
| Simulation | 2.31 | 4.85 | 8.33 | 12.11 | 16.41 |
| Theoretical | 2.468 | 4.672 | 8.445 | 12.672 | 16.911 |
| % Error | 6.61 | 3.78 | 1.37 | 4.51 | 3.00 |

Note: $f_{rp1}$... $f_{rp5}$: First, second, third, fourth and fifth peak resonant.

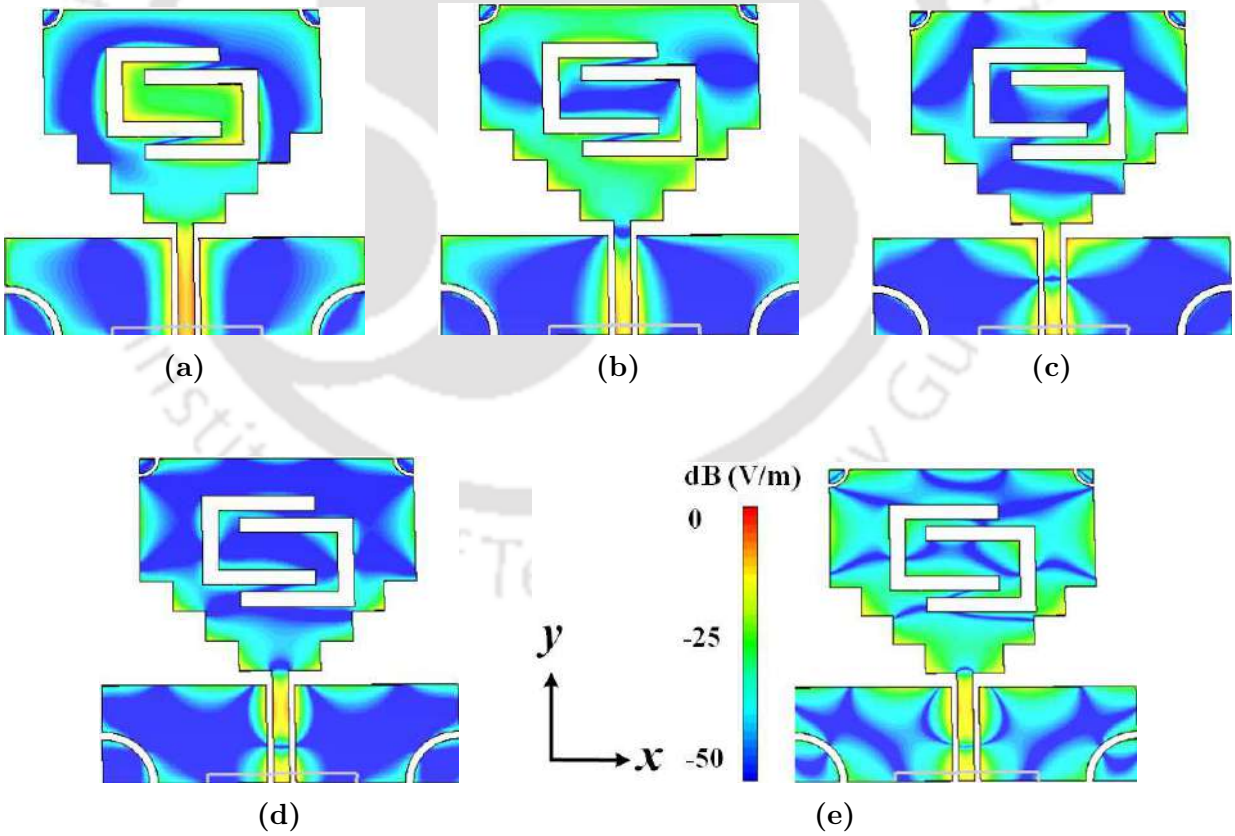


**Figure 3.5:** An electric field distribution of the proposed antenna on the slot and conductor at (a) 2.31 GHz, (b) 4.85 GHz, (c) 8.33 GHz, (d) 12.11 GHz and (e) 16.41 GHz.

The electric field distributions of the designed antenna at these peak resonant frequencies are shown in Figure 3.5. As seen, the first, second, and third peak resonant frequencies are

generated by the slot, while the fourth and fifth peak resonant frequencies are generated by the rectangular patch. Table 3.2 represents a comparison between the theoretical and simulation results of peak resonant frequencies of the designed antenna.

**Table 3.3:** Simulated peak resonant frequency and corresponding impedance of the Antenna 1

| Resonance | Simulated frequency (GHz) | Impedance (Ω) |
|---|---|---|
| First | $f_{rp1} = 9.539999$ | $Z_1(f_{rp1}) = 97.51 + j3.98$ |

Note: $f_{rp1}$: First peak resonant

**Table 3.4:** Simulated peak resonant frequencies and corresponding impedance of the Antenna 2

| Resonance | Simulated frequency (GHz) | Impedance (Ω) |
|---|---|---|
| First | $f_{rp1} = 4.798775$ | $Z_1(f_{rp1}) = 68.49 + j4.50$ |
| Second | $f_{rp2} = 8.623375$ | $Z_1(f_{rp2}) = 86.42 - j14.75$ |
| Third | $f_{rp3} = 11.847321$ | $Z_1(f_{rp3}) = 84.03 + j2.82$ |
| Fourth | $f_{rp4} = 16.359999$ | $Z_1(f_{rp4}) = 61.52 - j0.66$ |

Note: $f_{rp1}$... $f_{rp4}$: First, second, third, and fourth peak resonant

**Table 3.5:** Simulated peak resonant frequencies and corresponding impedance of the Antenna 3

| Resonance | Simulated frequency (GHz) | Impedance (Ω) |
|---|---|---|
| First | $f_{rp1} = 2.76$ | $Z_1(f_{rp1}) = 127.86 - j39.34$ |
| Second | $f_{rp2} = 5.16$ | $Z_1(f_{rp2}) = 96.04 - j4.09$ |
| Third | $f_{rp3} = 7.98$ | $Z_1(f_{rp3}) = 90.46 - j2.04$ |
| Fourth | $f_{rp4} = 12.09999$ | $Z_1(f_{rp4}) = 81.98 + j6.55$ |
| Fifth | $f_{rp5} = 16.136198$ | $Z_1(f_{rp5}) = 55.04 - j7.15$ |

Note: $f_{rp1}$... $f_{rp5}$: First, second, third, fourth and fifth peak resonant

The impedance bandwidth behavior of the proposed antenna is shown in Figure 3.6, where the best impedance match is obtained from the proposed antenna (about 162.2% impedance bandwidth). The simulated peak resonant frequencies and their corresponding impedance are presented in Tables 3.3–3.7.

The simulated 3D radiation patterns close to these resonances are plotted in Figure 3.7. The radiation pattern looks like a donut, similar to a dipole pattern, at the first resonant frequency,

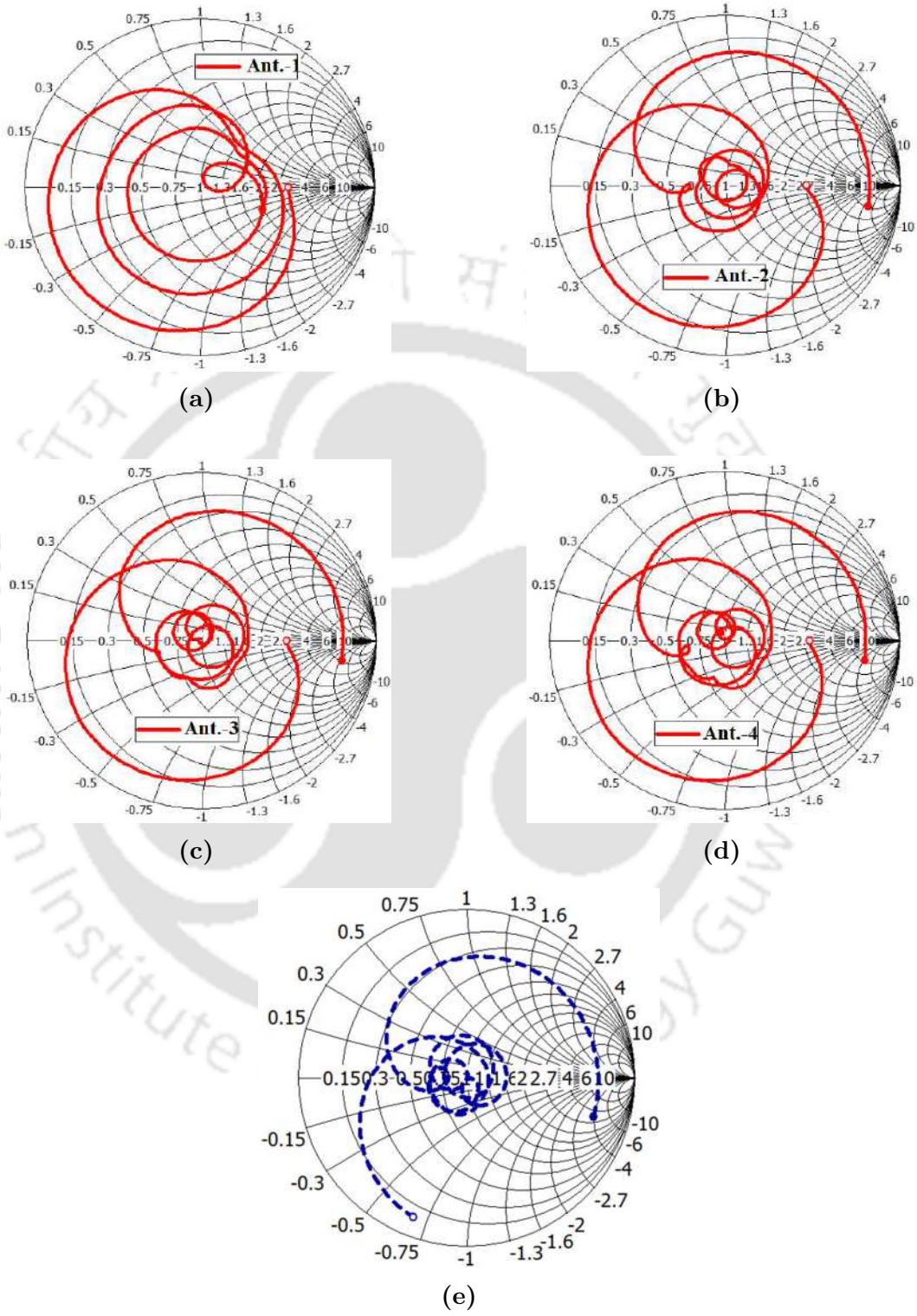


**Figure 3.6:** Comparison of simulated results of impedance matching (a) Antenna 1, (b) Antenna 2, (c) Antenna 3, (d) Antenna 4, and (e) Antenna 5 (proposed antenna).

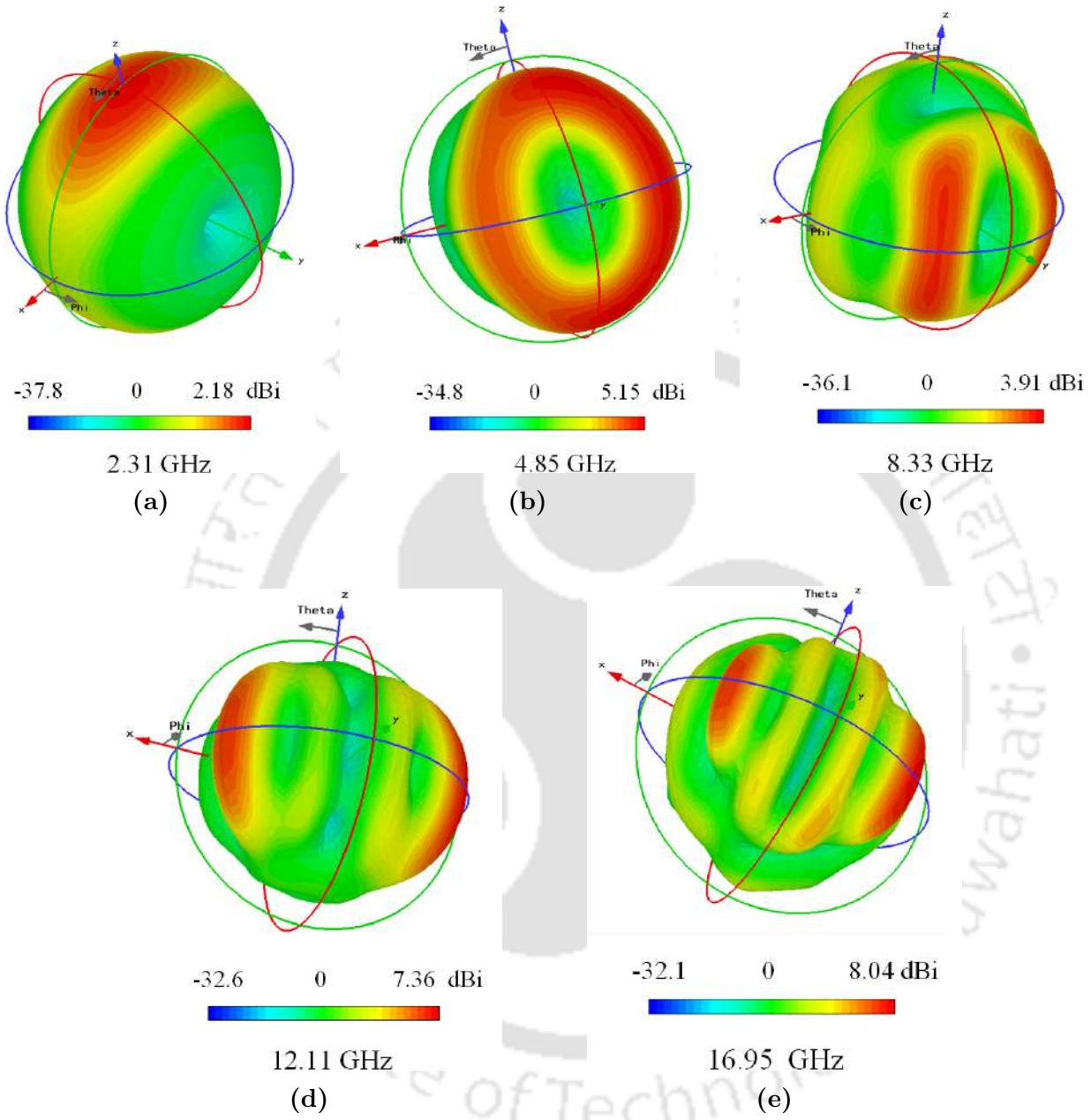


**Figure 3.7:** Simulated 3D radiation patterns of the UWB proposed antenna at (a) 1.55 GHz, (b) 2.31 GHz, (c) 4.85 GHz, (d) 8.33 GHz, (e) 12.11 GHz, and (f) 16.95 GHz.

as shown in Figure 3.7(a). At the second harmonic, the pattern changes its shape to a slightly pinched donut with the gain increase around $\theta = 45°$ in Figure 3.7(b). When at the third, fourth, and fifth harmonics, the patterns are squashed in negative z-direction and humps form in the up-right directions (gain increasing), as shown in Figure 3.7(c)–3.7(e), respectively. It is also noticed that the patterns on the H-pane are almost omni-directional at lower resonances

**Table 3.6:** Simulated peak resonant frequencies and corresponding impedance of the Antenna 4

| Resonance | Simulated frequency (GHz) | Impedance (Ω) |
|---|---|---|
| First | $f_{rp1} = 2.74$ | $Z_1(f_{rp1}) = 133.16 - j36.78$ |
| Second | $f_{rp2} = 5.18$ | $Z_1(f_{rp2}) = 94.47 - j2.99$ |
| Third | $f_{rp3} = 7.82$ | $Z_1(f_{rp3}) = 91.99 + j1.56$ |
| Fourth | $f_{rp4} = 12.22$ | $Z_1(f_{rp4}) = 83.66 + j7.37$ |
| Fifth | $f_{rp5} = 16.16$ | $Z_1(f_{rp5}) = 61.39 - j5.74$ |

Note: $f_{rp1}$... $f_{rp5}$: First, second, third, fourth and fifth peak resonant

**Table 3.7:** Simulated peak resonant frequencies and corresponding impedance of the Antenna 5 (proposed)

| Resonance | Simulated frequency (GHz) | Impedance (Ω) |
|---|---|---|
| First | $f_{rp1} = 2.31$ | $Z_1(f_{rp1}) = 100.072 + j2.742$ |
| Second | $f_{rp2} = 4.85$ | $Z_1(f_{rp2}) = 77.771 + j0.357$ |
| Third | $f_{rp3} = 8.33$ | $Z_1(f_{rp3}) = 72.499 - j16.679$ |
| Fourth | $f_{rp4} = 12.11$ | $Z_1(f_{rp4}) = 77.504 - j0.897$ |
| Fifth | $f_{rp5} = 16.41$ | $Z_1(f_{rp5}) = 62.392 + j0.986$ |

Note: $f_{rp1}$... $f_{rp5}$: First, second, third, fourth and fifth peak resonant

(1st and 2nd harmonics) and become distorted at the higher harmonics. The transition of the radiation patterns from a simple donut pattern at the first resonance to the complicated patterns at higher harmonics indicates that this antenna must have gone through some major changes in its behavior.

## 3.3 Parametric Study

### 3.3.1 Parametric Effect of CPW-fed Ground Length ($l_g$) and Width ($w_g$)

Figures 3.8 and 3.9 shows $S_{11}$ with the variation of length ($l_g$) and width ($w_g$) of the ground plane. From the figure, it is observed that an increase in ground length $l_g$ from 12.5 to 13.3 mm, the reflection coefficient moves towards a higher frequency band and better return loss

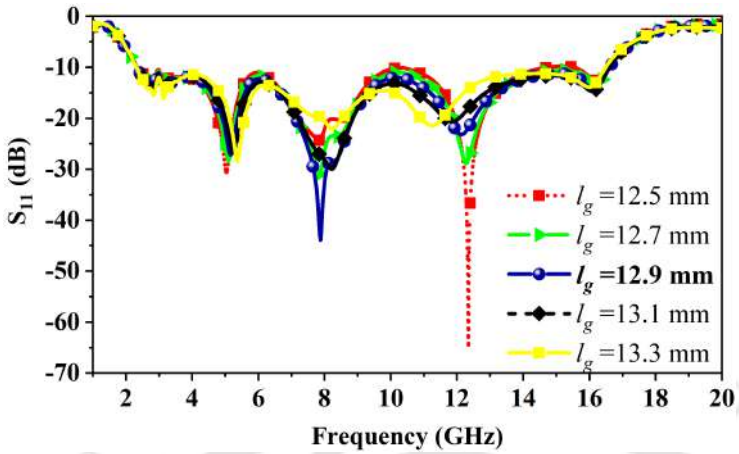


**Figure 3.8:** Simulation $S_{11}$ results of the UWB antenna with a variation of $l_g$.

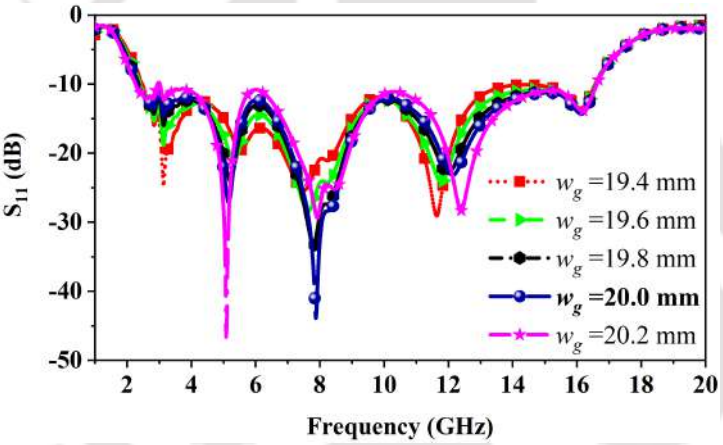


**Figure 3.9:** Simulation $S_{11}$ results of the UWB antenna with a variation of $w_g$.

is achieved as expected. Similarly, as width ($w_g$) increases, the upper sideband frequency increases slightly. At $w_g = 20$ mm, it provides better gain and enhanced impedance bandwidth performance over a frequency band as shown in Figure 3.9.

### 3.3.2 Parametric Effect of $l_1$, $w_1$ and $m_1$ of C-Slot

In Figure 3.1(a), the symmetrical C-slot has horizontal slot $l_1$, vertical slot $w_1$, and thickness $m_1$. Figure 3.10 shows the simulated $S_{11}$ performance with the variation of C-slot $l_1$. It is observed from the $S_{11}$ results that the upper, as well as lower side-band frequency, are affected due to the horizontal slot length of the C-slot of the proposed antenna. More specifically an increase in length $l_1$ of the slot from 13.05 to 14.35 mm reduce return loss performance as well

as bandwidth. It is also observed that the wideband performance is reduced with a further increase in length $l_1$ from 13.95 to 14.35 mm. The wider impedance bandwidth of 164.52% is achieved when length $l_1 = 13.95$ mm. The impact of the length of $w_1$ from 11.2 to 12.4 mm, the vertical slot is shown in Figure 3.11 where $w_1$ varies from 11.2 to 12.4 mm. It is observed that with the increase in $w_1$, the upper side-band frequency decreases slightly but when $w_1$ decreases the upper and lower side-band frequency is greatly affected. For good wideband operation, the vertical slot length $w_1 = 12$ mm is more suitable due to its low cross-polarization level and stable radiation patterns.

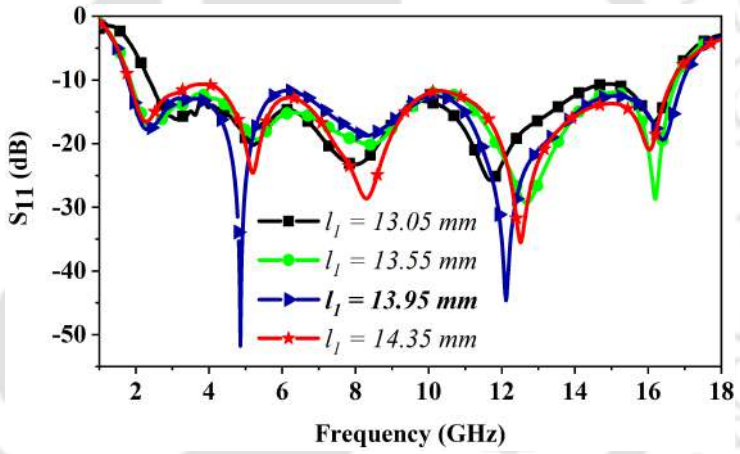


**Figure 3.10:** Simulated $S_{11}$ results with a variation of C-slot length $l_1$.

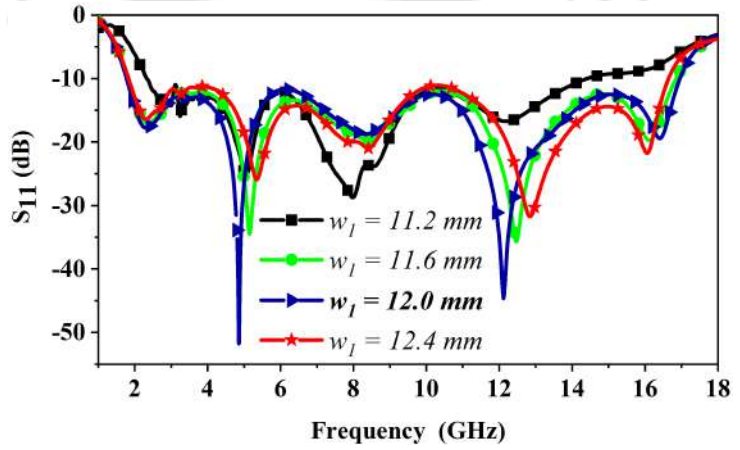


**Figure 3.11:** Simulated $S_{11}$ results with different values of C-slot width $w_1$.

Figure 3.12 shows the $S_{11}$ performance with a variation of thickness ($m_1$) from 1.2 to 2.4

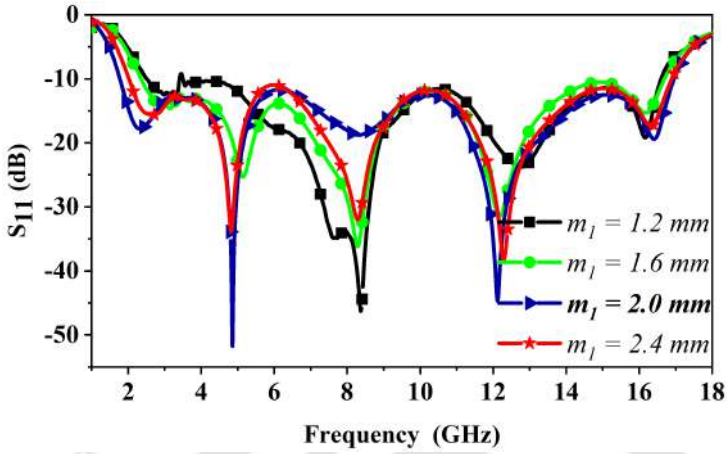


**Figure 3.12:** Simulated $S_{11}$ results with a variation of C-slot thickness $m_1$.

mm. It is observed that the first and second peak resonances shift to higher frequencies with a decrease of $m_1$. As $m_1$ increases, the equivalent capacitance $C_{eq}$ of the C-shape slot decreases which in turn decreases the propagation constant $\beta$ ( i.e., $\beta \propto \sqrt{C_{eq}}$). As a result, decreases the effective dielectric constant $\sqrt{\epsilon_{eff}} = \beta \ / \ C_{eq}$. The guided wavelength $\lambda_g = \lambda_0 \ / \ \sqrt{\epsilon_{eff}}$ satisfies the resonance condition when the length of the radiating slot is kept constant. It is observed from the figure at $m_1 = 2.0$ mm that the proposed antenna shows a wider bandwidth (i.e., 1.77–16.96 GHz).

### 3.3.3 Coupled Mode Theory (CMT)

In general, the coupled microwave resonators are different in geometry and have different self-resonant frequencies as shown in Figure 3.13.

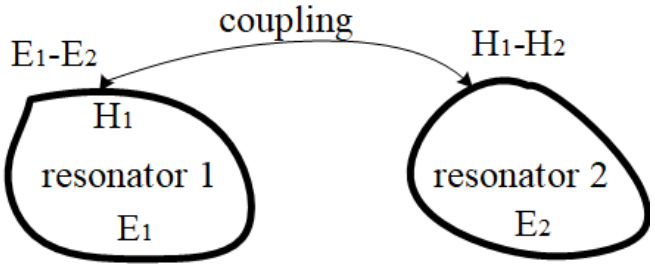


**Figure 3.13:** General coupled microwave resonators (resonators 1 and 2 can be different in structure and have different resonant frequencies).

As referred to in Figure 3.13 the coupling coefficient $k$ may be defined as a ratio of coupled energy to stored energy;

$$k = \frac{\iiint \varepsilon \mathbf{E}_1.\mathbf{E}_2 dv}{\sqrt{\iiint \varepsilon |\mathbf{E}_1|^2 dv \times \iiint \varepsilon |\mathbf{E}_2|^2 dv}} + \frac{\iiint \mu \mathbf{H}_1.\mathbf{H}_2 dv}{\sqrt{\iiint \mu |\mathbf{H}_1|^2 dv \times \iiint \mu |\mathbf{H}_2|^2 dv}} \tag{3.15}$$

where at resonance condition all fields are determined, and the volume integrals are over entire effective regions with permittivity of $\varepsilon$, permeability of $\mu$, electric field vector of $\mathbf{E}$, and magnetic field vector of $\mathbf{H}$. The first term top represents the electric coupling while the second term is a magnetic coupling. Mathematically described by the dot operation of their space vector fields of the coupled resonators, which allows the coupling to have either a positive or negative sign. Let's take the example of electric and magnetic couplings that exist in a circuit model as shown in Figure 3.14. $J = \omega C_m$ represented the electric coupling admittance inverter while the magnetic coupling is represented by an impedance inverter $M = \omega L_m$ and $I_1$, $I_2$, and $I_3$, respectively are denoted by the external currents flowing into the coupled resonator circuit.

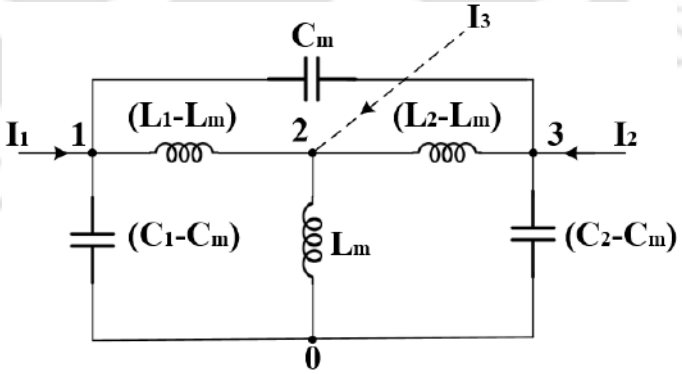


**Figure 3.14:** Asynchronously tuned coupled resonator circuit with both the electric and magnetic couplings.

According to the coupled resonator circuit model of Figure 3.14, by assuming all internal currents flow outward each node we can define a definite nodal admittance matrix with a reference at node '0'

$$\begin{bmatrix} I_1 \\ I_2 \\ I_3 \end{bmatrix} = \begin{bmatrix} y_{11} & y_{12} & y_{13} \\ y_{21} & y_{22} & y_{23} \\ y_{31} & y_{32} & y_{33} \end{bmatrix} \cdot \begin{bmatrix} V_1 \\ V_2 \\ V_3 \end{bmatrix} \tag{3.16}$$

with

$y_{11} = j\omega C_1 + \frac{1}{j\omega(L_1 - L_m)}$

$y_{12} = y_{21} = -\frac{1}{j\omega(L_1 - L_m)}$

$y_{13} = y_{31} = -j\omega C_m$

$y_{22} = \frac{1}{j\omega L_m} + \frac{1}{j\omega(L_1 - L_m)} + \frac{1}{j\omega(L_2 - L_m)}$

$y_{23} = y_{32} = -\frac{1}{j\omega(L_2 - L_m)}$

$y_{33} = j\omega C_2 + \frac{1}{j\omega(L_2 - L_m)}$

For actual resonance, it implies that

$$\begin{bmatrix} V_1 \\ V_2 \\ V_3 \end{bmatrix} \neq \begin{bmatrix} 0 \\ 0 \\ 0 \end{bmatrix} for \begin{bmatrix} I_1 \\ I_2 \\ I_3 \end{bmatrix} = \begin{bmatrix} 0 \\ 0 \\ 0 \end{bmatrix} \tag{3.17}$$

For this requires the admittance matrix could be zero;

$$\begin{bmatrix} y_{11} & y_{12} & y_{13} \\ y_{21} & y_{22} & y_{23} \\ y_{31} & y_{32} & y_{33} \end{bmatrix} = \begin{bmatrix} 0 & 0 & 0 \\ 0 & 0 & 0 \\ 0 & 0 & 0 \end{bmatrix} \tag{3.18}$$

After some manipulations, we can arrive at

$$\omega^4(L_1C_1L_2C_2 - L_m^2C_1C_2 - L_1L_2C_m^2 + L_m^2C_m^2) \\ -\omega^2(L_1C_1 + L_2C_2 - 2L_mC_m) + 1 = 0 \tag{3.19}$$

There are four solutions to (3.18). However, only the two positive ones are of interest ( considering either $L_m = 0$ or $C_m = 0$), and expressed as;

$$\omega_1 = \sqrt{\frac{R_B - R_C}{R_A}} \\ \omega_2 = \sqrt{\frac{R_B + R_C}{R_A}} \tag{3.20}$$

with

$$\mathrm{R}_A = 2(L_1C_1L_2C_2 - L_m^2C_1C_2 - L_1L_2C_m^2 + L_m^2C_m^2)$$

$$\mathrm{R}_B = (L_1C_1 + L_2C_2 - 2L_mC_m)$$

$$\mathrm{R}_C = \sqrt{R_B^2 - 2R_A}$$

Coupled mode theory (CMT) is a physical phenomenon of coupled transmission line theory [50, 51]. In this theory, a system of two coupled resonators can be analyzed as the superposition of two modes with lower and higher frequencies wherein the resonators move in-phase and anti-phase, respectively. In the present study, $\omega_+$ and $\omega_-$ given below are the coupled mode frequencies and uncoupled mode frequencies, respectively [52].

$$\omega_\pm = \omega_o \pm \sqrt{\left(\frac{\omega_2 - \omega_1}{2}\right)^2 + \mid K \mid^2} \tag{3.21}$$

Where $\omega_o = (\omega_2 + \omega_1)/\ 2$ and $K$ represents an un-normalized coupling coefficient. Given $\omega_1 = \omega_2$, a normalized coupling coefficient calculated [53 ] is given as follows:

$$k = \frac{\omega_+^2 - \omega_-^2}{\omega_+^2 + \omega_-^2} \tag{3.22}$$

Putting (3.21) with $\omega_1 = \omega_2$ into (3.22), gives $k = (2\omega_o K)/(\omega_o^2 + K^2)$. Given $K^2 \ll \omega_o^2$, we

have

$$K \sim \omega_o k/2 \tag{3.23}$$

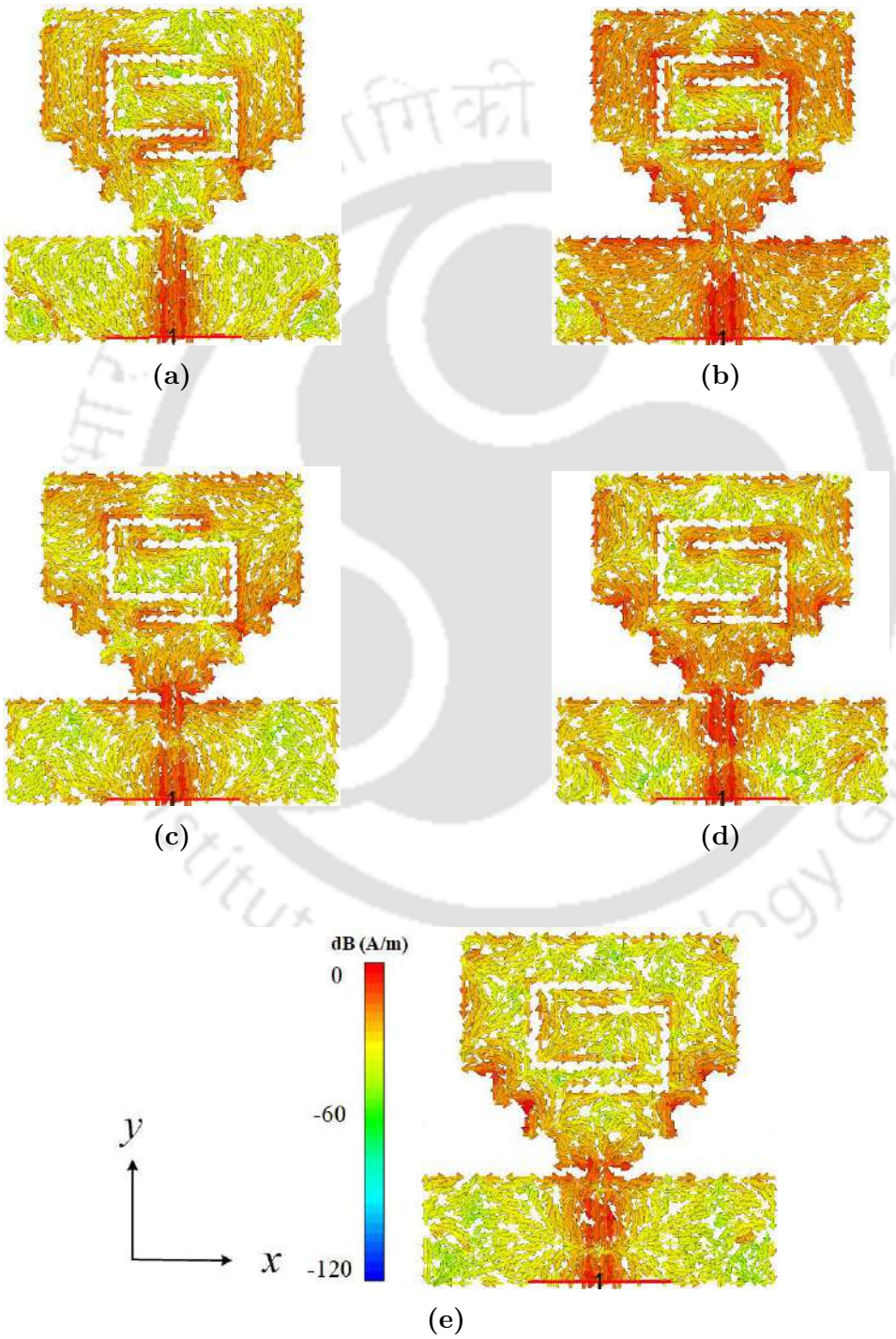


**Figure 3.15:** Simulated current distribution of the proposed antenna five peak resonant frequencies at (a) 2.31 GHz, (b) 4.85 GHz, (c) 8.33 GHz, (d) 12.11 GHz and (e) 16.41 GHz.

In the proposed antenna the simulated surface current distributions on the surface of the radiating patch at five peak resonant frequencies 2.31, 4.85, 8.33, 12.11, and 16.41 GHz are shown in Figure 3.15. It is also observed from the figure that the lower and higher modes exist near their resonance frequencies. The more charge accumulation on the surface of the patch and the C-shaped slot is noticed as a result, the parameters $l_1$, $w_1$ and $m_1$ controlling the first, second and third peak resonant frequency as shown in Figure 3.15(a), 3.15(b) and 3.15(c). The current distribution on the three pairs of the notches is high compared to other parts of the patch element as shown in Figure 3.15(d) and 3.15(e). As a result, the geometrical parameters $w_2 \times l_2$, $w_3 \times l_3$, $w_4 \times l_4$, $l_1$, $m_1$, and parameters of the QCRS for all the regions of the antenna plays an important role in controlling the fourth and fifth peak resonant frequencies. Since the distributions of charges in the rectangular patch and C-shaped slot are in phase at the lower mode and anti-phase at the higher mode, the CMT is relevant to the C-shaped slots.

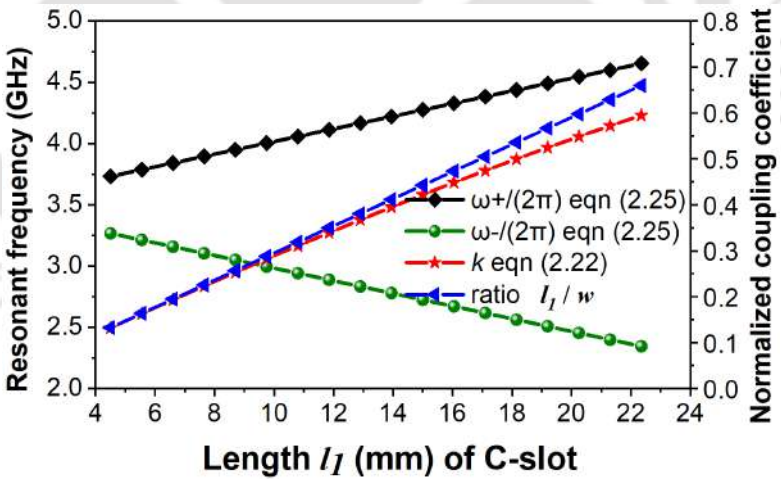


**Figure 3.16:** Variation of resonant frequency and coupling coefficient with respect to $l_1$ of the C-slot keeping all other dimensions constant.

According to (3.21), larger the difference between resonant frequencies greater the coupling coefficient. The ratio of the slot length $l_1$ to the rectangular patch width $w$ (i.e., $l_1/w$), controls the coupling coefficient due to the fraction of the $TM_{01}$ mode current intercepted by the slot. It is observed from the ratio analysis, greater the value of $l_1$ more difference in the resonant frequencies. This performance is presented in Figure 3.16 for the proposed antenna varying only

$l_1$ while all other parameters remain constant. From Figure 3.16, the first-order approximation of $k$ ( Eq. (3.16)) using the CMT resonant frequencies) is;

$$k \sim l_1/w \tag{3.24}$$

Combining Eq. (3.21) and Eq. (3.23) with $\omega_1 = \omega_2$, we have

$$\omega_{\pm} = \omega_o \left(1 \pm l_1/(2w)\right) \tag{3.25}$$

Equation (3.25) represents the relationship between the coupled mode frequencies and uncoupled mode frequencies derived from the CMT. Depending on the frequency, the surface current distribution of the C-shaped slot and rectangular patch edges have in-phase and anti-phase relationships. From Figure 3.15, it is observed that at the point of contact i.e., at the feed line and patch, the direction of the surface current is reversed. Since the surface current flows in the reverse direction, the cancellation of radiation fields produces high attenuation near peak resonant frequencies.

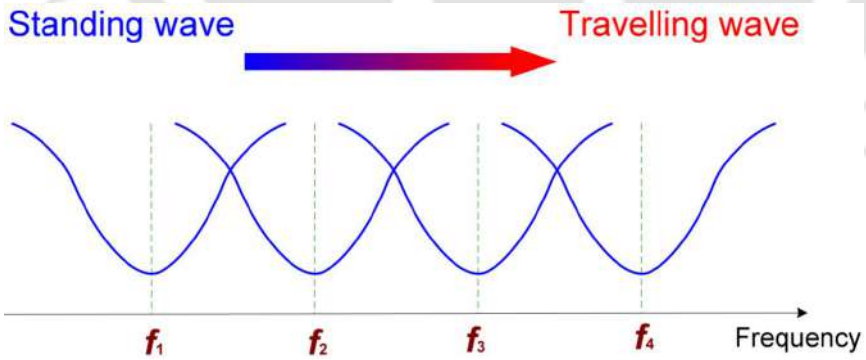


**Figure 3.17:** Operational principle of CPW fed staircase-shaped UWB antenna.

### 3.3.4 Operating Principle of CPW-fed Symmetrical Staircase-Shaped UWB Antenna

Figure 3.17 depicts the operating principle of the symmetrical staircase-shaped slot UWB antenna. It has been demonstrated that the proposed antenna's ultra-wideband ($-10$ dB) frequency operation results from the overlapping of closely distributed resonance modes. When

the wavelength is greater than the antenna dimension at the low-frequency end (the first resonance), the EM wave can readily "couple" into the antenna structure, causing it to operate in an oscillating mode or a standing wave. The antenna begins to function in a hybrid mode of standing and traveling waves as the frequency increase. Since the EM wave needs to travel down to the antenna structure, which is large in terms of wavelength, towards the high-frequency end, the traveling wave becomes more crucial to the antenna operation. The main rectangular patch and the ground plane, when combined to form slots, can effectively sustain the traveling wave for the CPW-fed antenna. Therefore, an ideal symmetrical staircase-shaped slot antenna fed by CPW can exhibit an extremely wide -10 dB impedance bandwidth.

### 3.3.5 Bandwidth Dimension Ratio (BDR)

The antenna bandwidth dimension ratio (BDR) [40], which is defined as the amount of percentage bandwidth (% BW) with respect to the electrical length and width of the proposed antenna at lower sideband frequency is expressed below:

$$BDR = \frac{\%BW}{\lambda_{LfL}\lambda_{WfL}} \tag{3.26}$$

where $\lambda_{LfL}$ and $\lambda_{WfL}$ are the electrical length and width of the proposed antenna at a lower band frequency that meets $-10$ dB impedance bandwidth. Larger the value of BDR, the smaller the dimension and wider the impedance bandwidth. A very excellent BDR value i.e., 3290.71 is observed and a detailed comparison is given in Table 3.8.

## 3.4 TLM-RLC Circuit Model of the Proposed Antenna

The development of an electrical equivalent circuit diagram of the proposed antenna assuring the TLM-RLC model is shown in Figure 3.18. In this figure, the inductance $L_R$ is introduced by the microstrip feed line as shown in Figure 3.18(a). To draw the TLM-RLC circuit of the simple CPW-fed patch, the patch is considered as a parallel plate transmission line connecting radiating slots as shown in Figure 3.18(b). The shunt capacitances $C_{R1}$ and $C_{R2}$ are the gaps between the feed line and CPW-fed ground plane of both sides. The C-shaped slot considering

a combination of three rectangular slots (one vertical slot and two horizontal slots), which is represented in Figure 3.18(c). The proposed antenna contains a symmetrical staircase-shaped and two pairs of QCRS as shown in Figure 3.18(d). Furthermore, $C_{11}$, $C_{eqt}$, and $C_{21}$ are coupling capacitors. While $L_{11}$, $L_{12}$, $L_{eqt}$, $L_{21}$, and $L_{22}$ are the inductances on both sides of the symmetric ground plane of the proposed antenna.

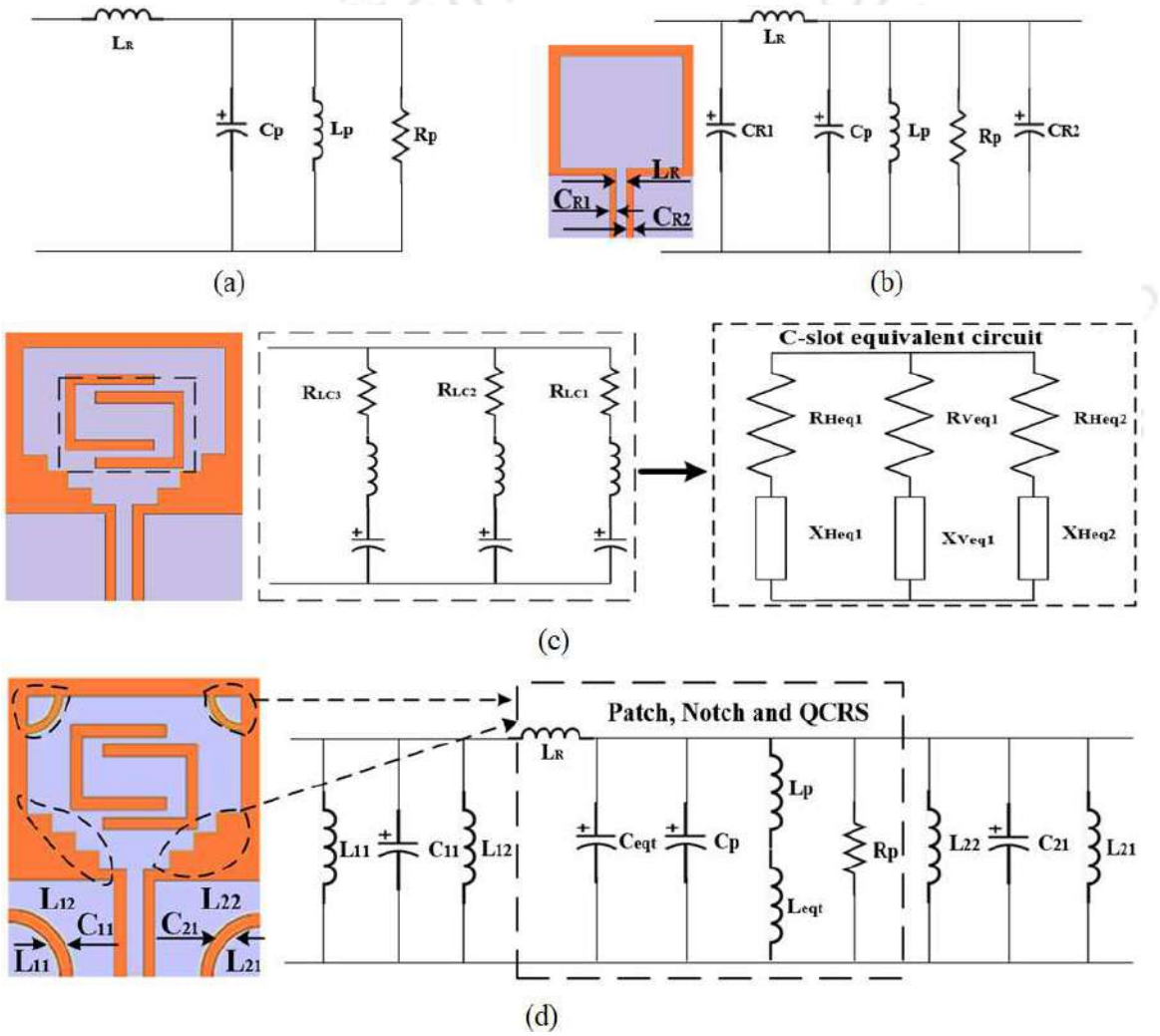


**Figure 3.18:** Equivalent transmission line model (TLM)-RLC circuit elements of proposed antenna (a) Basic patch antenna, (b) basic patch with CPW-fed, (c) C-shaped slot and (d) patch, notch and QCRS.

The simplified TLM-RLC circuit model is shown in Figure 3.19(a). An optimization process is performed by using the NI AWR simulator and all parameter values are labeled in Figure 3.19(b) (R in (Ω), C in (pF), and L in (nH)). Therefore, the impedance (Z) of the final simplified

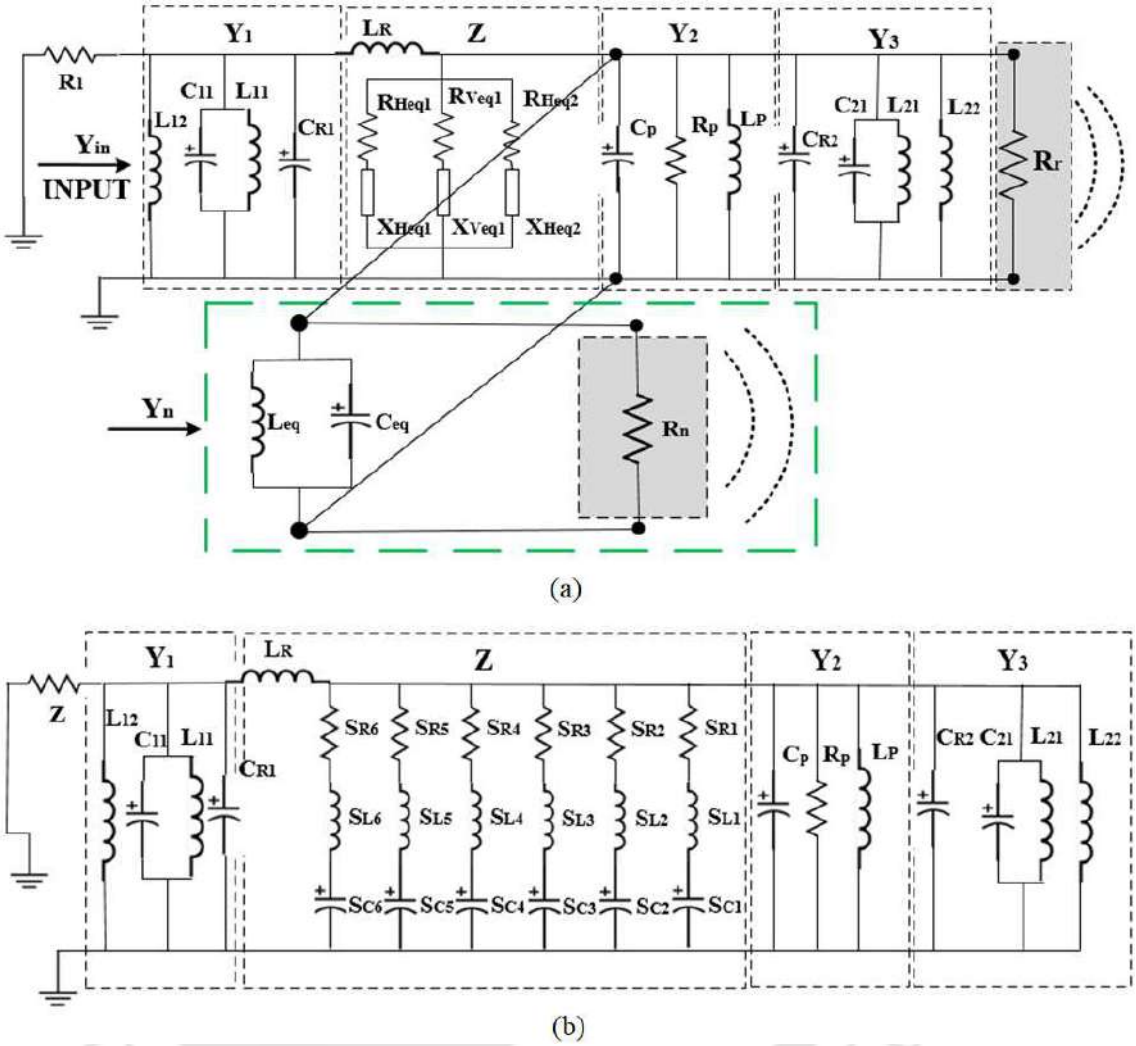


**Figure 3.19:** Equivalent transmission line model (TLM)-RLC circuit model of the proposed antenna (a) Equivalent circuit model (b) simplified circuit model with RLC values [$L_R = 0.362$, $L_{11} = 5050$, $L_{12} = 233\times\ 10^{-3}$, $L_p = 253$, $L_{21} = 14.56$, $L_{22} = 15.08$, $S_{L1} = 1.03$, $S_{L2} = 1.47$, $S_{L3} = 1.54$, $S_{L4} = 1.06$, $S_{L5} = 1.36$, $S_{L6} = 1.35$ ] all dimensions are in nH, [$C_{11} = 2.09\times\ 10^{-12}$, $C_p = 1.2\times\ 10^{-11}$, $C_{21} = 0.0124$, $C_{R1} = 0.0957$, $C_{R2} = 0.0042$, $S_{C1} = 8.5\times\ 10^{-5}$, $S_{C2} = 0.01931$, $S_{C3} = 1.24\times\ 10^{-5}$, $S_{C4} = 0.0011$, $S_{C5} = 0.0005$, $S_{C6} = 0.051$ ] all dimensions are in pF and [$Z = 50$, $R_p = 365$, $S_{R1} = 1.75$, $S_{R2} = 1.6$, $S_{R3} = 1.94$, $S_{R4} = 2.12$, $S_{R5} = 1.55$, $S_{R6} = 2.31$ ] all dimensions are in Ω.

TLM-RLC equivalent circuit is given by:

$$Z = \frac{1}{G_{TC} + jB_{TC}} + j\omega L_R \tag{3.27}$$

The admittance $Y_{Heq1}$ of the horizontal slot equivalent circuit is given by:

$$Y_{Heq1} = \frac{1}{R_{Heq1} + jX_{Heq1}} = G_{1C} + jB_{1C} \tag{3.28}$$

The admittance $Y_{Veq1}$ of the vertical slot equivalent circuit is given by:

$$Y_{Veq1} = \frac{1}{R_{Veq} + jX_{Veq}} = G_{2C} + jB_{2C} \tag{3.29}$$

Similarly, the admittance of the horizontal slot equivalent $Y_{Heq2}$ the circuit is given by:

$$Y_{Heq2} = \frac{1}{R_{Heq2} + jX_{Heq2}} = G_{3C} + jB_{3C} \tag{3.30}$$

Hence, the total conductance $G_{TC}$ and susceptance $B_{TC}$ are given as follows:

$$\begin{aligned} G_{TC} &= G_{1C} + G_{2C} + G_{3C} \\ B_{TC} &= B_{1C} + B_{2C} + B_{3C} \end{aligned} \tag{3.31}$$

Total admittance $Y_C$ of C-slot and feed-line $L_R$ of the proposed antenna is given by:

$$Y_C = 1/Z \tag{3.32}$$

For the final proposed antenna, total admittance Y of an electrical equivalent circuit is given by

$$Y = Y_1 + Y_2 + Y_3 + Y_C \tag{3.33}$$

where $Y_1$, $Y_2$, and $Y_3$ are

$$Y_1 = j\left(\omega C_{R1} + \omega C_{11} - \frac{L_{11} + L_{12}}{\omega L_{11} L_{12}}\right) \tag{3.34}$$

$$Y_2 = R_p + j\omega C - \frac{j}{\omega L} \tag{3.35}$$

$$Y_3 = j\left(\omega C_{R2} + \omega C_{21} - \frac{L_{21} + L_{22}}{\omega L_{21} L_{22}}\right) \tag{3.36}$$

where $C = C_p \parallel C_{eqt}$ and $L = L_p \parallel L_{eqt}$

Figure 3.19(a) shows an LC circuit model of Antenna 5 (proposed) and explains, how the center frequencies and the bandwidths can be controlled by an LC circuit of the notched structure. The radiation resistance of the antenna element and the notch are $R_r$, $R_n$, respectively.

$L_{eq}$ and $C_{eq}$ represent an inductor and capacitor of the notch resonator circuit. The notch admittance $Y_n$ of the parallel RLC resonator circuit is given by [54]:

$$Y_n = \frac{1}{R_n} + j\omega C_{eq} + \frac{1}{j\omega L_{eq}} \tag{3.37}$$

$$Y_{in} = Y + \frac{1}{R_r} + \frac{J_1^2}{Y_n} \tag{3.38}$$

where $J_1$ is the Bessel function of the parallel RLC resonator circuit and near the resonant frequency is given by:

$$\omega_o = \frac{1}{\sqrt{L_{eq}C_{eq}}} \tag{3.39}$$

Putting Eq. (3.39) in Eq. (3.37) with $\omega = \omega_o + \Delta\omega$, Eq. (3.37) is reduced to

$$Y_n = \frac{1}{R_n} + \frac{j}{\omega L_{eq}}(\omega^2 L_{eq}C_{eq} - 1) \approx \frac{1}{R_n} + j2C_{eq}\Delta\omega \tag{3.40}$$

The bandwidth of the RLC parallel resonant circuit approximately equals twice the -3 dB bandwidth of the parallel $R_n$ and $2C_{eq}$ as shown in Eq. (3.41) and Eq. (3.42). Here, the fractional bandwidth (FBW) represents [48]:

$$BW = \frac{2}{R_n \times 2C_{eq}} = \frac{1}{R_n C_{eq}} \tag{3.41}$$

$$FBW = \frac{BW}{\omega_o} = \frac{1}{\omega_o R_n C_{eq}} \tag{3.42}$$

Finally, the proposed UWB antenna model gives approximately the same behavior and a very wider impedance bandwidth is constituted by several adjacent resonances which can be represented by TLM-RLC circuits simulated result as shown in Figure 2.20.

## 3.5 Simulation and Measurement Performance

The proposed symmetrical staircase-shaped UWB antenna fabricated and measured for the validation is shown in Figure 3.21(a) and 3.21(b). The proposed antenna is fabricated on a 0.8 mm thickness Rogers RT/5880 substrate with co-planar waveguide (CPW)-fed line and a

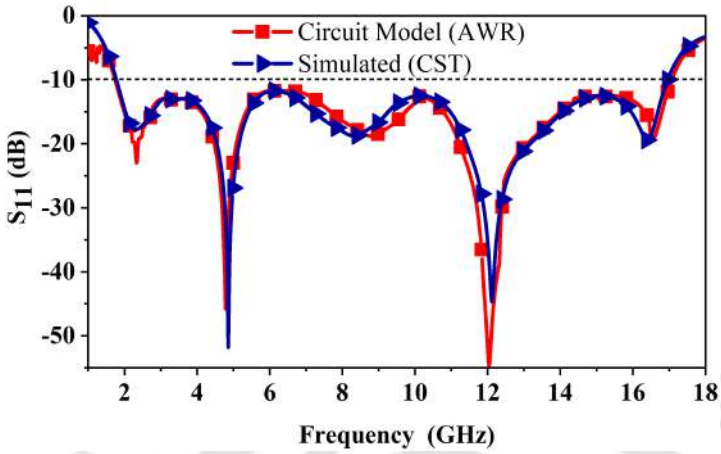


**Figure 3.20:** Simulated and equivalent transmission line circuit model response of the proposed antenna.

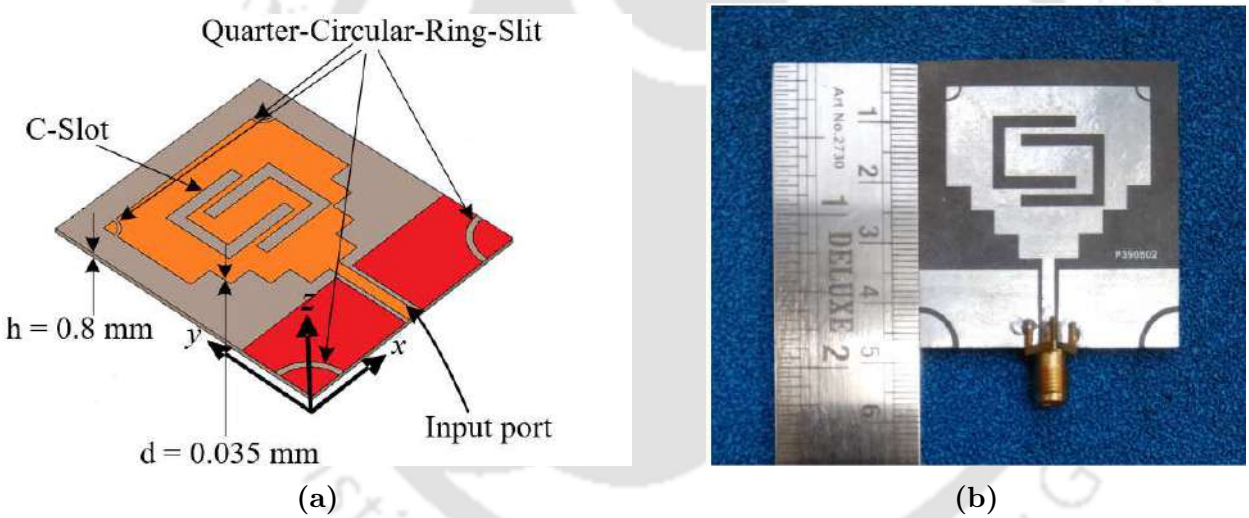


**Figure 3.21:** (a) Structure of staircase-shaped UWB proposed antenna and (b) top view photograph of the prototype.

50 Ω SMA connector are connected with the vertical edge. The total volume of the antenna is $46.32 \times 43.48 \times 0.8$ mm$^3$. The $S_{11}$ results are measured with a vector network analyzer (Rohde and Schwarz ZVA24). The peak gain, efficiency, and radiation patterns are measured with an antenna measurement environment for 1–18 GHz band in an anechoic chamber (size: $6 \times 4 \times 6$ m$^3$) as shown in Figure 3.22(a) and 3.22(b).

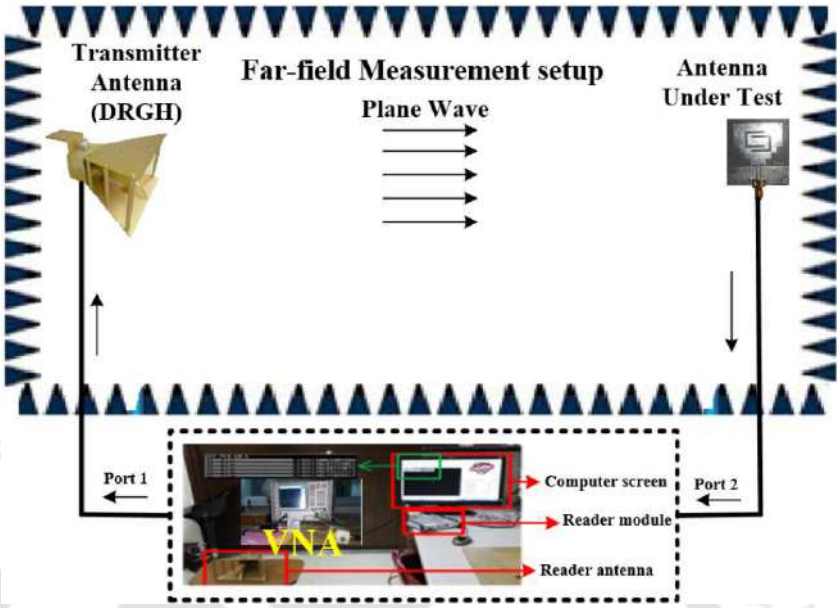


(a)

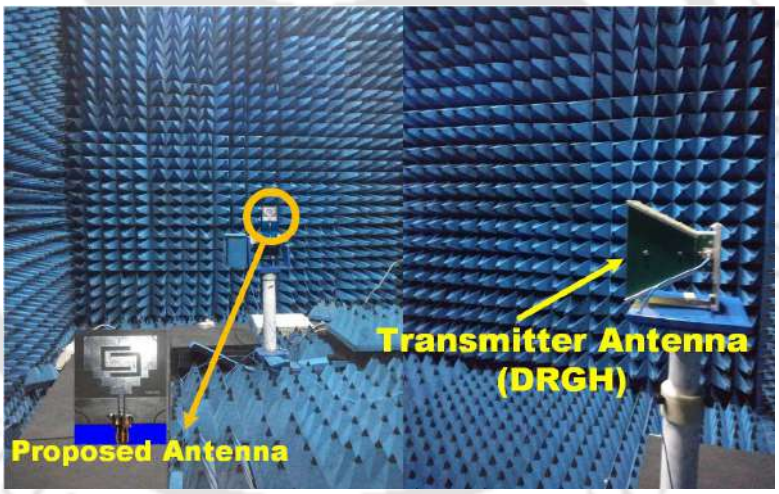


(b)

**Figure 3.22:** Antenna measurement setup (a) block diagram and (b) actual measurement environment.

### 3.5.1 Reflection Coefficient Performance

The measured and simulated $S_{11}$ parameters of the proposed antenna is shown in Figure 3.23. The inset figure shows a photograph of the fabricated antenna. The measured results show a very wider impedance bandwidth from 1.55–16.95 GHz (percentage of the bandwidth 166.51 %) with a bandwidth ratio of 10.94:1. The simulated results obtained using the CST

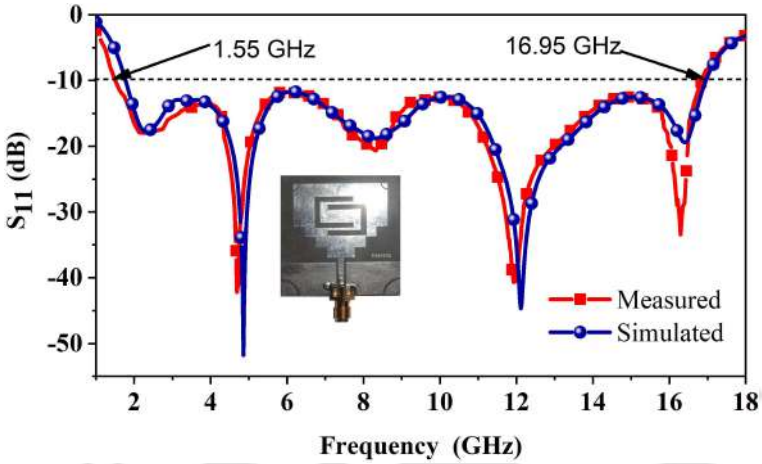


**Figure 3.23:** Measured and simulated $S_{11}$ performance of the proposed UWB antenna.

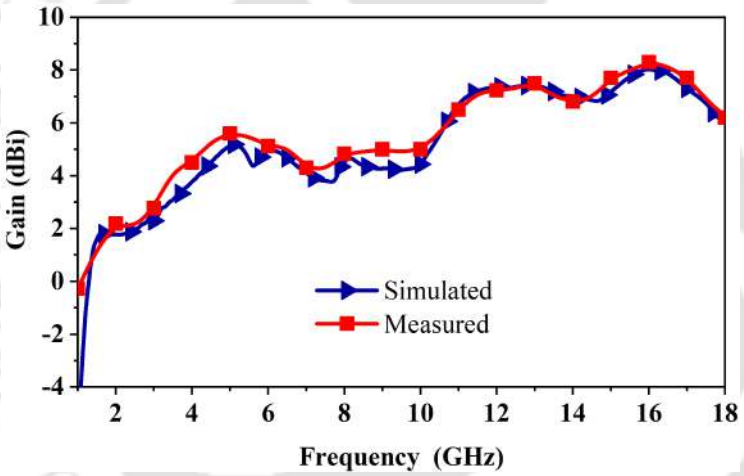


**Figure 3.24:** Measured and simulated peak gain of the proposed UWB antenna.

simulator closely match with the measured results for the entire operating band. The small difference in the lower sideband, as well as the higher sideband, is mainly due to the fabrication tolerance.

### 3.5.2 Gain and Efficiency Performance

The gain of the presented antenna simulated using the CST simulator and compared with the measured results as shown in Figure 3.24. It is seen that the measured gain closely matches with the simulated results over the operating band. The peak gain varies from 2 to 8.3 dBi with the increases of frequency up to 17 GHz. For efficiency measurement, at first measure the peak

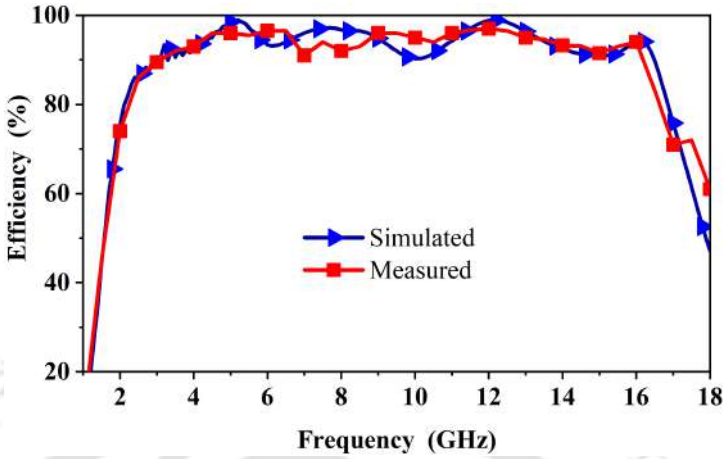


**Figure 3.25:** Measured and simulated efficiency of the proposed UWB antenna.

gain, radiation intensity, and reflection coefficient. The directivity computes automatically using the radiation intensity and all calculation is done using the software. The antenna efficiency is computed using the equation given below:

$$Efficiency = \frac{G(\theta,\phi)}{D(\theta,\phi)}(1- \mid \Gamma \mid^2) \tag{3.43}$$

The radiation efficiency performance is shown in Figure 3.25. The measured efficiencies from 1 to 17 GHz are about 82–96% and have a little deviation from the simulated result due to the fabrication tolerance.

### 3.5.3 Radiation Patterns Performance

The simulated and measured radiation patterns of the proposed antenna in the E- and H-plane at 1.55, 2.31, 4.85, 8.33, 12.11, and 16.95 GHz are shown in Figure 3.26 and 3.27 respectively. The measured results nearly match with the simulated results in both cases E-plane (yz plane) and H-plane (xz plane). Figure 2.26 and 2.27 show that the antenna radiates equally in both x-direction ( i.e., positive x-axis and negative x-axis) and does not change the radiation patterns shape with increase in frequency. The simulated and measured radiation patterns show that the cross-polarization is about 20 dBi lower than the co-polarization value at the boresight of the designed antenna in all cases whereas the E-plane at 16.95 GHz, the

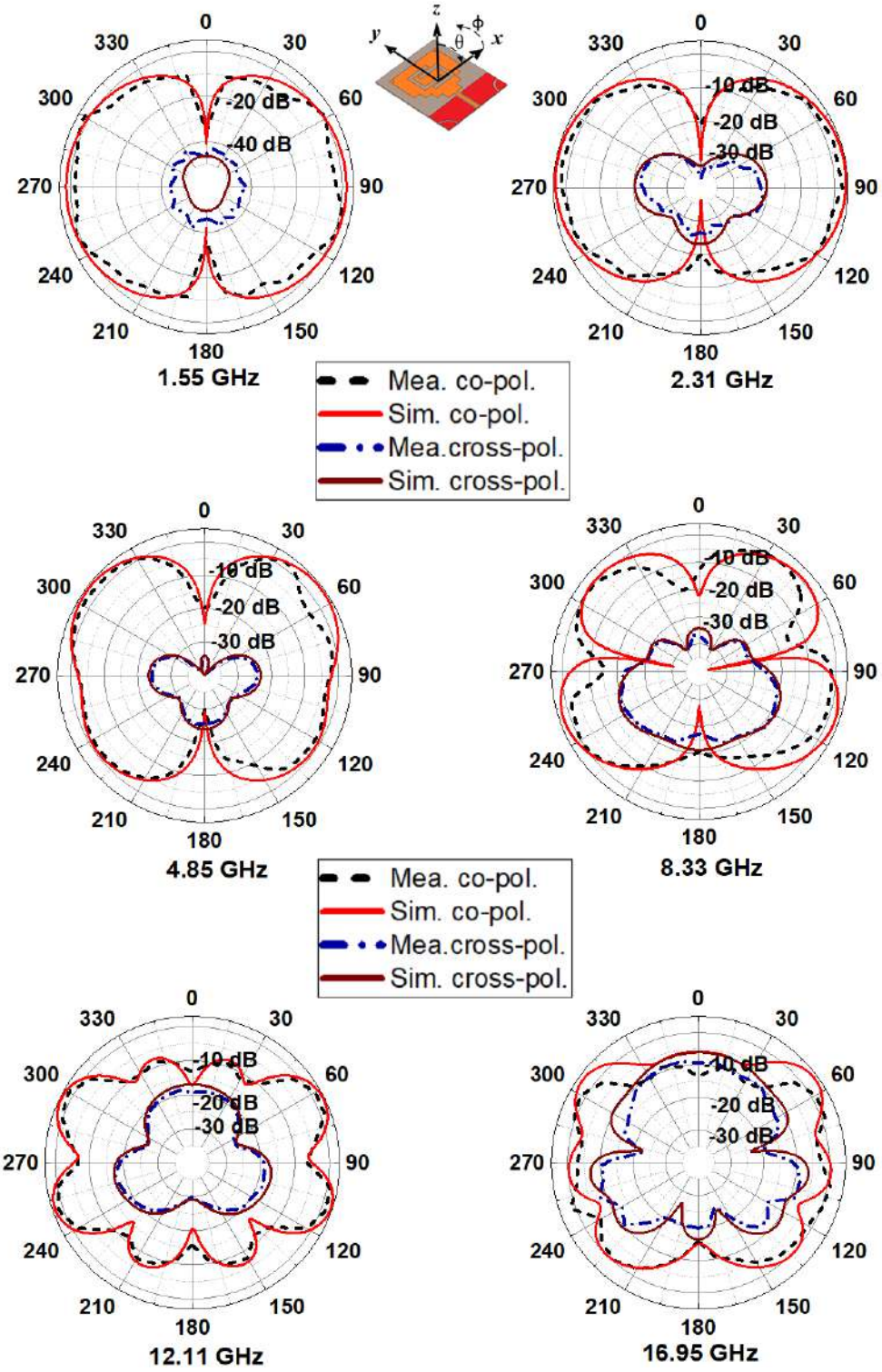


**Figure 3.26:** Measured (dashed curve) and simulated (solid curve) E-plane (yz plane) radiation patterns of the proposed antenna at 1.55, 2.31, 4.85, 8.33, 12.11, and 16.95 GHz.

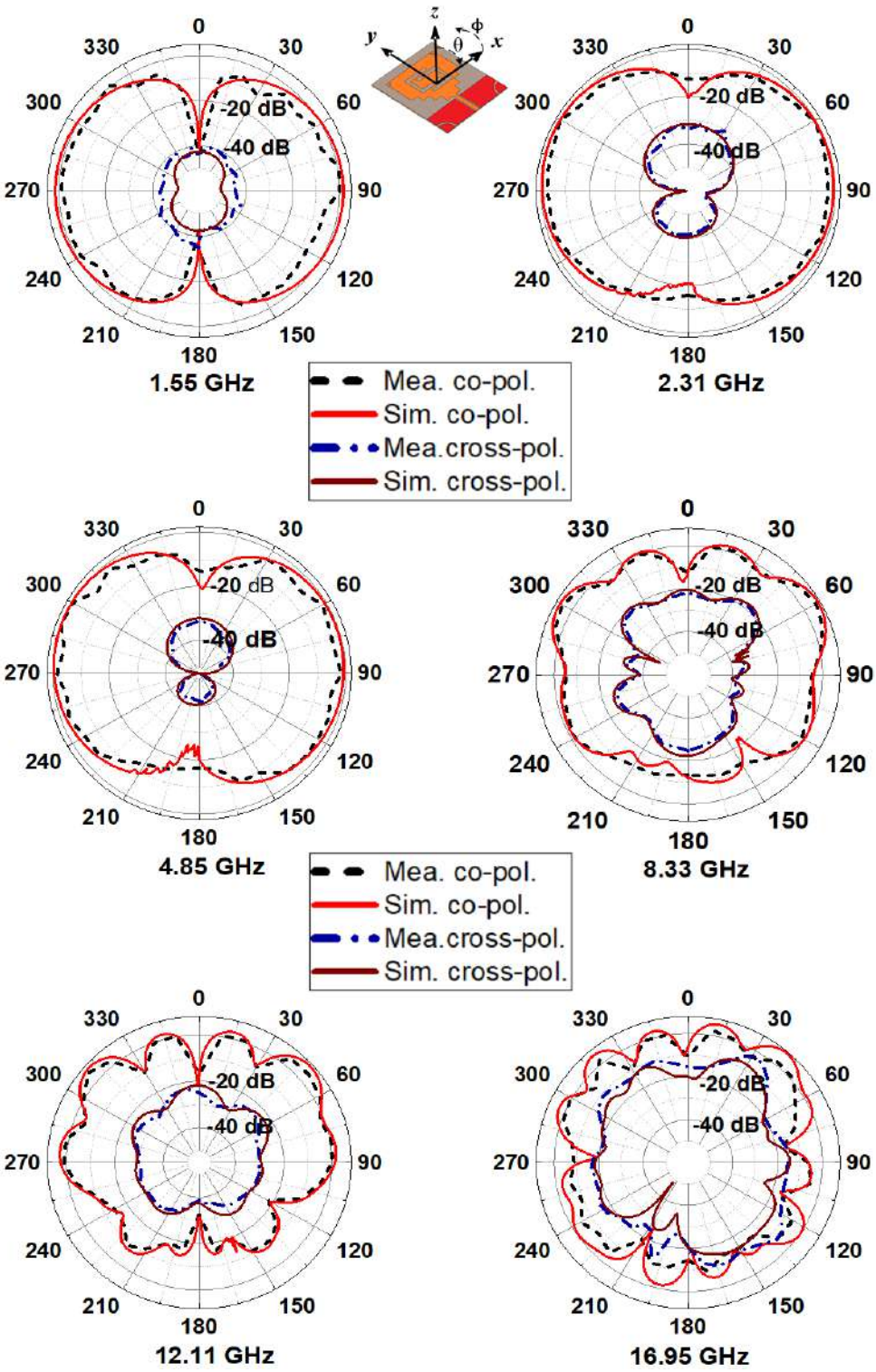


**Figure 3.27:** Measured (dashed curve) and simulated (solid curve) H-plane (xz plane) radiation patterns of the proposed antenna at 1.55, 2.31, 4.85, 8.33, 12.11, and 16.95 GHz.

cross-polarization and co-polarization value less difference. The measured results indicate that the proposed antenna has stable and nearly omnidirectional radiation patterns in the UWB band.

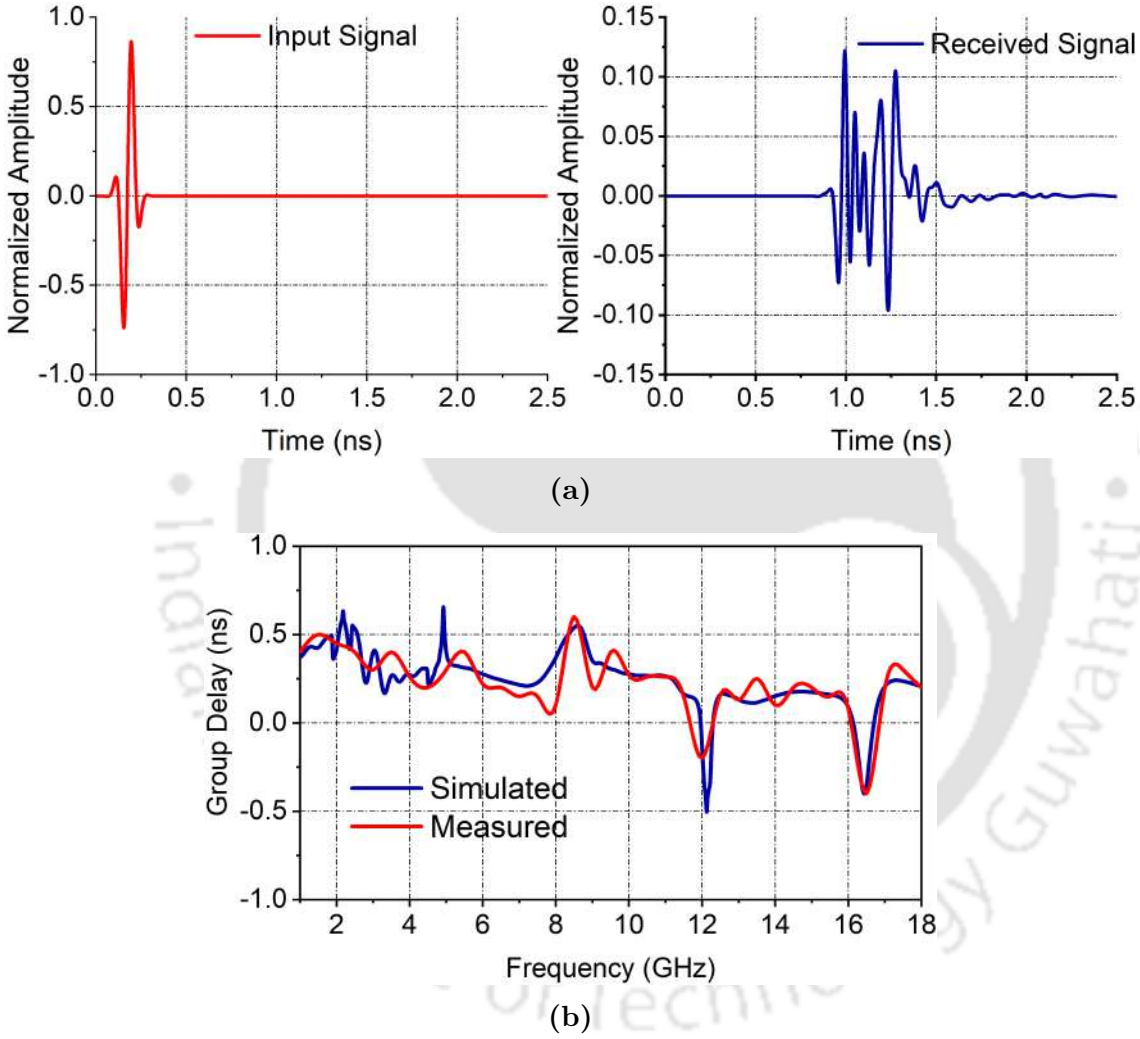


**Figure 3.28:** Time domain analysis of the proposed antenna (a) normalized amplitude of the input and received signals and (b) group delay.

### 3.5.4 Time Domain Analysis

The time-domain analysis and frequency-domain analysis are of equal importance to study the time-domain characteristics of the designed antenna while the antenna transmits or receives the signal. The time domain analysis of the designed antenna is carried out by keeping two

**Table 3.8:** Comparison of proposed antenna with other recently reported antennas

| Ref. | Type | Dimension ($mm^3$) | Freq. ($GHz$) | FBW (%) | PG ($dBi$) | GV ($dBi$) | BDR |
|---|---|---|---|---|---|---|---|
| [34] | Slot antenna | $0.24 \times 0.32 \times 0.016\ \lambda_l^3$ | 3.1–10.9 | 111.42 | -1–4 | 5 | 1450.78 |
| [36] | Monopole | $0.35 \times 0.35 \times 0.006\ \lambda_l^3$ | 3.1–11 | 112.05 | 2.1 – 5.6 | 3.5 | 914.70 |
| [40] | Monopole | $0.37 \times 0.17 \times 0.007\ \lambda_l^3$ | 1.44–18.8 | 172 | 1–7 | 6 | 2734.50 |
| [42] | Slot antenna | $0.80 \times 0.80 \times 0.009\ \lambda_l^3$ | 2.83–18.2 | 146 | 2-6.5 | 4.5 | 228.12 |
| [43] | Slot antenna | $0.88 \times 0.88 \times 0.006\ \lambda_l^3$ | 3.7–19.3 | 135 | -1-4.5 | 5.5 | 174.32 |
| [46] | Monopole | $0.25 \times 0.28 \times 0.001\ \lambda_l^3$ | 3–11 | 114 | -0.2 – 3.5 | 3.7 | 1727.78 |
| [47] | Slot antenna | $0.24 \times 0.29 \times 0.007\ \lambda_l^3$ | 2.9–11.8 | 121 | 2 – 6 | 4 | 1738.50 |
| [49] | Monopole | $0.39 \times 0.24 \times 0.005\ \lambda_l^3$ | 0.28–2.27 | 156.1 | 0.12 – 5.57 | 5.45 | 1667.73 |
| Work | Slot antenna | $0.23 \times 0.22 \times 0.004\ \lambda_l^3$ | 1.55–16.95 | 166.51 | 2 – 8.3 | 6.3 | 3290.71 |

FBW: Fractional bandwidth. PG: Peak gain. GV: Gain variation. BDR: Bandwidth dimension ratio.

similar antenna face-to-face at a distance of 30 cm from each other. A Gaussian pulse, having a center frequency of 9.5 GHz is transmitted and received by the transceiver antenna structures. Figure 3.28(a) demonstrates the incident and received pulses and Figure 3.28(b) variation of the group delay over the frequency.

The pulse fidelity factor is calculated when the transmitting and receiving antenna is kept face-to-face at some distance [55, 56]. To evaluate the degree of waveform distortion, the

correlation factor is calculated between input signal $S_1(t)$ and the output signal $S_2(t)$, the correlation factor ($\rho$) is expressed below:

$$\rho = max \left\{ \frac{\int S_1(t) S_2(t-\tau)\, dt}{\sqrt{S_1^2(t)}\sqrt{S_2^2(t)}\, dt} \right\} \tag{3.44}$$

where $\tau$ is the delay. It is observed that the pulse-preserving capability is the best when the orientation of the transmit-receive antenna and the system is facing face-to-face with each other and the correlation factor is found to be 0.8815. Group delay is related to the performance of the antenna gain and mathematically calculated by using the group delay equation [57]. It is observed that the group delay is almost constant and that variation less than 1ns across the entire operating band.

Table 3.8 gives the comparison of performances between the proposed symmetrical staircase-shaped UWB antenna and other UWB antennas proposed in the literature. The antenna type, dimension, frequency range, fractional bandwidth (% BW), peak gain, and bandwidth dimension ratio (BDR) are listed. The measured peak gain of the UWB antenna is greater than 2 dBi and reaches up to 8.3 dBi within the $-10$ dB impedance band. Table 3.8 demonstrates the effectiveness of the proposed structure in obtaining enhanced impedance bandwidth, better gain, and good radiation performance with a compact size. The proposed antenna has a smaller size than most of the literature but still maintaining a wider impedance bandwidth. Besides, the bandwidth dimension ratio (BDR) in all the listed types are low value, whereas the proposed antenna has a very high value i.e., 3290.71 which indicates a small size. Therefore, considering all the performance of the proposed antenna, it will be a good candidate for UWB applications.

## 3.6 Summary of the Chapter

A simple symmetrical staircase-shaped UWB antenna with wider impedance bandwidth over a 1.55 to 16.95 GHz (fractional BW = 166.51%) band is presented. From the comparison of the BDR, it is observed that the BDR of the proposed antenna is higher than the other antennas proposed in the literature. The comparison in terms of BDR verifies the advantages of compact size and wider bandwidth provided by the proposed antenna structure over other antenna structures. Owing to the advantages of compact size and wider bandwidth over other antenna structures, this antenna will be useful for UWB applications, mobile applications, wireless applications, satellite applications, radio determination applications (4.5–7 GHz and 13.4–14 GHz), etc. Finally, an electrical equivalent TLM-RLC circuit of the designed UWB antenna is presented based on the effect of each slot and antenna element. The simulated results of the TLM-RLC circuit model is nearly the same as the designed antenna results obtained from the CST simulator software. To further reduce the size and improve the impedance bandwidth of the designed star-shaped monopole antenna with better gain, a study is carried out which is discussed in the next chapter.

*Note: This work, Design of compact CPW-fed symmetrical staircase-shaped UWB antenna using transmission line model has been published in Progress In Electromagnetics Research C.*

# 4

# Design of CPW-fed Star-Shaped Monopole Antenna for UWB Applications using Transmission Line Model

## Contents

## 4.1 Introduction

In wireless communication systems, the application of ultra-wideband antenna is growing rapidly due to broad bandwidth, high speed data rate, flexible, robustness to fading, low cost, and capability of high security. These antennas covering the wider frequency range of 3.1–10.6 GHz are key components of such ultra-wideband (UWB) systems; hence, their design problems have become an active topic of research in recent years. Monopole antennas have drawn more attention in recent years for a suitable wider bandwidth and nearly omnidirectional radiation patterns. To enhance the impedance bandwidth, many techniques such as increasing substrate thickness, and modifying the radiator and ground plane [58]–[60] are adopted. Since limited space is available in electronic devices, a design of compact wider band antennas having good matching input impedance characteristics and better radiation patterns similar to larger size antennas are required. The wideband impedance bandwidth is achieved by using space-filling concepts, different fractal antennas, CPW-fed antennas with dual-reverse-arrow fractal structure, flexible bow-tie slot antenna, a rose-curve shape monopole antenna, wideband fractal shapes structure, and tapered slot antenna [34–38, 61, 62]. To achieve wider bandwidth and better impedance matching, a semi-circular patch [63], quasi-radiating patch [64], modified meandered slot [41], microstrip-fed parasitic-coupled monopole hybrid design, [46] and optimized surrogate-based patch [65] are proposed. However, the monopole antennas mentioned above have a large physical size and complex geometry to realize the required operating frequency bands. Therefore, a compact and simple monopole antenna with a wider bandwidth covering the UWB frequency band is necessary.

In this chapter, a compact simple star-shaped monopole antenna (SSMA) structure with wider impedance bandwidth and an acceptable level of in-band return loss is proposed. Since the design and the fabricated antenna has a pair of symmetrical quarter-circular-slit (QCS) and partly-hexagonal-ring-slit (PHRS) defected ground plane, three peaks resonant i.e., 2.8 GHz, 6.1 GHz, and 9.4 GHz are observed. As a result, wider impedance bandwidth, better impedance matching, and antenna close to omnidirectional radiation patterns are achieved.

An excellent wider impedance bandwidth i.e., 135% (2.36–12.1 GHz) and good return loss is achieved. Then, an equivalent transmission line model (TLM) of the proposed antenna is developed. An optimization is used in Applied Wave Research (AWR) simulator to find the transmission line parameters such as resistance (R), inductance (L), and capacitance (C) of the TLM-RLC equivalent circuit using the $S_{11}$ simulated parameters [28, 29, 49] of the proposed antenna.

This chapter is divided into the following sections: section 4.2 explains the design steps and enhancement in impedance bandwidth, impedance matching, parametric studies and the mathematical modeling of the transmission line model (TLM)-RLC circuit model of the proposed antenna. The reflection coefficient $S_{11}$, peak gain, and radiation pattern parameters at different frequencies like 2.8, 6.1, and 9.4 GHz are compared. The simulation and experimental results of the $S_{11}$, peak gain, and radiation patterns in both planes are presented in section 4.3. The experimental results match quite well with the simulation results, thus validating the practical feasibility of the design. The principal outcomes of this research work are explained in section 4.4.

## 4.2 Design Process and Working Principle

### 4.2.1 Antenna Configuration

The 12-point star has been designed using four circles having three corners to make equilateral triangles with each radius of 11.0 mm, and thus 9-point star will be obtained as shown in Figure 4.1. The geometry of a compact CPW-fed star-shaped monopole antenna (SSMA) is shown in Figure 4.2. A wider impedance bandwidth and high gain performances are achieved by introducing a pair of quarter-circular-slit (QCS) and partly-hexagonal-ring-slit (PHRS). The proposed antenna having an area of $39 \times 29.5$ mm$^2$ ($S_L \times S_W$) and a thickness of 1.6 mm is fabricated on FR-4 substrate. The dielectric constant of the substrate is 4.3 and the loss tangent of 0.025. The electromagnetic software CST is used to design and optimize the proposed SSMA. The detailed optimized dimension of the SSMA is shown in Table 4.1.

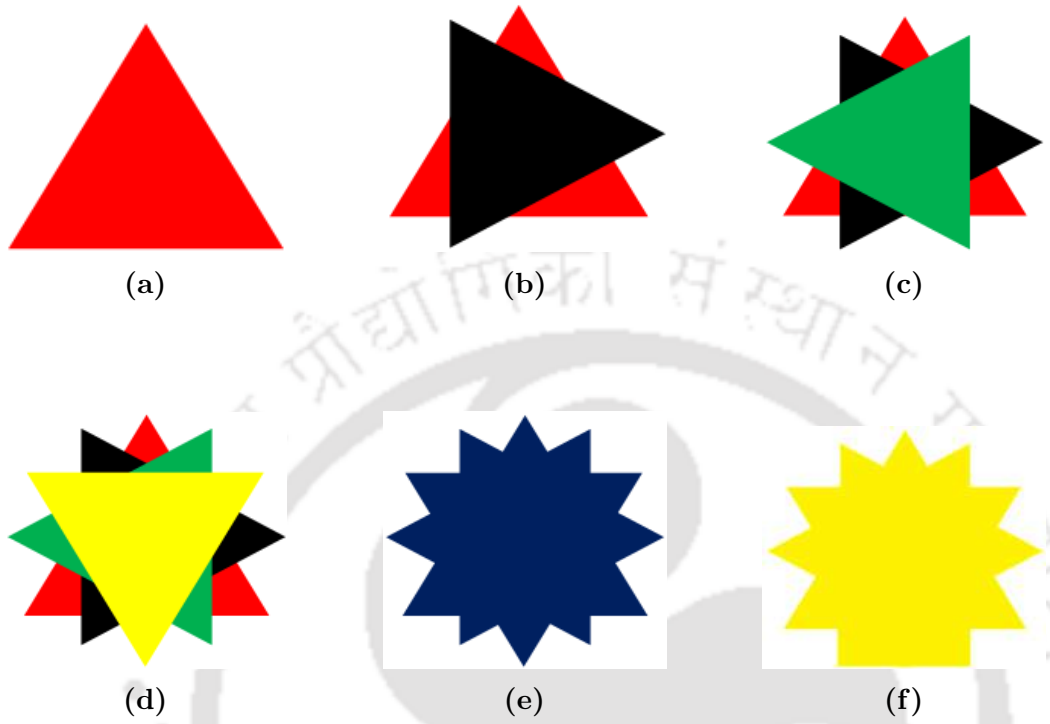


**Figure 4.1:** Geometrical configuration of 9-point star-shaped (a) one-equilateral triangles, (b) two-equilateral triangles, (c) three-equilateral triangles, (d) four-equilateral triangles, (e) merge all triangles and (f) nine-point star.

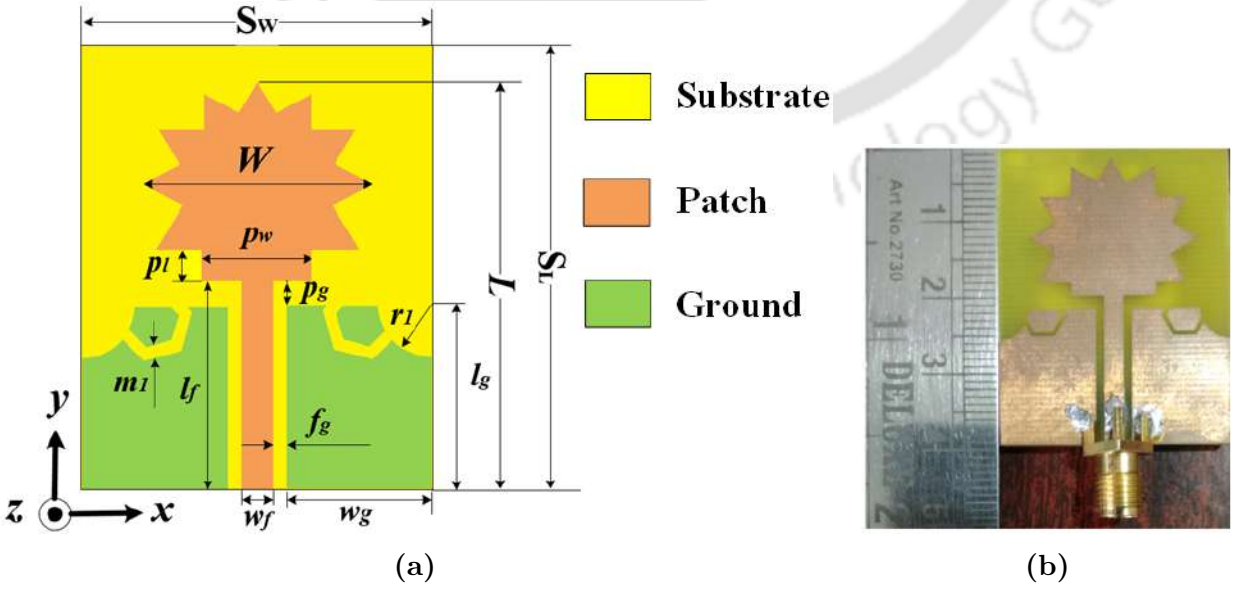


**Figure 4.2:** (a) Geometry of the proposed SSMA top view and (b) prototype.

**Table 4.1:** Optimized parameters of the proposed SSMA

| Parameters | Value (mm) | Parameters | Value (mm) | Parameters | Value (mm) |
|---|---|---|---|---|---|
| $S_L$ | 39 | $p_l$ | 3.5 | $m_1$ | 0.6 |
| $S_W$ | 29.5 | $p_g$ | 2.2 | $r_1$ | 4 |
| $W$ | 22 | $l_g$ | 17.8 | $w_f$ | 2.5 |
| $L$ | 37 | $l_f$ | 19.5 | $w_g$ | 12.7 |
| $p_w$ | 2.5 | $f_g$ | 1.05 | $h$ | 1.6 |

### 4.2.2 Design Evolution and Enhanced Bandwidth

The SSMA design evolution is shown in Figure 4.3(a). The proposed SSMA width ($W$) and length ($L$) calculated for the entire geometry is given as:

$$W = \frac{c}{2f_r\sqrt{((\epsilon_r+1)/2)}} \tag{4.1}$$

$$L = \sqrt{3}W \tag{4.2}$$

where $c$ is the velocity of the light in vacuum, $\epsilon_r$ is the relative permittivity of the substrate, and $f_r$ (= 3.5 GHz) is the resonant frequency.

**First step:** The Antenna 1 is a simple CPW-fed star-shaped radiator whose simulated $S_{11}$ result is shown in Figure 4.3(b). It is observed from Antenna 1, that the impedance bandwidth performance is from 2.63–6.49 GHz (normalized bandwidth 84.65%). It shows only one resonance band (it cannot provide better characteristics performance of $S_{11} \leq -10$ dB) and its frequency can be expressed as [38],

$$f_{ext} \approx \frac{c}{\sqrt{\epsilon_{eff}}L_{path}} \tag{4.3}$$

where $L_{path}$ is the external path length and $\epsilon_{eff}$ is the effective dielectric constant.

**Second step:** To enhance the impedance bandwidth performance is shown in Figure 4.3(b) for Antenna 2 in which a pair of quarter-circular-slit (QCS) is introduced on the defected ground plane with radius $r_1 = 4.0$ mm. It is noted two resonant frequencies with poor return loss which

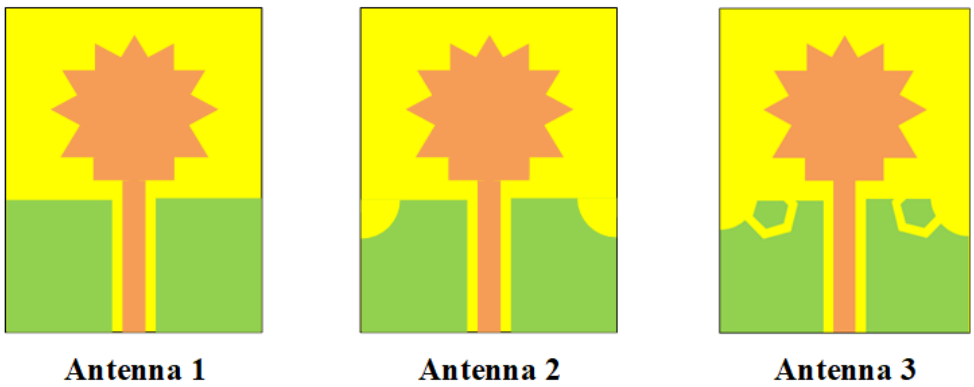


(a)

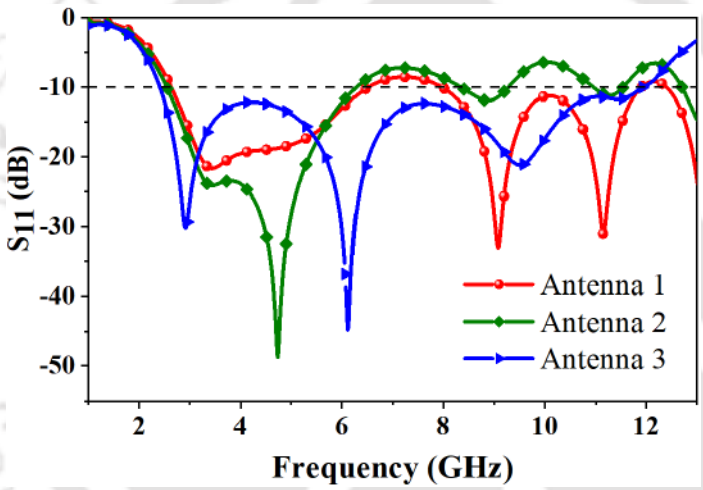


(b)

**Figure 4.3:** Evolution of the SSMA design (a) Antenna 1, Antenna 2, Antenna 3 (proposed) and their corresponding (b) $S_{11}$.

can not provide a wideband impedance bandwidth.

**Third step:** In this final design, a pair of symmetrical partly-hexagonal ring slits (PHRS) are introduced on both sides of the defective ground plane in order to further enhance the impedance bandwidth's $S_{11}$ performance. An excellent wider impedance bandwidth i.e., 135% (2.36–12.16 GHz) and good return loss are achieved.

The simulated surface current density distribution of the proposed SSMA at 2.8, 6.1, and 9.4 GHz are shown in Figures 4.4(a), 4.4(b), and 4.4(c), respectively. For detailed analysis, the surface current density distribution of different frequencies is plotted in Figure 4.4. The results reveal that the surface current is more concentrated at the bottom circumference at 2.8

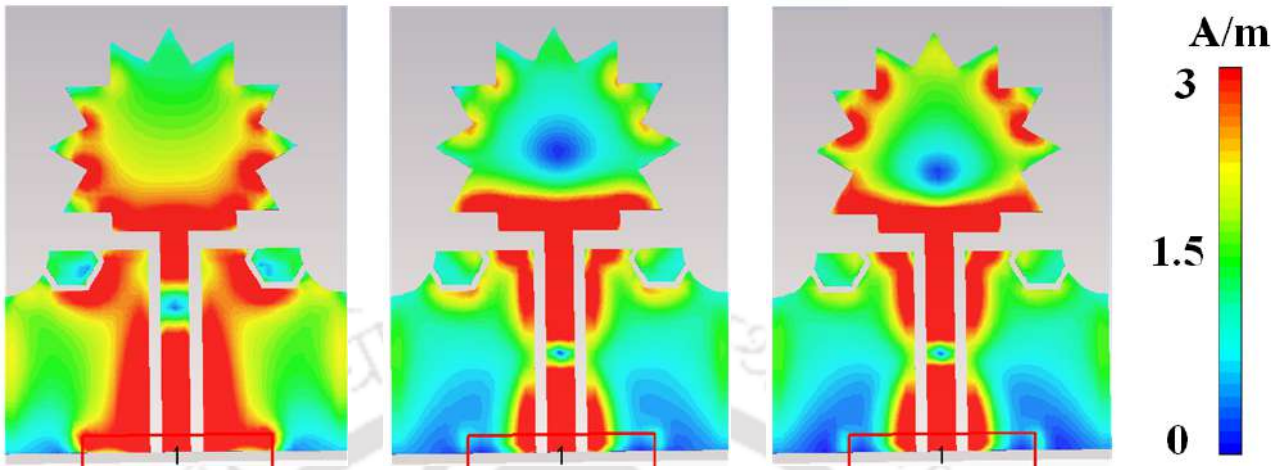


**Figure 4.4:** Surface current density distribution of the SSMA at (a) 2.8 GHz, (b) 6.1 GHz and (c) 9.4 GHz.

GHz and less at 6.1 GHz of the star-shaped radiator. Also, it is observed in Figure 4.4(a) and 4.4(c), that a large surface electric current density flows along the contour of the star-shaped metallic radiator. In particular, at 2.8 , 6.1, and 9.4 GHz, the surface current is concentrated near the feed line edge of the CPW ground plane, thereby fine-tuning impedance matching of the upper-side frequency bands. Therefore, an optimized partly-hexagonal-ring-slit (PHRS) thickness of $m_1 = 0.6$ mm, quarter-circular-slit (QCS) radius $r_1 = 4$ mm, and feed gap $f_g = 1.05$ mm gives the best results with a wider bandwidth and a high gain.

### 4.2.3 Parametric Study

#### 4.2.3.1 Effect of QCS Radius ($r_1$) and PHRS Thickness ($m_1$)

The effects of QCS radius $r_1$ and PHRS thickness $m_1$ of the ground plane on $S_{11}$ results are shown in Figures 4.5(a) and 4.5(b) respectively. It is found that the upper side-band frequency is reduced with increasing radius $r_1$ and impedance matching becomes poor for larger values. At $r_1$= 4.0 mm better return loss as well as matching is achieved. Similarly, it is found that the upper side-band frequency will reduce with the reduction of $m_1$ thickness of PHRS. The optimized slit thickness $m_1$ is found to be 0.6 mm for better results as shown in Figure 4.5(b).

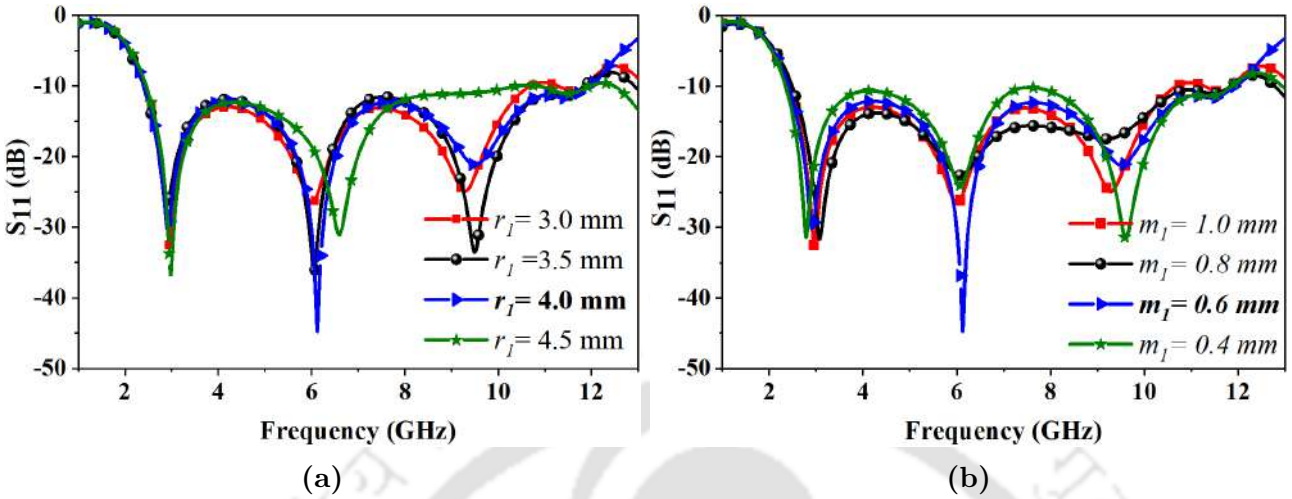


**Figure 4.5:** Simulated $S_{11}$ performance of the SSMA as a function of (a) $r_1$ and (b) $m_1$.

## 4.3 Transmission Line-RLC Circuit Model

The methodology to obtained the electrical equivalent circuit diagram of the proposed SSMA assuring transmission line model (TLM) is shown in Figure 4.6. In this figure, the microstrip-feed line introduces the inductance $L_r$ which is shown in Figure 4.6(a). The star-shaped radiator of the proposed SSMA contains a 9-point circumference of the star, each step takes part in tuning the capacitive and inductive coupling between the radiator and ground plane. Then, each star point is represented by the circuit as shown in Figure 4.6(b). Furthermore, $C_{g1}$ and $C_{g2}$ are the coupling capacitor. While $L_{g1}$, $L_{g2}$, $L_{g3}$, and $L_{g4}$ are caused by the inductances on both sides of the symmetric ground plane. The shunt capacitances $C_{gl}$ and $C_{gr}$ are due to the gaps between the feed line and CPW-fed ground plane as shown in Figure 4.6(c). Therefore, the radiating element of the designed SSMA is represented as several parallel circuits of series RLC as shown in Figure 4.6(d).

An optimization process is performed by using the NI AWR simulator and all the circuit parameters such as ( R ($\Omega$), L (nH) and C (pF) ) are obtained as follows: [ $L_r$ = 0.015, $L_p$ = 354, $S_{L1}$ = 12.88, $S_{L2}$ = 17.16, $S_{L3}$ = 1.52, $S_{L4}$ = 0.97, $S_{L5}$ = 27490, $S_{L6}$ = 792000, $S_{L7}$ = 5920 ] all dimensions are in nH, [ $C_p$ = 3.811$\times$ $10^{-11}$, $S_{C1}$ = 0.675$\times$ $10^{-5}$, $S_{C2}$ = 0.3798, $S_{C3}$ = 0.0647, $S_{C4}$ = 0.6469, $S_{C5}$ = 7.39$\times$ $10^{-12}$ , $S_{C6}$ = 2.04, $S_{C7}$ = 1.543 ] all dimensions

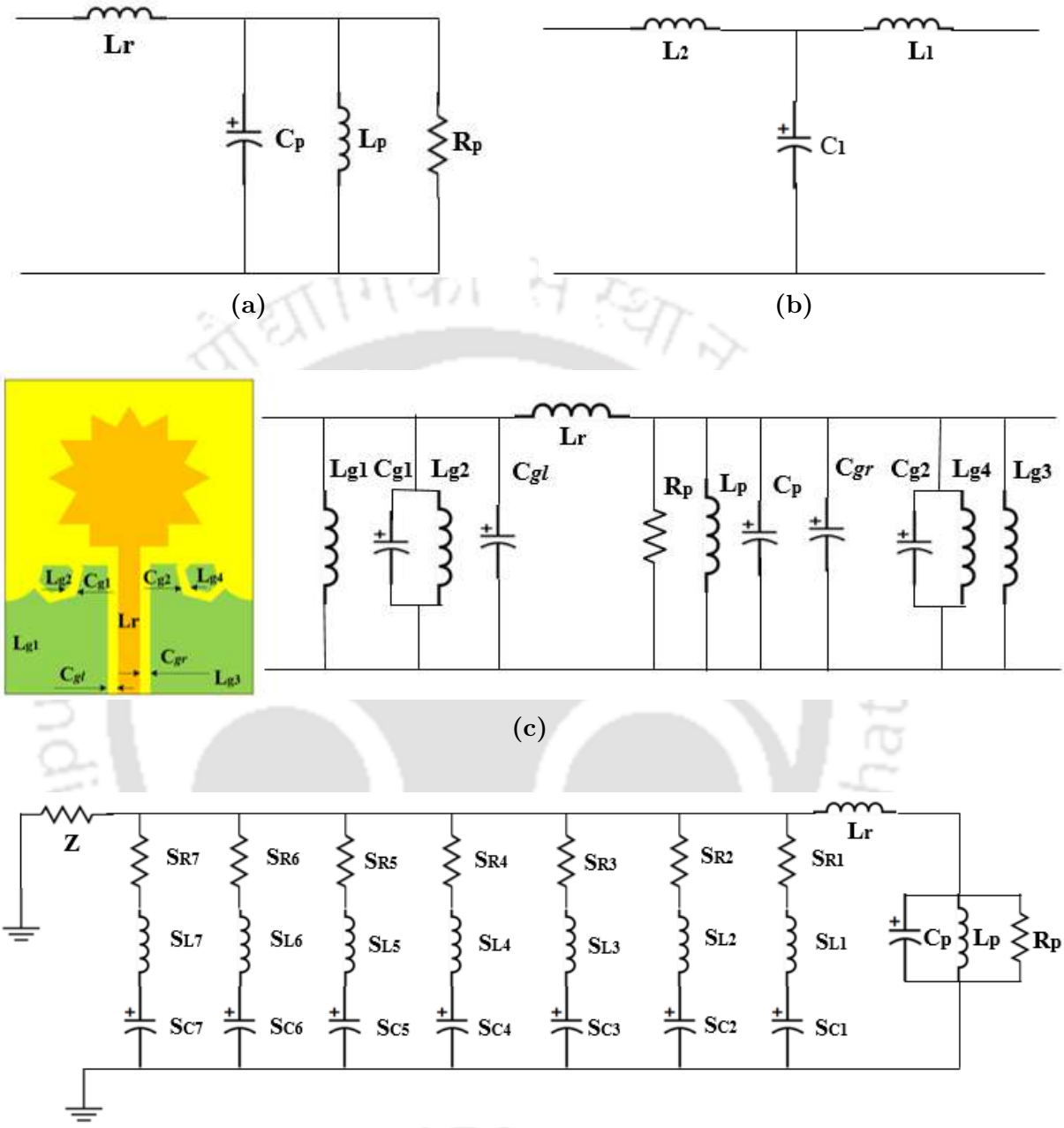


**Figure 4.6:** Equivalent transmission line model-RLC circuit elements of the proposed SSMA (a) basic patch antenna, (b) star-shaped step discontinuities, (c) all slit and gap structure and (d) simplified RLC circuit model.

are in pF and [$Z = 50$, $R_p = 1582$, $S_{R1} = 2.11$, $S_{R2} = 2.17$, $S_{R3} = 5.87$, $S_{R4} = 3.6$, $S_{R5} = 3.41$, $S_{R6} = 3.4$, $S_{R7} = 2.62$ ] all dimensions are in Ω. Finally, the proposed SSMA model gives approximately the same behavior and a very wider impedance bandwidth by several adjacents

resonances which can be represented by TLM-RLC circuits simulated result using NI AWR simulator as shown in Figure 4.7.

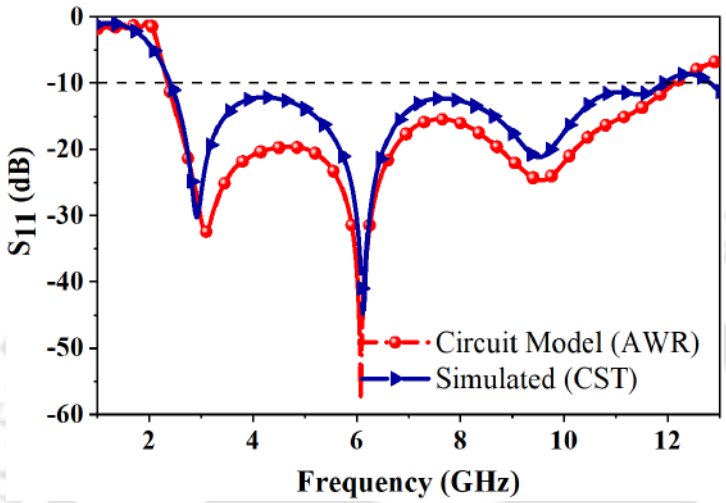


**Figure 4.7:** Simulated and equivalent transmission line circuit model response of the SSMA.

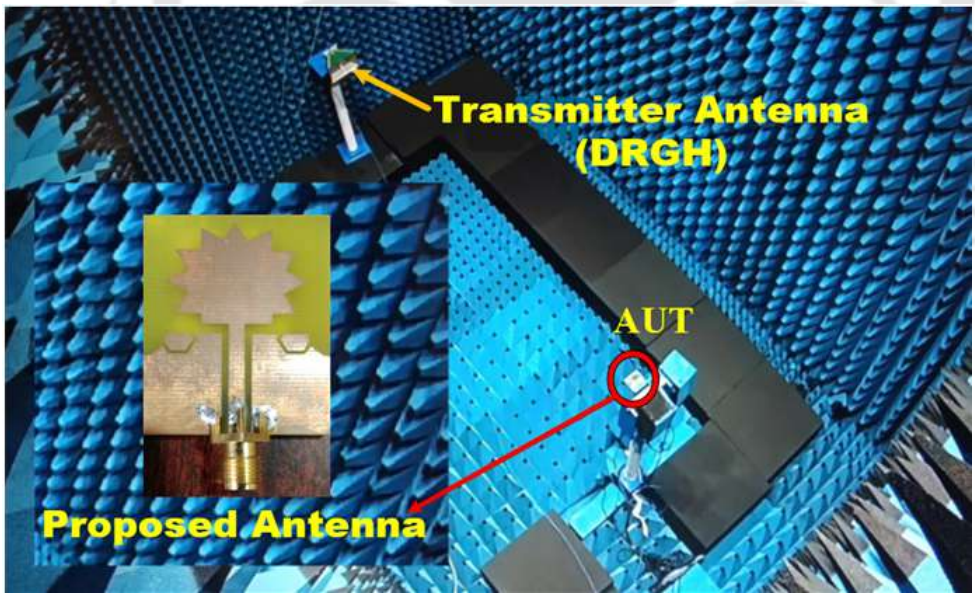


**Figure 4.8:** Actual antenna measurement environment in an anechoic chamber.

## 4.4 Simulated and Experimental Results

The performance of the proposed SSMA is analyzed using CST simulator (CST vers. 17) software and the results are verified with experimental results. The $S_{11}$ results are measured

with a vector network analyzer (VNA) (Anritsu MS46122B). The gain and radiation patterns are measured with an antenna measurement environment for 1–13 GHz band in an anechoic chamber (size: $6 \times 4 \times 6$ m$^3$) as shown in Figure 4.8 and a photograph of the prototype shown in Figure 4.2(b).

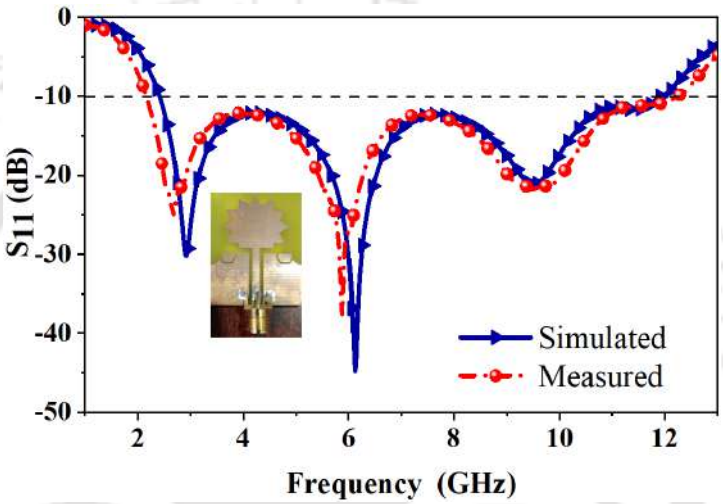


**Figure 4.9:** Measured and simulated $S_{11}$ performance of the SSMA.

### 4.4.1 Reflection Coefficient Performance

The simulated and measured reflection coefficient $S_{11}$ results are depicted in Figure 4.9 and the inset shows a photograph of the fabricated antenna. The measured impedance bandwidth from 2.21–12.13 GHz (139%) whereas the simulated impedance bandwidth from 2.36–12.16 GHz (135% $S_{11} \leq -10$ dB has been achieved. The measured $S_{11}$ results show that the impedance bandwidth is shifted a little to lower frequencies than the simulated results. It is maybe due to the alignment imperfection between various PCB layers, fabrication tolerances, and SMA connector. Since the proposed antenna is symmetric in shape, the $S_{11}$ performance is maintained within the permissible operating frequency band.

### 4.4.2 Gain Performance

The measured and simulated peak gain of the SSMA boresight ($\phi = 0°$, $\theta = 0°$) is shown in Figure 4.10. The measured peak gain for the lower side band is <1.56 dBi, and the upper

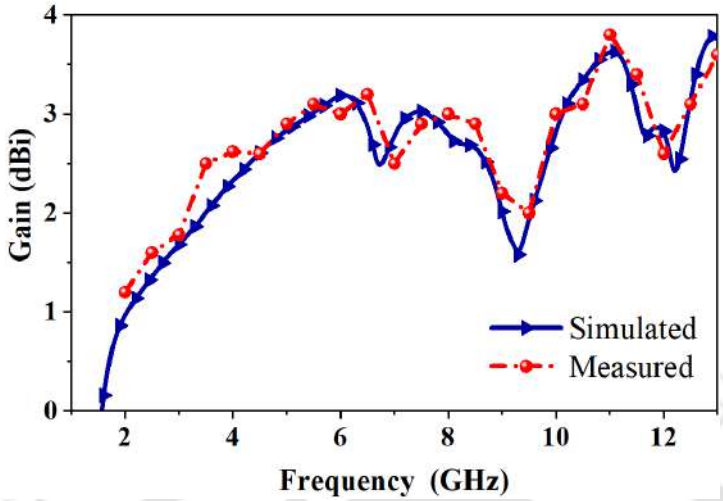


**Figure 4.10:** Measured and simulated peak gain of the SSMA.

side band is >3.6 dBi. The measured peak gain at the WiMAX band center frequency of 3.5 and 5.8 GHz are 2.55 dBi and 3.2 dBi, respectively. The measured peak gain at the WLAN 5.2 band center frequencies of 5.2 and 5.5 GHz are 2.95 and 3.05 dBi, respectively. For X-band satellite communication 7.8–9.3 GHz, the measured peak gain from 3.0–1.75 dBi is achieved.

**Table 4.2:** Comparison of the proposed antenna with other recently reported antennas

| Ref. | Antenna type | Dimension ($mm^2$) | Frequency ($GHz$) | Fractional BW (%) | Maximum gain ($dBi$) |
|---|---|---|---|---|---|
| [58] | Monopole | 42 ×50 | 2.69 – 10.16 | 116.30 | 6 |
| [59] | Monopole | 35 ×20 | 3.00 – 10.5 | 111.11 | 4.16 |
| [61] | Monopole | 28 ×30 | 2.95 – 13.95 | 130.17 | 3.2 |
| [35] | Bow-tie | 80 ×60 | 2.21 – 4.0 | 57.7 | 6.20 |
| [34] | Tapered slot | 30 ×28 | 2.78 – 12.3 | 126.00 | 6.23 |
| [36] | Monopole | 36.9 ×36.9 | 3.1 – 11 | 112.05 | 5.6 |
| [37] | Fractal | 60 ×60 | 10 – 50 | 133 | 9.5 |
| [46] | Monopole | 28 ×25 | 2.7 – 11 | 121.16 | 3.5 |
| This work | Monopole | 29.5 ×39 | 2.2 – 12.1 | 139.00 | 3.6 |

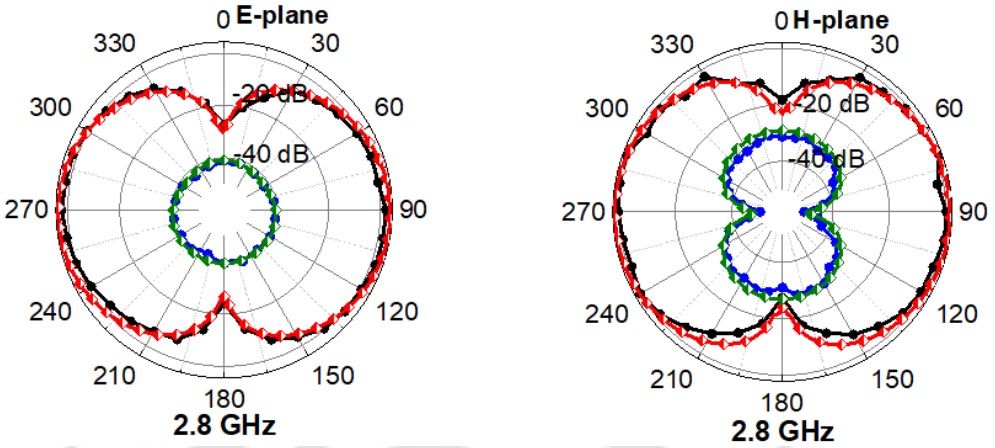


(a)

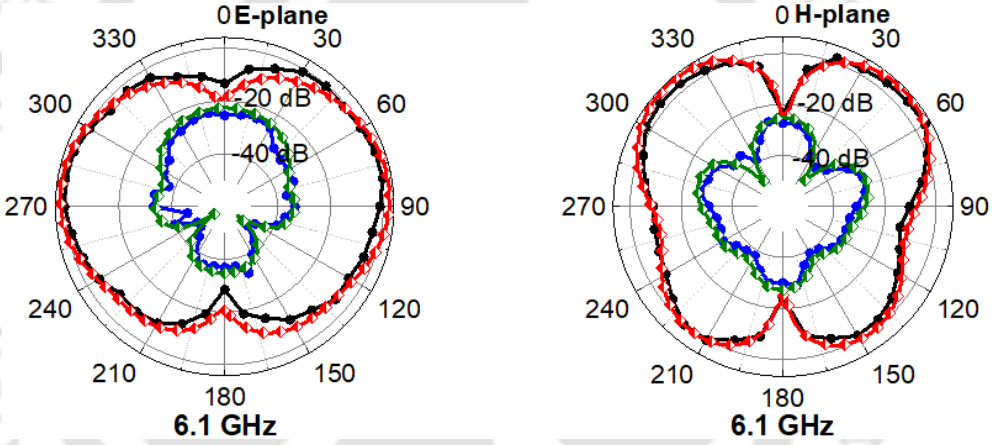


(b)

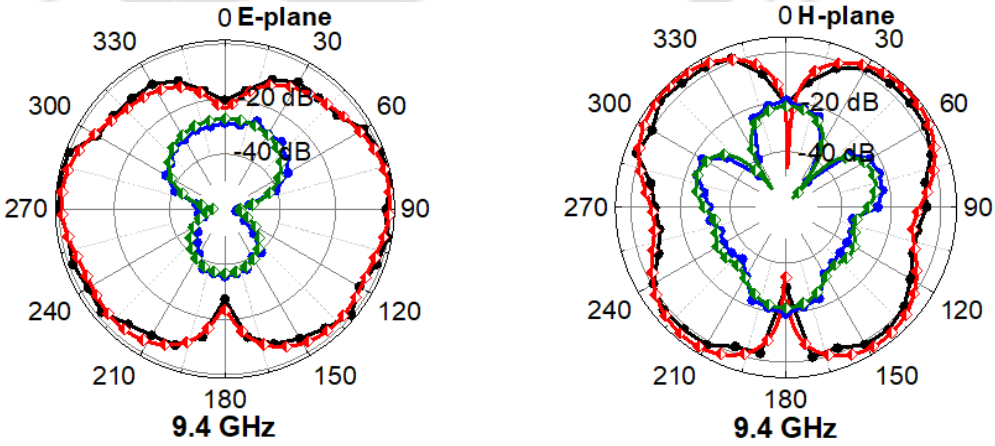


(c)

**Figure 4.11:** Simulated and measured radiation patterns of E-plane (left) and H-plane (right) of the SSMA at (a) 2.8 GHz, (b) 6.1 GHz and (c) 9.4 GHz.

### 4.4.3 Radiation Patterns Performance

The measured and simulated radiation patterns of the proposed SSMA in the E- and H-plane at 2.8, 6.1, and 9.4 GHz are shown in Figure 4.11. It is observed that the proposed SSMA exhibits nearly omnidirectional patterns in both planes. The E- and H-plane cross-polarization components are below −30 dBi in both measured and simulated results. Table 4.2 represents a comparison performance of SSMA with other antennas presented in the literature.

It is seen that this design performs better in almost all the parameters. The antenna type, dimension, bandwidth, and maximum gain are listed in Table 4.2. The measured fractional bandwidth of the SSMA is exhibiting better 139% with a peak gain of 3.6 dBi within the −10 dB impedance band. Table 4.2 expresses the performance of the design antenna structure in obtaining enhanced impedance bandwidth and shows better radiation close to omnidirectional patterns with a compact size. Therefore, considering the performance of the SSMA, it will be a good candidate for UWB applications.

## 4.5 Summary of the Chapter

The compact coplanar waveguide-fed SSMA using the quarter-circular-slit and partly hexagonal-ring-slit defected ground structure is proposed and verified experimentally. The impedance bandwidth performance of the SSMA is significantly enhanced by introducing QCS and PHRS. The impedance bandwidth and broad side maximum gain of the SSMA are 2.2–12.21 GHz (VSWR $< 2$) and the 3.6 dBi, respectively. Owing to the advantages of high gain, good radiation pattern close to omnidirectional, wider bandwidth, and compact size, the proposed SSMA is suitable for UWB applications. Because of the above-said advantages, the proposed antenna can be used in applications where the ultra-wideband is required such as UWB, mobile, wireless , satellite radio determination applications, etc. To study the linear polarization to circular polarization (CP) using traveling wave series-fed circular slits array with defected ground structure (DGS) and compact structure, a study is carried out which is discussed in the next chapter.

*Note: This work, Design of CPW-fed Star-Shaped Monopole Antenna for UWB Applications using Transmission Line Model, in Wireless Personal Communications (under review) (Springer https://www.springer.com).*

# 5

# Compact Quad-Band CP Series-Fed Circular Slit Microstrip Array Antenna Using Machine Learning

## Contents

## 5.1 Introduction

Recently, due to the increasing demands for modern wireless communication systems, the research on small and microstrip antenna arrays, radiating elements, feeding structures, and polarizations have attracted enormous attention. Due to its advantages of overcoming multi-path fading, non-line-of-sight applications, and providing better mobility compared to linearly polarized antennas, the circularly polarized (CP) antenna is getting popular in wireless communication systems. In recent years, many researchers are designing CP antennas as well as minimizing the size using different techniques [66]–[69]. The operating principle of CP antennas is to excite two orthogonal modes with equal amplitude and in-phase quadrature. This can be achieved by introducing different techniques to design the multi-band CP antennas which will be applied to various communication systems, such as global positioning systems (GPS) and satellite communications [70]–[74]. The dual-band CP antennas have been proposed with a single feed, cavity-backed square annular slot [70], truncated corner square slots loaded with a set of split-ring resonators [71], and an S-shaped slot center of the square radiator [72]. The single-feed microstrip patch antennas with the annular-ring slot on the square radiator or $4 \times 4$ arrays with 90° phase difference power dividers have also been demonstrated for dual-band applications [73], [74]. Although these antennas generate a CP wave in their two bands, the antenna size is increased and 3 dB axial ratio bandwidth (ARBW) is narrowed.

Furthermore, single-feed microstrip patch antennas with loading stubs and etching slots on the square patch or multi stacked patches with a slit have also been discussed for triple-band applications [75], [76]. However, these single-feed CP patch antennas have less than 3.5% ARBW with the large size discussed. In [77], multiple L-shaped slits on the hexagonal slot as a radiator is proposed and triple CP bands i.e., 1.7%, 3.86%, and 5.23% are achieved. In [78], a square slot with the metallic strips and split-ring resonator configuration, the 3 dB ARBWs improved are presented. Though these antennas had small sizes the ARBWs were still less than 11%. Recently, a quad-band CP antenna has been reported in [79], using inverted-U-shaped radiators and the ARBWs of 5.4%, 8.3%, 3.7%, and 2.9% are achieved.

Among the various established techniques to design an antenna array, the sequential rotation technique (SRT) is found to be effective for CP array antenna in terms of improving the array's bandwidth, radiation patterns, and polarization purity. Several designs of CP array antenna have been discussed, but the SRT is one of the most popular methods investigated in the literature to generate the CP operation [80]–[84]. In an SRT, phase shiftings of $90^o$ and $180^o$ are achieved by applying $\lambda/4$ transmission lines with an L-shaped radiator [80]. A series feed network is reported [81], consisting of $\lambda/4$ transformer sections and adding an L-shaped ground strip in the radiator array to reduce cross-polarization. In [82]–[84], the array elements are fed by different feeding networks like rat-race, Wilkinson power divider, and microstrip line. However, antenna configurations of these designs are usually large and the uses of a complex feeding network structure complicate the fabrication of the antenna. The antennas mentioned above are either thick in profile or large in aperture size, which motivates us to develop a compact multi-band CP antenna to some extent as well as improved the ARBW and IBW with maintain the minimum axial ratio using a series-fed circular slit array patch.

In this chapter, a new design of dual-CP TWSCSMA antenna effectively deals with a novel series-fed circular slit microstrip array which involves a compact annular ring TWSCSMA antenna with four split-ring resonators (SRR) unit cells with a double-annular ring on the defected ground plane. The proposed dual-CP TWSCSMA antenna has a distinct separation of the four CP bands (ARBW of 16.26%, 12.52%, 8.22%, and 13.82%) with improved operational impedance bandwidth (IBW of 33.85% and 50.73%) and minimum axial ratio ($< 1.2$ dB). Since the proposed antenna is electrically small, the achieved gain is low. However, the size of the antenna is compact with wide band IBW and ARBW characteristics. The machine learning regression (MLR) algorithm is used to predict the accurate model performance requirements of the dual-CP TWSCSMA antenna for desired two IBW and four wide ARBW. The parameters of the dual-CP TWSCSMA antenna obtained using CST Microwave Studio are validated with the experimental results.

This chapter is divided into the following sections: section 5.2 states the theoretical analysis of circular polarization generation, design evolution, circular polarization mechanism, and

current distribution analysis. In section 5.3, the MLR algorithms model is discussed. The reflection coefficient $S_{11}$, axial ratio performance, peak gain, and radiation patterns parameters at different frequencies such as 2.5, 3.5, 3.8, and 5.2 GHz are presented in section 5.4. The experimental results match quite well with the simulation results, thus validating the practical feasibility of the design. The principal outcomes of this research work are explained in section 5.5.

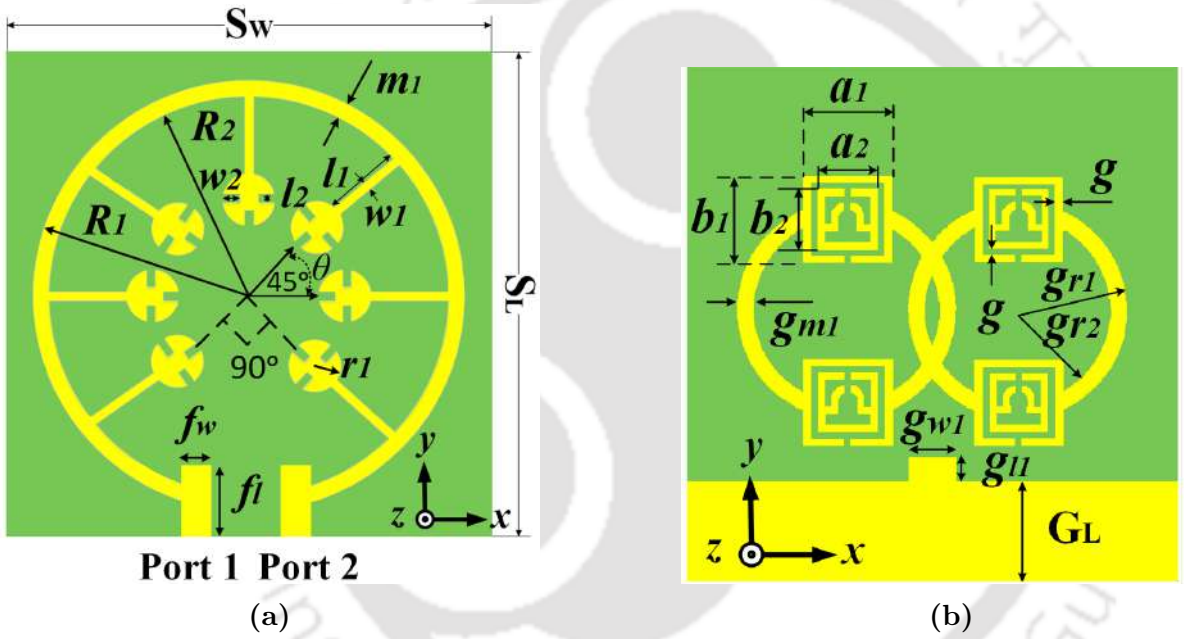


**Figure 5.1:** Geometry of dual-CP TWSCSMA antenna (a) top and (b) bottom view.

## 5.2 Antenna Design and Analysis

### 5.2.1 Antenna Configuration

The geometry of the compact dual-CP TWSCSMA antenna top view is illustrated in Figure 5.1(a). As shown in Figure 5.1(a), the proposed antenna is fed by a 50 Ω microstrip-fed printed on top of the 2 mm-thick FR-4 substrate having $\epsilon_r = 4.3$ and loss tangent $(\tan\delta) = 0.025$. In this figure, seven series-fed circular slit array elements in an annular ring are placed at an angle of $45^o$ from each other. The bottom of the TWSCSMA antenna consists of four SRR unit cells

with a double-annular ring on the defected ground structure (DGS) as shown in Figure 5.1(b). The values of all geometrical dimensions corresponding to Figure 5.1 are shown in Table 5.1.

The four SRR unit cells ($a_1 = b_1 = 7$ mm) with double-annular rings (outer radius $g_{r1} = 9$ mm and inner radius $g_{r2} = 8$ mm) are introduced in the ground plane to improve the operational bandwidth and minimize the axial ratio. To realize the left-hand circular polarization (LHCP) wave, the input RF signal for port 1 has a 45° phase increment in the clockwise direction. Similarly, to get the right-hand circular polarization (RHCP) wave, port 2 is fed with a phase increment of 45° in an anticlockwise direction for each circular slit patch. Using this concept, we can realize dual-CP radiation.

**Table 5.1:** Geometric parameters values of the proposed antenna

| Parameters | Value (mm) | Parameters | Value (mm) | Parameters | Value (mm) |
|---|---|---|---|---|---|
| $S_L$ | 41 | $w_1$ | 0.4 | $G_L$ | 8.2 |
| $S_W$ | 41 | $w_2$ | 0.4 | $g_{w1}$ | 3.4 |
| $R_1$ | 19 | $l_1$ | 12.4 | $g_{l1}$ | 2 |
| $R_2$ | 18.2 | $l_2$ | 0.7 | $g_{r1}$ | 9 |
| $m_1$ | 0.8 | $a_1$ | 7 | $g_{r2}$ | 8 |
| $f_w$ | 2.2 | $b_1$ | 7 | $g_{m1}$ | 1 |
| $f_l$ | 6.9 | $a_2$ | 5 | $g$ | 0.5 |
| $r_1$ | 2.2 | $b_2$ | 5 | $h$ | 2.0 |

### 5.2.2 Theoretical Analysis of Circular Polarization Generation

Figure 5.1(a) shows the circular slit patches arranged in a concentric ring fashion which is fed in series with the proper phase shifts. Seven circular slit patches are rotated sequentially by 45° and fit in an annular ring radiator that has an outer radius $R_1 = 19$ mm and inner radius $R_2 = 18.2$ mm.

To understand the polarization of the proposed antenna, an $N$ number of uniform series-fed circular slit array (SCSA) elements as shown in Figure 5.2 are fed from port 1 or port 2 to get LHCP or RHCP waves respectively. The radiation elements are symmetrically distributed

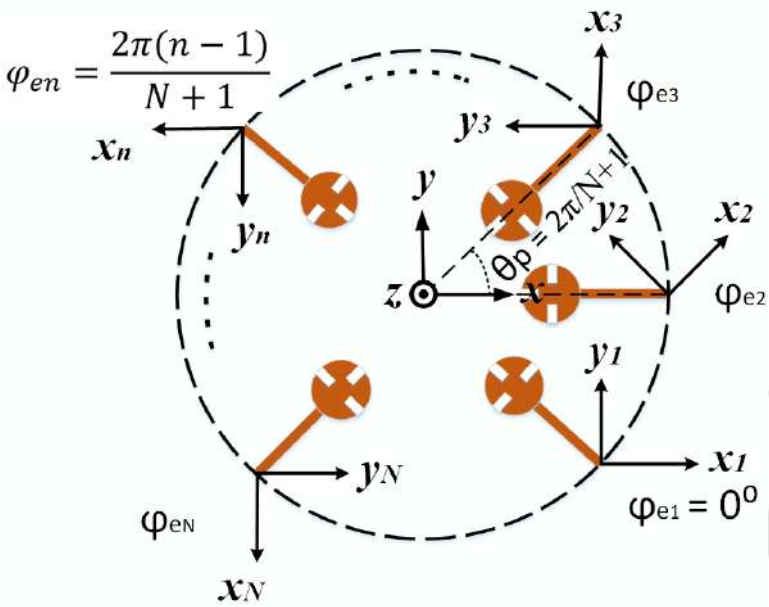


**Figure 5.2:** Configuration of $N$ element of a series-fed circular slit array.

around the z-axis so that the angle $\theta_p$ between adjacent elements is $2\pi/(N+1)$. It is assumed that each element is fed with uniform amplitude with an excitation current phase of the $n^{th}$ element $\varphi_{en}$. The parameters shown in Figure 5.2 are expressed as:

$$\theta_p = 2\pi/(N+1) \tag{5.1}$$

$$\varphi_{en} = -\frac{2\pi(n-1)}{N+1}, \quad 1 \leq n \leq N = 7 \tag{5.2}$$

$$\begin{bmatrix} \hat{x}_n \\ \hat{y}_n \end{bmatrix} = \begin{bmatrix} cos(\theta_p(n-1)) & sin(\theta_p(n-1)) \\ -sin(\theta_p(n-1)) & cos(\theta_p(n-1)) \end{bmatrix} \begin{bmatrix} \hat{x} \\ \hat{y} \end{bmatrix} \quad (1 \leq n \leq N) \tag{5.3}$$

A plane wave propagates in the $z$-direction can have both $x$ and $y$ components of the electric field as expressed below:

$$\boldsymbol{E} = (\hat{x}E_x + \hat{y}E_y)e^{-jkz} \tag{5.4}$$

The E-field ($\boldsymbol{E}$) on the sequentially rotated patches as shown in Figure 5.2 can be decom-

posed into an RHCP component $\boldsymbol{E}_{RHCP}$ and an LHCP component $\boldsymbol{E}_{LHCP}$ as expressed below:

$$\boldsymbol{E} = \mid \boldsymbol{E}_{RHCP} \mid (\hat{x}_n - j\hat{y}_n) + \mid \boldsymbol{E}_{LHCP} \mid (\hat{x}_n + j\hat{y}_n) \tag{5.5}$$

Since the circular array is rotationally symmetric, $\boldsymbol{E}_{RHCP}$ is equal for different radiation elements. It is also true for $\boldsymbol{E}_{LHCP}$. Therefore, the resultant $\boldsymbol{E}_{RHCP}$ and $\boldsymbol{E}_{LHCP}$ are expressed as:

$$\begin{aligned}
&\sum_{n=1}^{N} \boldsymbol{E}_{RHCPn}\ e^{j\varphi_{en}} \\
&= \sum_{n=1}^{N} \mid \boldsymbol{E}_{RHCPn} \mid (\hat{x}_n - j\hat{y}_n)\ e^{j\varphi_{en}} \\
&= \sum_{n=1}^{N} \mid \boldsymbol{E}_{RHCPn} \mid (\hat{x} - j\hat{y})\, e^{j\theta_p(n-1)}\, e^{j\varphi_{en}}
\end{aligned} \tag{5.6}$$

$$\begin{aligned}
&\sum_{n=1}^{N} \boldsymbol{E}_{LHCPn}\ e^{j\varphi_{en}} \\
&= \sum_{n=1}^{N} \mid \boldsymbol{E}_{LHCPn} \mid (\hat{x}_n + j\hat{y}_n)\ e^{j\varphi_{en}} \\
&= \sum_{n=1}^{N} \mid \boldsymbol{E}_{LHCPn} \mid (\hat{x} + j\hat{y})\, e^{-j\theta_p(n-1)}\, e^{j\varphi_{en}}
\end{aligned} \tag{5.7}$$

The AR of the proposed antenna is given as

$$AR_{dB} = 20\log_{10}\frac{\mid \boldsymbol{E}_{RHCP} \mid + \mid \boldsymbol{E}_{LHCP} \mid}{\mid \boldsymbol{E}_{RHCP} \mid - \mid \boldsymbol{E}_{LHCP} \mid} \tag{5.8}$$

The above expression is based on the boresight at the center of the ring being the origin of the spherical coordinate system.

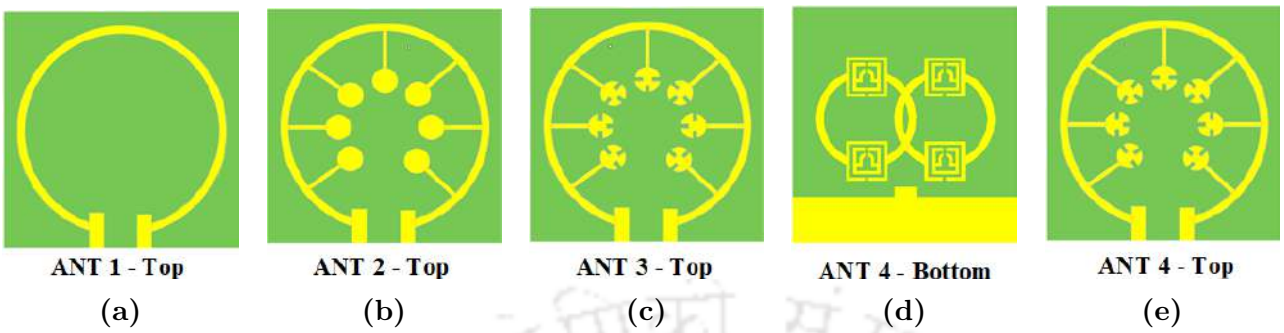


**Figure 5.3:** Evolution of the dual-CP TWSCSMA antenna.

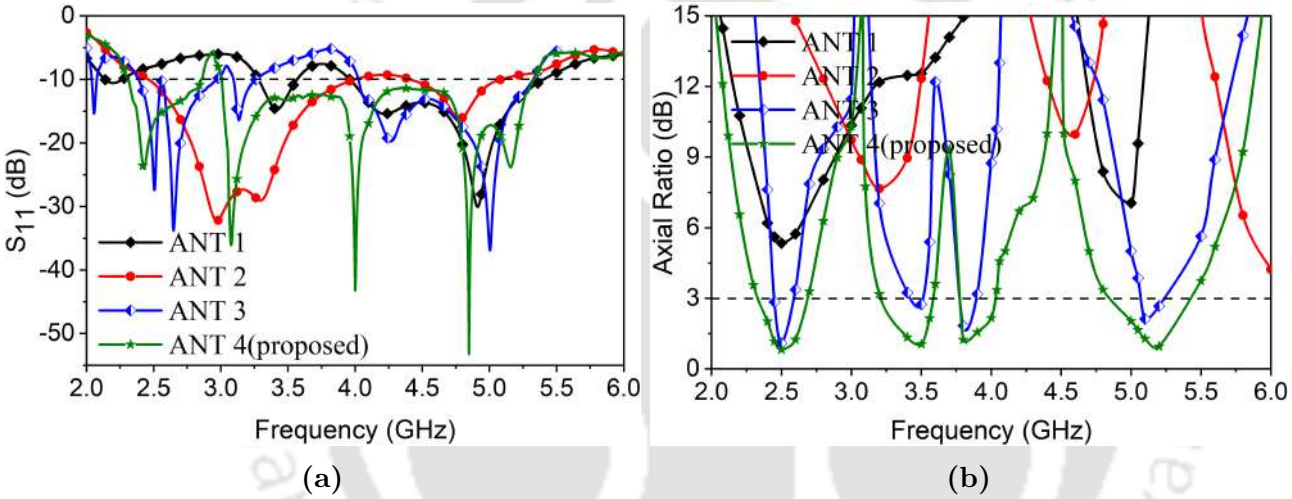


**Figure 5.4:** Evaluations of simulated (a) $S_{11}$ and (b) AR of the proposed TWSCSMA antenna.

### 5.2.3 Design Evolution and CP Mechanism

The different design steps and their configurations are shown in Figure 5.3 to understand the CP performance of the antenna. The different antennas are simulated using CST Microwave Studio software. The circular radiators are very popular because they are simple to fabricate and have small cross-polarization radiation [85, 86]. Therefore, the design starts with an annular ring radiator of radius $R_1 = 19$ mm and $R_2 = 18.2$ mm as shown in ANT 1 of Figure 5.3. Due to the increased current path in an annular ring, wider IBW and ARBW compared to circular patches [87] are achieved. For a traditional annular ring patch antenna, the $TM_{11}$ mode is the fundamental resonant mode, $\lambda_g$ is the wavelength of the lower resonating frequency $f_g$ that can

be expressed as follows:

$$\lambda_g = \frac{c}{f_g\sqrt{\epsilon_{eff}}} \tag{5.9}$$

where $\epsilon_{eff}$ is the effective dielectric constant. As seen in Figure 5.1(a), the mean circumference of a series-fed annular ring equals the wavelength at nearly the first resonant frequency [88]. The resonant frequency is calculated as follows:

$$f_{11} \approx \frac{c}{\pi(R_1 + R_2)}\left(\frac{1+\epsilon_r}{2\epsilon_r}\right)^{\frac{1}{2}} \tag{5.10}$$

where $f_{11}$ is the resonant frequency and $\pi(\mathrm{R}_1 + R_2)$ is the mean circumferences of the annular ring of the ANT 1. Based on the detail parameters, the calculated resonance frequency is approximately $f_{11} = 2.17$ GHz.

To clarify the proposed antenna performance process, the IBW and ARBW performances of ANT 1–ANT 4 have been compared in Figure 5.4. It is noticed in Figure 5.4(a) that the simple annular structure ANT 1 has two narrow impedance bands below −10 dB about 3–3.5 GHz and 3.7–5.53 GHz. However, it is a linearly polarized wave. The ARBW is greater than 15 dB in two frequencies within the bandwidth as shown in Figure 5.4(b). CP is generated by two orthogonal $\boldsymbol{E}$ vectors ($\boldsymbol{E}_{HOR}$, $\boldsymbol{E}_{VER}$) with equal amplitude and 90° phase difference, where $\boldsymbol{E}_{HOR}$ and $\boldsymbol{E}_{VER}$ represent the complex voltage in the horizontal and vertical planes, respectively.

The seven symmetrical circular slit patches of radius ($r_1 =$) 2.2 mm are added as series-fed on the annular ring patch of ANT 1 so that the $S_{11}$ performance shows an improvement in lower and decrease upper frequency in terms of bandwidth. This may be due to the increased current path induced by the horizontal annular ring. More importantly, the ARBW also drops significantly from about 15 dB to around 8 dB at 3.2 GHz and 4.5 GHz.

In ANT 3, three rectangular slits (size: $l_2 = 1.7$ mm and $w_2 = 0.4$ mm) placed by 90° from each other are introduced in each of seven circular slit patches which act as the quasi-lumped-resonators (QLR) [84]. When QLRs are introduced in ANT 2 which is a linear polarized (LP) antenna with different radiated phases of 90°, the total radiated field in the z-direction of wave propagation can be expressed as follows:

$$\boldsymbol{E} = \boldsymbol{E}_{ANT} + \boldsymbol{E}_{QLR} = \frac{E_o}{2}\ e^{-jkz}\ [(1+j)\hat{x} + (1-j)\hat{y}] \tag{5.11}$$

where $\boldsymbol{E}_{ANT}$ and $\boldsymbol{E}_{QLR}$ are the radiated field by a series-fed annular-ring antenna and QLRs respectively. Since both the radiated fields are perpendicular and magnitudes are the same, the CP radiation pattern is obtained. The position and dimensions of the QLRs i.e., $l_2 = 1.7$ mm and $w_2 = 0.4$ mm of the ANT 2 are optimized to obtain the quad-band CP characteristics at the intended frequencies of 2.5, 3.5, 3.8, and 5.2 GHz. The $S_{11}$ performance shows better improvement in lower and upper frequencies in terms of bandwidth. The ARBW also drops significantly from about 8 dB to around 2 dB at 2.5, 3.5, 3.8, and 5.2 GHz. However, at this stage, the antenna does not possess wide IBW and CP characteristics.

For further improvement in IBW, ARBW, and better impedance matching, four SRR unit (area of 49 mm$^2$ (7 mm×7 mm)) cells with double-annular rings are loaded with ANT 3 such that its position on the ground plane allows neutralizing unwanted surface coupling waves on the radiator as shown in ANT 4. In the transmission line model of the SRR, L and C values determine the frequency of operation of the proposed antenna [86]. The length $(b_1, b_2)$ and width $(a_1, a_2)$ of the unit cells are adjusted to ensure 90° phase difference between the field components so that the bandwidths (IBW, ARBW) are significantly improved in ANT 4 as shown in Figure 5.4. As a result, a compact dual-CP TWSCSMA antenna achieves two wide −10 dB IBW from 2.213 to 2.982 GHz (29.62%) and from 3.071 to 5.342 GHz (53.81%) and less than 3 dB in four CP bands of 15.23% (2.382–2.723 GHz), 12.80% (3.213–3.652 GHz), 9.02% (3.741–4.092 GHz), and 11.65% (4.754–5.342 GHz) when it is excited either in port 1 or port 2.

### 5.2.4 Current Distribution Analysis

The simulated current distribution of CP bands are studied at phases $\omega t = 0°$, $\omega t = 90°$, $\omega t = 180°$ and $\omega t = 270°$ as shown in Figure 5.5(a)–(d) at frequencies of 2.5, 3.5, 3.8, and 5.2 GHz respectively for port 1. It is observed that as the phase changes by 90°, the current distribution vector at all the resonant frequencies rotates clockwise +z-direction. Hence, the

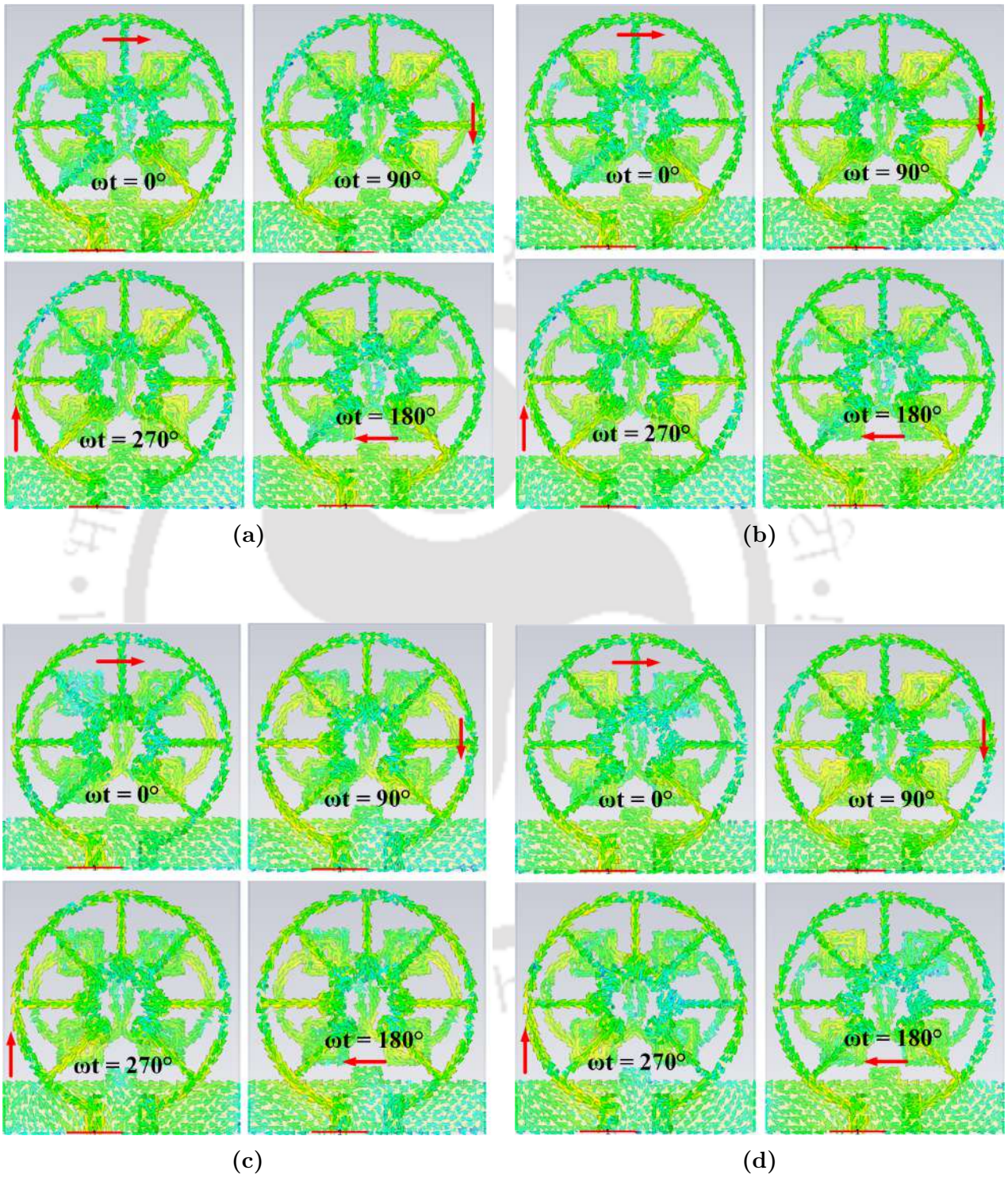


**Figure 5.5:** Surface current distributions at (a) 2.5, (b) 3.5, (c) 3.8 and (d) 5.2 GHz for port 1.

LHCP is obtained at the CP bands for port 1. And also, it is observed that the current reverses its direction when the feeding port is changed to port 2 hence, the RHCP is obtained at the

four CP bands for this configuration.

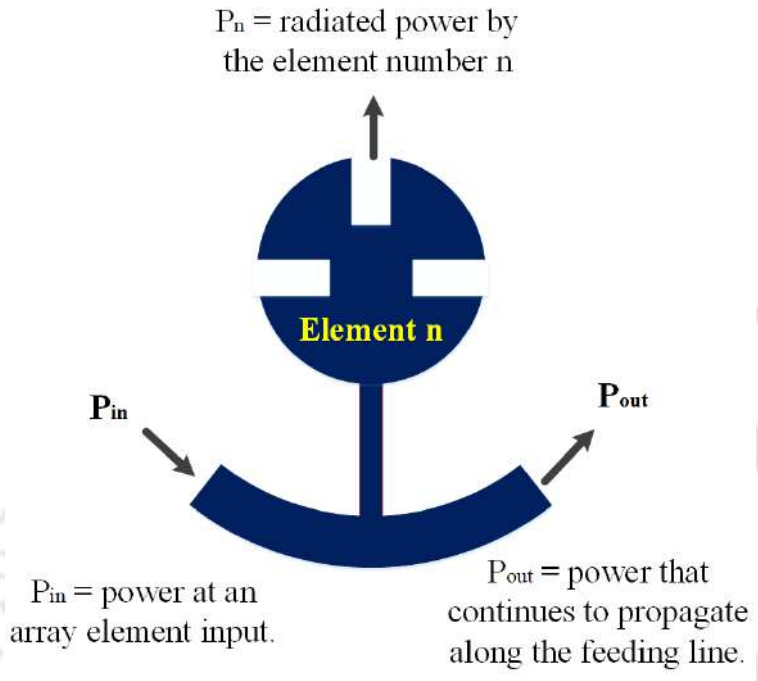


**Figure 5.6:** Power on the single radiating element.

### 5.2.5 Radiated Power Analysis of Array Elements

Suppose the power fed to array element $n$ is $P_{in}$, the power radiated $P_n$ by that element, and $P_{out}$ is the power that continues to propagate along the feeding line as shown in Figure 5.6 and then the ratio of $P_n$–$P_{in}$ can be defined as the power coupling coefficient $\alpha$

$$\alpha = \frac{1 - |S_{11}|^2 - |S_{21}|^2}{1 - |S_{11}|^2} = \frac{P_n}{P_{in}} \tag{5.12}$$

The reflection and transmission coefficient of each element are denoted by $S_{11}$ and $S_{21}$, respectively. The reflection coefficient terms can be neglected ($|S_{11}|^2$ equals 0) due to the presence of multiple reflections on the transmission line [76]. When $|S_{11}|^2$ is small enough, $\alpha$ can be expressed as follows:

$$\alpha = 1 - |S_{21}|^2 \tag{5.13}$$

Assume that dielectric, ohmic losses, and the effect of mutual coupling between elements to

be negligible. Let the total power fed into the array be 1 W, the power radiated by element 1 can be expressed as follows:

$$p_1 = \alpha \tag{5.14}$$

For element 2

$$p_2 = (1 - p_1)\alpha = (1 - \alpha)\alpha \tag{5.15}$$

For element 3

$$p_3 = (1 - p_2 - p_1)\alpha = (1 - \alpha)^2\alpha \tag{5.16}$$

For element n

$$P_n = (1 - P_{n-1} - P_{n-2} - ... - P_2 - P_1)\,\alpha = \left((1 - \alpha)^{(n-1)}\right)\alpha \tag{5.17}$$

Then the total radiated $P_{total}$ can be expressed as:

$$P_{total} = \sum_{n=1}^{N} P_n = \frac{\alpha[1 - (1 - \alpha)^N]}{1 - (1 - \alpha)} = 1 - (1 - \alpha)^N \tag{5.18}$$

## 5.3 Antenna Parameter Optimization using MLR

The purpose of using machine learning regression (MLR) algorithms in antenna modeling is to predict new model parameters using the training data set generated by the computational EM model [90] and to evaluate the model's accuracy and generalization [91]. It can be realized by the input $x$ and the corresponding output $y$ parameters by connecting a model such that

$$y = M(x) \tag{5.19}$$

where $y \in \mathrm{Y} \subset \mathbb{R}^u$, while $u$ are the values of an output variable and $x \in \mathrm{X} \subset \mathbb{R}^c$, $c$ are the values of input modeling variables. The accuracy can be expressed as a function of the mean squared error (MSE) function:

$$MSE = \frac{1}{N}\sum_{i=1}^{N}\left(y_i^{pred} - y_i^{meas}\right)^2 \tag{5.20}$$

where $y_i^{pred}$ is the predicted value, $y_i^{meas}$ is the measured value and $N$ number of data samples.

The performance of the TWSCSMA antenna mainly depends on seven design parameters $f_l$, $l_1$, $R_1$, $R_2$, $r_1$, $G_L$, and $b_1$. These seven geometric parameters act as input variables for MLR models. In the present EM simulation, 35035 samples obtained using CST Microwave Studio, give reasonably high and stable $R^2$ values. The total sample points are collected by selecting the range of sample space of seven input parameters, $x$ as: $f_l \in [6.0, 6.8]$, $l_1 \in [5.6, 6.4]$, $R_1 \in [17.7, 18.5]$, $R_2 \in [18.6, 19.4]$, $r_1 \in [1.8, 2.6]$, $G_L \in [7.9, 8.7]$, and $b_1 \in [13.6, 14.4]$ with a step size of 0.2 for each parameter. The training data is defined by $\{ (x_i, y_i), \text{i} = 1, 2, \ldots n \}$, where the input is $x = (f_l, l_1, R_1, R_2, r_1, G_L, b_1)^T$. Then the model exercises the current input samples, predicts a new parameter which is compared with the target, and calculates the prediction error as shown in Figure 5.7. To search for the optimal design parameters based on the MLR model, a very fine grid over the entire sample space $x$ with step size 0.2 mm is generated, consisting of 35035 total sample data points. Three ML regression algorithms such as: artificial neural networks (ANN), decision tree regression (DTR) and decision forest regression (DFR) [92] are used for the proposed antenna modeling and comparison of the results.

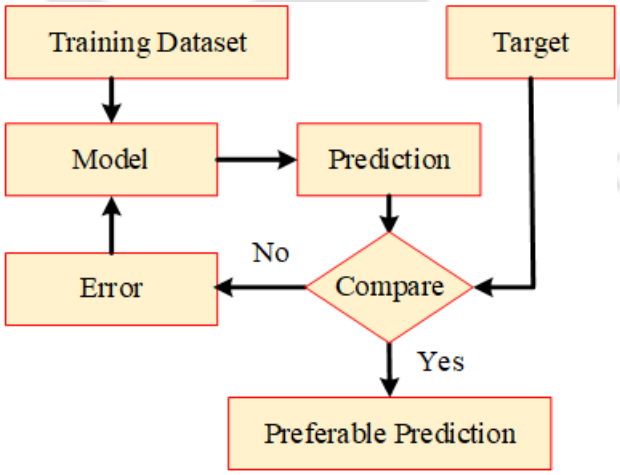


**Figure 5.7:** Perspective of MLR work.

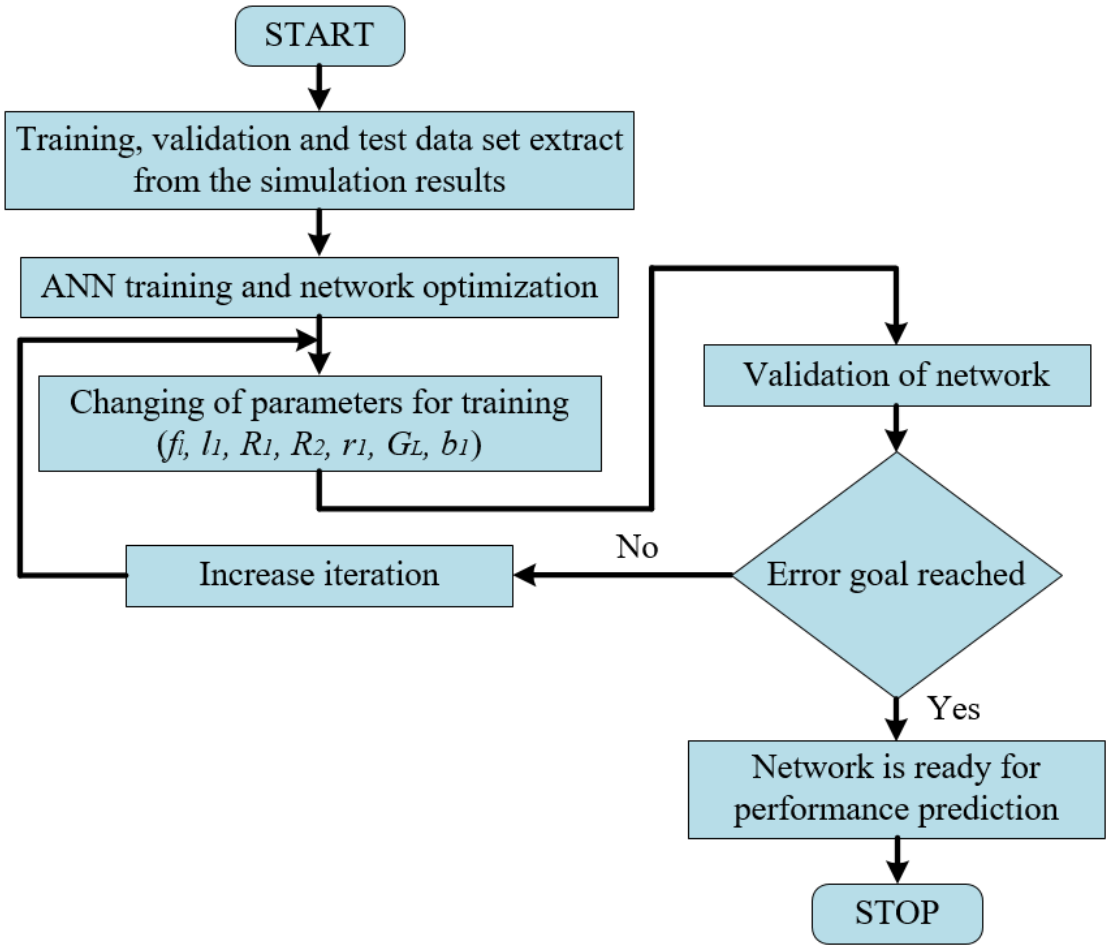


**Figure 5.8:** Workflow chart of ANN.

### 5.3.1 Artificial Neural Networks (ANN)

ANN model is used to calculate and develop a nonlinear regression based model of biological neurons. ANN is the structure of many layers and consists of input, hidden, and output layers; each layer contains neurons. Neurons are interconnected with the corresponding links (weights). In this work, multilayer perceptrons (MLPs) is trained by Levenberg-Marquardt (LM) algorithms [93], which has the capability of fast learning and good convergence and can be expressed as:

$$x_j^{k+1} = f\left(\sum_d W_{dj}^k \, x_d^k + B_{bj}^k\right) \tag{5.21}$$

where $W_{dj}^k$ is weighted connecting $d^{th}$ neuron in the layer $k$ to $j^{th}$ neuron in layer $k+1$; which are initialized randomly. $B_{bj}^k$ represents the bias of the $j_{th}$ neuron in layer $k$. In our analysis,

the data samples are divided into three parts: training data used 80% testing and validation using 10% each. The LM learning algorithm is used to develop the ANN model flow chart as shown in Figure 5.8 and the neural network toolbox of MATLAB [94] is used for training the neural network.

#### 5.3.1.1 ANN Implementation

The Levenberg-Marquardt (LM) algorithm is one of the most efficient training algorithms for small and medium-sized patterns for our problem setup, which only has five parameters in the input space and requires a regression model. The following are the steps needed to use MATLAB's ANN toolbox:

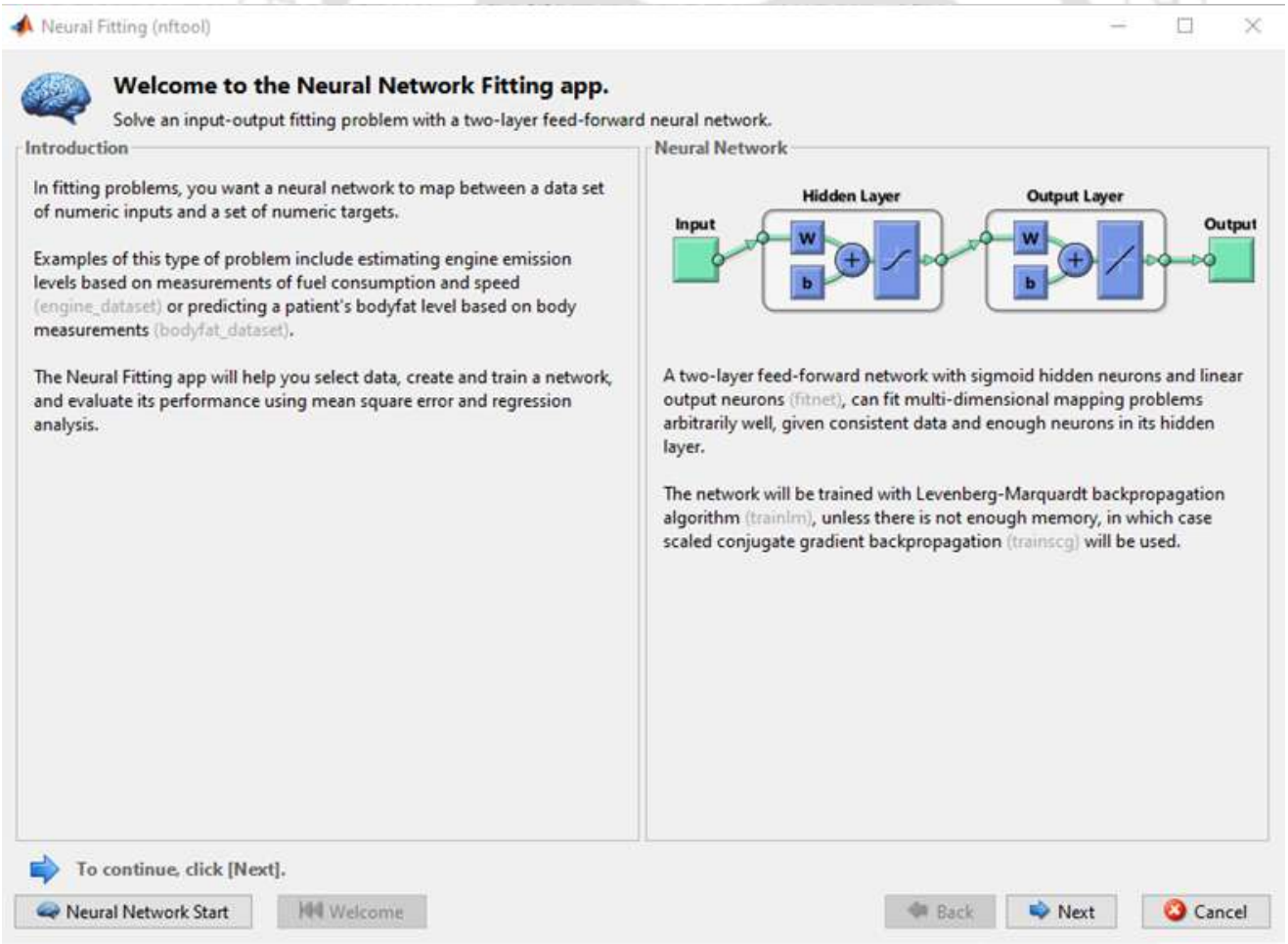


**Figure 5.9:** Matlab's Neural Fitting: Main Window.

**Step 1.** In the command window save the input data in one variable and output data in another variable. Then, Open the Neural Network Start GUI by clicking Apps > Neural Network Fitting or by using 'nnstart' command and then clicking Fitting app.

**Step 2.** From the nftool window that appears click Next as shown in Figure 5.9 below:

**Step 3.** In the Select Data window that appears, select input and output data using inputs and targets drop-down menu by choosing the variable where you stored this information in Step 1. Select 'Matrix rows' to store each sample point as a row element as shown in Figure 5.10.

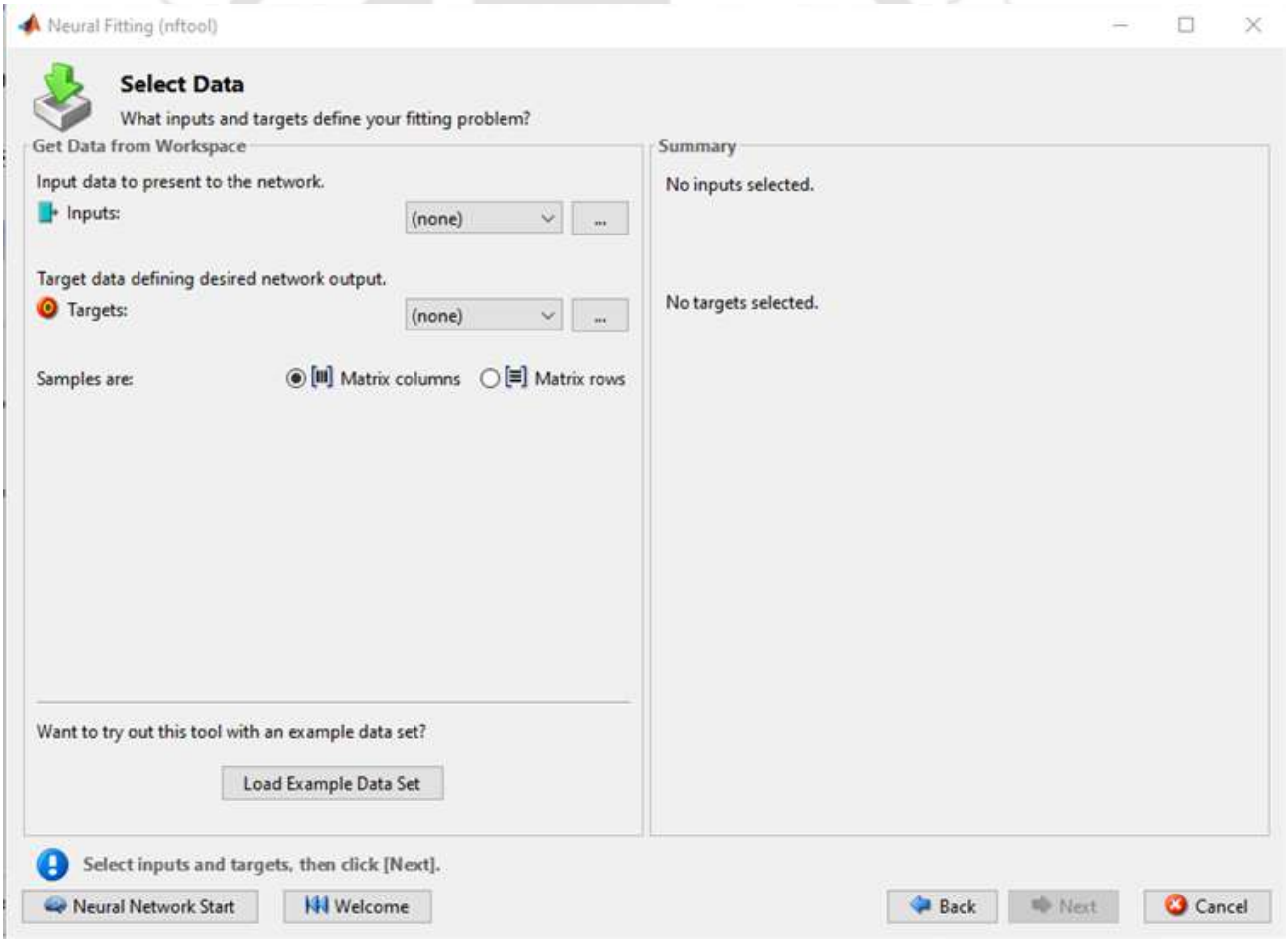


**Figure 5.10:** Matlab's Neural Fitting: Select Data Window.

**Step 4.** Click Next and then the validation and test data window appear, as shown in Figure 5.11 in the following figure. The validation and test data sets are each set to 10% of the

original data and the remaining is training data.

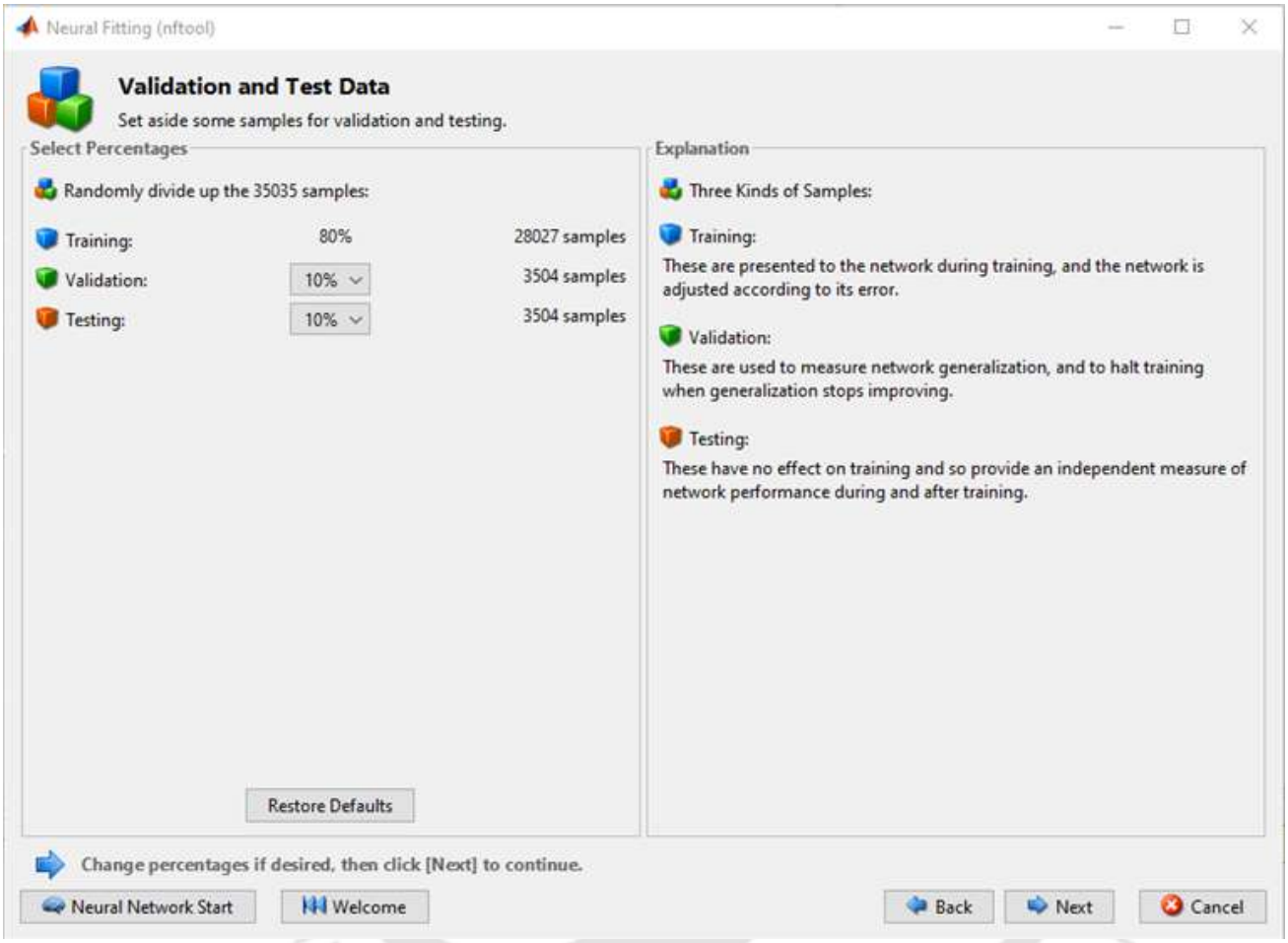


**Figure 5.11:** Matlab's Neural Fitting: Validation and Test Data Window.

**Step 5.** Click on Next and select the number of hidden neurons. For this work, we have chosen 10 numbers of a hidden neuron. To choose the number of nodes in the hidden layer, we monitored the R- values between the estimated output and actual output in the training, testing, and validation data. The details about the 'R-value' are mentioned in the subsequent paragraphs. The multilayer perceptrons (MLPs) consists of three layers: an input layer, an output layer, and a hidden layer, as shown in Figure 5.12.

**Step 6.** Click on Next and select the Levenberg-Marquardt training algorithm in the Train Network Window that appears and then select train as shown in Figure 5.13.

**Step 7.** Then a validation window as shown in Figure 5.14 appears until the training gets

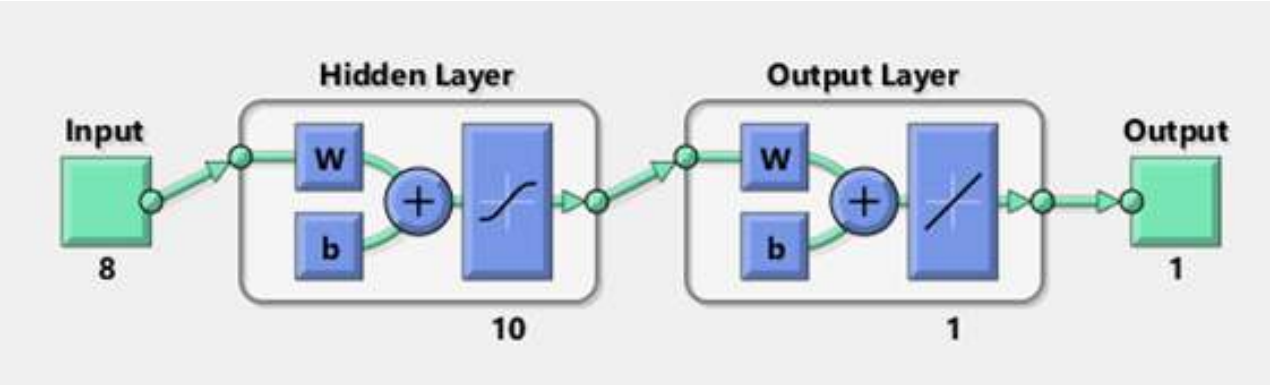


**Figure 5.12:** ANN Architecture based on MLP.

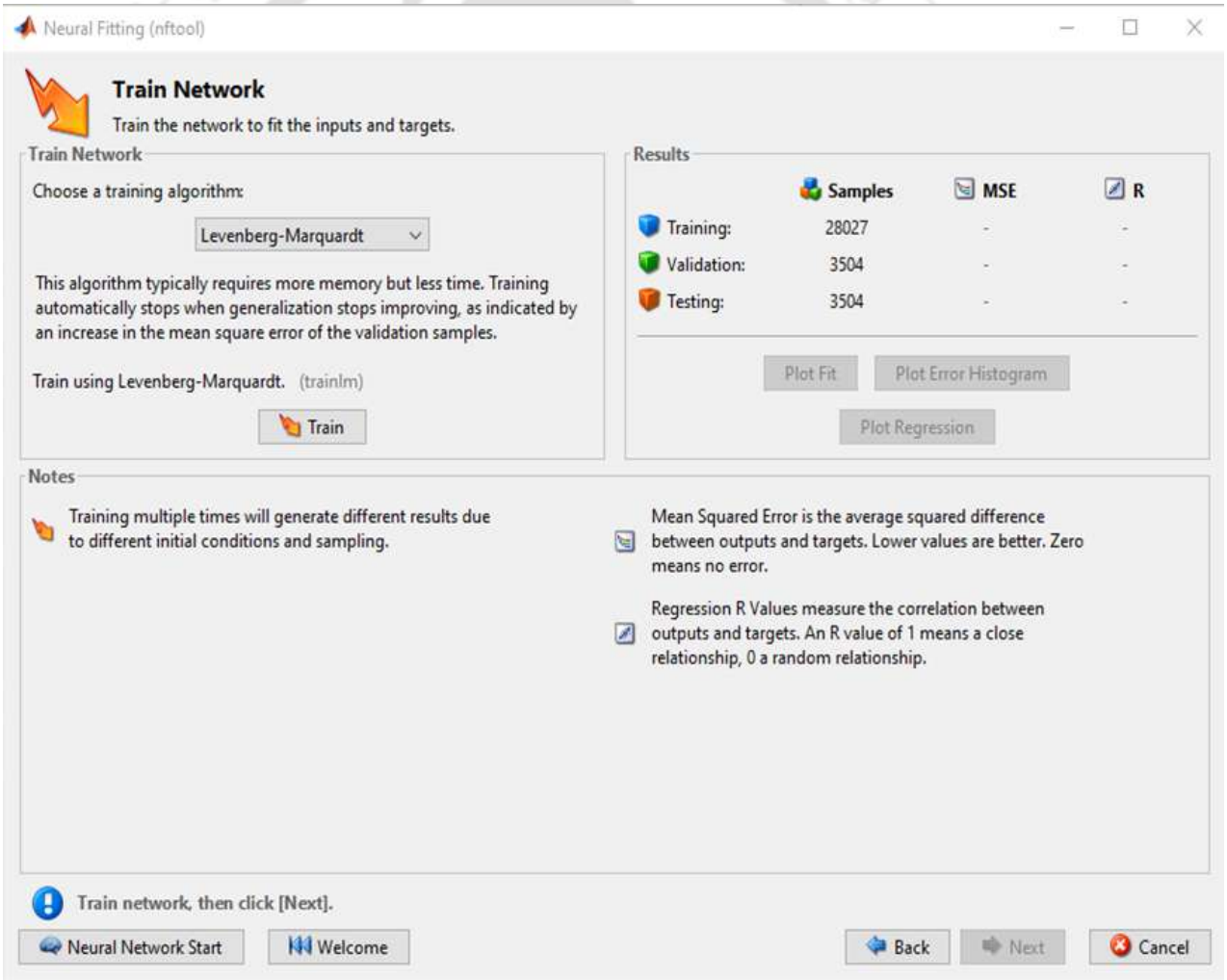


**Figure 5.13:** Matlab's Neural Fitting: Train Network Window.

complete. In this window, details about the ANN model can be observed, like epochs, time taken to train, gradient descent while the data is being modeled, number of validation checks

and iterations made, etc. The plots related to the model fit can be checked from this window, where we mostly check the error histogram and regression values.


**Figure 5.14:** Matlab's Neural Fitting: Validation Window.

**Step 8.** In this window under plots, click 'Regression'. Then, a network fit window as

shown in Figure 5.15 appears. This is used to validate the network performance. The details related to these plots are explained later in this section.

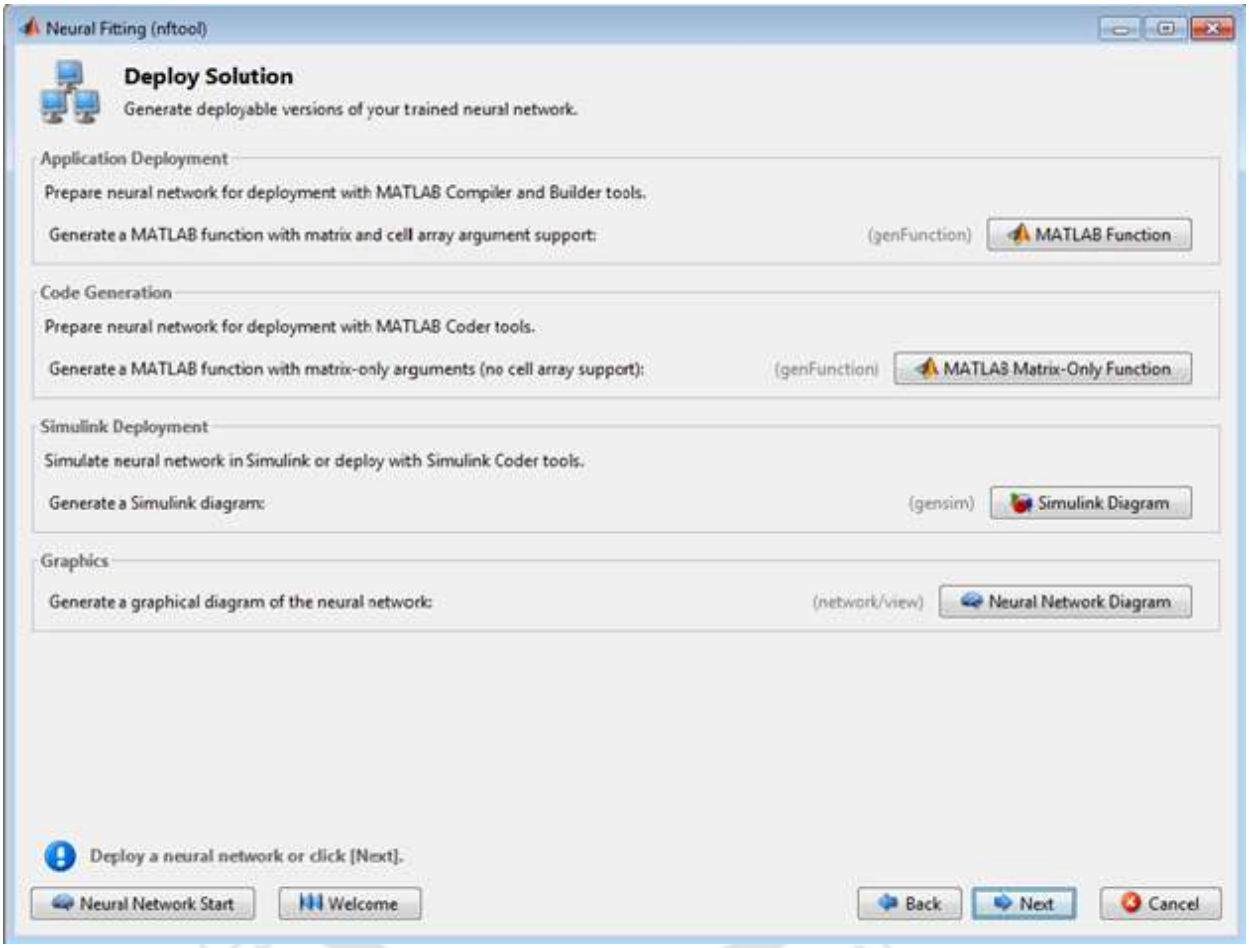


**Figure 5.15:** Matlab's Neural Fitting: Validation Window.

**Step 9.** Click Next in the Neural Network Fitting App and then the 'Deploy Solution Window' appears. To evaluate the network by selecting Matlab Matrix-Only Function and saving it as a Matlab function file.

In our analysis, the data collected from the .slp file is divided into three parts: 80% of the data is used for training, and 10% each used for testing and validation, respectively. The input layer consists of 8 design parameters, a hidden layer of 10 hidden nodes, and one node makes up the output layer. We choose the R-values between the estimated output and actual output in the training, testing, and validation data to determine the hidden layer's number of nodes.

The term "R-value" in this context refers to the coefficient of correlation, which is essentially a statistical measure that describes how strongly two variables are related [101] [102]. This statistic is also known as the Pearson product moment correlation coefficient in honor of its creator Karl Pearson, as noted in [102]. The following mathematical method can be used to determine the R-value between two variables, $y_1$ and $y_2$:

$$r = \frac{n\sum y_1 y_2 - (\sum y_1)(\sum y_2)}{\sqrt{n(\sum y_1^2) - (\sum y_1)^2}\sqrt{n(\sum y_2^2) - (\sum y_2)^2}} \tag{5.22}$$

Where, n is the number of pairs of data.

By varying the number of hidden nodes from 2 to 15, we can check the R-value for training, testing, and validation based on the whole data set. The model with 10 hidden nodes has the highest R-value without being overfitting for the training, testing, and validation sets. Figure 5.16 Training, Testing and Validation, the outcomes of using 10 hidden nodes for this ANN model are shown in plots of ANN fit. These are the regression graphs that show the network output as estimated by the ANN in relation to the output values found in the training, validation, and test sets (target output). For fitting to be considered as a nearly perfect fit, the data should align along a nearly 45° degree line, which is an indicator that the network outputs are approximately equal to the targets. As can be observed from Figure 5.16, the fit is reasonably good for all data sets, as the R values in each case of 0.982 or above. If this fit was not sufficient, we could improve it by re-training the network by clicking 'Retrain' in the neural network toolbox. The horizontal axis in Figure 5.16 represents the true output value, while the vertical axis in each plot represents the output projected using the fitted-ANN model. The four plots in this figure, which may be seen clockwise starting at the top-left, correspond to the training data, validation data, all combined data, and testing data, respectively. If the fit line in each of these plots aligns closely to 45° line, the more accurate are the predictions for the corresponding data. Each plot's associated R-value for the training, validation, combined, and testing sets of data is also noted at the top. The fact that these numbers are so near to 1 further shows how well the ANN fitting in this work worked.

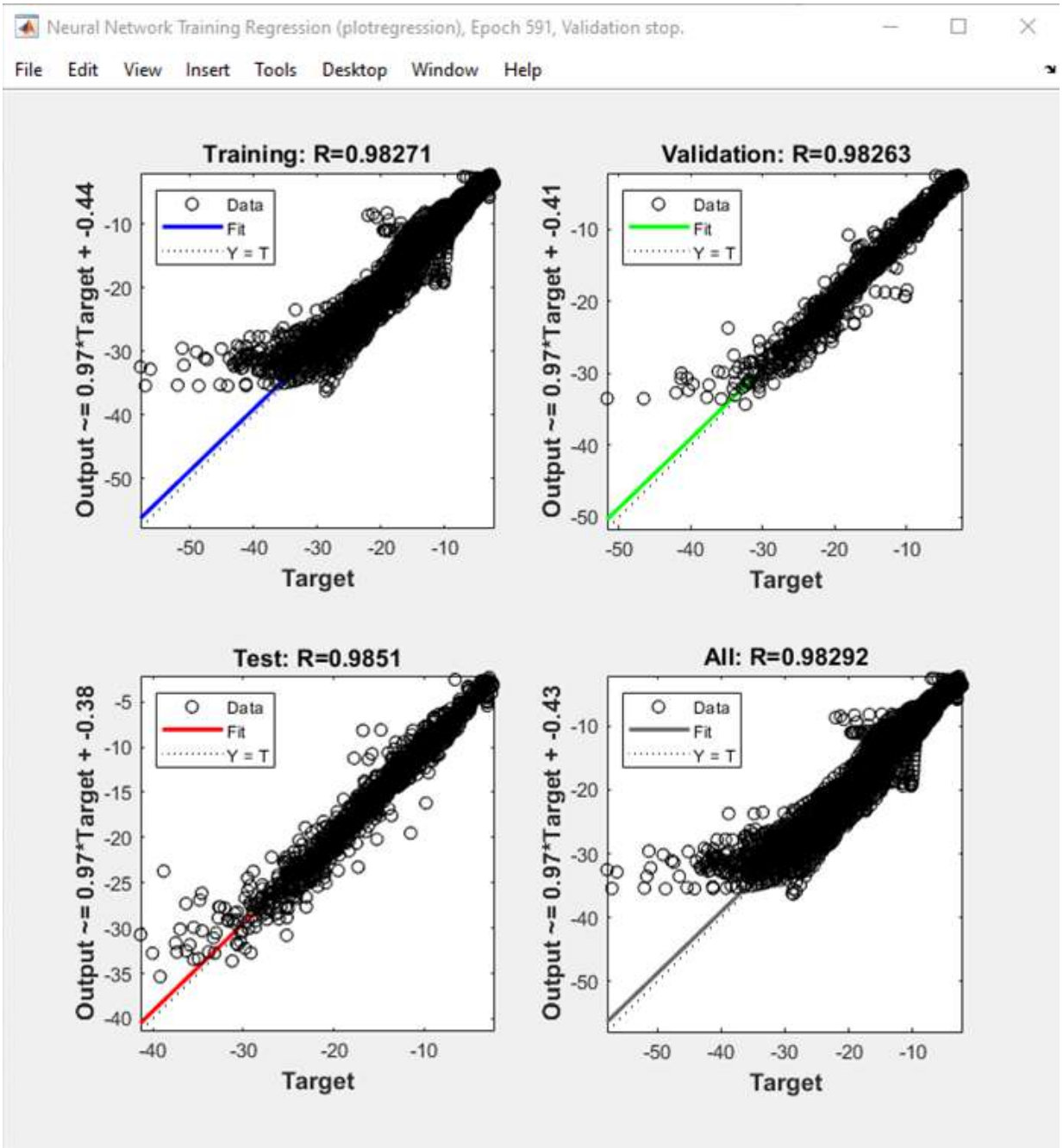


**Figure 5.16:** Training, Testing and Validation Plots of ANN fit.

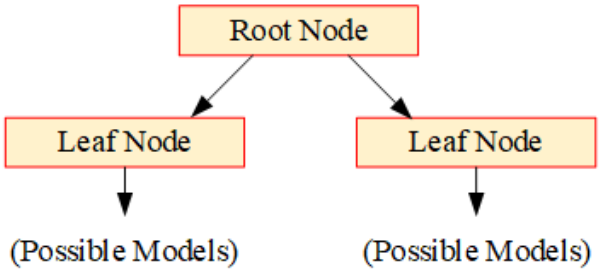


**Figure 5.17:** Perspective of decision tree regression.

### 5.3.2 Decision Tree Regression (DTR)

The decision tree is a regression or classification model built in the form of a tree and is also known as a predictive model [95]. In a decision tree, for predicting the class of the given dataset, the algorithm starts from the root node of the tree. This algorithm compares the values of the root attribute with the record (real dataset) attribute and, based on the comparison, follows the branch and jumps to the next node. It is a stepwise method that optimizes the parameter values in the model and then minimizes/corrects them in the following step as shown in Figure 5.17 [96]. From the figure, it is shown that the several decision trees combine and produce a better accurate model. The aim is to achieve approximation predictions that deviate from the original target and the accuracy can be expressed as a function of the mean square error (MSE) function:

$$MSE = \frac{1}{N}\sum_{i=1}^{N}\left(Y_i - \hat{Y}_i\right)^2 \tag{5.23}$$

where $Y$ is the actual value, $\hat{Y}$ is the prediction value and $N$ number of data samples.

### 5.3.3 Decision Forest Regression (DFR)

The regression model consists of an ensemble method that builds multiple decision trees and integrates their predicted models to obtain a more accurate and stable model rather than depend on an individual tree [97], [98]. Each tree in the forest learns randomly from the samples of the training data as shown in Figure 5.18. In this method, a novel training data of $\dot{x}_i$, $\dot{y}_i$ $_{i=1}^{n}$ are randomly generated from the original training data sample of $x_i$, $y_i$ $_{i=1}^{n}$, and have the same number of samples known as bootstrapping. In bagging, a predefined number set to $|p|$

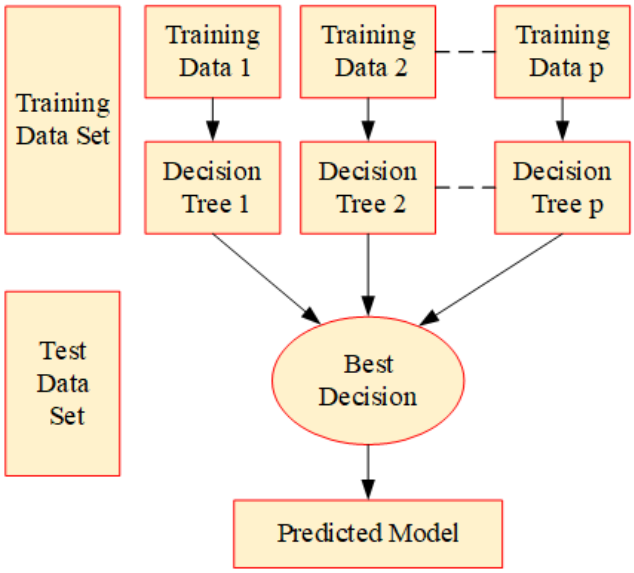


**Figure 5.18:** Perspective of decision forest regression.

of bootstrap samples $\dot{x}_i$, $\dot{y}_i\ {}_{i=1}^{p}$ is generated according to [99], which indicates that 63.2 % of the bootstrap reserved sample. Hence, a decision tree algorithm is applied to each bootstrap sample of $\dot{x}_i$, $\dot{y}_i\ {}_{i=1}^{p}$ to generate $|p|$ number of trees for the forest regression [100].

### 5.3.4 Results and Discussions for MLR

The comparison of $S_{11}$ and AR performance of the proposed antenna obtained from EM simulation, measurement, and MLR prediction models such as ANN, DTR, and DFR regression for port 1 is shown in Figure 5.19 and 5.20 respectively. It is observed from the figures that the design accuracy parameters performance of the DTR and DFR are better than ANN and the same are depicted in Table 5.2. Similarly, the $S_{11}$ and AR regression performance of the proposed antenna obtained using ANN, DTR, and DFR regression models for port 1 is shown in Figure 5.21 and 5.22 respectively. It is observed from Figure 5.21 and 5.22, that the fit is reasonably good for all data sets, as the $R^2$ values in the DTR and DFR 0.99 or above. In each plot of Figure 5.21 and 5.22, the output predicted by using the fitted ANN, DTR, and DFR model has represented by the vertical axis and the true output value (simulation) is represented by the horizontal axis. From this figure, the fit line in each of these plots aligns closely with the linear regression line and the more accurate predictions for data obtained using DTR and

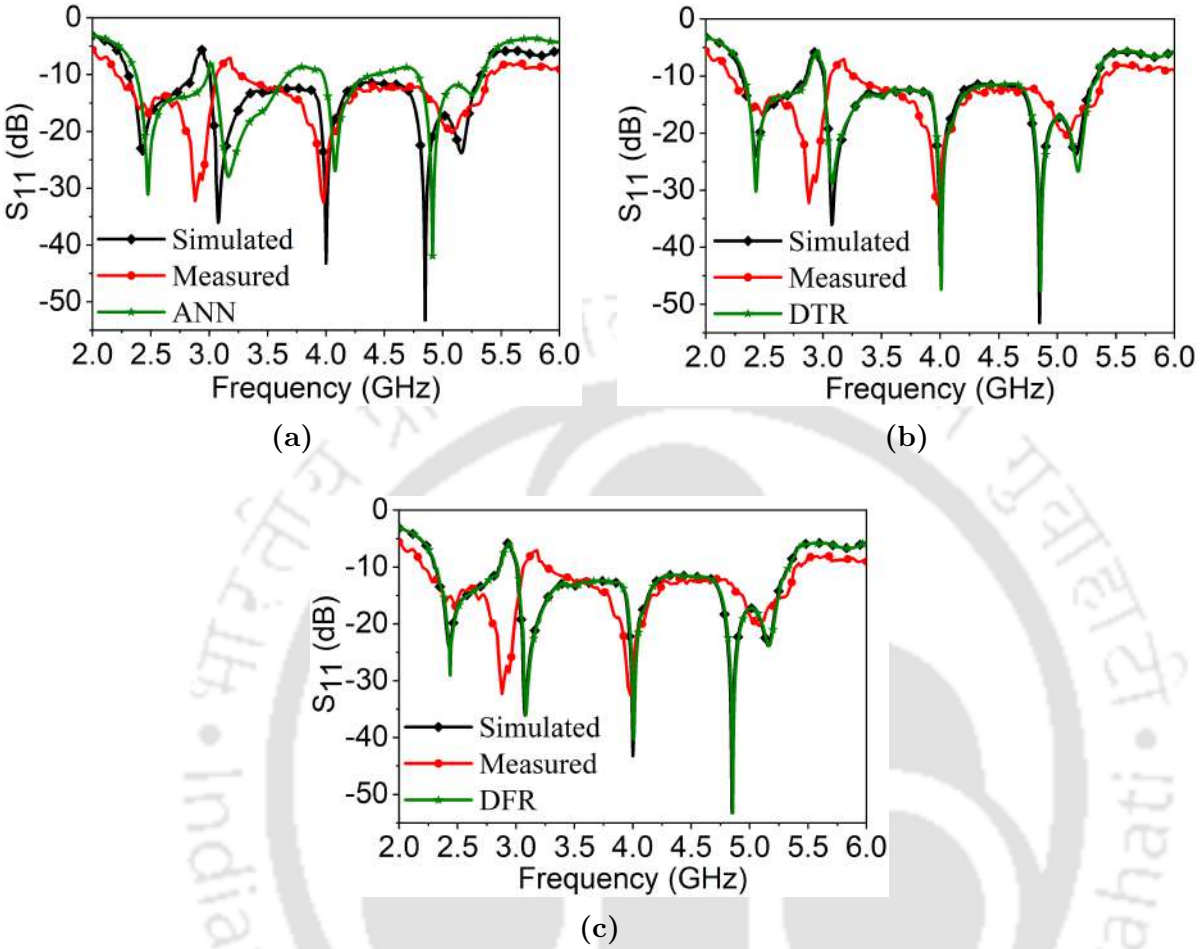


**Figure 5.19:** Comparison of $S_{11}$ of simulation, measurement and (a) ANN, (b) DTR, and (c) DFR for port 1.

DFR models. Hence, the regression models DTR and DFR predicted nearly the same IBW and ARBW realized from the EM simulation results compared to the ANN model.

**Table 5.2:** Accuracy comparison between regression models

| Regression model | MSE | RMSE | RAE | RSE |
|---|---|---|---|---|
| Artificial neural networks (ANN) | 1.892 | 3.017 | 0.922 | 1.026 |
| Decision tree regression (DTR) | 0.036 | 0.487 | 0.022 | 0.026 |
| Decision forest regression (DFR) | 0.049 | 0.237 | 0.029 | 0.069 |

MSE: Mean squared error. RMSE: root mean squared error. RAE: relative absolute error. RSE: relative squared error.

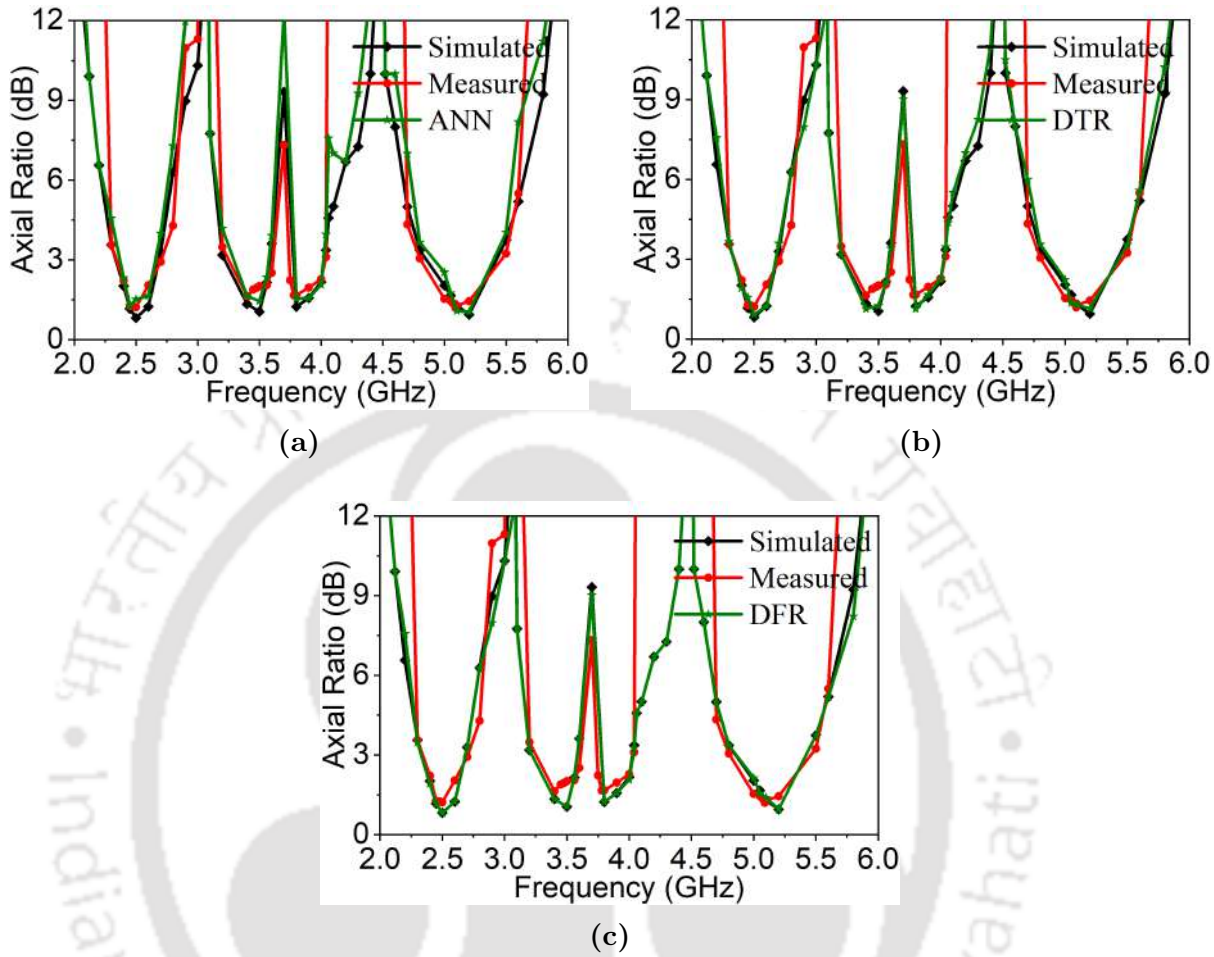


**Figure 5.20:** Comparison of AR of simulation, measurement and (a) ANN, (b) DTR, and (c) DFR for port 1.

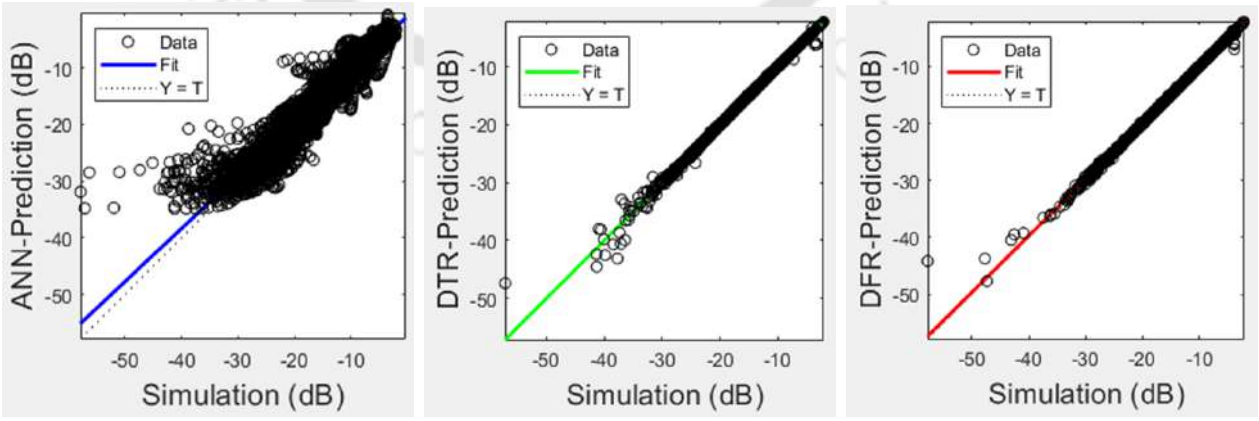


**Figure 5.21:** Regression performance of $S_{11}$ (a) ANN, (b) DTR, and (c) DFR for port 1.

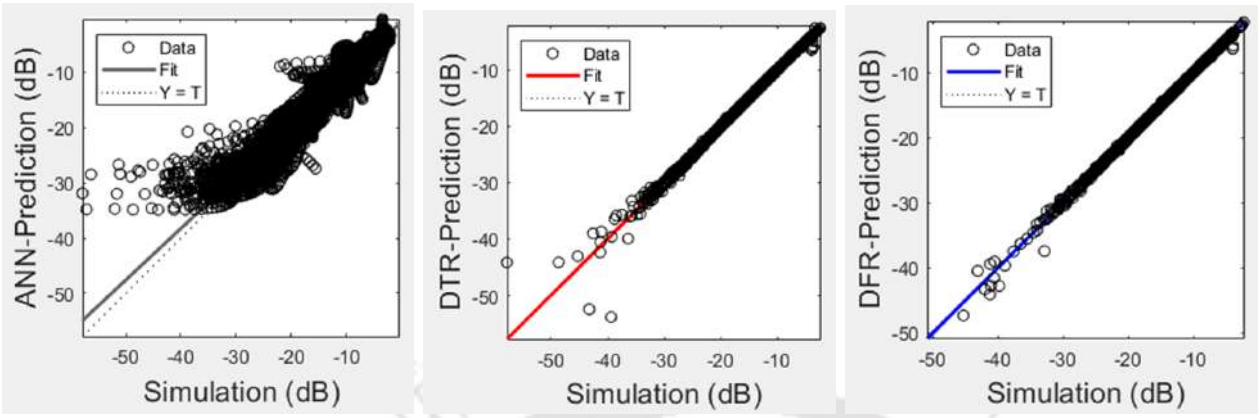


**(a)** **(b)** **(c)**

**Figure 5.22:** Regression performance of AR (a) ANN, (b) DTR, and (c) DFR for port 1.

## 5.4 Simulated and Measured Results

To verify the design concept, the proposed antenna in Figure 5.1 is fabricated and tested. The measurement set-up inside the anechoic chamber, the top and bottom view of the fabricated prototype dual-CP TWSCSMA antenna are shown in Figure 5.23(a), 5.23(b), and 5.23(c), respectively. The $S_{11}$, AR, radiation patterns, peak gain, and efficiency are measured with an Anritsu-MS-46122B vector network analyzer (VNA) in the anechoic chamber of size: $6 \times 4 \times 6$ $m^3$.

### 5.4.1 Reflection Coefficient Performance

The simulated and measured $S_{11}$ results are depicted in Figure 5.24. The measured two IBW of 33.85% (2.185–3.075 GHz) and 50.73% (3.252–5.462 GHz), $S_{11} \leq -10$ dB have achieved for both the ports. The measured $S_{11}$ results show that the first and second impedance bandwidth is shifted a little to higher frequencies than the simulated results. It is maybe due to the alignment imperfection between various PCB layers, fabrication tolerances and SMA connector. Since the proposed antenna is symmetric in shape, the $S_{11}$ performance is maintained within the permissible range for the feeding of ports 1 or 2.

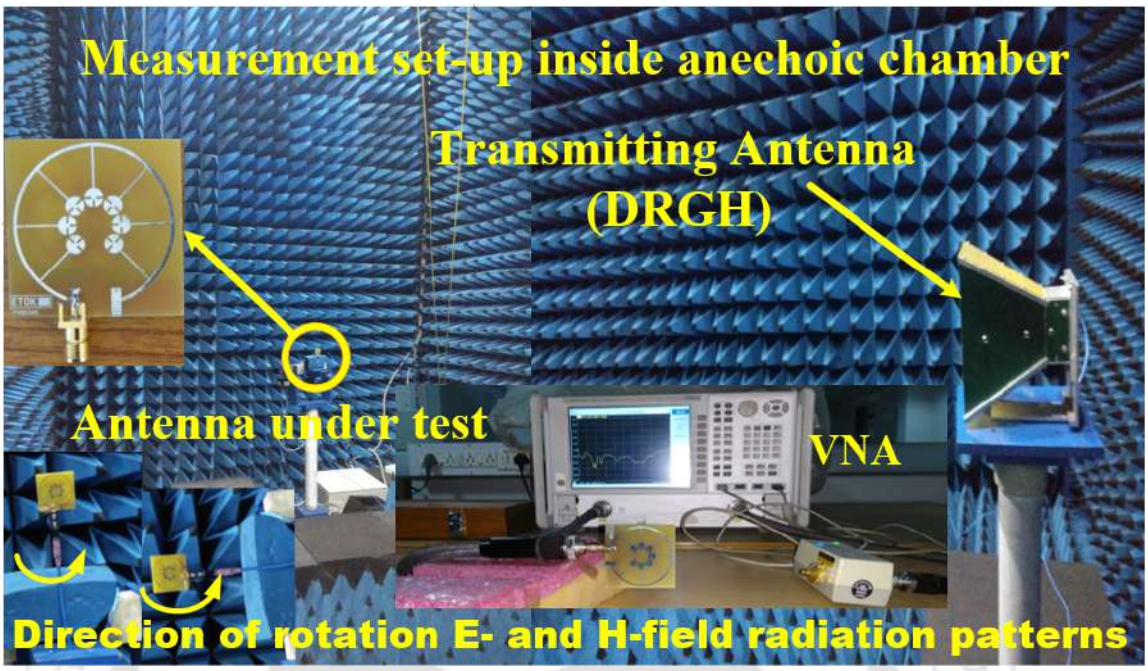


(a)

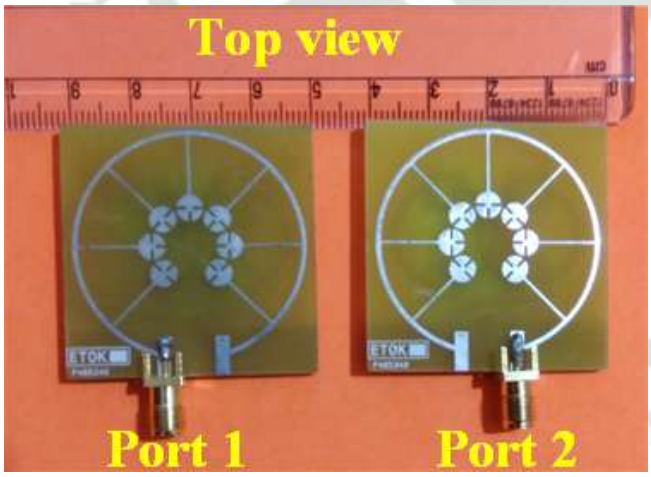


(b)

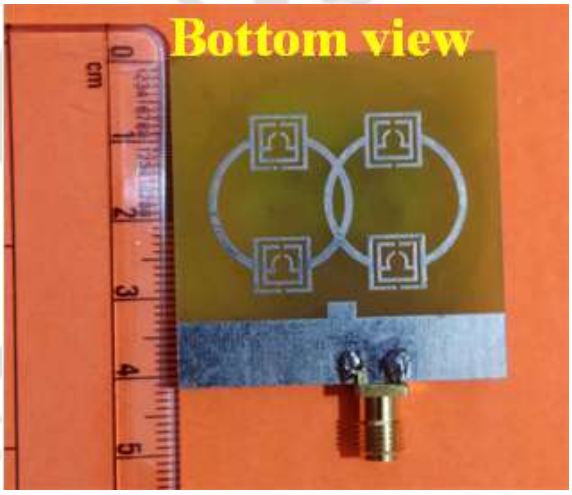


(c)

**Figure 5.23:** (a) Measurement set-up inside anechoic chamber, (b) prototype top, and (c) bottom view.

### 5.4.2 Axial Ratio Performance

Figure 5.25 shows the simulated and measured AR of the dual-CP TWSCSMA antenna with ports 1 and 2. The results indicate that the designed antenna can maintain $< 3$ dB AR

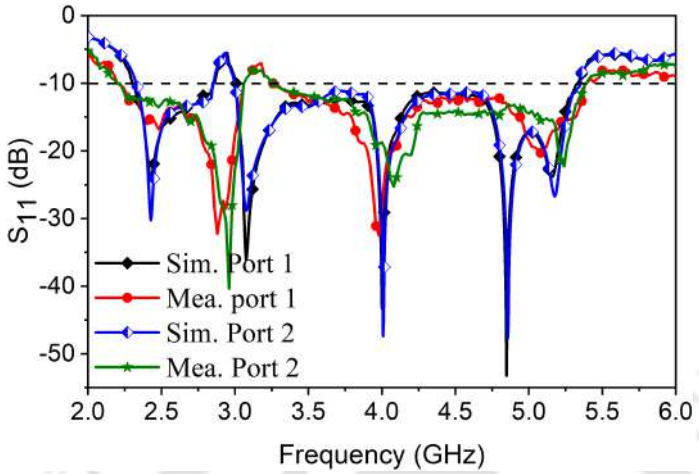


**Figure 5.24:** Measured and simulated $S_{11}$ of the dual-CP TWSCSMA antenna.

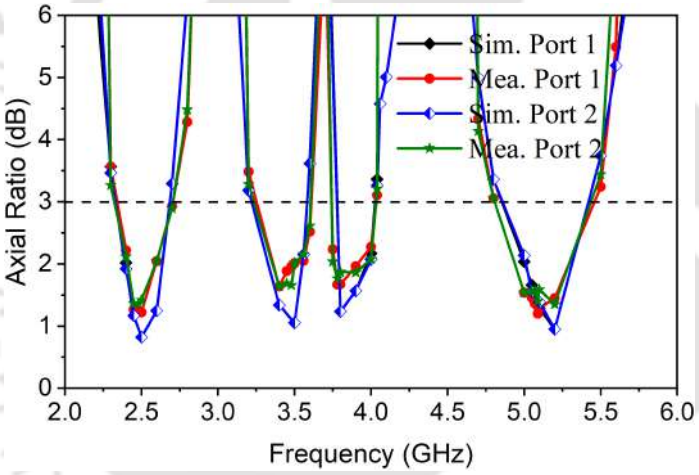


**Figure 5.25:** Measured and simulated AR of the dual-CP TWSCSMA antenna.

over a wide beamwidth of about $32^o$. It is seen from the figure that the measured AR for four CP bands such as 2.321–2.733 GHz (16.26%), 3.222–3.652 GHz (12.52%), 3.732–4.052 GHz (8.22%), 4.751–5.455 GHz (13.82%) at 2.5, 3.5, 3.8, and 5.2 GHz are less than 1.2 dB. Thus, measured AR characteristics validate and ensure the polarization quality of traveling-wave series-fed arrays.

### 5.4.3 Radiation Patterns Performance

Since the radiation patterns of the antenna excited either from port 1 or port 2 are similar, the measured and simulated radiation patterns for $\phi = 0°$ and $\phi = 90°$ planes at 2.5, 3.5,

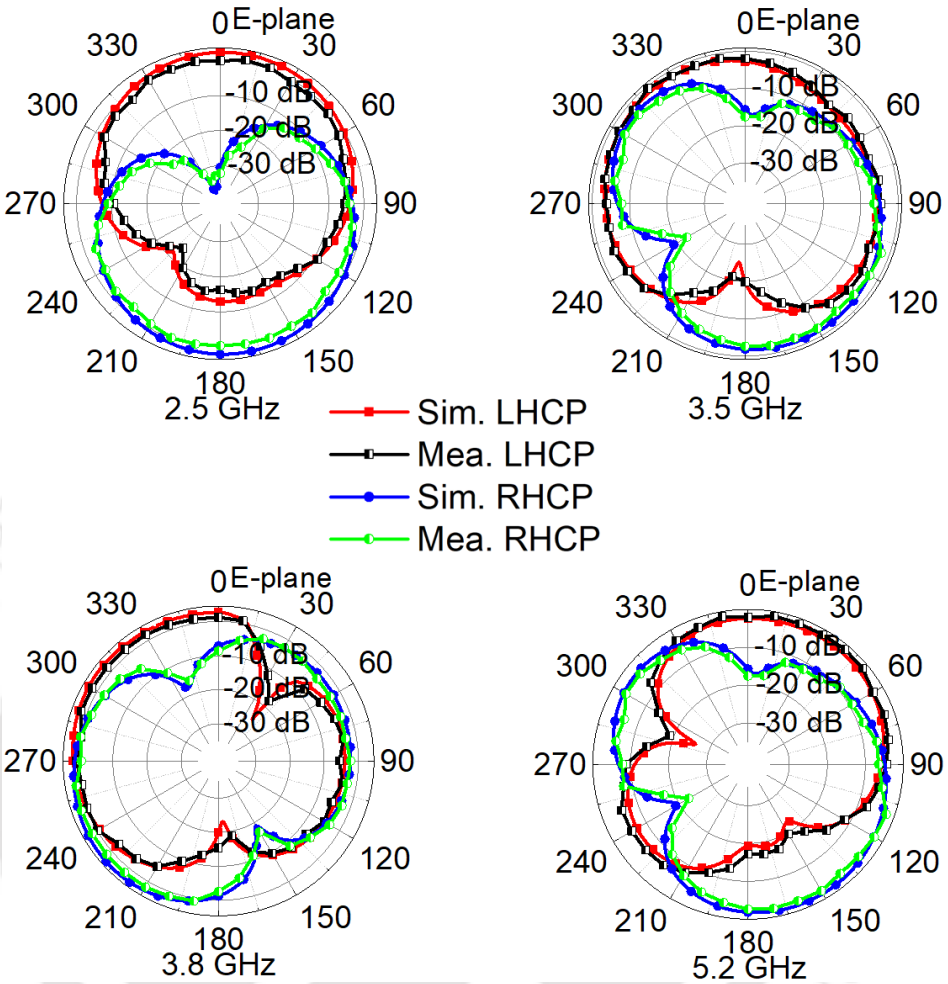


**Figure 5.26:** Radiation patterns at 2.5, 3.5, 3.8 and 5.2 GHz of E-plane for port 1.

3.8, and 5.2 GHz when only port 1 is excited is shown in Figure 5.26 and 5.27, respectively. The asymmetrical antenna structure around a central axis at the feeding position (for port 1) contributes to the tilting of the radiation patterns for different frequency bands. The radiation patterns are not symmetrical at these four frequencies, however, tilting is more prominent at 3.5 and 3.8 GHz. In both planes i.e., E- and H-plane, the radiation patterns are symmetrical and LHCP is stronger than RHCP by approximately 26, 14, 13, and 18 dB for 2.5, 3.5, 3.8, and 5.2 GHz respectively, in the boresight direction. The difference in the LHCP and RHCP patterns results between the simulation and experiment may be due to the detector sensitivity. This confirms the satisfactory quad-band CP performance.

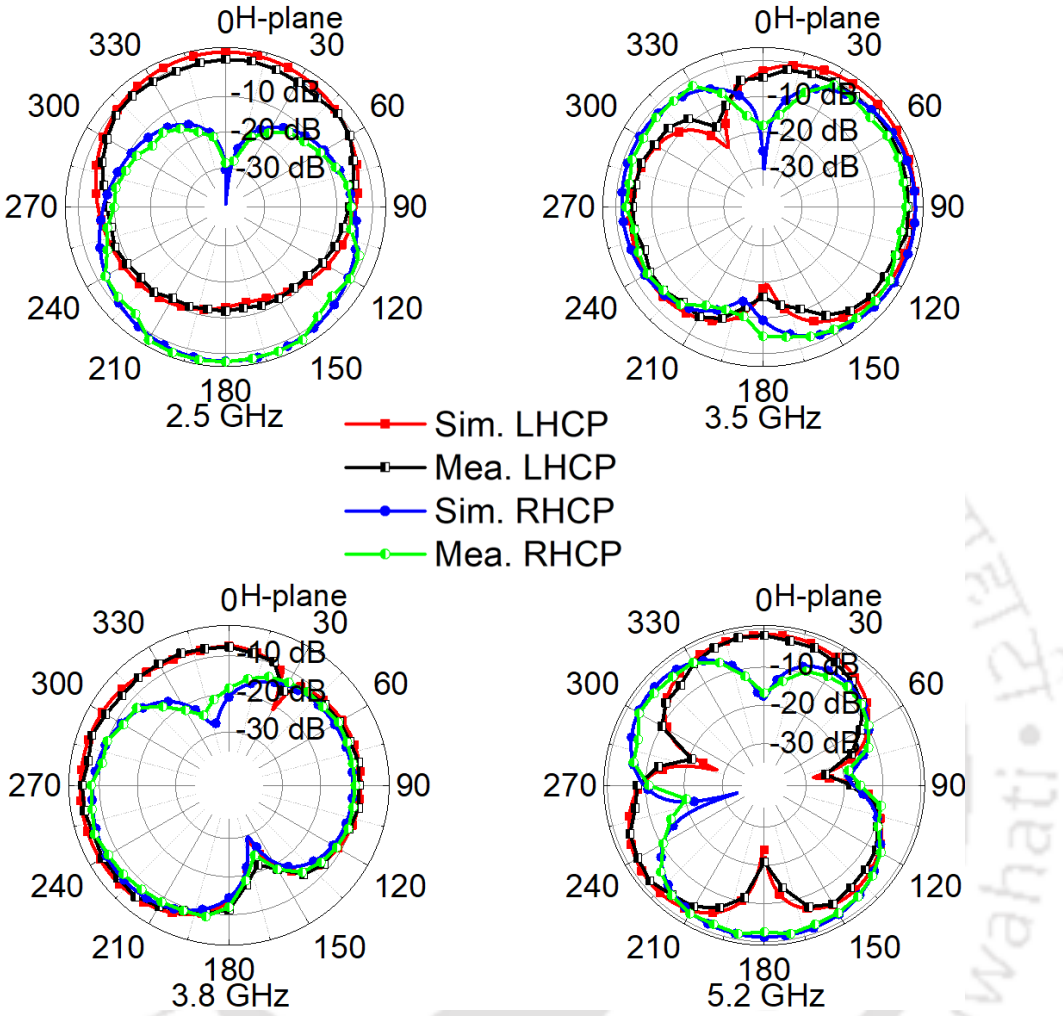


**Figure 5.27:** Radiation patterns at 2.5, 3.5, 3.8 and 5.2 GHz of H-plane for port 1..

### 5.4.4 Gain and Efficiency Performance

Figure 5.28(a) shows the measured and simulated peak gain of the proposed antenna for LHCP (port 2 terminated) and RHCP (port 1 terminated) radiation. It is observed from the figure that the peak gain of the proposed antenna for both LHCP and RHCP are more or less the same. The maximum measured peak gains are 2.51, 4.72, 4.52, and 2.86 dBic at 2.5, 3.5, 3.8, and 5.2 GHz, respectively. The measured peak gain is maintained between 2.51 and 4.72 dBic within the operational bandwidth.

For radiation efficiency measurement, first the gain $G(\theta, \phi)$, radiation intensity, and reflection coefficient $\Gamma$ of the designed antenna are measured. The directivity $D(\theta, \phi)$ is computed

**Table 5.3:** Comparison of multiband CP antennas

| Ref. | Feeding | Dimension ($mm^3$) | Frequency (GHz) | IBW (%) | ARBW (%) | Peak gain (dBic) |
|---|---|---|---|---|---|---|
| [70] | ML | $100 \times 100 \times 1.6$ | 1.19-1.23, 1.56-1.58 | 3.7, 1.2 | 0.9, 0.6 | 1.1, 1.45 |
| [71] | ML | $70 \times 70 \times 1.6$ | 2.84-3.24, 4.24-4.92 | 12.9, 8.5 | 3.1, 4.2 | 7.3, 8.5 |
| [72] | ML | $115 \times 115 \times 1.524$ | 1.103-1.297, 1.444-1.636 | 16, 12.5 | 6.9, 0.6 | 2, 1.34 |
| [73] | CP | $80.8 \times 80.8 \times 1.52$ | 1.12-1.69 | 40.57 | 6.56, 7.74 | 7.72, 8.11 |
| [74] | MLPDN | $110 \times 110 \times 0.8$ | 5.0-6.2, 7.2-8.9 | 21, 21.2 | 13.2, 12.8 | 14.5, 17.5 |
| [75] | ML | $94.35 \times 94.35 \times 0.8$ | 2.36-2.48, 3.34-3.41, 4.03-4.43 | 5, 2, 9.5 | 0.53,0.66, 0.83 | 7.5, 8.7, 8.7 |
| [76] | CP | $80 \times 80 \times 1.6$ | 1.16-1.18, 1.21-1.23, 1.56-1.59 | 2, 1.5, 2 | 3.4, 0.81, 0.83 | 5.6,5.6, 6.3 |
| [77] | ML | $60 \times 60 \times 1.52$ | 3.22-4.5, 4.76-5.98 | 33.16, 22.72 | 1.7, 3.86, 5.23 | 5.5,4.63, 6.77 |
| [78] | ML | $50 \times 50 \times 1.56$ | 1.48-1.87, 2.39-2.71, 3.02-3.16 | 21.4, 12.8, 4.5 | 4.37, 10.9, 3.57 | 2.7,4.2, 3.5 |
| [79] | ML | $133.2 \times 133.2 \times 1.52$ | 2.37-2.75, 3.4-8 | 14.84, 80.70 | 5.4, 8.3, 3.7, 2.9 | 5.95, 6.92, 6.37, 6.07 |
| Work | ML | $41 \times 41 \times 2.0$ | 2.18-3.07, 3.25-5.46 | 33.85, 50.73 | 16.26, 12.52, 8.22, 13.82 | 2.51, 4.62, 4.32, 2.76 |

IBW: Impedance bandwidth. ARBW: axial ratio bandwidth. ML: microstrip line. CP: coaxial probe. MLPDN: microstrip line with power divider network.

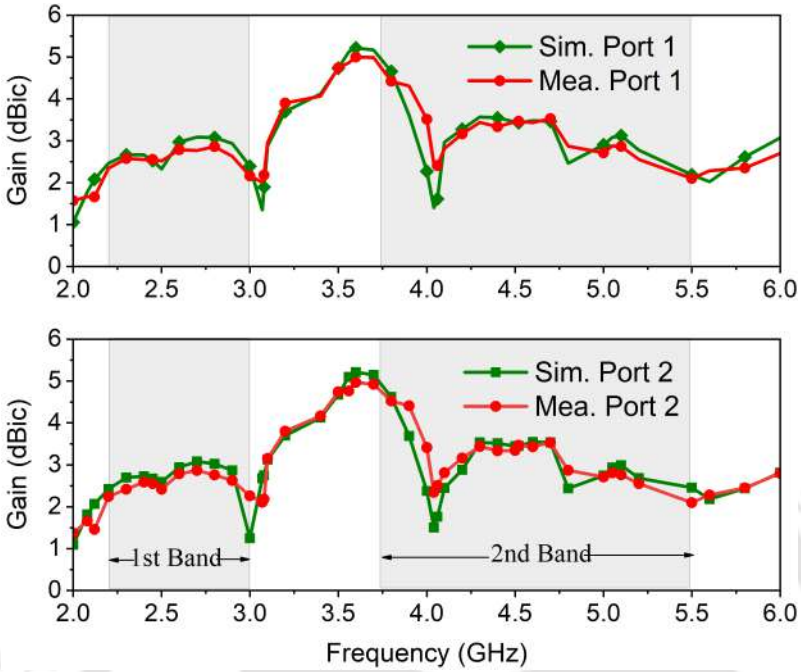


(a)

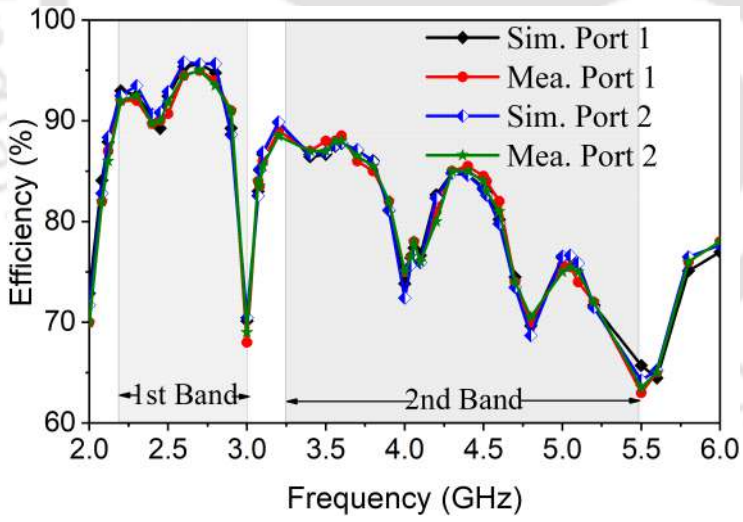


(b)

**Figure 5.28:** Measured and simulated the dual-CP TWSCSMA antenna (a) peak gain and (b) efficiency.

automatically using the radiation intensity. Using this above parameters, the antenna efficiency ($\eta$) is computed using the equation given below:

$$\eta = \frac{G(\theta, \phi)}{D(\theta, \phi)}(1 - \mid \Gamma \mid^2) \tag{5.24}$$

The measured and simulated radiation efficiency performance is shown in Figure 5.28(b). The measured efficiency from 2.2 to 5.5 GHz are about 65%–95% within the operational band and there is a small deviation in the measurement result from the simulation result due to the fabrication tolerance.

The comparison between the proposed work (TWSCSMA antenna) with other reported multi-band CP antennas are listed in Table 5.3. It is observed that multi-band CP antennas in [70]–[79] occupy 4.75, 2.33, 5.99, 2.95, 2.87, 2.11, 3.04, 1.62, 1.18, and 8.02 times more volume than the TWSCSMA antenna respectively. Hence, the proposed structure gives a compact size among the others. Moreover, the TWSCSMA antenna has a better wide IBW and ARBW. Therefore, considering the performance of the proposed antenna, it will be a good candidate for WiMAX and WLAN applications.

## 5.5 Summary of the Chapter

In this chapter, a compact dual-CP TWSCSMA antenna for the WiMAX and WLAN is proposed. The antenna supports a quad-band CP operation with better performance at 2.5/3.5/3.8/5.2 GHz frequency bands. The quad-band operation is obtained using seven series-fed circular slit array elements in an annular ring on the radiator. The two $\leq -10$ dB IBW of 33.85% and 50.73%, four CP bands $< 3$ dB ARBW of 16.26%, 12.52%, 8.22%, and 13.82% for port 1, and reduction in mutual coupling between the circular slit array elements are achieved by introducing SRR unit cells with double-annular rings on the defected ground plane to neutralize unwanted surface coupling waves on the radiator. MLR technique is used to predict the optimal values with accuracy model performance requirements of the design parameters of the proposed antenna for EM simulation samples which will provide the best performance in terms of IBW and ARBW. By analyzing the results of the simulation and experiments, it is observed that the proposed antenna shows a compact size, the better two IBW and four-CP bands than other multi-band CP antennas proposed in the literature. In the next chapter, a study is carried out to further enhance the impedance as well as axial ratio bandwidth of the proposed monopole CP antenna with extended ground loop plane and compact structure.

*Note: This work, "Compact Quad-Band CP Series-Fed Circular Slit Microstrip Array Antenna Using Machine Learning" has been published in IEEE Access.*

# 6

# Compact UWB CP Inverted L-Shaped-Hook Monopole Antenna with Minimum $BR_{(10/3)dB}$ for Wireless Applications

## Contents

## 6.1 Introduction

In recent years, research on compact antennas with various radiating elements, feeding arrangements, and polarization has drawn attention as a result of the growing need for wireless communication systems. The circular polarization (CP) antenna is currently in high demand for high-speed wireless communication systems because it has advantages such better mobility and flexibility over linearly polarized (LP) antennas [103, 104]. Due to their ability to reduce multipath interference, polarization mismatch, and the Faraday rotation effect [105], CP antennas have received a great deal of interest in the applications like GPS, mobile satellites, radio frequency identification (RFID), and microwave sensing [87, 106–111]. Exciting two orthogonal modes with equal amplitude and in-phase quadrature is the fundamental idea of CP antennas. This can be accomplished by adding some extended DGS antennas that are fed by co-planar waveguides (CPW) and/or symmetric or asymmetric monopole or slotted radiators [112]–[117]. These include an L-shaped monopole patch with inverted L-shaped ground strips [112] to increase the axial ratio bandwidth (ARBW) while reducing the antenna size, two rectangular parasitic elements and an I-shaped grounded stub [113], a rectangular monopole and a square ring with an open gap at the bottom [114], and a printed square slot patch and halberd-shaped metal strip introduced on the ground plane [115].

By using an I-shaped rectangular patch with adding a stub on the ground plane, a maximum of 44.9% and 76.9% of ARBW and IBW are achieved, respectively when individually considered [116]. A monopole radiator with an L-shaped slot on the ground plane achieves ARBW of 33% and IBW of 40% [117]. However, it is discussed how these CPW-fed CP monopole antennas have less than 64% ARBW and less gain. Meeting the demands of modern wideband communication systems is exceedingly challenging.

However, in single-fed patch CP antennas, the working bandwidth is typically limited by their narrow ARBW. By adjusting the size of the dual slits of the microstrip H-shaped patch CP antenna, the overlapping bandwidth of 3.95% between IBW and the ARBW is obtained [104]. When a material with a high dielectric constant is utilized, the narrow bandwidth of

parallel plates is characterized as having a high Q-factor ($Q = f_r \ / \ BW$). The IBW of a LP microstrip antenna defined by a maximum allowable voltage standing wave ratio ($VSWR_{max} \approx 2$), is given [125] as follows:

$$IBW_{LP} = \frac{VSWR_{max} - 1}{\sqrt{VSWR_{max}}Q} \tag{6.1}$$

where $Q$ is the quality factor of the antenna. Evidently, a closed form expression for the IBW of a CP microstrip antenna is not discussed in the literature. This can be verified by using the expressions for the IBW and ARBW, which are expressed as [109] below:

$$IBW_{CP} = \frac{\sqrt{2(VSWR_{max} - 1)}}{Q} \tag{6.2}$$

and

$$ARBW_{CP} = \frac{AR_{max} - 1}{\sqrt{AR_{max}}Q} \tag{6.3}$$

The maximum achievable BR using Eq. (6.2) and (6.3) for a patch CP antenna is expressed as:

$$BR|_{IBW/ARBW} = \frac{IBW}{ARBW} \tag{6.4}$$

where maximum axial ratio ($\text{AR}_{max}$) $= \sqrt{2}$ ($< 3$ dB), $VSWR_{max} \approx 2$ ($\leq -10$ dB), and BR in (6.4) represents as $BR|_{(10/3)dB} \approx 4$. The 3 dB ARBW for CP antennas is around 4 times smaller than the highest attainable -10 dB IBW. The measured value of the bandwidths (IBW and ARBW) of the patch CP antennas reported in [87, 104] is 3.95%. However, when looking at ARBW and IBW independently, they are the highest values that may be achieved. The key to creating a microstrip patch CP antenna with wide overlapping bandwidth is to tailor the frequency of ARBW to be close to the frequency of IBW. A C-shaped monopole with a rectangular vertical stub attached to the ground plane is suggested in [118] as a potential CP radiator. A broad AR bandwidth has been attained in a monopole with a hexagonal form and a slotted patch [119]. Though both the antennas are small in size, the ARBWs are still less than 66%.

Recently, using semicircular patches on the top and bottom sides, a UWB CP antenna with

an ARBW of 89% and IBW of 103% is reported in [120]. In [121] introduces a UWB 2 × 2 array CP antenna, which is a larger size than other UWB CP antennas. The size of this UWB array is 200×200 mm$^2$, while the ARBW of 92.5%, IBW of 132.8%, and $BR|_{10/3} \approx 1.435$. The antennas mentioned above are either thick in profile or large in aperture size, which motivates us to develop a compact UWB CP antenna to some extent as well as improve ARBW and IBW with the minimum AR and $BR|_{(10/3)dB}$ using an asymmetrical inverted L-shaped-hook monopole (ILSHM) antenna.

Therefore, this work is aimed to look into an improved design structure that can replace the antennas proposed in the literature for a couple of advanced features:

(i)A compact CPW-fed monopole radiator with an extended ground loop plane occupying a smaller space and

(ii) improved ARBW and IBW for keeping minimum BR.

In this chapter, the UWB CP monopole antenna comprising of two rectangular slits etched on the monopole radiator which is positioned asymmetrically around a central axis is addressed. A rectangular conductor strip is added with a half-circular patch to design the proposed monopole antenna. The combined radiating structure proposed in this work can produce UWB CP radiation by placing two inverted L-shaped conductor strips along with the ground loop top corners and two pairs of rectangular notches at the ground loop bottom part. The experimental findings support the simulation results that the proposed CPW-fed ILSHM antenna has UWB AR and IBW, higher gain, and radiation pattern stability over a wide operational bandwidth. Additionally, this analysis is able to significantly reduce the $BR|_{(10/3)dB}$ ($\approx 1.121$) level. Considering $BR|_{(10/3)dB} \approx 1$ and a CPW-fed low profile, the proposed antenna has several advantages.

This chapter is divided into the following sections: section 6.2 states the design evolution, enhanced impedance bandwidth and circular polarization generation. Discussed the parametric studies of rectangular slit length and ground width in section 6.3. The reflection coefficient $S_{11}$, axial ratio performance, peak gain, surface current distribution at frequency of 3.5 GHz, and radiation patterns parameters at different frequencies such as 5.5, 9.2, and 18.1 GHz are

presented in section 6.4. The experimental results match quite well with the simulation results, thus validating the practical feasibility of the design. The principal outcomes of this research work are explained in section 6.5.

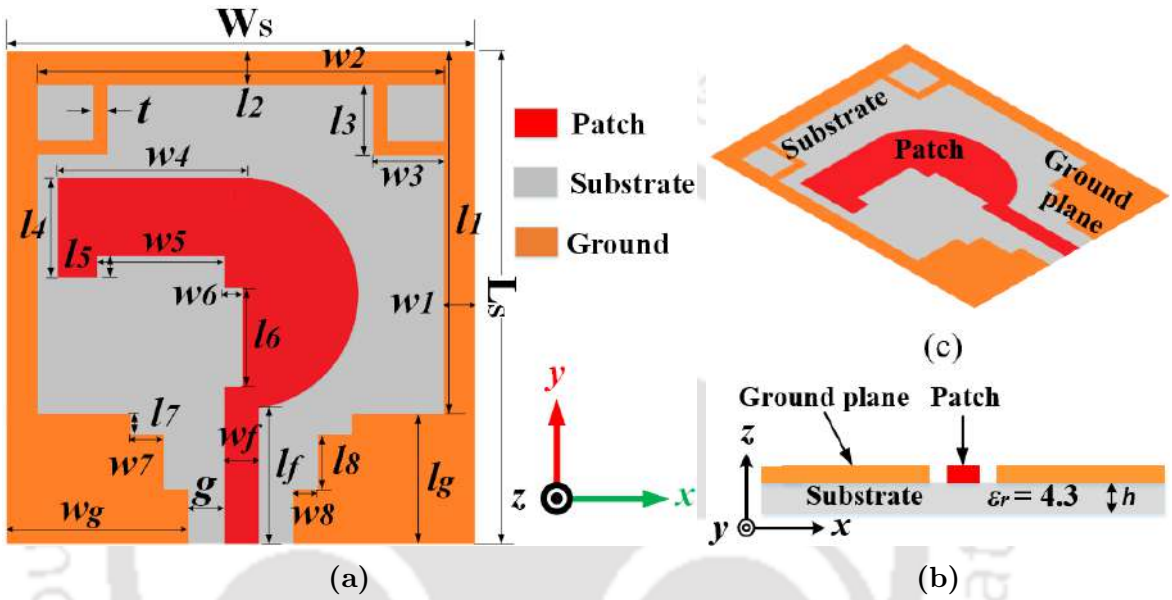


**Figure 6.1:** Geometry of the ILSHM antenna (a) Top view, (b) Side view, and (c) Isometric view.

**Table 6.1:** Value of geometric parameter of the proposed antenna

| Parameters | Value (mm) | Parameters | Value (mm) | Parameters | Value (mm) |
|---|---|---|---|---|---|
| $L_S$ | 34.8 | $t$ | 1.7 | $w_7$ | 2.9 |
| $W_S$ | 32.8 | $l_4$ | 6.5 | $l_8$ | 3.6 |
| $l_1$ | 27.4 | $w_4$ | 10.3 | $w_8$ | 1.1 |
| $w_1$ | 2.4 | $l_5$ | 0.8 | $l_f$ | 6 |
| $l_2$ | 2.4 | $w_5$ | 7 | $w_f$ | 1.9 |
| $w_2$ | 28 | $l_6$ | 5 | $l_g$ | 7.4 |
| $l_3$ | 6.3 | $w_6$ | 1.3 | $w_g$ | 13.2 |
| $w_3$ | 6.7 | $l_7$ | 0.7 | $g$ | 2.25 |

## 6.2 Antenna Design Process

### 6.2.1 Antenna Configuration

Figure 6.1 shows the top view geometry of the proposed UWB ILSHM CP antenna which is printed on a 0.8 mm thickness FR-4 substrate ($\epsilon_r = 4.3$ and $\tan\delta = 0.025$). And DGS is printed on the top of the substrate. The ILSHM antenna is designed and optimized using the CST Microwave Studio (CST vers. 17) software. Two rectangular slits and two pairs of rectangular notches are inserted on the radiator and ground loop planes, respectively, to achieve the UWB CP and IBW performance. The antenna is printed on the xy plane, and the overall dimension is $34.8 \times 32.8 \times 0.8$ mm$^3$. The ILSHM antenna design specifications are provided in Table 6.1. The next section discusses the step-by-step design process of the ILSHM antenna.

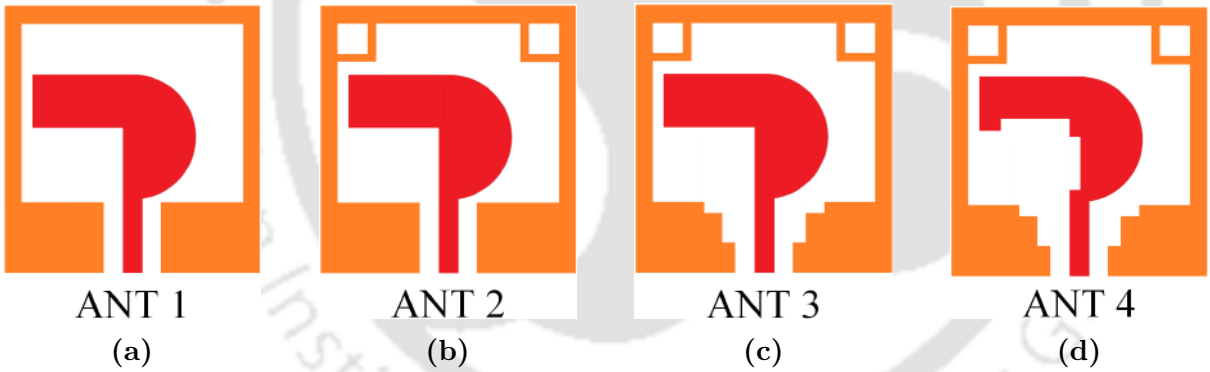


**Figure 6.2:** Evolution of UWB ILSHM CP antenna.

### 6.2.2 Design Evolution, Enhanced IBW and CP Generation

In order to understand the CP generation and IBW performance of the proposed antenna, the evolution of the antenna is depicted in Figure 6.2. The evolution of the antenna is covered in four steps such as ANT 1, ANT 2, ANT 3, and ANT 4 (proposed).

**First step:** ANT 1 is depicted in Figure 6.2(a) where a half-circle with a rectangular strip conductor is introduced along with CPW-fed extended ground loop plane. The simulated $S_{11}$ and AR results are presented in Figure 6.3. Due to the external current path and inability to

provide a wide IBW with wide AR performance as illustrated in the figure, two narrow band −10 dB performances and one AR of below 3 dB at approximately 6.5 GHz of ANT 1 are obtained. The expression of the lower band frequency of ANT 1 is given as [41]:

$$f_{ext} \approx \frac{c}{\sqrt{\epsilon_{eff}} L_{path}} \tag{6.5}$$

where $L_{path}$ is the external path length and $c$ is the speed of light in vacuum.

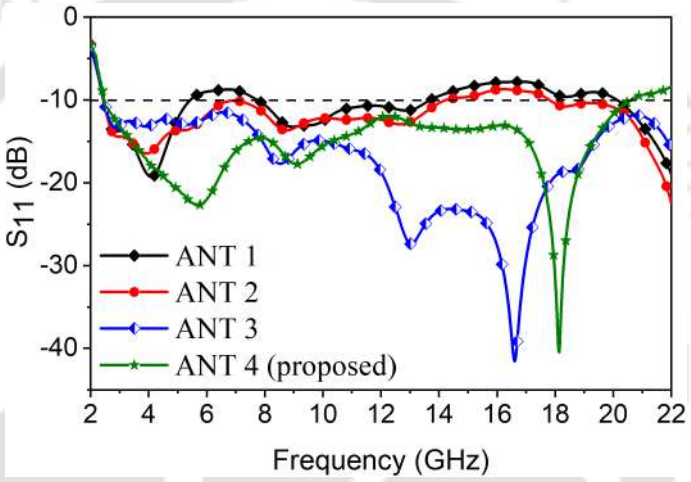


**(a)**

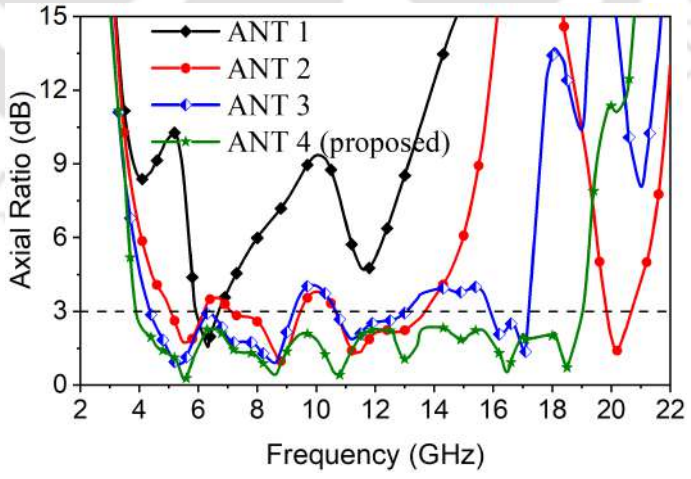


**(b)**

**Figure 6.3:** Evolution of the ILHSM antenna for (a) $S_{11}$ and (b) AR.

**Second step:** Two orthogonal electric field vectors are excited with equal amplitude by symmetrically introducing L-shaped strip conductors at the top corners of the ground loop plane

with dimensions of $l_3 = 6.3$ mm and $w_3 = 6.7$ mm. The degree of symmetry determines the phase-time difference between the excited vectors. From Figure 6.3 it is observed that one wide-band IBW from 3.4 to 14.2 GHz and four broad CP bands 4.79–5.30, 9.12–10.34, 11.26–12.93, and 19.55–20.13 GHz are obtained.

**Third step:** In this stage (ANT 3), two pairs of notches are etched close to the feeding line so that the currents flowing on each side of the ground loop are uneven and phase-shifted. Which in turn generates an improved circular polarization as shown in Figure 6.3. The $S_{11}$ and AR plots reveal a very wider IBW and three narrow CP bands, respectively in this stage of antenna revolution.

**Fourth step:** Although the inverted L-shaped hook monopole has a very wide IBW, it does not completely cover the CP radiation with a wider bandwidth. In order to significantly improve the IBW and ARBW, two rectangular slits are introduced to the primary radiator of the ANT 3 while maintaining the same ground loop plane size. Due to the etched two optimized rectangular slits (width size $w_5$, $w_6$, and length size $l_5$, $l_6$) with monopole radiator, the higher CP mode is merged and generates a continuous wider ARBW from 3.348 to 19.138 GHz (140.44%).

## 6.3 Parametric Study

In this section, the influences exerted by various geometrical parameters on the performance of reflection coefficient $S_{11}$ and axial ratio are discussed. To demonstrate $S_{11}$ and axial ratio performance, an illustration with the length of the slit $l_6 = 5.0$ mm and the width of the ground plane $w_g = 13.2$ mm influence the CP band of the antenna are originally used. Parametric analyses are done to describe how changing $l_6$ and $w_g$ affect the performance of the antenna. One parameter is investigated at a time while the dimensions of other parameters remain constant.

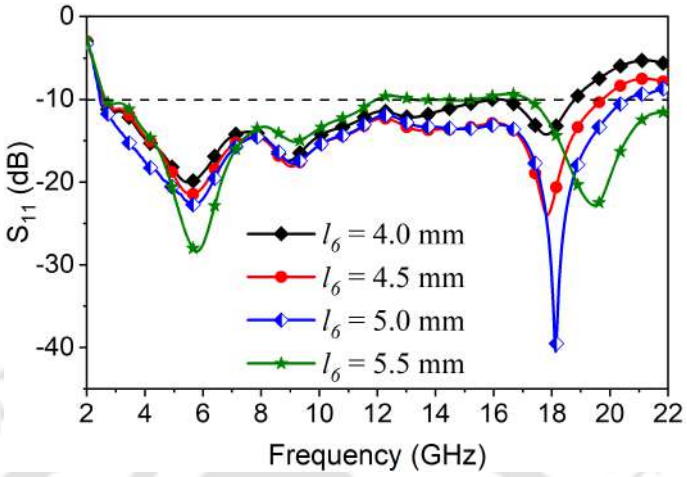


**(a)**

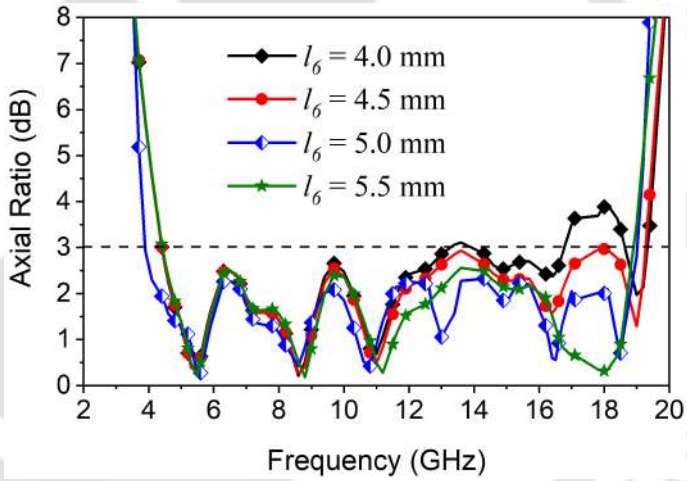


**(b)**

**Figure 6.4:** Variation ($l_6$) of simulated (a) $S_{11}$ and (b) AR of ILHSM antenna.

### 6.3.1 Parametric Effect of Rectangular Slit Length ($l_6$) of the ILHSM Radiator

A parametric analysis for various rectangular slit length ($l_6$) of the proposed ILHSM radiator is shown in Figure 6.4. According to the figure, altering $l_6$ affects the higher frequency band and decreases both IBW and ARBW. The optimal value of the length $l_6 = 5.0$ mm is obtained for good impedance matching in order to achieve the UWB IBW and ARBW.

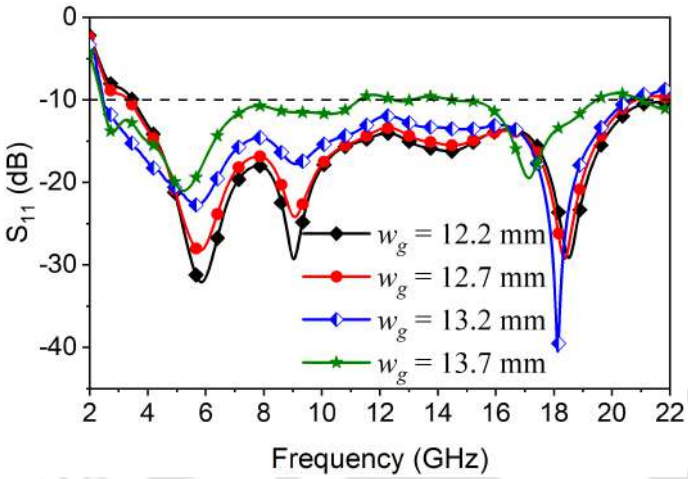


(a)

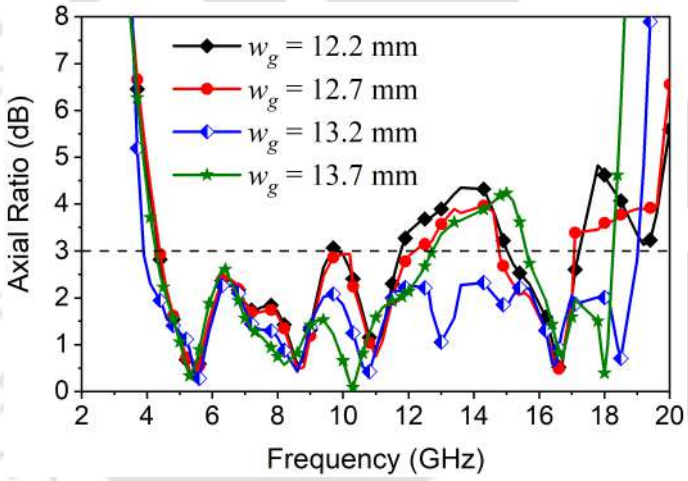


(b)

**Figure 6.5:** Variation ($w_g$) of simulated (a) $S_{11}$ and (b) AR of ILHSM antenna.

### 6.3.2 Parametric Effect of CPW-fed Ground Width ($w_g$)

Figure 6.5 illustrates the simulated return loss $S_{11}$ and AR for different widths ($w_g$) of the CPW-fed ($w_g$ = 12.2, 12.7, 13.2, and 13.7 mm) when both $W_s$ and $L_s$ are fixed at 32.8 and 34.8 mm, respectively. The IBW and ARBW are not significantly affected by variation in feed length ($l_6$). However, both bandwidths are affected with a variation of CPW-fed width ($w_g$) as shown in the figure. The propagation constant $\beta$ ( i.e., $\beta \propto \sqrt{L_{eq}}$) depends on the gap $g$ of the feed line and the width of the ground plane $w_g$. As $w_g$ increases, the inductance $L_{eq}$ of the $w_g$ increases and reduces the effective dielectric constant, which is $\sqrt{\epsilon_{eff}} = \beta \ / \ L_{eq}$. When

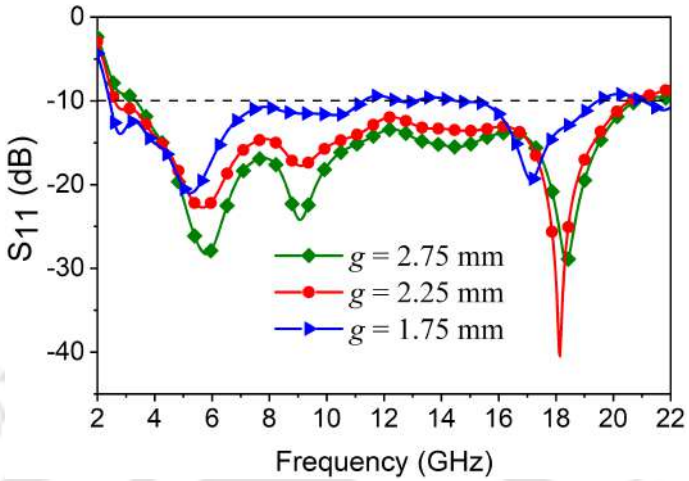


(a)

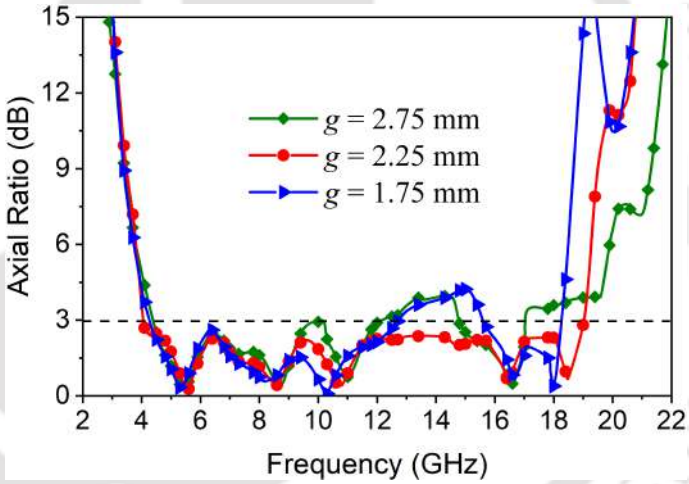


(b)

**Figure 6.6:** Variation gap ($g$) of simulated (a) $S_{11}$ and (b) AR of ILHSM antenna.

the width of $w_g$ = 13.2 mm is maintained constant, the fundamental resonance condition is satisfied by the guided wavelength $\lambda_g = \lambda_0 \ / \ \sqrt{\epsilon_{eff}}$. As a result, matching in the resonant frequency can be achieved if the length is kept constant while the width is changed.

### 6.3.3 Parametric Effect of CPW-fed Ground Gap ($g$)

Figure 6.6 illustrates the reflection coefficient $S_{11}$ curves by varying the ground-fed gap ($g$) of the CPW-fed. As ground gap ($g$) decrease, the $S_{11}$ performance at higher band no impact on impedance bandwidth in the higher region but at lower band significantly affected. Whereas

the higher CP mode is found to shift to lower band as ground gap $g$ decreases. This is explicable as the gap can control the distributions of current in the loop, which creates the higher resonant mode. In conclusion, the value of ground gap $g$ is optimized to be 2.25 mm.

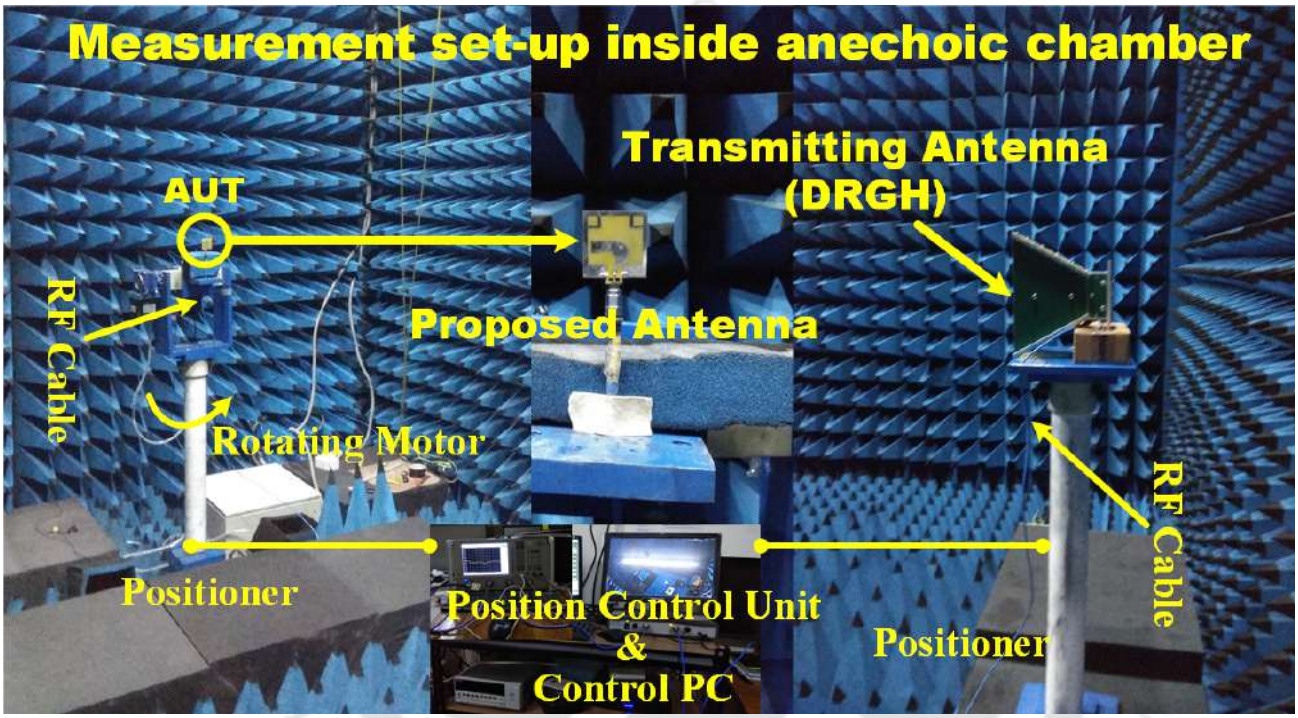


**Figure 6.7:** Measurement setup inside the anechoic chamber.

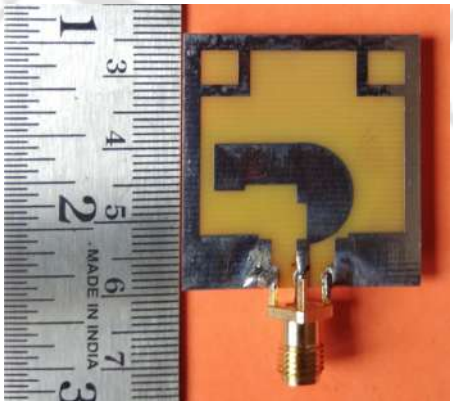

**Figure 6.8:** Fabricated proposed antenna.

## 6.4 Simulation and Measurement Performance

The reflection coefficient $S_{11}$, AR, peak gain, and radiation patterns of the proposed antenna [122] are measured using a KEYSIGHT-E5080B vector network analyzer (VNA) with an antenna measurement environment for 1–22 GHz band in an anechoic chamber (size: $6 \times 4 \times 6$ $m^3$ as shown in Figure 6.7 and Figure 6.8 depicts the top view of the fabricated antenna.

The mobility of RF cables and system connectivity are two factors that have an impact on the accuracy of antenna measurement results. The precision of the data is influenced by the probe, the motor movements used to rotate the antenna, and the impact of RF connectors. The surroundings, RF cable bending, and interconnections all affects the precision of antenna parameter measurements. The reflection-free environment has a precision error value of 0.05 dB, and RF cable stability has a value of ± 0.01 dB. All the measuring devices are calibrated properly before using for an antenna measurement. The measurement setup within an anechoic chamber with a double ridge guide horn (DRGH) antenna at one end and an antenna under test (AUT) at the other are depicted in the figure. The radiation patterns of the antenna at intervals of various frequencies are measured in two principal planes such as azimuth and elevation. The measurement typically takes into account of two polarization orientations, one measurement is being carried out horizontally polarized and the other vertically polarized. In order to generate the right-hand circular polarization (RHCP) or left-hand circular polarization (LHCP) with one rotation for each measurement of AR, the conventional DRGH antenna is rotated by $90^o$ [123]. The substitution approach entails primarily using a conventional antenna to reduce the path loss to 0 dB, followed by measuring the path loss of the AUT and determining the peak gain.

The ARBW is widely known to be a serious limitation of single feed CP antennas. Therefore, the characterization of ARBW is important. A plane wave propagates in the $z$-direction can have both $x$ and $y$ components of the electric field as expressed below:

$$\boldsymbol{E} = (\hat{x}E_x + \hat{y}E_y)e^{-jkz} \tag{6.6}$$

The RHCP and LHCP fields and the AR of the proposed ILSHM CP antenna are computed using the measured $E_\theta = |E_\theta| \quad \measuredangle \, E_\theta$ and $E_\phi = |E_\phi| \quad \measuredangle \, E_\phi$ as follows [124]:

$$\mathbf{E}_{RHCP} = \frac{1}{\sqrt{2}} \left( \mathbf{E}_\theta + j\mathbf{E}_\phi \right), \mathbf{E}_{LHCP} = \frac{1}{\sqrt{2}} \left( \mathbf{E}_\theta - j\mathbf{E}_\phi \right) \tag{6.7}$$

$$AR_{dB} = 20 \log_{10} \left( \frac{| \mathbf{E}_{RHCP} | + | \mathbf{E}_{LHCP} |}{| \mathbf{E}_{RHCP} | - | \mathbf{E}_{LHCP} |} \right) \tag{6.8}$$

### 6.4.1 Reflection Coefficient and Axial Ratio Performance

The measured and predicted $S_{11}$ performance of the proposed ILSHM CP antenna are shown in Figure 6.9. It is seen from the figure that the measured and simulated -10 dB IBW of the proposed antenna are from 2.243 to 20.653 GHz (160.82%) and 2.315 to 20.558 (159.52%), respectively. In Figure 6.10 depicts simulated and measured 3 dB ARBW from 3.348 to 19.138 GHz (140.44%) and 3.126 to 18.985 GHz (143.45%), respectively. The measured and simulated results show a good degree of agreement and the small discrepancy is primarily attribute to fabrication, SMA connector, and dimensional tolerance.

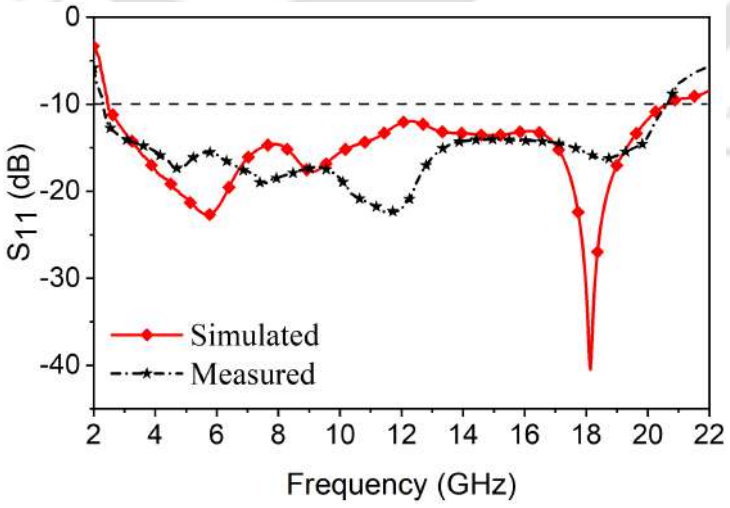


**Figure 6.9:** Measured and simulated $S_{11}$ of the ILHSM antenna.

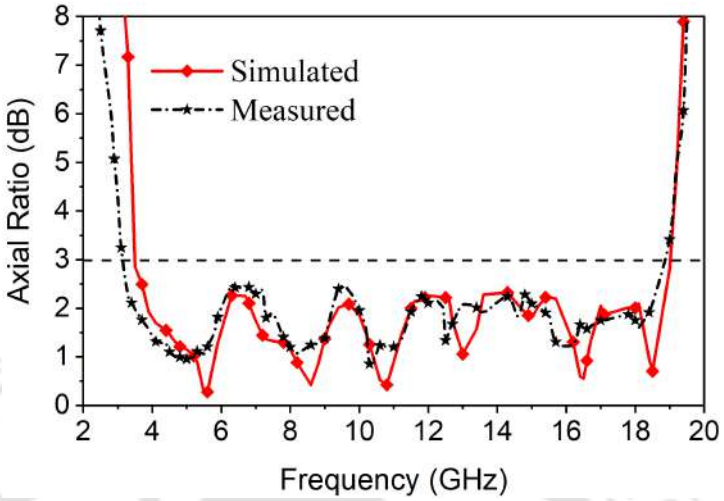


**Figure 6.10:** Measured and simulated axial ratio of the ILHSM antenna.

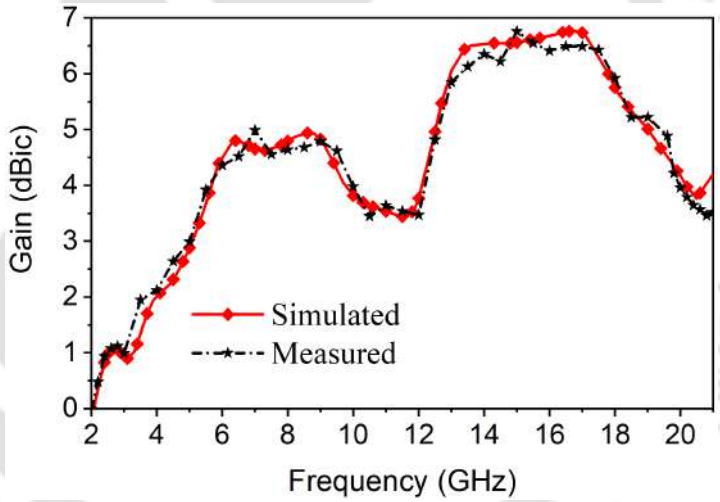


**Figure 6.11:** Measured and simulated peak gain of the ILHSM antenna.

### 6.4.2 Gain Performance

The measured and simulated peak gains of the proposed antenna are shown in Figure 6.11. According to Figure 6.11, the maximum measured gain is found to be 6.76 dBic at 15.15 GHz, and it varies from 1.2 to 6.76 dBic for the working frequency band from 2.24 –20.65 GHz. The L-shaped strip conductor and two rectangular slits used in the proposed antenna may cause the fluctuation in the gain performance of the proposed antenna.

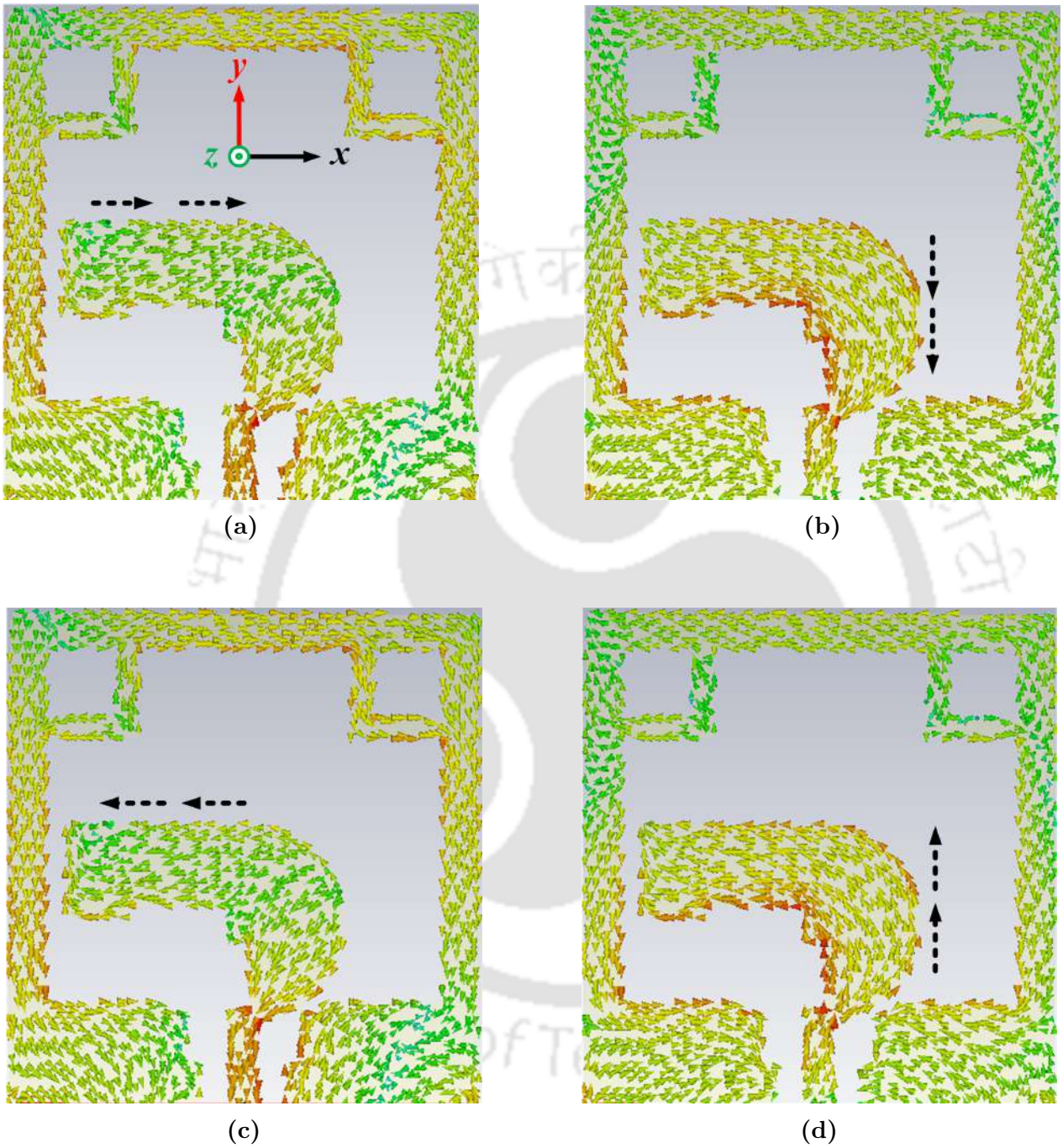


**Figure 6.12:** Surface current at 3.5 GHz for (a) $0^o$ , (b) $90^o$ , (c) $180^o$ , and (d) $270^o$.

### 6.4.3 Surface Current Distribution Performance

To understand the CP behavior of the proposed antenna, the time-varying surface current distribution of the antenna at 3.5 GHz for the orientation of the current fields on the surface

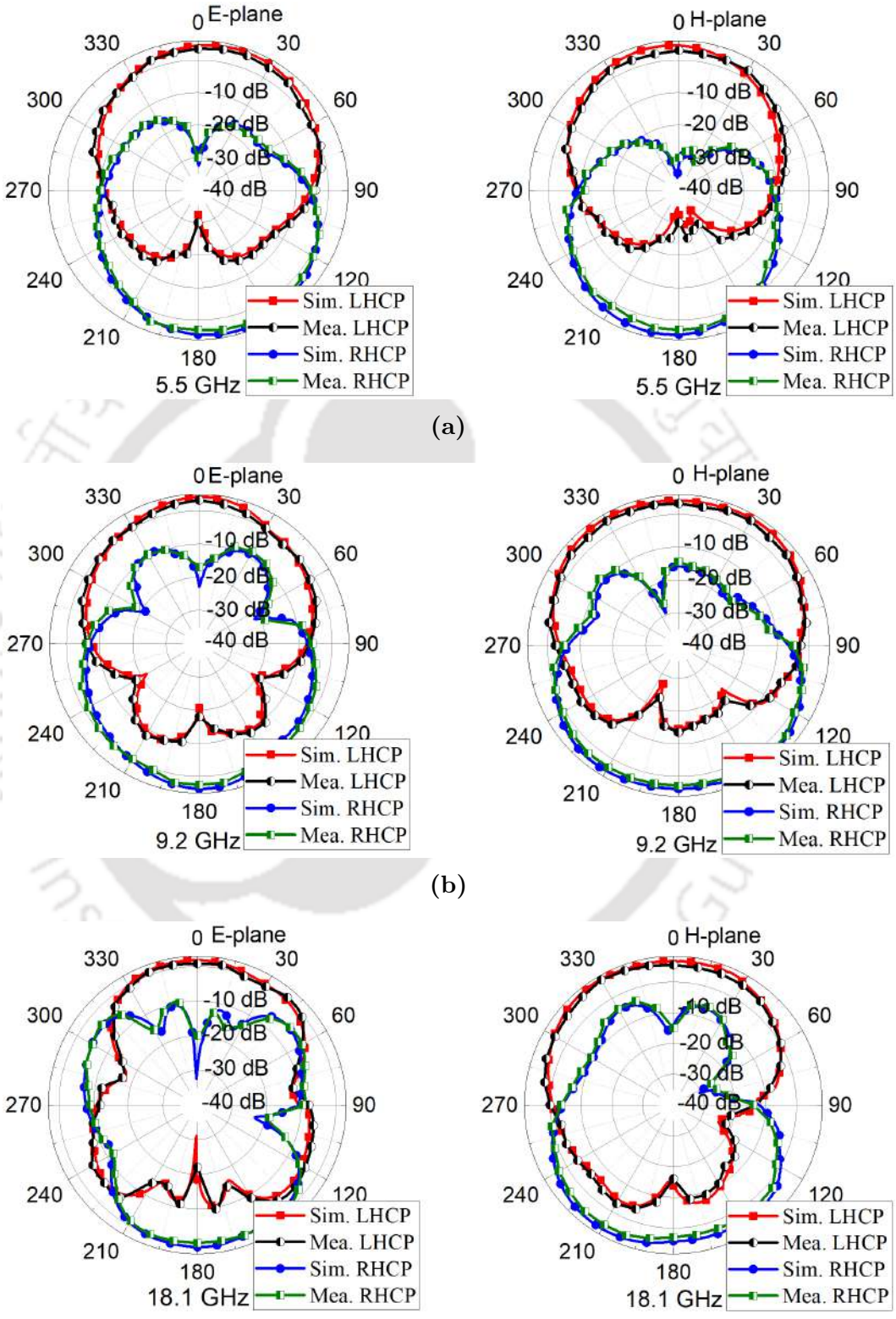


**Figure 6.13:** Radiation patterns at (a) 5.5 GHz, (b) 9.2 GHz, and (c) 18.1 GHz.

of the patch is highlighted at four angular times (0°, 90°, 180°, and 270°) is shown in Figure 6.12. For easy understanding of the field directions, the xy-coordinates are attached to the figure. The current amplitude shown in the pictures is kept fixed for all time instances. The current distribution at the azimuth of the antenna traces a clockwise path when observed from +z-direction, which indicates that the sense of polarization at this frequency is LHCP while facing a broadside direction.

### 6.4.4 Radiation Patterns Performance

The radiation pattern of the proposed antenna is characterized and compared in both E- and H-planes at various frequencies of 5.5, 9.2, and 18.1 GHz as shown in Figure 6.13. The radiation pattern measurements are done in an anechoic chamber using two-antenna measurement setup. The radiation patterns are drawn for the case where one of the antennas is excited while the other is terminated with a matched load of 50Ω. It can be observed that as the frequency increases, the electrical dimensions of the antenna increase and as a result, the number of lobes increases and this is also caused by diffraction from the edges of the ground plane, which has very large electrical dimensions at larger frequencies. At lower frequencies, the maximum value of the radiation patterns point to the - y-axis significantly, because its feed section of inverted-L-shaped-hook lies in the -y-axis. The LHCP is presented in the +z-direction and the RHCP is presented in the -z-direction in the bidirectional radiation pattern. For both cases, an excellent agreement between simulations and measurements is observed. The patterns also show good stability with frequency. These implied that a large and uniform coverage for UWB system operation can be attained with our design.

Finally, comprehensive benchmarking with the recently reported CP antenna designs has been performed. The major performance figures including the antenna size, impedance bandwidth, the AR bandwidth, gain variation, and the bandwidth ratio are compared and summarized in Table 6.2. As shown in the table, the wideband CP antennas reported in the literature to occupy approximately 1.04 to 43.8 times more volume than the volume of the ILSHM CP antenna. As a result, compared to the other structures reported in the literature, the proposed

**Table 6.2:** Comparison of UWB CP antennas

| Ref. | Dimension ($mm^3$) | IBW (GHz) | IBW (%) | ARBW (GHz) | ARBW (%) | GV (dBic) | BR |
|---|---|---|---|---|---|---|---|
| [87] | $180 \times 180 \times 0.8$ | 1.5–2.2 | 38 | 1.35–1.82 | 29.7 | $> 3$ | 1.279 |
| [109] | $150 \times 150 \times 1.0$ | 1.6-2.42 | 41 | 1.63-2.27 | 33 | 6.3-6.5 | 1.242 |
| [111] | $37 \times 32 \times 0.8$ | 2.21-2.77 | 22.5 | 2.28-2.77 | 19.4 | max. 5.7 | 1.159 |
| [112] | $70 \times 70 \times 1.6$ | 1.53-1.611 | 5.2 | 1.545-1.605 | 3.81 | max. 1.8 | 1.364 |
| [113] | $75 \times 63 \times 1.6$ | 1.81-3.83 | 71.63 | 2.2-2.9 | 27.45 | 1.5-2.5 | 2.609 |
| [114] | $55 \times 50 \times 1.0$ | 1.48-4.24 | 96.5 | 2.05-3.95 | 63.3 | 0.5-3.5 | 1.524 |
| [115] | $62 \times 62 \times 3.0$ | 1.8-4.5 | 86 | 2.25-3.75 | 50 | $> 2.5$ | 1.72 |
| [119] | $42 \times 42 \times 1.5$ | 2.3-7.6 | 107 | 3.45-6.4 | 59.9 | 2.3-4.6 | 1.786 |
| [120] | $95 \times 95 \times 2.2$ | 2.9-9 | 103 | 3-7.8 | 89 | 8-11 | 1.157 |
| [121] | $200 \times 200 \times 1.0$ | 1.17-5.79 | 132.8 | 1.75-4.76 | 92.5 | max.12.6 | 1.435 |
| Work | $34.8 \times 32.8 \times 0.8$ | 2.243-20.653 | 160.82 | 3.126-18.985 | 143.45 | 1.2-6.76 | 1.121 |

IBW: Impedance bandwidth ($S_{11} \leq -10$ dB); ARBW: axial ratio bandwidth ($< 3$ dB); GV: gain variation; BR: bandwidth ratio.

structure is compact. Additionally, as compared to the work done on previous wide band CP antennas, the proposed ILSHM CP antenna exhibits a notable improvement in IBW and 3 dB ARBW. It is clear that the proposed design operates in the UWB band and offers benefits such as simple manufacturing, compactness, improved IBW and ARBW, and superior peak gain for the complete frequency band from 2.24 to 20.65 GHz. The analysis of the simulation and experimental data reveals that the proposed antenna exhibits a small size, ultra-wideband IBW, ARBW, and despite the ratio of the small bandwidth $BR|_{(10/3)dB} \approx 1.121$, it has successfully illustrated the fundamentals of the design of a UWB CP antenna.

## 6.5 Summary of the Chapter

In this chapter, a compact simple structure CPW-fed ILSHM CP antenna with UWB -10 dB IBW and 3 dB CP ARBW is presented for wireless applications. The UWB CP is achieved by symmetrical excitation of a defected ground loop plane and ILSHM antenna. The overall footprint of the structure is only $L_S \times W_S = 0.269\lambda_l \times 0.254\lambda_l$, when $\lambda_l$ corresponds to the wavelength measured at the lowest resonance frequency. The measured IBW ($VSWR_{max} < 2$) result from 2.243 to 20.653 GHz (160.82%) and $< 3$ dB ARBW from 3.216 to 18.985 GHz (143.45%) are achieved. Despite the ratio of the small bandwidth $BR|_{(10/3)dB} \approx 1.121$, it has demonstrated the essence of the design of a compact UWB CP antenna without involving any complex circuitry. Moreover, the ARBW of 143.45 % for the proposed ILSHM antenna is also much wider than the other antennas in the literature. The miniaturization of the ILSHM antenna is realized by an extended ground loop plane while retaining the UWB characteristics with minimum AR and BR. The proposed monopole antenna which will be suitable for wireless communication applications is simple in design, small in size, and easy to manufacture.

*Note: This work,Compact UWB CP Inverted L-Shaped-Hook Monopole Antenna with Minimum $BR_{(10/3)dB}$ for Wireless Applications (under preparation).*

# 7

# Conclusion and Future Work



## Contents

## 7.1 Summary of the Present Work

The primary purpose of this thesis is to investigate a compact microstrip antenna for hand-held devices targeted for wireless applications. This thesis presents a detailed explanation of the novel compact microstrip antennas and the different methods such as slot, slit, and defected ground structure techniques used in literature for antenna performance improvement. Supporting multi-band communication by working on different wireless frequency standards, further improvement in antenna radiation parameters with high center frequency ratio, and size reduction of a multiband antenna using different slot size structures is needed.

Another important parameter in the UWB antenna is BDR which is the ratio of bandwidth dimension. Designs for UWB antenna to increase the BDR as well as decrease the antenna size simultaneously are not reported as per the best of the author's knowledge. Hence, the design of an antenna that has both capabilities is an area of research for efficient wireless communication technology. The signal transmission equation, i.e., the Friis equation has terms which depend on the polarization of the transmitter and receiver antenna. If the polarization is not the same, the maximum signal will not be transferred to the receiver due to polarization mismatch. A linear polarized antenna sometimes is placed at 90° or $180^{circ}$ orientation according to the power density contour at the receiver end. And also, due to its advantages of overcoming multipath fading, non-line-of-sight applications, and providing better mobility compared to linearly polarized antennas, the circularly polarized (CP) antenna is getting popular in wireless communication systems.

In chapter 2, it is described how future spectrum management approaches for WLAN/ WiMAX/ C-band downlink satellite communications can use a novel design of a triple-band antenna with a high center frequency ratio and significantly suppress cross-polarization levels. This antenna has a double annular ring slot, two L-shaped slots, one I-shaped slot, and a DGS based on an ellipse-shaped slit. In addition, the transmission line model of the proposed antenna is presented and it shows the antenna behavior based on the effect of each RLC circuit element. It is seen that the characteristics of the output from the RLC circuit model closely resemble

with the simulation results obtained using the CST simulator. Therefore, the requirements and challenges associated with designing a triple-band antenna are explored. When the proposed antenna is fabricated, the simulation and the measured results are close to each other which in turn validates the design.

In chapter 3, a CPW-fed symmetrical staircase-shaped antenna is design having enhanced IBW and better gain compared to the triple-band antenna is discussed. The main goal of the proposed approach is to designed a compact antenna with an enhance impedance bandwidth. And also the proposed antenna should able to control the coupling coefficient between the C-shaped slots which is introduced due to the flow of a fraction of the $TM_{01}$ mode current flowing in the slots so that the radiation reasonably maintains the radiation characteristics. As a result, the proposed antenna has a wider impedance bandwidth, a fair gain, and better impedance matching. It has been noted that the performance of TLM closely matches with the outcomes of the simulation performed using CST simulator software. The prototype is successfully implemented, fabricated, and the results of the experiment are compared.

In chapter 4, the method of improving the IBW of the star-shaped monopole antenna is discussed. A novel concept for efficiently using the reduced space and enhancement in impedance bandwidth of the proposed antenna is discussed in detail. The proposed antenna operational principle, design procedure, simulated and measured results are presented in this chapter.

In chapter 5, introduces a compact dual-band and dual-CP traveling wave series-fed circular slit microstrip array (TWSCSMA) antenna operating in quad-band CP at 2.5/3.5/3.8 GHz WiMAX and 5.2 GHz WLAN applications. The radiating structure consists of an annular ring traveling wave series-fed circular slit array elements, rotates in sequence with seven circular quasi-lumped resonators contributing to two-IBW and quad CP bands. The four split-ring resonators with double-annular rings are introduced on the defected ground plane to improve the impedance matching, IBW, and ARBW effectively. Thus, measured IBW and AR characteristics validate and ensure the polarization quality of traveling-wave series-fed arrays. Furthermore, modern machine learning regression techniques are used to predict the parameter accuracy of the model performance requirements for the optimal design of the proposed

antenna. The TWSCSMA antenna demonstrates a compact, low profile, wide impedance bandwidth, and minimum axial ratio which is making it a good candidate for WiMAX and WLAN applications.

In chapter 6, the practical challenges in designing and integrating a small UWB monopole CP antenna, where the frequency band of IBW will closely match with a frequency band of ARBW with a small BR. The design procedure of a CPW-fed monopole for integration into a compact patch is explored in this chapter. The main goal of the proposed approach is to obtain a small bandwidth ratio of $BR_{(10/3)dB} \approx 1.121$ and the radiator should reasonably maintain the radiation characteristics of the monopole antenna. The proposed antenna is fabricated and the measured results matched with the simulation results, thus validating the design.

## 7.2 Suggestions for the Future Work

The suggestions for further research are given as follows:

- The work in this thesis is based on enhancing the impedance bandwidth, better radiation patterns at high frequency, and gain of zeroth order resonant antennas for wireless applications. In the future we may go for enhanced bandwidth and higher gain by employing array configurations.
- Variations in current topology can be explored including fractal geometries to produce wider bandwidth.
- Use of reactive loadings can be applied to implement frequency or pattern reconfigurability.
- It is seen that both dual-circularly polarized TWSCSMA and ILSHM CP antennas operate in a higher mode at higher frequency. A more detailed understanding of the traveling wave mechanism series-fed as well as a monopole, maintaining the minimum axial ratio and small bandwidth ratio could lead to improved design of the wider band and UWB CP antennas.

- A wider band or UWB system may sometimes be required to provide filtering in those bands to avoid potential interference owing to the coexistence of wider band and UWB systems with frequency bands set separately for other wireless systems. Future research may focus on creating slot and monopole antennas with band rejection capabilities.

- Although still at the prototype stage, metamaterials can be efficiently designed, based on the fundamental concepts of Transmission Line theory. This can potentially be applied for optical/microwave applications in the Terahertz frequency range.

# A

# Appendix

## Contents

## A.1 Fresnel Integrals

$$C(x) = \int_0^x \cos\left(\frac{\pi}{2}\tau^2\right) d\tau \tag{A.1}$$

$$S(x) = \int_0^x \sin\left(\frac{\pi}{2}\tau^2\right) d\tau \tag{A.2}$$

## A.2 Fixed Transmit and Receive Antennas

A transmitted far-field at time $t$ can be expressed as:

$$E(f, t, (r, \theta, \psi)) = \frac{\alpha_s(\theta, \psi, f)\cos 2\pi f(t - r/c)}{r} \tag{A.3}$$

where, ($r$, $\theta$, $\psi$) represents the point $\mathbf{u}$ in space at which the electric field is being measured, $r$ is the distance from the transmit antenna to $\mathbf{u}$ and ($\theta$, $\psi$) represents the elevation and azimuth angles. The constant $c$ is the speed of light and $\alpha_s(\theta, \psi, f)$ is the scaling factor for antenna losses.

The received waveform in response to the above transmitted signal is as follows:

$$E_r(f, t, \mathbf{u}) = \frac{\alpha(\theta, \psi, f)\cos 2\pi f(t - r/c)}{r} \tag{A.4}$$

where $\alpha(\theta, \psi, f)$ is the product of the antenna patterns of transmitting and receiving antennas in the given direction.

## A.3 Rectangular Patch Width and Length Calculation

The initial values (at low frequencies) of the effective dielectric constant are referred to as the static values, and they are given by [85]

$$W/h > 1$$

$$\epsilon_{eff} = \frac{\epsilon_r + 1}{2} + \frac{\epsilon_r - 1}{2}\left[1 + 12\frac{h}{W}\right]^{-1/2} \tag{A.5}$$

A very popular and practical approximate relation for the normalized extension of the length is [85]

$$\frac{\Delta L}{h} = 0.412\frac{(\epsilon_{eff} + 0.3)\left(\frac{W}{h} + 0.264\right)}{(\epsilon_{eff} - 0.258)\left(\frac{W}{h} + 0.8\right)} \tag{A.6}$$

Since the length of the patch has been extended by $\Delta L$ on each side, the effective length of the patch is now ($L = \lambda/2$ for dominant $TM_{010}$ mode with no fringing)

$$L_{eff} = L + 2\Delta L \tag{A.7}$$

For an efficient radiator, a practical width $W$ that leads to good radiation efficiencies is [85]

$$W = \frac{1}{2f_r\sqrt{\mu_\circ\epsilon_\circ}}\sqrt{\frac{2}{\epsilon_r+1}} = \frac{v_\circ}{2f_r}\sqrt{\frac{2}{\epsilon_r+1}} \tag{A.8}$$

where $v_0$ is the free-space velocity of light.

The actual length $L$ of the patch given by

$$L = \frac{c}{2f_r\sqrt{\epsilon_{eff}}\sqrt{\mu_\circ\epsilon_\circ}} - 2\Delta L \tag{A.9}$$

Fractional bandwidth

$$\frac{\Delta f}{f_o} = \frac{VSWR-1}{Q_t\sqrt{VSWR}} \tag{A.10}$$

where $Q_t$ is the total quality factor

$$\frac{1}{Q_t} = \frac{1}{Q_{rad}} + \frac{1}{Q_c} + \frac{1}{Q_d} + \frac{1}{Q_{sw}} \tag{A.11}$$

where $W$ is $P_W$ and $L$ is $P_L$ in the thesis.

## A.4 Coplanar Waveguide Fed Calculation

The closed-form expression for the effective dielectric constant of the coplanar waveguide (CPW) is represented as

$$\epsilon_{eff} = 1 + q(\epsilon_r - 1) \tag{A.12}$$

where $q$ is called the filling fraction.

$$q = \frac{1}{2}\frac{K(k_4)}{K'(k_4)}\frac{K'(k_3)}{K(k_3)}$$

$$k_3 = \frac{a}{b}\sqrt{\frac{1-b^2/c_\circ^2}{1-a^2/c_\circ^2}}$$

$$k_4 = \frac{\sinh\left(\frac{\pi a}{2h}\right)}{\sinh\left(\frac{\pi b}{2h}\right)}\sqrt{\frac{1-\sinh^2\left(\frac{\pi b}{2h}\right)/\sinh^2\left(\frac{\pi c_\circ}{2h}\right)}{1-\sinh^2\left(\frac{\pi a}{2h}\right)/\sinh^2\left(\frac{\pi c_\circ}{2h}\right)}}$$

$$Z_{ocp} = \frac{30\pi}{\sqrt{\epsilon_{eff}}}\left(\frac{K'(k_3)}{K(k_3)}\right) \tag{A.13}$$

## A.5 Modes of Operation

For the rectangular patch, the $TM_{mn}$ mode has a normalized electric field that is given by

$$E_z^{mn}(x,y) = \cos\left(\frac{m\pi x}{L}\right)\cos\left(\frac{n\pi y}{W}\right) \tag{A.14}$$

For the circular patch, the $TM_{np}$ mode has a normalized electric field that is given by

$$E_z(\rho,\phi) = \cos(n\phi)\frac{J_n\left(\frac{x'_{np}\rho}{a}\right)}{J_n(x'_{np})} \tag{A.15}$$

## A.6 Radiation Patterns

### A.6.1 Rectangular Patch

The far-field radiation pattern of the rectangular patch is given by

$$E_\theta^{patch}(r,\theta,\phi) = -2Wh\left(\frac{E_0}{\eta_0}\right)\cos\phi(1-\Gamma^{TM}(\theta))\cos\left(k_x\frac{L}{2}\right)\left(k_y\frac{W}{2}\right)(k_{z1}h) \tag{A.16}$$

$$E_\phi^{patch}(r,\theta,\phi) = -2Wh\left(\frac{E_0}{\eta_0}\right)(\cos\theta\sin\phi)(1-\Gamma^{TE}(\theta))\cos\left(k_x\frac{L}{2}\right)\left(k_y\frac{W}{2}\right)(k_{z1}h) \tag{A.17}$$

where

$$E_0 = \left(\frac{-j\omega\mu_0}{4\pi R}\right)e^{-jk_0R} \tag{A.18}$$

and

$$k_x = k_0\sin\theta\cos\phi \tag{A.19}$$

$$k_y = k_0\sin\theta\sin\phi \tag{A.20}$$

$$k_{z1} = k_0N_1(\theta) \tag{A.21}$$

with

$$N_1(\theta) = \sqrt{\epsilon_r\mu_r - \sin^2\theta} \tag{A.22}$$

### A.6.2 Circular Patch

The far-field patterns of a resonant circular patch are similar to those of the resonant rectangular patch on the same substrate material. The normalized field of the dominant $TM_{11}$ mode is described by

$$E_z(\rho,\phi) = \cos(\phi)\frac{J_1\left(\frac{x_{11}^{'}\rho}{a}\right)}{J_1(x_{11}^{'})} \tag{A.23}$$

For this mode, the far-field pattern is given by

$$E_\theta(r,\theta,\phi) = \left[2\pi\frac{E_0}{\eta_0}(ah)\right]\cos\phi\ (k_{z1}h)J_1^{'}(k_0 a\sin\theta)(1-\Gamma^{TM}(\theta)) \tag{A.24}$$

$$E_\phi(r,\theta,\phi) = -2\pi\left[\frac{E_0}{\eta_0}(ah)\right]\sin\phi\ (k_{z1}h)J_{inc}(k_0 a\sin\theta)(1-\Gamma^{TE}(\theta))\cos\theta \tag{A.25}$$

where

$$J_{inc}(x) = \frac{J_1(x)}{x} \tag{A.26}$$

### A.6.3 Sequentially Rotated Arrays

The total radiated fields of a sequentially rotated array can be written as

$$\mathbf{E}_t(\theta,\phi) = \sum_{m=1}^{M}\mathbf{E}_m(\theta,\phi) \tag{A.27}$$

where $\mathbf{E}_m$ is the radiated field of the $m$ th element.
The array radiates a perfect CP for $0 < p < M$ can be written as

$$\mathbf{E}_t(0,0) = \frac{M}{2}(a-b)(\hat{\theta}-j\hat{\phi}+\frac{1}{2}(a+b)(\hat{\theta}+j\hat{\phi})\ \frac{\sin p\pi}{\sin\frac{p\pi}{M}}\ exp\left[-j\left(\frac{(M-1)p\pi}{M}\right)\right] \tag{A.28}$$

### A.6.4 Antenna Gain Measurement

The ratio of received power ($P_r$) to the transmitted ($P_t$) is given by Friis as follows:

$$\frac{P_r}{P_t} = e_{cdt}\ e_{cdr}\ e_{rt}\ e_{rr}\left(\frac{\lambda}{4\pi R}\right)^2 D_t(\theta_t,\ \phi_t)\ D_r(\theta_r,\ \phi_r)|\hat{\rho}_t\ .\ \hat{\rho}_r|^2 \tag{A.29}$$

where
$e_{cdt}$ is $T_x$ antenna radiation efficiency

$e_{cdr}$ is $R_x$ antenna radiation efficiency

$e_{rt}$ is the refection efficiency of $T_x$ antenna

$e_{rr}$ is the refection efficiency of $R_x$ antenna

$R$ is the transmission distance

$\lambda$ is the working wavelength

$D_t(\theta_t,\ \phi_t)$ is the directivity of the $T_x$ antenna

$D_r(\theta_r,\ \phi_r)$ is the directivity of the $R_x$ antenna

$\hat{\rho}_t$ polarization unit vector of Tx antenna

$\hat{\rho}_r$ polarization unit vector of Rx antenna

# References


[1] T. K. Sarkar, "History of Wireless," John Wiley and Sons, 2006.

[2] T. S. Rappaport, "Wireless Communications Principles and Practice Pearson," 2nd Edition 2002.

[3] C. A. Balanis, "Microstrip Antennas," Antenna Theory, Analysis and Design, Third Edition, John Wiley Sons, 2010.

[4] K. D. Prasad, "Antenna wave and propagation," Satya Parkashan, 1983.

[5] K. -Lu. Wong, "Planar Antennas for Wireless Communications," by Wiley Interscience, 2003.

[6] J. H. Lu and K. L. Wong, "Theory of miniaturized shorting-post microstrip antennas," *IEEE Trans. Antennas Propaga.*, vol. 48, no.1, pp.41–47, Jan. 2000.

[7] R. Porath, "Slot-loaded meandered rectangular microstrip antenna with compact dual frequency operation," *Electronic Letters*, vol. 34, pp.1048–1050, May 1998.

[8] D. H. Schaubert, D. M. Pozar, and A. Adrian, "Effect of microstrip antenna substrate thickness and permittivity," *IEEE Trans. Antennas Propaga.*, vol. 37, no.6, pp.677–682, Jun. 1989.

[9] IEEE-SA. IEEE 802.11n-2009-Amendment 5: Enhancements for Higher Throughput. Technical report, 2009.

[10] C. A. Balanis, "Antenna Theory," *John Wiley & Sons.*, In INC Hoboken, pp. 811–882, 2005.

[11] S. A. H. Saghanezhad and Z. Atlasbaf, "Miniaturized dual-band CPW-fed antennas loaded with U-shaped metamaterials," *IEEE Antennas Wireless Propag. Lett.*, vol. 14, pp. 658–661, March 2015.

[12] M. -Ju. Chiang, T. F. Hung, J. Y. Sze and S. S. Bor, "Miniaturized dual-band CPW-fed annular slot antenna design with arc-shaped tuning stub," *IEEE Trans. Antennas Propag.*, vol. 58, no. 11, pp. 3710–3715, Nov. 2010.

[13] M. Li, X. Q. Lin, J. Y. Chin, R. Liu, and T. J. Cui, "A novel miniaturized printed planar antenna using split-ring resonator," *IEEE Antennas Wireless Propag. Lett.*, vol. 7, pp. 629–631, Oct. 2008.

[14] M. Yang, Z. N. Chen, P. Y. Lau , X. Qing, and X. Yin, "Miniaturized patch antenna with grounded strips," *IEEE Trans. Antennas Propag.*, vol. 63, no. 2, pp. 843–848, Feb. 2015.

[15] M. A. Antoniades and G. V. Eleftheriades, "A compact multiband monopole antenna with a defected ground plane," *IEEE Antennas Wireless Propag. Lett.*, vol. 7, pp. 652–655, Sept. 2008.

[16] T. T. Le, Y. -Deok Kim and T. -Yeoul Yun, "A triple-band dual-open-ring high gain high-efficiency antenna for wearable applications," *IEEE Access*, vol. 9, pp. 118435–118442, Sept. 2021.

[17] J. Pei, A. -Guo Wang, S. Gao, and W. Leng, "Miniaturized triple-band antenna with a defected ground plane for WLAN/WiMAX applications," *IEEE Antennas Wireless Propag. Lett.*, vol. 10, pp. 298–301, March 2011.

[18] M. -Tien Wu and M. -Lin Chuang, "Multibroadband slotted bow-tie monopole antenna," *IEEE Antennas Wireless Propag. Lett.*, vol. 14, pp. 887–890, Apr. 2015.

[19] W. C. Mok, S. H. Wong, K. M. Luk, and K. F. Lee, "Single-layer single-patch dual-band and triple-band patch antennas," *IEEE Trans. Antennas Propag.*, vol. 61, no. 8, pp. 4341–4344, Aug. 2013.

[20] Y. -Jhu Chen, T. -Wei Liu, and W. -Hua Tu, "CPW-fed penta-band slot dipole antenna based on comb-like metal sheets," *IEEE Antennas Wireless Propag. Lett.*, vol. 16, pp. 202–205, Feb. 2017.

[21] J. -Feng Qian, F. -Chang Chen, K. -Ran Xiang, and Q. -Xin Chu, "Resonator loaded multi-band microstrip slot antennas with bidirectional radiation patterns," *IEEE Trans. Antennas Propag.*, vol. 67, no. 10, pp. 6661–6666, Oct. 2019.

[22] A. Boukarkar, X. Q. Lin, Y. Jiang, and Y. Q. Yu, "Miniaturized single-fed multiband patch antennas," *IEEE Trans. Antennas Propag.*, vol. 65, no. 2, pp. 850–854, Feb. 2017.

[23] Y. Dong, H. Toyao, and T. Itoh, "Design and characterization of miniaturized patch antennas loaded with complementary split-ring resonators," *IEEE Trans. Antennas Propag.*, vol. 60, no. 2, pp. 772–785, Feb. 2012.

[24] S. Mathew, R. Anitha, U. Deepak, C. K. Aanandan, P. Mohannan, and K. Vasudevan, "A compact tri-band dual-polarized corner-truncated sectoral patch antenna," *IEEE Trans. Antennas Propag.*, vol. 63, no. 12, pp. 5842–5845, Dec. 2015.

[25] T. H. Chang and J. F. King, "Compact multi-band H-shaped slot antenna," *IEEE Trans. Antennas Propag.*, vol. 61, no. 8, pp. 4345–4349, Aug. 2013.

[26] K. L. Wong and C. Y. Huang, "Triple-wideband open-slot antenna for the LTE metal-framed tablet device," *IEEE Trans. Antennas Propag.*, vol. 63, no. 12, pp. 5966–5971, Dec. 2015.

[27] R. Xu, J. Li, Y. X. Qi, Y. Guangwei, and J. J. Yang , "A design of triple-wideband triple-sence circularly polarized square slot antenna," *IEEE Antennas Wireless Propag. Lett.*, vol. 16, pp. 1763–1766, Feb. 2017.

[28] A. Katyal and A. Basu, "Analysis and optimisation of broadband stacked microstrip antennas using transmission line model," *IET Microw. Antennas & Propag.*, vol. 11, iss. 1, pp. 81–91, Feb. 2017.

[29] W. H. A. A. Amro and M. K. Abdelazeez, "Analysis and optimisation of super-wideband monopole antenna with tri-band notch using a transmission line model," *IET Microw. Antennas & Propag.*, vol. 13, iss. 9, pp. 1373–1381, June 2019.

[30] A. Molisch, F. K. Balakrishnan, D. Cassioli, C. -Chin Chong, S. Emami, A. Fort, J. Karedal, J. Kunisch, H. Schanntz, and K. Siwiak, "A comprehensive model for ultrawideband propagation channels," *Proc. IEEE Global Telecommun. Conf. (GLOBECOM)*, pp. 3648–3653, 2015.

[31] D. Porcino and W. Hirt, "Ultra-wideband radio technology: potential and challenges ahead," *IEEE Commun. Mag.*, pp. 66–74, July 2003.

[32] *FCC First Report and Order on Ultra-Wideband Technology*, document FCC, pp. 02–48, Feb. 2002.

[33] S. C. Chiu and S. Y. Chen, "Miniaturization of CPW-fed slot antenna using a pair of interdigital capacitors," *in Proc. IEEE Antennas Propag. Soc. Int. Symp.*, (APSURSI), Orlando, FL, USA, pp. 1380–1381, July 2013.

[34] H. Orazi and H. Soleiman, "Miniaturisation of UWB triangular slot antenna by the use of DRAF," *IET Microw. Antennas & Propag.*, vol. 11, iss. 4, pp. 450–456, Feb. 2017.

[35] M. O. Sallam, S. M. Kandil, V. Volski, G. A. E. Vandenbosch, and E. A. Soliman, "Wideband CPW-fed flexible bow–tie slot antenna for WLAN/WiMAX systems," *IEEE Trans. Antennas Propag.*, vol. 65, no. 8, pp. 4274–4277, Aug. 2017.

[36] O. A. Safia, M. Nedil, L. Talbi, and K. Hettak, "Coplanar waveguide-fed rose-curve shape UWB monopole antenna with dual-notch characteristics," *IET Microw. Antennas & Propag.*, vol. 12, iss. 7, pp. 1112–1119, Jan. 2018.

[37] A. Azari, "A New Super Wideband Fractal Microstrip Antenna," *IEEE Trans. Antennas Propag.*, vol. 59, no. 5, pp. 1724–1727, May 2011.

[38] Z. -Hong Tu, W. -Ao Li, and Q. -Xin Chu, "Single-layer differential CPW-fed notch-band tapered-slot UWB antenna," *IEEE Antennas Wireless Propag. Lett.*, vol. 13, pp. 1296–1299, May 2014.

[39] N. Tasouji, J. Nourinia, C. Ghobadi, and F. Tofigh, "A novel printed UWB slot antenna with reconfigurable band–notch characteristics," *IEEE Antennas Wireless Propag. Lett.*, vol. 12, pp. 922–925, Jun. 2013.

[40] K. -Ren Chen, C. Y. D. Sim, and J. -Sheen Row, "A compact monopole antenna for super wideband applications," *IEEE Antennas Wireless Propag. Lett.*, vol. 10, pp. 488–491, Apr. 2011.

[41] X. Fang, G. Wen, D. Inserra, Y. Huang, and J. Li, "Compact wideband CPW-fed meandered-slot antenna with slotted Y-shaped central element for Wi-Fi, WiMAX, and 5G applications," *IEEE Trans. Antennas Propag.*, vol. 66, no. 12, pp. 7395–7399, Dec. 2018.

[42] A. Dastranj, and H. Abiri, "Bandwidth enhancement of printed E-shaped slot antennas fed by CPW and microstrip line," *IEEE Trans. Antennas Propag.*, vol. 58, no. 4, pp. 1402–1407, Apr. 2010.

[43] M. N. Moghadasi, A. Danideh, R. Sadeghifakhr, and M. -Reza Azadi, "CPW-fed ultra wideband slot antenna with arc-shaped stub," *IET Microw. Antennas & Propag.*, vol. 3, iss. 4, pp. 681–686, Sept. 2009.

[44] H. Liu, S. Zhu, P. Wen, X. Xiao, W. Che, and X. Guan, "Flexible CPW-fed fishtail-shaped antenna for dual-band applications," *IEEE Antennas Wireless Propag. Lett.*, vol. 13, pp. 770–773, Apr. 2014.

[45] J. Wu, Z. Zhao, Z. Nie, and Q. Liu, "A printed UWB Vivaldi antenna using stepped connection structure between slot line and tapered patches," *IEEE Antennas Wireless Propag. Lett.*, vol. 13, pp. 698–701, Apr. 2014.

[46] R. Eshtiaghi, J. Nourinia, and C. Ghobadi, "Electromagnetically coupled band-notched elliptical monopole antenna for UWB applications," *IEEE Trans. Antennas Propag.*, vol. 58, no. 4, pp. 1397–1402, Apr. 2010.

[47] Y. Yang, Z. Zhao, X. Ding, Z. Nie, and Q. -Huo Liu, "Compact UWB slot antenna utilizing traveling-wave mode based on slot line transitions," *IEEE Trans. Antennas Propag.*, vol. 67, no. 1, pp. 140–150, Jan. 2019.

[48] Y. D. Dong, W. Hong, Z. Q. Kuai, and J. X. Chen, "Analysis of planar ultrawideband antennas with on-ground slot band-notched structures," *IEEE Trans. Antennas Propag.*, vol. 57, no. 7, pp. 1886–1893, July 2009.

[49] E. T. Ashong and Y. -Bae Jung, "Bandwidth enhancement and size reduction of printed monopole antenna using bounding box structure," *IET Microw. Antennas & Propag.*, vol. 13, iss. 9, pp. 1484–1490, Apr. 2019.

[50] J. R. Pierce, *Coupled modes*, in Almost All About Waves, *MIT Press*, Ch. 6, pp. 47, 1974.

[51] H. A. Haus and W. Huang, "Coupled-mode theory," *in proceedings of the IEEE*, vol. 79, no. 10, pp. 1505–1518, Oct. 1991.

[52] S. L. Chuang, "Waveguide couplers and coupled mode theory," in Physics of Optoelectronic Devices, 1st ed., New York, NY, USA: *Wiley*, Ch. 8, Sec. 2.2, pp. 291, 1995.

[53] J. -S. Hong, "Couplings of asynchronously tuned coupled microwave resonators," *in IEEE Proceedings-Microwaves, Antennas and Propagation*, vol. 147, no. 5, pp. 354–358, Oct. 2000.

[54] S. Liu, S. S. Qi, W. Wu, and D. G. Fang, "Single-layer single-patch four-band asymmetrical U-slot patch antenna," *IEEE Trans. Antennas Propag.*, vol. 62, no. 9, pp. 4895–4899, Sept. 2014.

[55] Y. -Ying Yang, Q. -Xin Chu, and Z. -An Zhe, "Time domain characteristics of band notched ultrawideband antenna," *IEEE Trans. Antennas Propag.*, vol. 57, no. 10, pp. 3426–3430, Oct. 2009.

[56] Z. N. Chen and M. Y. W. Chia, "Broadband planar antenna design and applications," *John Wiley & Sons.*, New York, NY, USA, 2006.

[57] W. Wiesbeck, G. Adamiuk, and C. Sturm, "Basic properties and design principles of UWB antennas," *Proc. IEEE.*, vol. 97, no. 2, pp. 372–385, Feb. 2009.

[58] M. Mahdavi, Z. Atlasbaf, and K. Forooraghi, "A very compact CPW-FED ultra-wideband circular monopole antenna," *Microw. Opt. Technol. Lett.*, vol. 54, no. 7, pp. 1665–1668, July 2012.

[59] R. Zaker and A. Abdipour, "Bandwidth enhancement and miniaturization of fork-shaped monopole antenna," *IEEE Antennas Wireless Propag. Lett.*, vol. 10, pp. 697–700, July 2011.

[60] M. Koohestani and M. Golpour, "U-shaped microstrip patch antenna with novel parasitic tuning stubs for ultra wideband applications," *IET Microwaves, Antennas & Propag.*, vol. 4, iss. 7, pp. 938–946, Feb. 2010.

[61] J. Pourahmadazar, C. Ghobadi, and J. Nourinia, "Novel modified pythagorean tree fractal monopole antennas for UWB applications," *IEEE Antennas Wireless Propag. Lett.*, vol. 10, pp. 484–487, Apr. 2011.

[62] A. Bekasiewicz and S. Koziel, "Compact UWB monopole antenna for internet of things applications," *Electron. Lett.*, vol. 52, iss. 7, pp. 492–494, Apr. 2016.

[63] T. Li, C. Zhu, X. Cao, and J. Gao, "Bandwidth enhanced of compact monopole antenna with triple band rejections," *Electron. Lett.*, vol. 52, iss. 1, pp. 8–10, Jan. 2016.

[64] M. S. Ellis, A. R. Ahmed, J. J. Kponyo, J. Nourinia, C. Gbobadi, and B. Mohammadi, "Miniaturised printed monopole antenna with a linked ground plane and radiator," *Electron. Lett.*, vol. 54, iss. 11, pp. 676–677, May 2018.

[65] S. Koziel and A. Bekasiewicz, "A structure and simulation-driven design of compact CPW-fed UWB antenna," *IEEE Antennas Wireless Propag. Lett.*, vol. 15, pp. 750–753, March 2016.

[66] X. Jiang, Z. Zhang, Y. Li, and Z. Feng, "A low-cost wideband circularly polarized slot array with integrated feeding network and reduced height," *IEEE Antennas Wireless Propag. Lett.*, vol. 15, pp. 222–225, Feb. 2016.

[67] S. Karamzadehl, V. Rafii, H. Saygin, and M. Kartal, "Polarisation diversity cavity back reconfigurable array antenna for C-band application," *IET Microw. Antennas Propag.*, vol. 10, no. 9, pp. 955–960, Feb. 2016.

[68] J. -Yi Sze and S. -Piao Pan, "Design of CPW-fed circularly polarized slot antenna with a miniature configuration," *IEEE Antennas Wireless Propag. Lett.*, vol. 10, pp. 1465–1468, Dec. 2011.

[69] M. -Shuang Wang, X. -Qi Zhu, Y. -Xin Guo, and W. Wu, "Compact circularly polarized patch antenna with wide axial-ratio beamwidth," *IEEE Antennas Wireless Propag. Lett.*, vol. 17, no. 4, pp. 714–718, Apr. 2018.

[70] W. -Ta Hsieh, T. -Hsuan Chang, and J. -Fu Kiang, "Dual-band circularly polarized cavity-backed annular slot antenna for GPS receiver," *IEEE Trans. Antennas Propag.*, vol. 60, no. 4, pp. 2076–2080, Apr. 2012.

[71] K. Kandasamy, B. Majumder, J. Mukherjee, and K. P. Ray, "Dual-band circularly polarized split ring resonators loaded square slot antenna," *IEEE Trans. Antennas Propag.*, vol. 64, no. 8, pp. 3640–3645, Aug. 2016.

[72] Nasimuddin, Z. N. Chen and X. Qing, "Dual-band circularly polarized S-shaped slotted patch antenna with a small frequency-ratio," *IEEE Trans. Antennas Propag.*, vol. 58, no. 6, pp. 2112–2115, June 2010.

[73] S. Lee, Y. Yang, K. Y. Lee and K. C. Hwang, "Dual-band circularly polarized annular slot antenna with a lumped inductor for GPS application," *IEEE Trans. Antennas Propag.*, vol. 68, no. 12, pp. 8197–8202, Dec. 2020.

[74] C. -Xu Mao, S. Gao, Y. Wang, Q. -Xin Chu, and X. -Xia Yang, "Dual-band circularly polarized shared-aperture array for C/X-band satellite communications," *IEEE Trans. Antennas Propag.*, vol. 65, no. 10, pp. 5171–5178, Oct. 2017.

[75] Q. Tan and F. -Chang Chen, "Triband circularly polarized antenna using a single patch," *IEEE Trans. Antennas Propag.*, vol. 19, no. 12, pp. 2013–2017, Dec. 2020.

[76] O. P. Fallade, M. U. Rehman, Y. Gao, X. Chen, and C. G. Parini, "Single feed stacked patch circular polarized antenna for triple band GPS receivers," *IEEE Trans. Antennas Propag.*, vol. 60, no. 10, pp. 4479–4484, Oct. 2012.

[77] J. G. Baek and K. C. Hwang, "Triple-band unidirectional circularly polarized hexagonal slot antenna with multiple L-shaped slits," *IEEE Trans. Antennas Propag.*, vol. 61, no. 9, pp. 4831–4835, Sept. 2013.

[78] P. M. Paul, K. Kandasamy, and M. S. Sharawi, "A triband circularly polarized strip and SRR-loaded slot antenna," *IEEE Trans. Antennas Propag.*, vol. 66, no. 10, pp. 5569–5573, Oct. 2018.

[79] T. V. Hoang, T. T. Le, and H. C. Park, "Quad-band circularly polarized antenna for 2.4/5.3/5.8-GHz WLAN and 3.5-GHz WiMAX applications," *IEEE Antennas Wireless Propag. Lett.*, vol. 15, pp. 1032–1035, March 2016.

[80] D. J. Bisharat, S. Liao, and Q. Xue, "Wideband unidirectional circularly polarized antenna with L-shaped radiator structure," *IEEE Antennas Wireless Propag. Lett.*, vol. 16, pp. 12–15, Feb. 2017.

[81] V. Rafii, J. Nourinia, C. Ghobadi, J. Pourahmadazar, and B. S. Virdee, "Broadband circularly polarized slot antenna array using sequentially rotated technique for C-cand applications," *IEEE Antennas Wireless Propag. Lett.*, vol. 12, pp. 128–131, Jan. 2013.

[82] Q. Luo, S. Gao, M. Sobhy, J. T. S. Sumantyo, J. Li, G. Wei, J. Xu, and C. Wu, "Dual circularly polarized equilateral triangular patch array," *IEEE Trans. Antennas Propag.*, vol. 64, no. 6, pp. 2255–2262, Jun. 2016.

[83] Y. Shen, S. -Gang Zhou, G. -Long Huang, and T. -Huat Chio, "A compact dual circularly polarized microstrip patch array with interlaced sequentially rotated feed," *IEEE Trans. Antennas Propag.*, vol. 64, no. 11, pp. 4933–4936, Nov. 2016.

[84] Y. Qasaymeh, A. Almuhasien, and K. Issa, "Design of compact dual circularly polarized ring series-fed quasi-lumped antenna array," *Progress In Electromagnetics Research.*, vol. 103, pp. 111–121, Jun. 2020.

[85] C. A. Balanis, "Antenna Theory: Analysis and Design," 4th ed. Hoboken, NJ: John Wiley & Sons; 2016.

[86] D. M. Pozar, "RCS reduction for a microstrip antenna using a normally biased ferrite substrate," *IEEE Microw Guided Wave Lett.*, vol. 2, no. 5, pp. 196-198, 1992.

[87] Y. -Xin Guo, L. Bian, and X. Q. Shi, "Broadband circularly polarized annular-ring microstrip antenna," *IEEE Trans. Antennas Propag.*, vol. 57, no. 8, pp. 2474-2477, Aug. 2009.

[88] Y. -Fang Lin, H. -Ming Chen, and S. -Chieh Lin, "A new coupling mechanism for circularly polarized annular-ring patch antenna," *IEEE Trans. Antennas Propag.*, vol. 56, no. 1, pp. 11-16, Jan. 2008.

[89] A. Ishikawa, T. Tanaka, and S. Kawata, "Frequency dependence of the magnetic response of split-ring resonators," *J. Opt. Soc. Amer. B, Opt. Phys.*, vol. 24, no. 3, pp. 510–515, March 2007.

[90] Q. Wu, Y. Cao, H. Wang, and W. Hong, "Machine-learning-assisted optimization and its application to antenna designs: opportunities and challenges," *China Communications*, pp. 152-164, Apr. 2020.

[91] Q. Wu, H. Wang, and W. Hong, "Multistage collaborative machine learning and its application to antenna modeling and optimization," *IEEE Trans. Antennas Propag.*, vol. 68, no. 5, pp. 3397-3409, May 2020.

[92] W. Y. Al-Rashdan and A. Tahat, "A comparative performance evaluation of machine learning algorithms for fingerprinting based localization in DM-MIMO wireless systems relying on big data techniques," *IEEE access*, vol. 8, pp. 109522-109534, Jun. 2020.

[93] M. T. Hagan and M. B. Menhaj, "Training feedforward networks with the Marquardt Algorithm," *IEEE Trans. Antennas Propag.*, vol. 5, no. 6, pp. 989-993, Nov. 1994.

[94] H. Demuth and M. Beale, "Neural network toolbox for use with MATLAB-user's guide version 4.0," MathWorks, Natick, MA, USA, Tech. Rep., 2004.

[95] R. S. M. -Castillo, E. Morgado, and R. G. -Esteban, "On the use of decision tree regression for predicting vibration frequency response of handheld probes," *IEEE Sensors Journal*, vol. 20, no. 8, pp. 4120-4130, Apr. 2020.

[96] T. M. Mitchell, *Machine Learning.* The McGraw-Hill Companies, Inc., 1997.

[97] L. Rokach, "Decision forest: Twenty years of research," *Information Fusion*, vol. 27, pp. 111-125, 2016.

[98] M. N. Adnan and M. Z. Islam, "Forest PA: Constructing a decision forest by penalizing attributes used in previous trees," *Expert Systems with Applications*, vol. 89, pp. 389-403, 2017.

[99] J. Han, J. Pei, and M. Kamber, *Data Mining: Concepts and Techniques.* Morgan Kaufmann Publishers, 2006.

[100] L. Breiman, J. Friedman, R. Olshen, and R. Stone, "Classification and regression trees," *in Regression Trees. CRC press*, pp. 216-265, 2017.

[101] T. Gneiting, "Compactly supported correlation functions," *Journal of Multivariate Analysis*, vol. 83, no. 2, pp. 493-508, 2002.

[102] [Online]. Available: https://mathbits.com/MathBits/TISection/Statistics2/correlation.htm.

[103] S. Gao, Q. Luo, and F. Zhu, "Introduction to circularly polarized antennas," *in Circularly Polarized Antennas.* Hoboken, NJ, USA: Wiley, pp. 1-28, 2013.

[104] W. C. Liu and P. C. Kao, "Design of a probe-fed H-shaped microstrip antenna for circular polarization," *J. Electromagn. Waves Appl.*, vol. 21, no. 7, pp. 857-864, 2007.

[105] E. Brookner, W. Hall, and R. Westlake, "Faraday loss for L-band radar and communications systems," *IEEE Trans. Aerosp. Electron. Syst.*, vol. AES-21, no. 4, pp. 459-469, Jul. 1985.

[106] S. C. Mukhopadhyay, A. Lay-Ekuakille, and A. Fuchs, *New Developments and Applications in Sensing Technology*, Berlin, Germany: Springer-Verlag, 2011.

[107] D. Gangwar, A. Sharma, B. K. Kanaujia, S. P. Singh, and A. Lay-Ekuakille, "Characterization and performance measurement of low RCS wideband circularly polarized MIMO antenna for microwave sensing applications," *IEEE Trans. Instrum. Meas.*, vol. 69, no. 6, pp. 3847-3854, Jun. 2020.

[108] F. -S. Chang, K. -L. Wong, and T.-W. Chiou, "Low-cost broadband circularly polarized patch antenna," *IEEE Trans. Antennas Propag.*, vol. 51, no. 10, pp. 3006-3009, Oct. 2003.

[109] K. M. Mak and K. M. Luk, "A circularly polarized antenna with wide axial ratio beamwidth," *IEEE Trans. Antennas Propag.*, vol. 57, no. 10, pp. 3309-3312, Oct. 2009.

[110] W. L. Langston and D. R. Jackson, "Impedance, axial-ratio, and received-power bandwidths of microstrip antennas," *IEEE Trans. Antennas Propag.*, vol. 52, no. 10, pp. 2769-2773, Oct. 2004.

[111] K. L. Chung, "A wideband circularly polarized H-shaped patch antenna," *IEEE Antennas Wireless Propag. Lett.*, vol. 58, no. 10, pp. 3379-3383, Oct. 2010.

[112] S. W. Zhou, P. H. Li, Y. Wang, W. H. Feng, and Z. Q. Liu, "A CPW-fed broadband circularly polarized regular-hexagonal slot antenna with L-shape monopole," *IEEE Antennas Wireless Propag. Lett.*, vol. 10, pp. 1182-1185, July 2011.

[113] R. K. Saini, S. Dwari, and M. K. Mandal, "CPW-fed dual-band dual-sense circularly polarized monopole antenna," *IEEE Antennas Wireless Propag. Lett.*, vol. 16, pp. 2497-2500, Aug. 2017.

[114] K. Ding, Y. X. Guo, and C. Gao, "CPW-fed wideband circularly polarized printed monopole antenna with open loop and asymmetric ground plane," *IEEE Antennas Wireless Propag. Lett.*, vol. 16, pp. 833-836, Apr. 2017.

[115] J. -Yi Sze and S. -Piao Pan, "Design of CPW-fed circularly polarized slot antenna with a miniature configuration," *IEEE Antennas Wireless Propag. Lett.*, vol. 10, pp. 1465-1468, Dec. 2011.

[116] L. Zhang, Y. C. Jiao, Y. Ding, B. Chen, and Z. B. Weng, "CPW-fed broadband circularly polarized planar monopole antenna with improved ground-plane structure," *IEEE Trans. Antennas Propag.*, vol. 61, no. 9, pp. 4824-4828, Sept. 2013.

[117] S. A. Rezaeieh, A. Abbosh, and M. A. Antoniades, "Compact CPW-fed planar monopole antenna with wide circular polarization bandwidth," *IEEE Antennas Wireless Propag. Lett.*, vol. 12, pp. 1295-1298, Aug. 2013.

[118] K. Ding, C. Gao, T. Yu, and D. Qu, "Broadband C-shaped circularly polarized monopole antenna ," *IEEE Trans. Antennas Propag.*, vol. 63, no. 2, pp. 785-790, Feb. 2015.

[119] A. Sharma, D. Gangwar, R. P. Singh, R. Solanki, S. Rajpoot, B. K. Kanaujia, S. P. Singh, and A. L. -Ekuakille, "Design of compact wideband circularly polarized hexagon-shaped antenna using characteristics mode analysis," *IEEE Trans. Instrum. Meas.*, vol. 70, pp. 6008308-6008308, Jun. 2021.

[120] W. Tan, X. Shan, and Z. Shen, "Ultrawideband circularly polarized antenna with shared semicircular patches," *IEEE Trans. Antennas Propag.*, vol. 69, no. 6, pp. 3555-3559, Jun. 2021.

[121] R. Xu, S. S. Gao, J. Liu, J. -Ying Li, Q. Luo, W. Hu, L. Wen, X -Xia Yang, and J. T. S. Sumantyo, "Analysis and design of ultrawideband circularly polarized antenna and array," *IEEE Trans. Antennas Propag.*, vol. 68, no. 12, pp. 7842-7853, Dec. 2020.

[122] B. Y. Toh, R. Cahill, and V. F. Fusco, "Understanding and measuring circular polarization," *IEEE Trans. Educ.*, vol. 46, no. 3, pp. 313-318, Aug. 2003.

[123] B. Li, Y. Deng, J. Zhang, and Z. Zhou, "Novel method for measuring the axial ratio of circularly polarized antennas based on the cross-polarization," *in Proc. 6th AsiaPacific Conf. Antennas Propag.*, (APCAP), pp. 1-3, Oct. 2017.

[124] M. Akbari, S. Gupta, M. Farahani, A. R. Sebak, and T. A. Denidni, "Gain enhancement of circularly polarized dielectric resonator antenna based on FSS superstrate for MMW applications," *IEEE Trans. Antennas Propag.*, vol. 64, no. 12, pp. 5542-5546, Dec. 2016.

[125] Y. T. Lo, D. Solomon, and W. F. Richards, "Theory and experiment on microstrip antennas," *IEEE Trans. Antennas Propag.*, vol. AP-27, pp. 137-145, Mar. 1979.

# LIST OF PUBLICATIONS

**Journal Publications:**

1. **Budhadeb Maity** and Sisir Kumar Nayak, "Design of compact microstrip-fed triple-band slot antenna with defected ground structure for wireless communications," *Journal of Electromagnetic Waves and Application*, Taylor Francis Ltd, pp. 1-15, Feb. 2022, doi.org 10.1080/09205071.2022.2041491, [Chapter 2].

2. **Budhadeb Maity** and Sisir Kumar Nayak, "Design of compact CPW-fed symmetrical staircase-shaped UWB antenna using transmission line model," *Progress In Electromagnetics Research C*, vol. 115, pp. 187-203, Sept. 2021 ,doi:10.2528/PIERC21073002, [Chapter 3].

3. **Budhadeb Maity** and Sisir Kumar Nayak, "Design of CPW-fed star-shaped monopole antenna for UWB applications using transmission line model," *Springer Wireless Personal Communications*, (under review) (Springer https://www.springer.com) [Chapter 4].

4. **Budhadeb Maity** and Sisir Kumar Nayak, "Compact quad-band CP series-fed circular slit microstrip array antenna using machine learning," *IEEE Access*, vol. 10, pp. 116650-116661, August 2022, doi: 10.1109/ACCESS.2022.3199656, [Chapter 5].

5. **Budhadeb Maity** and Sisir Kumar Nayak, "Compact UWB CP inverted L-shaped-hook monopole antenna with minimum $BR_{(10/3)dB}$ for wireless applications," (under preparation) [Chapter 6].

6. **Budhadeb Maity** and Sisir Kumar Nayak, "A super wideband CPW-fed elliptical slot monopole antenna for wireless applications," *Progress In Electromagnetics Research C*, vol. 130, pp. 139-154, Feb. 2023, doi:10.2528/PIERC22120505.

7. **Budhadeb Maity** and Sisir Kumar Nayak, "Compact bowtie-shaped microstrip patch antennas with low cross-polarization and wideband harmonic suppression," AEU - International Journal of Electronics and Communications, Elsevier (accepted).

**Conference Publications:**

1. **Budhadeb Maity** and Sisir Kumar Nayak, "A high gain sub-6-GHz array antenna for 5G applications," *IEEE international conference on Range Technology*, ICORT, ITR, DRDO, Chandpur, India, Feb. 2023.

2. S. K. Dash, **Budhadeb Maity**, S. Mohapatra, J. S. Varma, B. K. Behera, and J. R. Panda, "A planar concentric circular Ultra-wideband 5/6 GHz notch antenna for wireless application," *IEEE International Conference*, IITCEE, Bengaluru, India, Jan. 2023.

3. **Budhadeb Maity** and Sisir Kumar Nayak, "A high gain narrowband microstrip antenna array for wireless applications," *IEEE International Symposium on Antennas and Propagation*, ISAP, Taipei, Taiwan, pp. 1-2 Oct. 2021.

4. **Budhadeb Maity** and Sisir Kumar Nayak, "Design of compact CPW-fed microstrip slot antenna for S-band applications," *IEEE International Conference on Computing Communication and Networking Technologies*, ICCCNT, IIT Kharagpur, WB, India, July 2021.

5. **Budhadeb Maity** and Sisir Kumar Nayak, "Wideband CPW-fed U-shaped antenna array for WLAN and WiMAX applications," *IEEE International Conference on Computing Communication and Networking Technologies*, ICCCNT, IIT Kharagpur, WB, India, pp. 1-4, July 2020.

6. **Budhadeb Maity** and Sisir Kumar Nayak, "Compact CPW-fed multiband F-shaped slot antenna for wireless communications," *IEEE International Conference on Wireless Communications Signal Processing and Networking*, WiSPNET, SSN, Chennai, India, pp. 92-96, Aug. 2020.

7. **Budhadeb Maity** and Sisir Kumar Nayak, "CPW-fed double circular ring slot wideband antenna for WLAN/WiMAX applications," *IEEE International Conference on Wireless Communications Signal Processing and Networking*, WiSPNET, SSN, Chennai, India, pp. 122-125, Aug. 2020.

8. **Budhadeb Maity** and Sisir Kumar Nayak, "Design and analysis of T-slot microstrip patch antenna for WLAN applications," *IEEE international conference on Range Technology*, ICORT, ITR, DRDO, Chandpur, India, Feb. 2019.